Molecular clouds and stellar feedback: an investigation of synthetic line and continuum emission maps

vorgelegt von

Stefano Ebagezio
aus Torino, Italien

Köln, 2023

Sic luceat lux vestra coram hominibus
ut videant vestra bona opera
et glorificent Patrem vestrum qui in caelis est (Mt 5, 16)

ABSTRACT

Molecular clouds are complex systems and the search of adequate observational measurements to trace their evolution is still an open problem. In this thesis, we use produce synthetic emission maps of the ^{12}CO $(1-0)$, ^{13}CO $(1-0)$, [CI] $(1-0)$, and [CII] lines, as well as of the FIR continuum emission, to test to which extent these emission measurements can be used as tracers of the evolutionary stage of molecular clouds. We use numerical simulations of molecular clouds performed within the SILCC-Zoom project. These simulations include detailed stellar feedback due to ionizing radiation, external magnetic fields, and a chemical network evolved *on-the-fly*. We compare two different chemical networks, NL97 and NL99, and we find that NL97, even though it does not include neutral carbon, more accurately reproduces the abundances of CO and C^+. We then use NL97 in the rest of the work. We introduce a novel post-processing procedure for the C^+ abundance using CLOUDY, essential in HII regions to account for the higher ionization states due to stellar radiation. Furthermore, we show that assuming chemical equilibrium results in H and H_2 being underestimated and overestimated, respectively, by up to a factor of 2. The abundances of C^+ and CO are also, respectively, underestimated and overestimated. This is reflected and amplified in the estimation of the CO and [CII] luminosity as well. We also investigate the capability of the $L_{CO}/L_{[CII]}$ luminosity ratio to trace the H_2 mass fraction in the clouds, but find no clear trend. We then investigate the [CII]/FIR ratio in HII regions and in entire clouds with stellar feedback. In young HII regions the drop of the [CII]/FIR intensity ratio is mainly due to the strong FIR emission produced by hot and dense dust, and the contemporary saturation of the [CII] line. In more evolved HII regions, the second ionization of carbon is the main reason for the low [CII]/FIR ratio. The evolution of this ratio is reflected in the evolution of the $L_{[CII]}/L_{FIR}$ luminosity ratio in the entire clouds. This evolution can be schematized in three phases. Overall, $L_{[CII]}/L_{FIR}$ is well correlated with the total stellar luminosity $L_{\star,tot}$. The relation between $L_{[CII]}/L_{FIR}$ and $L_{\star,tot}$ can be fitted with a power-law. When $L_{\star,tot}$ is large, i.e., in evolved clouds which formed many massive stars, $L_{[CII]}/L_{FIR}$ is particularly low, determining an observable [CII]-deficit in these clouds. However, this relation breaks when the total FIR luminosity stars decreasing as a consequence of the cloud dispersal caused by the stellar feedback. The aspect of HII regions in molecular clouds strongly depends on the geometry of the cloud, and on the line of sight. Indeed, a certain HII region can have different properties when observed from different LOS, and apparent HII regions, which are actually only the result of projection effects, can be observed.

CONTENTS

List of Figures

1

INTRODUCTION

Star formation and the interstellar medium, in which and from which stars are formed, constitute a complex interplay. Our understanding of this interplay has increased much in the last decades. Back in 2008, the ASTRONET Science Vision Working Group, set up by several European funding agencies active in Astronomy, established a comprehensive long-term plan for the development of European astronomy. Four main scientific questions came as a result of this work: *What is the origin and evolution of stars and planets? How do Galaxies form and evolve? Do we understand the extremes of the Universe? How do we fit in?*

Even though these are very general questions, it is interesting to note that at least the first two have to do with the formation and the evolution of cosmic structures at different scales. The first question, in particular, clearly assesses the importance of studies to unveil the complex physics which regulates not only the pure stellar evolution, but also the conditions and environments which make the star formation possible in the first place and the effects that formed stars have on the environment where they formed.

Because of this, it is not surprising that in the last years the field of research has made substantial progress. First of all, important space missions have been providing new high-quality observations of star-forming environments. This is the case, for instance, of the SOFIA mission, which provided fundamental observations of the [CII] 158 μm line, and many other lines as well, for a lot of star-forming regions, or of the Herschel mission, which allowed unprecedented access to the far-infrared spectral range with instruments optimized for star formation research, or even of the ALMA telescope array. Recently, the James Webb Space Telescope has been launched and infrared images of the Universe with unprecedented quality are expected to come, and the first, preliminary images obtained even reinforce these expectations. Furthermore, the Fred Young Submillimeter Telescope in Chile will provide, presumably from 2024, high-quality images at submillimeter to millimeter wavelengths, enabling, for instance, mapping of the [CII] at high-redshift, throwing new light on the cosmic cycle of star formation in the early Universe.

Spectroscopic observations of star-forming regions clearly show that their chemical variety is huge. Because of this, a broad understanding of the processes which participate in the cosmic cycle of star formation must necessarily include the knowledge of the chemical species and reactions that populate the interstellar medium. Spectroscopic observations permitted to discover several hundreds of chemical species and laboratory spectroscopy achieved extremely important results in terms of understanding the properties of the chemical species observed in relation to the different environments. In this context, the Cologne Database for Molecular Spectroscopy and the Leiden Atomic and Molecular Database are two important databases for atomic and molecular species relevant in an astronomical context. The physics and the chemistry of the interstellar medium are deeply interconnected: the abundance of the different species depend on the physical conditions of the interstellar medium. In turn, its chemical configuration affects the evolution, since heating and

cooling processes, as well as the star formation itself, are influenced by the type and abundance of the various chemical species.

Numerical simulations play an important role in helping and improving the understanding of the cycle of star formation. By means of numerical simulations of the interstellar medium it is possible to reproduce the processes which create molecular clouds (the dense regions of the interstellar medium where stars actually form) and determine the star formation. It is also possible to simulate the effects that star formation has on these molecular clouds, namely the dissipation and, eventually, the destruction of the cloud because of the stellar feedback, reproducing in this way the cosmic cycle of star formation.

Comparing the results from numerical simulations, in which the included physics and the chemistry is exactly known, with real observations enables, in principle, to throw light on the real physics and chemistry of the interstellar medium. However, such a comparison is often difficult because of the insufficient realism either of the physics of the chemistry or the numerical simulations. It is, indeed, very difficult to accurately model, at the same time, both the complex physics of the interstellar medium and the equally complex chemistry. The difficulties typically concern both the implementation of these complex phenomena into working code and the enormous computational time which would be required to accurately model both the physics and the chemistry at the same time. Because of this, most simulations tend to favour either the complexity of the chemical network included, or the completeness of the physical phenomena modelled.

The work presented in this thesis aims to give a contribution towards the reduction in this gap between simulations and real observations. We use state-of-the-art simulations of the life-cycle of molecular clouds, with many complex physical phenomena included (momentum injection by means of supernova explosions, self-gravity, magnetic field, gas heating and cooling, star formation and stellar feedback, for instance) and chemical networks which traces the evolution of a relatively large number of species. We produce synthetic emission maps of the simulated molecular clouds which can be used, in principle, for comparison with real observations. We focus, in our analysis, on the emission from carbon-bearing species and dust grains. This is motivated by the fact that many high-quality observations of these elements have become available in recent years (e.g., thanks to the already mentioned SOFIA, Herschel, and ALMA).

The main questions we aim to answer in this work are:

1. To which extent the chemical networks we use are reliable in predicting the observed abundances and properties of the species of our interest? (Chapter 6)

2. How can the molecular hydrogen in the interstellar medium be traced adequately by the other chemical species that we model? (Paper I and Chapter 6)

3. Which physical phenomena must be taken into account to accurately reproduce the observed [CII] line emission coming from HII regions? (Paper I)

4. Which information can be obtained about the evolution of HII regions and star-forming molecular clouds by analysing their [CII] and FIR continuum emission? (Paper II)

The scientific results listed above are accompanied by an overview of the relevant physical and chemical processes which determine the evolution of the interstellar medium (Chapter 2). Furthermore, Chapter 3 provides an accurate description of the numerical methods used in the simulations and in the radiative transfer

calculations. In this context, the code used to post-process the abundance of C^+ in the HII regions is shown, with comments, in the Appendix A, as it has been used for the first time for the work described in this thesis.

2

ASTROPHYSICAL BACKGROUND

It is well known that stars form in particular regions of the so-called interstellar medium (ISM), a gaseous medium which permeates the space between the stars in a galaxy. This is, however, a relatively recent discovery, as in the old worldview they were supposed to be eternal objects located in a spherical shell surrounding the rest of the universe, not subject to the physical laws that rule the terrestrial world.

Fundamental milestones in the understanding of the star formation are the works of Ambartsumian (1949) and Becklin & Neugebauer (1967). The first consists in the estimation of the age of a certain type of stellar cluster which turned out to be only 10^6 years old, the second is the first evidence of ongoing star formation, namely a black body source in the Orion nebula bright in infrared, but with no optical counterpart. These two fundamental works lead the scientific community to realize that most stars are much younger than the age of the universe and that star formation is not a phenomenon only of the early stage of the universe, but happens at any cosmic time and, in particular, is still ongoing at present days in specific regions of the galaxies.

These and many other scientific works indicated that the ISM is ultimately the origin of new stars. Understanding star formation means then unveiling the relation between the ISM and stars. This task is far from complete: its complexity derives from the enormous variety in physical and chemical processes involved, as well as from the different environments. Noting that, as a mere example, the typical density of a medium-size star (the Sun, for instance) has a typical number density of 10^{23} cm^{-3} and the average density of all ISM is only approximately 1 cm^{-3} probably gives an impression of such variety that one needs to consider to investigate star formation. In this huge abundance of environments, a primary role is played by a particular phase of the ISM called *molecular clouds* (MCs). These are, as the name suggests, particularly dense ($\gtrsim$ 100 cm^{-3}) and cold regions where hydrogen is mostly in molecular form. These are actually the birthplace of stars and because of this they are often referred to as *stellar nurseries*. As we are interested in star formation, this phase of the ISM will be studied in detail in this thesis.

The ISM is composed of several elements. Hydrogen is by far the most common and can be found in ionized (H$^+$), neutral (H), and molecular (H$_2$) form. The second most common element is helium (He), followed by all the other natural elements of the periodic table, to which astronomers generically refer as *metals*. Among all them, in this thesis we will consider in particular carbon in its atomic form, single and double ionized forms (C, C$^+$ and C^{2+}), as well as carbon monoxide (CO). Furthermore, a small fraction of the ISM, typically of the order of 1% in number density, is composed of small dust grains, with typical size of approximately 100 micrometers, and mostly consisting in carbonaceous and silicate species.

Astronomers observe the ISM in a broad range of wavelengths, using both the line emission of the various gas species and the continuum emission coming from dust. These observations are then used to infer the characteristics of the different regions of the ISM, such as density, temperature, magnetic fields strength, star form-

ation rate and many other quantities. In the following, we describe with more detail the properties of the ISM, as well as the physics concepts needed to understand the results obtained in this work.

2.1
The Interstellar Medium

2.1.1
Composition of the ISM

The ISM is defined as the medium permeating the space between stars in a galaxy. Its main components are gas, dust, radiation fields, magnetic fields, and cosmic rays. We now briefly describe each of these components; then, we describe the various states that the ISM can assume.

Gas

Interstellar gas constitutes, in terms of mass, the vast majority of the ISM. Hydrogen is by far the most abundant element within the interstellar gas: it represents about 70% of the total gas mass. After hydrogen, the second most common element is helium, which represents approximately 28% of the gas mass. The remaining 2% is constituted by *metals*, that is, in astronomy, all elements with atomic number larger than 2 (Li, Be, ...) (Draine, 2011).

The hydrogen gas can be found in ionized (H^+), neutral (H), and molecular (H_2) form. As reported in Draine (2011), atomic hydrogen is, in mass, the most common form in the ISM, representing about 60% of the total hydrogen. Then, 23% of hydrogen is ionized and 17% is molecular. In any case, these numbers might be, in a certain sense, misleading, as H^+ is typically located in much less dense regions than H, and therefore the volume of ISM filled with ionized hydrogen is even larger than the volume filled with atomic hydrogen. If we consider the volume filling factors, defined simply as the ratio between the volume occupied by a certain species and the total volume (of the ISM, in this case), we find that H^+, H, and H_2 have volume filling factors of 0.64, 0.31, and 0.05, respectively (Spitzer, 1978; Tielens, 2005). Looking at the mass and volume fractions of the different states of hydrogen we can already learn than H^+ generally occupies vast, diffuse regions of the ISM and that H_2 is mainly located in very dense, albeit small, regions, and this is why its volume filling factor is so small, whereas the mass fraction is much larger. Atomic hydrogen exhibits intermediate features between H^+ and H_2.

As opposed to hydrogen and helium, which are mostly created during the big bang, metals are only produced in complex thermonuclear reactions in the stars or during supernova explosions and ejected in the ISM. It is worth mentioning that, even if they only constitute about 2 % of the gas mass, and even less in terms of number density as they are heavier than hydrogen, metals play an important role in the physics and the chemistry of the ISM, mostly by cooling the gas. Because of this, the amount of metals is a crucial parameter in the description of the ISM.

Dust

The dust mass in the ISM is of the order of 1% of the gas mass (Hildebrand, 1983; Klessen & Glover, 2016). Typical grain sizes are $5 - 250$ nm and, although numerous chemical elements contribute to form them, they can be modeled as a mixture
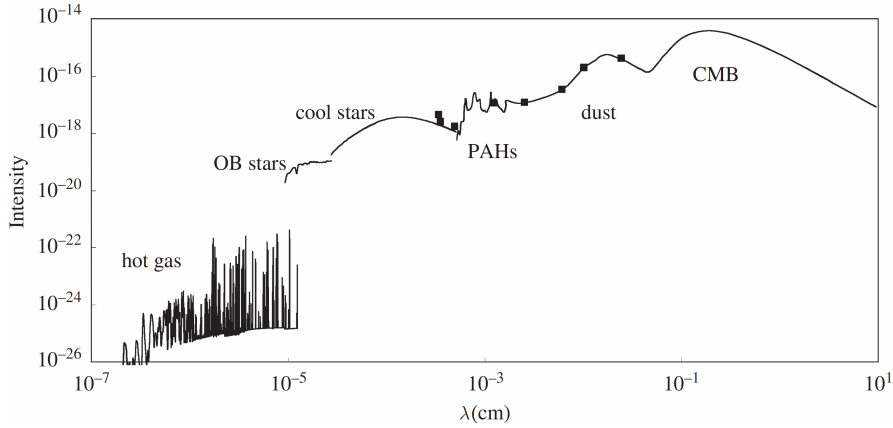
Figure 1: The mean intensity (in erg cm^{-2} s^{-1} Hz^{-1} sr^{-1}) of the ISRF in the solar neighborhood. The highest energy part of the spectrum, i.e., the shortest wavelengths, is dominated by the hot gas. Then, moving to longer wavelengths, the spectrum is dominated by stellar radiation, polyciclic aromatic hydrocarbons (PAHs), stellar dust and, at the lowest energies, by the cosmic microwave background (CMB). Figure is taken from Tielens (2005).

of carbonaceous and silicate grains (Weingartner & Draine, 2001). Dust plays a role mainly in producing a general extinction of the light from distant sources, because of absorption and scattering, and in polarizing the starlight because of the alignment of the dust grain with the galactic magnetic fields. Furthermore, gust-grain reactions are relevant for the chemistry of the ISM (see e.g. Holdship et al., 2017).

Radiation fields

Besides the "massive" part of the ISM, composed of gas and dust, the interstellar medium is also permeated by electromagnetic fields, generated by a number of physical phenomena happening inside and outside the galaxies. Overall, we refer to this radiation as the interstellar radiation field (ISRF).

The ISRF spectrum spans over a large range of wavelengths: as shown in Fig. 1, there is radiation from $\sim 10^{-7}$ cm (corresponding to 10 Å) up to over 10 cm. We can divide the spectrum in several regimes:

- *Extreme ultraviolet* (EUV) regime, corresponding to $\lambda < 912$ Å, that is, those wavelengths shorter than the *Lyman limit*, the ionization energy of hydrogen (13.6 eV). In this regime, where we include also X- and Gamma-rays, emission is dominated by bound-bound, bound-free, and free-free emission in hot plasmas and, at the most extreme energies, by extraglactic sources as well. There are also numerous emission lines in this regime.

- *Far ultraviolet* (FUV) regime, roughly spanning from the aforementioned Lyman edge to ~ 4 eV, or 310 nm. In this regime, O- and B-type hot stars are the main radiation sources. The FUV regime is of particular interest for the study of molecular clouds and the ISM in general, as it is strongly connected with the hydrogen chemistry. Indeed, this regime has been studied deeply for decades: a pioneer in this field was Harm Habing, who gave the name to the *Habing field*, corresponding to 1.2×10^{-4} erg cm^{-2} s^{-1} sr^{-1} (Habing, 1968). A decade later, Draine (1978) estimated the typical FUV intensity in the solar neighborhood to be $G_0 = 1.7$ Habing fields. This is still the canonical value

used.

It is worth mentioning than even if the most of the spectrum of such OB stars lies in the FUV regime, a non-negligible fraction of photons emitted have energy higher than 13.6 eV and are therefore able to ionize the hydrogen surrounding them. This creates the so-called *HII regions* (see below in this chapter).

- *Visible* light, as well as soft UV and near infrared (NIR) is dominated by later type stars, as well as by Policycle Aromatic Hydrocarbons (PAHs), mostly in the NIR.

- *Far infrared* (FIR), including wavelengths from a few μm to ~ 1000 μm (for instance, it is assumed to be the region between 3 and 1100 μm in Pabst et al. (2022)). Here, the dust continuum emission, typically by dust grains absorbing starlight, dominates the spectrum.

- the *microwave* regime is dominated, as the name itself suggests, by the Cosmic Microwave Background (CMB), which is relevant for wavelengths larger than ~ 600 μm. The CMB spectrum is a practically perfect black body spectrum at a temperature of 2.726 K (Fixsen, 2009).

Magnetic fields

Magnetic fields play a major role in controlling the dynamics of the gas in the ISM. In the Galactic midplane, recent measurements (e.g. Beck & Wielebinski, 2013) suggest it to be about 3 μG. Of course, we cannot observe magnetic fields directly: the most common ways to infer information about it is observing the linear polarization of starlight dust continuum emission, as well as the Faraday rotation of background, polarized radio sources, and Zeeman splitting of the 21 cm lines (Tielens, 2005). Recent observations, like the ones carried out by Planck Collaboration et al. (2016); Soler et al. (2017); Planck Collaboration et al. (2020) and many more, show very detailed measurements of magnetic field morphology in nearby clouds. By looking at those measurements, one immediately realizes that the shape of the magnetic fields in a given region of the ISM is quite complicated.

In general, the amplitude of the magnetic field increases with the gas density. The simplest model to understand that is to assume a sphere of gas with isotropic density uniformly collapsing. In this case, the number density is $n \propto r^{-3}$, where r is the (decreasing) radius of the sphere. The module of the magnetic field, B, is related to r by $B \propto r^{-2}$ (this is the so-called *flux freezing*, a consequence of the Maxwell equations). As a consequence, $B \propto n^{2/3}$. A good number of numerical simulations show good agreement with this assessment as long as B is weak. In case of strong magnetic fields, the relation between B and n is $B \propto n^{1/2}$ (Hennebelle & Inutsuka, 2019). This is a consequence of energy equipartition between magnetic and kinetic energy. The aforementioned review by Hennebelle & Inutsuka (2019) nicely discusses in more extensive way this topic. The densest regions of the ISM tend to assume either spheroidal, sheet-like, or filamentary structures (see e.g. Ganguly et al., 2022). In such structure, it is of interest to investigate the relative direction of the magnetic field **B** with respect to the structures themselves. Indeed, magnetic fields have an impact on the evolution of such structures and their effects depend both on the strength and on the direction of **B**. We will discuss it in detail in Section 2.2

Cosmic rays

Cosmic rays are an important source of energy in the ISM. They are relativistic particles mainly constituted of protons ($\lesssim 90\%$), α particles (He nuclei) ($\sim 10\%$), and about the 1% of heavier elements and electrons (Draine, 2011). They both give support against gravity for the gas in the ISM and heat and ionize the interstellar gas, even deep penetrating deep into the dense part of the ISM. As a result, the chemistry of the ISM is strongly influenced by the intensity of the cosmic rays flux (see e.g. Bisbas et al., 2021). They also trigger the beginning of gas outflows and have an impact on the outflow phase structure (Rathjen et al., 2022).

2.1.2

Phases of the interstellar medium

The interstellar medium, as we already mentioned, includes a huge variety of environments, characterized by different densities, temperatures, and ionization fractions. Based on these features, a common (for instance Ferrière, 2001; Tielens, 2005; Klessen & Glover, 2016, and many more) classification of the different regions of the ISM is the following:

- *Hot intercloud medium*, or *hot ionized medium* (HIM): it is the hottest ($\sim 10^5 - 10^6$ K) and least dense ($\sim 10^{-3}$ cm^{-3}) component of the ISM. This is the dominant component in the galactic halo and it is believed to be produced mainly trough shocks driven by supernovae explosions and stellar winds.

- *Warm ionized medium* (WIM): it is a mostly diffused component with typical density of $\sim 10^{-1}$ cm^{-3} and temperature of ~ 8000 K. The WIM represents about nine tenths of the total ionized gas in the ISM (Haffner et al., 2009). Here, the ionization is mostly due to collisions. Recently, denser environments (~ 10 cm^{-3}) with ionized gas have also been found; these are supposed to be ionized trough extreme ultraviolet photons from nearby star-forming regions (Langer et al., 2021).

- *Warm neutral medium* (WNM) and *cold neutral medium* (CNM): these are the two possible phases where neutral medium can be found. Observing the 21 cm emission line of atomic hydrogen is by far the most common way to trace this type of gas phase. The WNM has properties similar to the WIM (but of course it is mostly neutral), whereas the CNM has a typical density of ~ 50 cm^{-3} and temperature of ~ 100 K. The latter is mostly found in clumps (atomic clouds) with typical size of 50 pc (Spitzer, 1978); on the other hand, the WNM is in general diffuse, intercloud gas.

- *Molecular clouds* (MCs): they are the densest part of the ISM, where the gas is mostly molecular. They have typical temperatures of ~ 10 K and density of a few 100 cm^{-3}. These are the sites where star formation occurs. Because of their great relevance in the work presented in this thesis, we will describe their structure and avolution more in detail in the following (Section 2.2).

The different phases of the ISM are to some extent a didactic simplification to classify the complexity of the ISM, but on the other hand these different phases do have a physical meaning in term of stability. Indeed, not all possible gas conigurations within the ISM turn out to be stable over time: for instance, Field et al. (1969) showed that CNM and WNM are two stable solutions for an atomic gas in

thermal equilibrium. Any other configuration would be unstable and tend either to the CNM or the WNM configuration. Similarly, McKee & Ostriker (1977) claimed that supernovae explosions must lead to the formation of HIM and that such a HIM is quasi-stable.

2.1.3

Physical processes in the interstellar medium

There are numerous physical processes happening in the ISM. In this section we will give an overview of the main heating and cooling processes, as well as of the role played by turbulence and magnetic fields. We do not aim to be exhaustive here, as these processes would require several chapters in order to be described accurately and is out of scope for this thesis: what we aim to do here is to mention these processes and quickly describe them as long as the majority of them is included in the numerical simulations we work on. We refer to the cited literature for more details about these processes.

Gas heating

Gas heating is generally dominated by processes which couple the gas to the radiation field. In particular, this often happens through photo-ionization processes where ionizing photons hit dust grains and eject electrons which results in having a fraction of the incident energy converted in kinetic energy. Then, this kinetic energy is quickly distributed among the other atoms and ions in the gas (Bakes & Tielens, 1994; Wolfire et al., 2003) by collisions. If there are photons more energetic that 13.6 eV, hydrogen can be ionized forming H^+: this is a *HII region*. Vice versa, in case only photons with energy lower than 13.6 eV are available, hydrogen stays in atomic form, and only larger stable molecules and small dust grains are ionized.

Besides ionization, photodissociation plays also a role in heating the gas in molecular regions. Strong FUV fields dissociate H_2 molecules into H atoms. The regions where this phenomenon is relevant are indeed called *photodissociation regions* (PDRs). This process releases on average an energy of ~ 0.4 eV into the cloud for each dissociation (Black & Dalgarno, 1977). Furthermore, dust can also absorb photons, resulting in a heating process that leds, in turn, to the heating of the gas via collisions (e.g. Tielens, 2005).

Similarly, X-rays and CRs can heat up the ISM via collisional processes in the well-shielded gas. Indeed, these can penetrate deeply into the ISM and heat the gas significantly through collisions with the gas particles (Glassgold & Langer, 1973).

Finally, it is worth mentioning that collisonal de-excitation (the collision of an excited atom/molecule with another one and the transfer of such energy to the collided one in form of kinetic energy) of H_2 can also be important as a source of heat in those dense regions where the collisional timescale is smaller than the radiative decay timescale. Also the formation of the H_2 molecule itself is a source of heating, as it releases 4.48 eV energy per molecule (Goldsmith & Langer, 1978).

Gas cooling

Gas cooling is closely connected with line emission. Indeed, gas cools when its particles move from a higher to a lower excited state and, by doing this, emit a photon. The energy of this photon depend on the nature of the transition and on the quantum mechanics laws which regulate them. In principle, there are really a large number of transitions happening in the ISM. Practically, a few of them are

important and depend on the temperature of the gas.

At high temperatures, dipole-allowed transitions are dominant. In particular, at around $10\,000$ K the Lyman-α emission line dominates. At even higher temperatures, cooling due to metals is more important.

At lower temperatures, fine structure transitions are relevant: the most important example here is definitely the fine structure transition of C^+ at 158 μm, indicated with [CII], which dominates the cooling in cool gas (~ 100 K) (see e.g. Wolfire et al., 1995; Guevara et al., 2020, and many more). Due to the great importance of this line transition for this work, we will described it more in detail later on in this thesis (Section 2.4.2).

At temperatures of about 10 K, carbon monoxide (CO) is another important coolant of the gas. Line emission of CO is the result of rotational transitions and again, due to the great importance of this molecule for this work, we will describe it in more detail in Section 2.4.3.

Finally, dust also acts to some extent as a gas cooler (Leung, 1975; Hollenbach & McKee, 1989; Goldsmith, 2001). At sufficient low density, dust and gas are coupled trough collisions. As dust can quite efficiently radiate by continuum emission, it can possibly be colder than the surrounding gas. In this case, heat is transferred from gas to dust by means of collisions and then further irradiates trough FIR photons.

Turbulence

The different phases of the ISM have their characteristics because of the heating and cooling processes described above. As we said, they are, to some extent, a convenient classification, but on the other hand they also have stability properties because of which the ISM tend indeed to reach one or the other configuration. However, thermal instability and stellar feedback create turbulence and mix the gas.

The *Reynolds number* is defined as

$$\mathrm{Re} = \frac{\rho v L}{\mu} \, , \tag{2.1}$$

where ρ is the density of a fluid, v its velocity, L a characteristic length of the considered phenomenon, and μ the dynamical viscosity. A low Re indicates laminar flow, and a high Re indicates turbulent flow. In the cold ISM, for instance, Re $\sim 10^5 - 10^7$ (Elmegreen & Scalo, 2004), which definitely indicates a turbulent flow.

Turbulence means, by definition, that a fluid is subject to chaotic changes in pressure and velocity. Still, there exist theories of turbulence. The first one, for incompressible fluids, is by Kolmogorov (1941). The idea is that the turbulent flow is composed by "eddies" of different sizes. These different sizes are associated with different characteristic lengths and velocities. The large eddies are unstable and because of that they tend to break up and create smaller eddies, and the kinetic energy of the initial large eddy is divided into the smaller eddies that stemmed from it. This process is repeated several times and smaller and smaller eddies are formed and it is known as *energy cascade*, originally discussed by Lewis F. Richardson in 1920s. Finally, the eddies reach a sufficiently small length scale and the viscosity of the fluid can effectively convert the kinetic energy into internal energy. Energy is thus injected into the system at a large length scale, the *injection scale*, and, due to the process described, is dissipated at the *dissipation scale*, much smaller than the

injection scale. To formally express Kolmogorov's results, one has to first consider the velocity field of the fluid $\mathbf{u}(\mathbf{x})$. Then, one defines

$$\hat{\mathbf{u}}(\mathbf{k}) = \mathcal{F}\{\mathbf{u}(\mathbf{x})\} \, , \tag{2.2}$$

where $\hat{\mathbf{u}}(\mathbf{k})$ is the Fourier transform of $\mathbf{u}(\mathbf{x})$. Indicating with u_i the i-th component of $\hat{\mathbf{u}}(\mathbf{k})$, one defines the *energy spectrum* $E(k)$ such that $E(k)dk$ is the contribution to the kinetic energy given by the modes with $k, |\mathbf{k}| < k + dk$. Kolmogorov found that, for isotropic incompressible fluids,

$$E(k) \propto k^{-5/3} \, . \tag{2.3}$$

More complicated (and realistic) configurations, such as compressible fluids or presence of magnetic fields, change the exponent of k, but the general idea of the theory is preserved, as well as the role of the turbulence in the ISM, which is being the primary source of kinetic energy, as well as confining structures as a consequence of compressive velocity fluctuations.

There are several possible sources of turbulence in the ISM. Klessen & Glover (2016) identify four main phenomena originating turbulence, which are:

- gas accretion onto the galaxy through the cosmic web;

- rotational energy of the galactic disk;

- magnetorotational instabilities which happen in the galactic disk;

- supernova explosions, stellar winds, massive star radiation, and in general phenomena connected with stellar evolution.

The importance of those phenomena depend on the amplitude of the portion of the ISM considered. In this thesis we are mostly interested in dense, relatively small (~ 100 pc) regions in association with star formation and stellar evolution. Therefore, the driving of turbulence by means of stars will be, for us, the most relevant process.

2.2
Molecular clouds

Molecular clouds (MCs) are dense and cold regions of the ISM, where hydrogen is mostly in molecular form. Due to their high density, MCs are the regions where star formation actually happens. As we mentioned in Section 2.1.2, they are characterized by a typical temperature of ~ 10 K and a desity of some 100 cm^{-3}. In any case, they actually exhibit a large variety of physical conditions. A commonly used way to classify MCs uses the *visual extinction* A_V (Snow & McCall, 2006; Draine, 2011, for instance). This is a quantity which expresses how much radiation, typically FUV, is suppressed by the cloud. Intuitively, it is a measure of how "thick" the cloud is. The visual extinction is related with the column density of the cloud. Specifically,

$$A_V = A_{V,0} N_{tot} \, , \tag{2.4}$$

with N_{tot} the total column density of the cloud and $A_{V,0} = 1.87 \times 10^{21}$ mag cm^2 (Draine & Bertoldi, 1996; Glover et al., 2010)[1]. Based on that, MCs can be classified

---

[1]Other works assume slightly different values for $A_{V,0}$. For instance, Weingartner & Draine (2001); Röllig et al. (2007) assume 6.3×10^{22} mag cm^2 at solar metallicity

as

- *diffuse clouds*, if $A_V \sim 1$. These are typically small (~ 3 pc) and relatively warm ($T \sim 50$ K). Their typical mass is of about 50 $M_\odot$.

- *giant molecular clouds* (GMCs), if $A_V \gtrsim 2$. These have a number density of $n \sim 100$ cm^{-3} and temperature of about 15 K. They are the most massive clouds (~ 50 $M_\odot$) and size of $50 - 100$ pc. in this thesis, we will analyse mostly simulations of GMCs.

- *dark clouds*, if $A_V \sim 5$. They are somehow smaller, (~ 10 pc) and denser ($n \sim 500$ cm^{-3}) than GMCs.

- *dense cores*, if $A_V \sim 10$. Within these cores star formation actually takes place. They are characterized by small dimension (~ 0.1 pc) and high density (~ 10 cm^{-3}).

Even more than for the phases of the ISM, it is important to stress that this is a way of classifying a huge variety of environments, and therefore real (and simulated) clouds often have intermediate properties among those listed before. Furthermore, embedded structures are likely to occur: for instance, dense cores are normally located inside a less dense cloud (e.g., a GMC), as they are the result of the gravitational collapse of the larger cloud which surrounds them.

2.2.1

Life-cycle of molecular clouds

We summarize now briefly the *life-cycle* of a molecular cloud, that is, the processes leading to the formation of the cloud itself, the creation of structures and dense cores, the star formation, and the destruction of the cloud.

Cloud formation

Two fundamental works by Oort (1954) and Field (1965) suggest that MCs form due to thermal instability in warmer atomic gas. This initially forms small clouds which, by means of collisions, later dissipate energy and stick together. This simple model, however, cannot easily explain the formation of the largest MCs, especially given their relatively short lifetime. In the following decades, more refined models, normally implying the presence of converging flows of material, aimed to explain cloud formation more in detail. There are several phenomena that can drive such flows, and they probably operate together with each other. Some of these proposed phenomena are the Parker instability (Parker, 1966), where the gas accumulate as a consequence of the bending of magnetic field lines, a large-scale gravitational instability in the galactic disk, and compression due to supernovae (Inutsuka et al., 2015), which produce bubbles of gas with dense shells, where converging flows actually occur.

Structures and dense cores formation

Molecular clouds do have an internal structure. Studies on both observation and simulation sides (see e.g. Ganguly et al., 2022) show that MCs have a internal hierarchical structure where overdensities have a filamentary, sheet-like or spheroidal aspect. In the last decades, two main mechanisms have been investigated in order

to explain such structure formation: the *gravo-turbulent* and the *global hierarchical collapse* scenarios.

The gravo-turbulent scenario was originally proposed by Zuckerman & Evans (1974) and much refined in later years (e.g. Mac Low & Klessen, 2004; McKee & Ostriker, 2007; Hennebelle & Falgarone, 2012). Essentially, the idea is that the molecular cloud structure represents a turbulent cascade. External sources, such as supernova explosions, drive energy into the ISM. Then, energy is transferred to smaller scales (see *Turbulence* in Section 2.1.3) up to scales of about 0.1 pc. Structures forming at different scales are supersonically turbulent, and this prevents them from gravitational collapse. In this way, asymmetric structures (filaments, for instance) are a consequence of the inhomogeneous nature of turbulence. At ~ 0.1 pc, turbulence becomes subsonic, and this allows the formation of gravitationally bound cores, which are where star formation actually takes place (Arzoumanian et al., 2013).

On the other hand, the global hierarchical collapse scenario argues that MCs are undergoing multi-scale, multi-epoch gravitational collapse. This determines a mass and energy cascade, which is the analogous of the turbulent cascade in the gravo-turbulent scenario. The time scale of the collapse at small scales is shorter than at large scales: this means that dense cores collapse first and form stars, whose feedback disperses the parent clouds, counteracting the collapse still ongoing at larger scales. This prevents the cloud from a global collapse, i.e. keeps the star formation efficiency low, as widely observed (Leroy et al., 2008, for instance). A complete overview of this scenario can be obtained in the review paper by Vázquez-Semadeni et al. (2019).

There are, in principle, observations and measurements which can be done in order to discriminate between the two scenarios described above. As we explained, the gravo-turbulent scenario predicts unbound, or nearly virialized, clouds, whereas the global hierarchical collapse scenario implies gravitationally bound clouds. Some observations of gravitational accretion flows seem to support the presence of bound clouds, even though a bias of such observations towards dense structures (which tend to be bound in both scenarios) might undermine their reliability in favouring the global collapse scenario (Chevance et al., 2022). Also, in the gravo-turbulent scenario the star formation rate (SFR) should be constant throughout the entire lifetime of the MCs, whereas in the other scenario it should progressively increase till the onset of stellar feedback. Observtions are conflicting in this aspect, too. Overall, there is still no unanimously accepted answer on the most realistic structure formation scenario.

Star formation

Any model aiming to describe star formation in dense core has to explain some observational facts, the most important of which is the stellar initial mass function (IMF). This is the distribution of mass of the newly-formed stars, and it is found to be remarkably similar for even very different environments. The IMF is typically described as a power law:

$$\frac{dN}{dM} \propto M^{-\alpha} \, , \tag{2.5}$$

with $\alpha = 2.3$ (Salpeter, 1955; Kroupa, 2001) at solar metallicity. This distribution applies for quite massive stars ($\gtrsim 1\,\mathrm{M_\odot}$). There are two primary models which attempt to explain star formation and, in particular, the origin of the IMF: the *competitive accretion* and the *turbulent fragmentation* scenarios.

The competitive accretion scenario assumes that the dense ISM medium initially collapses because of the Jeans instability (Jeans, 1902; Binney & Tremaine, 2008) and forms sorts of "proto-protostars" which competitively accrete mass from the environment. This phenomenon, in its simplest form, is known as the *Bondi-Hoyle accretion* (Hoyle & Lyttleton, 1941; Bondi, 1952). This simple model has been refined in subsequent decades to better account for the observed IMF dsitribution (Eq. (2.5), which the simple Bondi-Hoyle accretion scenario could only broadly reproduce) and now, in its typical expression, assumes that an initial protostar cluster, where all the protostars are roughly at the Jeans mass, experience N-body interaction. As a consequence, some protostars are ejected from the centre of the cluster and do not accrete further mass, whereas those stars which remain in the cluster do accrete mass via gravitational channel, becoming then more massive (Klessen & Glover, 2016).

In contrast, the turbulent fragmentation scenario prescribes, as the name suggests, a primary role for the turbulence. Turbulence in molecular gas creates local overdensities and some of them (those which are gravitationally bound) collapse and form stars. We can schematise this process with two steps: in the first one, turbulence divides the molecular medium in clumps, only some of them being gravitationally bound and therefore forming stars. Then, the star formation process occurs, but given its limited efficiency only a fraction of the clump mass is converted into stellar mass. There is then a direct relation between clump mass and stellar mass, and assuming a certain distribution of the orignal molecular gas, a corresponding distribution of the clump mass can also be obtained (see e.g. Padoan et al., 1997; Hopkins, 2012).

Cloud destruction

Molecular clouds have a limited lifetime. Once stars form, they exhert a feedback on the clouds which in general act as an expanding force which contrast gravity and ultimately overcomes leading to the dispersion of the clouds.

It is possible to date MCs in the solar neighborhood by calculating the age of the embedded stars by means of the Hertzprung-Russel diagram. From these measurements a typical resulting age is of ~ 10 Myr (Elmegreen, 2000; Hartmann et al., 2001; Ballesteros-Paredes & Hartmann, 2007). This operation is more difficult for more distant objects, as stars are often not resolved: other techniques are then required. This is the case of Kawamura et al. (2009), that estimate the lifetime in MCs to ~ 25 Myr in the Large Magellanic Cloud. They use the data of a CO emission survey to identify clouds with little to no signs of ongoing star formation, clouds with HII regions, which are associated with ongoing star formation, and stars with well developed embedded star clusters. The relative abundance of such three different states suggests the relative lifetime. Then, separate dating of the stellar clusters enable to assess the absolute lifetime of these clouds. In general, it has been argued (Tan et al., 2006) that the lifetime of MCs is approximately 10 times their free-fall time[2], which gives a useful way to compare evolution of MCs with different size and density. In Paper II, we also propose a method to obtain the time passed since the onset of star formation in MCs by means of line and dust continuum emission measurements.

Stars formed in MCs exhert feedback on the clouds themselves, and this leads to the dispersion of such MCs. Massive stars ($\geq 8\,M_\odot$) are the main sources of

---

[2]The free-fall time is defined as the time that a body, a MC in this case, needs to collapse under its own gravitational force

feedback. The three main physical phenomena which determine stellar feedback are *supernova* (SNe) *explosions*, *stellar wind*, *ionizing radiation*, and *radiation pressure*. We will briefly discuss in the following the effects of such phenomena on MCs, and leave for Sec. 2.2.2 a more detailed description of the ionizing radiation, as it plays a particulary important role in the simulations which are analysed in this thesis.

Supernova explosions typical happen at the end of the life-cycle of stars with $\gtrsim 8M_\odot$ (exceptions for some mass and metallicity ranges are possible). According to the star mass, such explosion releases $2 - 5M_\odot$ mass at velocity of about $6000 - 7000$ km s^{-1} into the surrounding ISM and the temperature medium is heated to temperature even above 10^6 K (Janka et al., 2012). A SN explosion event can destroy the entire MC it is embedded in, but also trigger the condensation and formation of new clouds (Iffrig & Hennebelle, 2015; Gatto et al., 2015; Walch et al., 2015).

Stellar winds are constituted of the material ejected from stars throughout their life. Over the entire lifetime of a very massive star, the total amount of ejected energy is comparable with the $\sim 10^{51}$ erg of SNe (see e.g. Naab & Ostriker, 2017, and references therein), even if this happens over a much larger time period. Stellar winds contribute to reduce the density of the surrounding ISM, to heat it, and to enrich it in metals; the ejected momentum is comparable to the one ejected from SNe. The impact of stellar winds on the evolution of MCs is still highly debated: their effect on large (~ 100 pc) scale is, according to recent simulation works (Ali et al., 2022, for instance) at most secondary compared to photoionization, even though it can be responsible on producing small cavities (≤ 30 pc), especially in very dense regions of the cloud (Geen et al., 2020). Observations offer a broad range of results concerning the importance of winds, too: in some star-forming regions, like N81 in the Small Magellanic Cloud, they seem to be much lower than predicted by theoretical models and therefore of negligible importance (Martins et al., 2004), while they are, if not the main component, needed to explain the expansion velocity of the HII region in NGC 7538 (Beuther et al., 2022).

2.2.2

Ionizing radiation and radiation pressure

A massive star typically ejects $\sim 10^{53}$ erg in Lyman continuum photons over its lifetime, which is two order of magnitude more than the energy ejected in a SN explosion event. Such ejection ionizes part of the surrounding cloud creating a so-called *Strömgen sphere* (Strömgren, 1939). In its original and simplest expression, which assumes spherical symmetry, uniform gas density, steady state and one single ionizing source, the radius R_{S0} of this sphere corresponds to the distance from an ionizing source at which the ionization rate of neutral hydrogen equals the recombination rate of ionized hydrogen. Following Draine (2011),

$$R_{S0} = \left(\frac{3\, Q_0}{4\pi n_{\rm H}^2 \alpha_B} \right)^{1/3} , \qquad (2.6)$$

where Q_0 is the rate of emission of hydrogen-ionizing photons, i.e., those with $h\nu > 13.6$ eV, n_H is the hydrogen density and α_B is a recombination coefficient mildly dependent on the temperature. For typical cloud parameters, this means $R_{S0} \sim 3 - 4$ pc. Although all the aforementioned assumptions made to derive Eq. (2.6) are unrealistic in a real (and simulated) cloud, the dependencies found there are still qualitatively valid. From Eq. (2.6) we learn that $R_{S0} \propto Q_0^{1/3}$ and $R_{S0} \propto n_{\rm H}^{-2/3}$, mean-

ing that the HII regions tend to be larger the hotter and brighter the stars are, and smaller the denser the surrounding medium is.

The mean free path (mfp) of a an ionizing photon is

$$\text{mfp} = \frac{1}{n\left(\text{H}^0\right)\sigma_{\text{p.i.}}} \, , \tag{2.7}$$

where $n\left(\text{H}^0\right)$ is the density of neutral hydrogen, and $\sigma_{\text{p.i.}}$ is the photoionization cross section. This corresponds to ~ 0.1 pc, i.e., mfp $\approx R_{\text{S0}}/100$, which means that it is usually a good approximation to idealize the boundary between ionized and neutral hydrogen as a discontinuous transition, called *ionization front*, unless one is interested in studying the properties of such transition regions in detail (which are the PDRs discussed in Section 2.1.3) more than the HII regions or the entire cloud.

As we mentioned, the Strömgen approximation assumes steady state. Actually, ionization fronts are in general not stationary, rather they expand in the surrounding medium. The photoionization of molecular hydrogen process increases the number of free particles of a factor 4 ($\text{H}_2 \rightarrow 2\text{H}^+ + 2e^-$) and raises the temperature to $\sim 10^4$ K. This leads to a pressure increase by a factor of $\sim 10^3$. At this point, such high-pressure gas pushes away the surrounding cold, low-pressure gas.

At early times after a star forms and starts ejecting radiation, the ionization front propagates at high velocity v, typically of several hundreds km s^{-1}, and rapidly decreases with increasing time. It reaches a typical velocity of a few 10 km s^{-1} in the time needed to expand to reach a radius $r \approx R_{\text{S0}}$. As $v \lesssim 2c_{\text{ion}}$, being c_{ion} the sound speed of the ionized gas, typically ~ 10 km s^{-1}, a shock wave generates and moves ahead of the ionization front, compressing and accelerating the neutral gas (Draine, 2011). Now, the ionization from moves through a gas which is no longer steady, but already compressed and moving. Now the expansion of the HII region continues, progressively slowing down with time. Spitzer (1978) found that the radius r of the ionizing front follows now

$$r \propto t^{4/7} \, , \tag{2.8}$$

and therefore

$$v \propto t^{-3/7} \, . \tag{2.9}$$

The overall evolution of the ionization front with time is shown in Fig. 2, which is an adaptation from Draine (2011). The two different regimes of the expansion, with and without shock wave, are mostly evident in the velocity plot, where it clearly appears how the ionizing front rapidly decelerates from ~ 1000 to ~ 10 km s^{-1} in the first few 100 yr, then decelerates only slowly in the second phase of the expansion.

As a remark, the ionization front can be preceded by a *photodissociation front*, originated by those photons with 11.2 eV $< h\nu <$ 13.6 eV, i.e., those which can dissociate H_2 into atomic hydrogen, but not ionize it. Draine (2011) shows that such photodissociation front in general precedes indeed the ionization front only in the second phase of the expansion, when the shock wave is created. In this case, there is therefore a nested $\text{H}^+ - \text{H} - \text{H}_2$ structure from the inner to the outer part of the region around the massive star.

Another feedback process due to stellar radiation (not modelled in the simulations we analyze in this thesis) is the *radiation pressure*. An electromagnetic wave carries momentum, which is transferred to an opaque surfaces it strikes. The res-
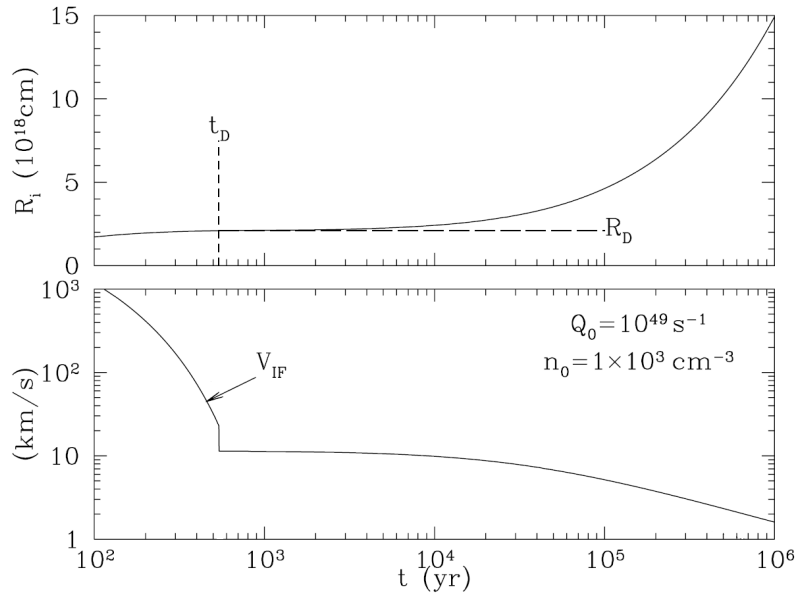
Figure 2: *Upper row*: ionization front R_i as a function of time. The instant when the shock front originates is t_D. Similarly, R_D is the radius at that instant. *Bottom row*: velocity V_{IF} of the ionization front as a function of time. Note that the time axis is in log-scale. Adapted from Draine (2011).

ulting pressure P exerted is given by $P = \langle S \rangle / c$, where $\mathbf{S} = \mathbf{E} \times \mathbf{H}$ is the Poynting vector. This can also be expressed in terms of photons:

$$P = \frac{h\nu}{c} \Phi_\nu \,, \tag{2.10}$$

where h is the Planck constant and Φ_ν is the photon flux at frequency ν. A flux of photons, like the one produced by stars, determines a pressure on the ISM particles. As a consequence of this, there is nonuniform density in the HII regions, as gas pressure gradients are required to counteract the effects of radiation pressure. In particular, the gas density is enhanced near the edge of the HII region, and diminished near the stars. This also means that radiation pressure acts as an inhibitor of star formation. Indeed, Matzner (2002) find that radiation pressure drives the structure of MCs after the onset of star formation, supporting them against gravitational collapse. As a consequence of this, further star formation in the same area is inhibited not only because of the resulting lower density, but also because of the final mass of the newly formed stars is reduced as the disk accretion is inhibited, and only effective at late stages (Rosen et al., 2019).

2.3

CARBON CHEMISTRY IN MOLECULAR CLOUDS

In this thesis, we produce synthetic emission maps of [CII] and CO lines of simulated molecular clouds. In order to do so, it is crucial to be aware of the main processes which regulate the abundance of the various carbon-bearing species in MCs.

The ISM is composed of hydrogen, helium, and metals, that is, all elements with atomic number $Z \geq 3$. All these chemical elements interact with each other forming

Table 2.1: Some important photodissociation reactions involving carbon (adapted from Tielens, 2005). The generix pedex "x" indicates that a certain generic reaction applies for species with x hydrogen atoms, where x can be 1, 2, or 3.

Reaction		
CH	$\rightarrow$	$C + H$
CO	$\rightarrow$	$C + O$
CH_x	$\rightarrow$	$CH_x^+ + e$
CH_x^+	$\rightarrow$	$CH_{x-1}^+ + H$
CH_2	$\rightarrow$	$CH + H$
CH_3^+	$\rightarrow$	$CH^+ + H_2$

a fairly complex scenario of chemical processes. These can be separated into two classes: gas-phase reactions, occurring, as the name suggests, among particles in the gas phase, and grain-surface reactions, which happen on the surfaces of the dust grains which permeate the ISM. Below, we briefly describe these chemical reactions and pay particular attention to those which have an impact on the formation and destruction of CO and C^+, as these are the species of most interest for this thesis. Nevertheless, we need to remark that all chemical reactions depend, in principle, on each other, as the abundance of the reagent of a certain reaction is the product of other reactions. Thus, it is extremely difficult to say, in general, which are the most important reactions in a certain environment and is even more complicated to code a chemical network. In Sections 3.4.2 and 6.1.1 we will describe the network used in our simulations, which is a considerable simplification of the real chemical processes happening in clouds. The information in this section are mainly taken from Tielens (2005), unless differently specified.

2.3.1

Gas-phase chemical reactions

The gas-phase chemical reactions include a large set of reaction, which we will now briefly explore.

Photodissociation

Photodissociation is a chemical reaction where photons break a chemical bond and a species constituted of at least two particles is separated. The generic photodissociation reaction is written in the form $AB + h\nu \rightarrow A + B$. The common example $H_2 + h\nu \rightarrow 2\,H$ has already been briefly discussed in Sec. 2.2.2 in relation to the photoionization fronts. In order for such kind of reactions to be possible, the presence of photons is necessary. In the ISM such photons originate from stars and dust grains. Photons originated by stars have an energy spectrum peaked at around $\sim 1\,\mu$m. Dust grains emit photons in the far infrared as a consequence of absorption of stellar light (and consequent heating). Typical dust temperatures are of $\sim 10 - 15$ K in atomic and molecular regions, and $\sim 30 - 40$ K in HII regions, where the main source of heating are O- and B-type stars (Strong et al., 2000). Overall, these processes contribute to form the *interstellar radiation field* (ISRF), described by the fundamental works of Habing (1968) and Draine (1978) (see Sec. 2.1.1)

The typical ISRF given in the these works refers to unshielded gas. Inside a dense region, like a molecular cloud, the radiation field is attenuated by dust.

As the ISRF is reduced inside dense clouds because of extinction, the importance of photodissociation reactions is lower inside dense regions than in their rims. Without aiming to be exaustive, some important photoreactions in the ISM are listed in Table 2.1. A major product of such reaction is neutral carbon, which is the product of photodissociation of CO and CH. Indeed, photons of the ISRF are one of the main causes of CO distruction in molecular clouds. Since, as we discussed before, the ISRF is exponentially attenuated with the column density of the cloud, CO is typically present in the dense, well-shielded regions of a cloud, and very rare, or absent, in the diffuse regions more exposed to external photons.

In general, the absorption of the incoming photons is due to dust. However, for some species, H_2 and CO for instance, extinction due to the absorption of incoming photons by the molecule under consideration itself is relevant. This phenomenon is called *self-shielding*.

Besides photons coming mainly from stars and dust forming the ISRF, high-energy cosmic rays are capable of producing far ultraviolet (FUV) photons which dissociate molecules. Unlike the less energetic photons, cosmic rays are barely shielded, therefore the reaction rate is roughly constant, provided a given FUV intensity, with no dependence on A_V.

Neutral-neutral reactions

Neutral-neutral reactions involve atoms and molecules. It is typically in the form of $A + B \leftrightarrow C + D$. Usually, in such reactions reagents and products are interchangeable, i.e., a certain reaction can happen both to the left and to the right. However, the reaction is exothermic (energy is released into the environment) in one direction and endothermic (energy is absorbed from the environment) in the other direction. According to the characteristics of the environment, and mostly its temperature, either the forward or the backward reaction has the higher rate.

Activation energy barriers are often in place for this kind of reactions. This is the energy required to break the bond associated with the molecular rearrangement. This also applies to exothermic reactions: even if the reaction releases energy, it is still necessary for the reagents to absorb some energy beforehand in order to overcome the potential barrier determined by repulsive electric forces in order to make the reaction possible. The presence of such barrier prevents in most cases these reactions from happening in the diffuse ISM or, even more, in molecular clouds. As we already mentioned, the Cold Neutral Medium (CNM) has a typical temperature of ~ 100 K, and MCs of ~ 10 K. Anyway, typical activation barriers are of the order of ~ 1000 K: as an example, for $H_2 + OH \rightarrow H_2O + H$ it is ≈ 3021 K (Redondo et al., 2021, assuming $E = kT$). As a consequence, neutral-neutral reactions are mostly relevant in the WNM and in the WIM. As in those regions the molecules which would be involved in such reactions are mostly dissociated by means of energetic photons, neutral-neutral reactions play overall only a modest role in the ISM. An important exception is given by those involving atoms or radicals with non-singlet electronic ground states, as these do not have activation barriers. Some important reactions of this type are reported in Table 2.2.

Ion-molecule reactions

Ion-molecule reactions normally occur rapidly because the polarization-induced interaction potential which overcomes any activation energy involved and typical reaction rates are about two ordesr of magnitude larger than neutral-neutral reactions.

Table 2.2: Some important neutral-neutral reactions involving carbon (adapted from Tielens, 2005).

Reaction		
C + OH	$\rightarrow$	CO + H
C + O_2	$\rightarrow$	CO + O
O + CH	$\rightarrow$	CO + H
O + CH	$\rightarrow$	HCO^+ + e
O + CH_2	$\rightarrow$	CO + H + H

Table 2.3: Some important ion-molecule reactions involving carbon (adapted from Tielens, 2005).

Reaction		
C^+ + OH	$\rightarrow$	CO^+ + H
C^+ + H_2O	$\rightarrow$	HCO^+ + H
He^+ + CO	$\rightarrow$	C^+ + O + He
CO^+ + H_2	$\rightarrow$	HCO^+ + H

On the other hand, ion-molecule reactions involve an ion and a molecule, which are rare to be found in the same regions of the ISM. Indeed, molecules are mostly located in well-shielded regions with high A_V, where the ISRF cannot effectively dissociate such molecules. Because of the same reason, the only way for atomic and molecular ions to exist in such environments is ionization by means of cosmic rays, whose rate is, as we discussed before in this section, practically independent from A_V. Therefore, the Cosmic Rays Ionization Rate (CRIR) is what ultimately drives ion-molecule reactions by regulating the abundances of the ionized companions in such reactions. Some important ion-molecule reactions involving carbon formation and destruction are listed in Table 2.3.

Other gas-phase reactions

In this paragraph we summarise briefly other types of gas-phase reactions, not included in the categories described before, which have a somewhat smaller overall impact on the chemistry of the ISM.

   Charge transfer reactions involve a neutral and an ionized species. The neutral reagent transfers an electron to the ion, reverting then the status of neutral and ionized. The most relevant reaction of this type is $O + H^+ \rightarrow O^+ + H$ as it is a way of producing O^+, which is important in other reactions.

   Radiative association reactions are characterized by the collision product being stabilized by means of emission on a photon. An example of this is $C^+ + H_2 \rightarrow CH_2^+$ and it is relevant (like most of this type of reactions) for the chemistry of the Polycyclic Aromatic Hydrocarbon (PAH) molecules, which we will not discuss in this thesis. Also *electron recombination* reactions, i.e., the capture of an electron by an ion to form a neutral atom, is of some relevance for PAHs and, in general, for carbon-hydrogen chemistry. Typical reactions are in form of $CH_x^+ + e \rightarrow [...]$, where the right-hand side is some combination of C, H, CH, CH_2, H_2. Another interesting reaction of this type is water formation through $H_3O^+ + e \rightarrow H_2O + H$.

Table 2.4: Some important reactions involving radicals on dust grain surface (adapted from Tielens, 2005).

Reaction		
H + O	→	OH
H + OH	→	H_2O
H + CH_x	→	CH_{x+1}
H + NH_x	→	NH_{x+1}
H + CN	→	HCN
O + O	→	O_2
O + C	→	CO
N + N	→	N_2

2.3.2

Grain-surface chemistry

The surface of dust grains is sometimes the location where chemical reactions between elements which are not part of the dust grain itself happen. Such grains provide a surface where reagent species accrete, react, and finally migrate. The reaction process is therefore characterised by four steps: *accretion*, *diffusion*, *reaction* and *ejection* (or *migration*). Describing the physics and the chemistry of these steps goes beyond the goal of this thesis; instead, we will describe the most important types of grain-surface reaction, with particular attention to those regarding carbon-bearing species, in the same way we proceeded for the gas-phase reactions.

Reactions involving radicals

Reactions involving radicals happen on the dust surface via collisions. They involve H, C, N, or O atoms with themselves or with radicals such as OH, CH, etc. These can also be quite long carbon-bearing molecules (e.g., CH_2CHO and similar). They are synthesis reactions, i.e., two reagents join in one product. Table 2.4 presents some of these reactions.

Reactions of with activation barriers

These are reactions which cannot happen in the gas-phase of the ISM because of the high activation barriers, but the prolonged residence time on grain surfaces allow them to happen. Indeed, reactions with a barrier of a few 1000 K are allowed to happen, with a probability given by the actual physics of such grain surface reactions. Table 2.5 summarises some of such reactions.

2.4
CO, [CII], and dust observations in molecular clouds

In Section 2.3 we discussed some of the main chemical reactions taking place in the ISM. Such reactions determine various abundances of chemical species in the ISM and their presence is sometimes observable, meaning that those species emit, or absorb, light at specific frequencies with specific characteristics, which make possible, in principle, for an observer to detect them when looking at a region of the ISM where they are located. In this section we will first give an overview of the physics regulating emission and absorption of chemical species, then we will

Table 2.5: Some important reactions involving hydrogen with activation barriers (adapted from Tielens, 2005).

Reaction		
H + CO	$\rightarrow$	HCO
H + H_2CO	$\rightarrow$	CH_3O
H + C_2H_2	$\rightarrow$	C_2H_3
H_2 + OH	$\rightarrow$	H_2O + H *
O + O_2	$\rightarrow$	O_3
O + CO	$\rightarrow$	CO_2
* from Meisner et al. (2017)		

present with some detail some observational facts regarding CO, C^+, and dust, which are the species which we also consider in this thesis.

2.4.1

BASIC CONCEPTS ON RADIATIVE TRANSFER

Einstein coefficients

It is a well-known quantum mechanical fact that electrons in ions, atoms, and molecules are found in different energy states. Whenever an electron undergoes a transition between two different states, it emits or absorbs a photon, depending on whether the final state has a higher or lower energy than the initial state. The energy $E = h\nu$ of this photon equals the energy difference between the two states. The rules determining which transitions are possible under which conditions are quite laborious to be exhaustively described. However, a single transition, which is the responsible for a specific emission or absorption line in the spectrum, can be modelled assuming a *two-level system*, that is a model where electrons can transition from an upper to a lower level and vice versa, and the rate of this transitions determines the strength of the process. We follow, in this section, the good description given by Rybicki & Lightman (1979) of radiative processes in Astrophysics.

There are three emission and absorption processes:

- *Spontaneous emission*. It is, as the name suggests, the spontaneous emission, i.e., without the need of an external radiation field, of a photon as a consequence of a transition of an electron from the upper level u to the lower level l. The probability of this transition to happen is given by the Einstein coefficient A_{ul}. This is a value in units of s^{-1}.

- *Absorption*. It is, indeed, the absorption of a photon with energy $E > h\nu_0$ by a system to which the energy of the photon is transferred and an electron moves to a higher excited state. The energy required from the electron ho get excited is $h\nu_0$. The probability of this process is proportional to the density of photons at frequency ν_0. This is different from the spontaneous emission, where no radiation field is required. More precisely, let us consider two levels of the system separated by energy $h\nu_0$. In reality, such separation is not infinitely sharp: it is actually descried by a line profile function $\phi(\nu)$, normalised, sharply peaked at $\nu = \nu_0$. Now, in presence of a radiation field J_ν we can

define the integrated radiation field $\vec{J}$ as

$$\vec{J} = \int_0^\infty J_\nu \phi(\nu) d\nu .$$ (2.11)

Given this definition, the Einstein coefficient describing absorption is B_{lu} and the transition probability is in this case $B_{lu}\vec{J}$.

- *Stimulated emission.* It is the phenomenon for which photons can, instead of being absorbed, stimulate the transition of an electron from more to a less excited state. The Einstein coefficient describing this process is B_{ul} and the transition probability is $B_{ul}\vec{J}$. Mathematically, stimulated emission can be considered as a sort of negative absorption, as it has the same qualitative dependence on the Einstein coefficients and $\vec{J}$.

The three mentioned Einstein coefficients are dependent on each other, so that knowing one of them is sufficient to determine the other two as well. The relations between these coefficients are:

$$\begin{cases} g_l B_{lu} = g_u B_{ul} \\ A_{ul} = \frac{2h\nu^3}{c^2} B_{ul} \end{cases} ,$$ (2.12)

where g_u and g_l are the statistical weights of the upper and lower level, respectively. A region characterised by gas with number density $n = n_u + n_l$ (where n_u and n_l are the density of particles in the upper and lower state) and given Einstein coefficient A_{ul} emits photons with a certain intensity. To describe this we define the *emission coefficient* j_ν as the energy emitted per unit time, volume, frequency, and solid angle. The expression of j_ν is

$$j_\nu = \frac{h\nu_0}{4\pi} n_u A_{ul} \phi(\nu) .$$ (2.13)

Analogously, we can define an *absorption coefficient* α_ν as the energy absorbed per unit time, volume, frequency, and solid angle. Its expression is

$$\alpha_\nu = \frac{h\nu}{4\pi} \left(n_l B_{lu} - n_u B_{ul} \right) \phi(\nu) .$$ (2.14)

Here, we took into account both the "real" absorption with the $n_l B_{lu}$ term and the stimulated emission with the $n_u B_{ul}$ term. This clarifies why we defined the stimulated emission as a sort of negative absorption before.

Radiative transfer equation

Let us consider a light ray and and construct an area dA normal to the direction of such ray. Let us also consider all rays passing trough dA whose direction is within a solid angle $d\Omega$. Then, the energy crossing dA in the time interval dt in the frequency range $d\nu$ is

$$dE = I_\nu \, dA \, dt \, d\Omega \, d\nu$$ (2.15)

and I_ν is the *specific intensity* of the light ray. We note that I_ν, because of the way it is defined, does not change as a function of distance from the source originating the light ray.

A light ray crossing a medium is subject to variations in I_ν. The simplest way to describe this change is to take into account emission and absorption occurring in the crossed medium, and neglecting, for the moment, other effects (e.g., scattering

of the photons on dust grains). If we do so, we obtain the simplest form of the
radiative transfer equation, which is

$$\frac{dI_\nu}{ds} = -\alpha_\nu \, I_\nu + j_\nu \, , \qquad (2.16)$$

where α_ν and j_ν are the absorption and emission coefficients defined in Eq. (2.14)
and (2.13), respectively. It is useful to introduce the *optical depth* τ_ν in order to write
the solution of Eq. (2.16). It is defined by

$$d\tau_\nu = \alpha_\nu \, ds \, . \qquad (2.17)$$

Using $d\tau_\nu$ instead of ds we obtain that the specific intensity at a given optical depth
is

$$I_\nu(\tau_\nu) = I_\nu(0)e^{-\tau_\nu} + \int_0^{\tau_\nu} e^{-(\tau_\nu - \tau_\nu')} \frac{j_\nu(\tau_\nu')}{\alpha_\nu(\tau_\nu')} \, d\tau_\nu' \, , \qquad (2.18)$$

where $I_\nu(0)$ is the specific intensity at a given conventional point where is set $\tau_\nu = 0$
(that is, for instance, the point where a light ray which ideally propagates in vacuum
enters a medium). The first term of the solution represents the contribution of the
initial intensity, which is diminished by absorption in the medium, and the second
term is the combined effect of absorption, spontaneous and stimulated emission in
the medium. Eq. (2.18) is normally written by using the definition of *source function*
S_ν, defined by

$$S_\nu = \frac{j_\nu}{\alpha_\nu} \, . \qquad (2.19)$$

In this way, the solution of Eq. (2.16) is

$$I_\nu(\tau_\nu) = I_\nu(0)e^{-\tau_\nu} + \int_0^{\tau_\nu} e^{-(\tau_\nu - \tau_\nu')} S_\nu(\tau_\nu') \, d\tau_\nu' \, . \qquad (2.20)$$

The solution of the radiative transfer equation presented here is still quite simple
and neglects important contributions, such as scattering which photons experience
when travelling in a certain medium. Anyway, it is instructive to understand which
"ingredients" are required to practically compute the specific intensity produced
by a given source, which is ultimately what we are interested in this thesis when
producing synthetic emission maps of the simulated molecular clouds we analyse.
We will give more details on how the radiative transfer equation is practically solved
in Section 3.5. here in the following, we instead specify what these "ingredients"
actually are, differenciating between line and continuum transfer.

- *Lines radiative transfer.* Performing line radiative transfer in molecular clouds
  typically means calculating the emerging specific intensity of the emission line
  of a specific investigated species (C^+ and CO in our case). The incident intens-
  ity $I_\nu(0)$ is normally set to zero, as the light comes from the cloud itself, unless
  one wants to consider either the light coming from the same line transition,
  but from external sources, or the light with different origin (e.g., stars, CMB,
  etc.) in its frequency component close to the investigated line. The emission
  and absorption coefficients must be calculated from the Einstein coefficients,
  the density of the investigated species and the level population. The Einstein
  coefficients are a consequence of the specific atomic physics of the investigated
  species, and of the nature of the transition in particular. Typically, the emis-
  sion coefficient A_{ul} is given and the B coefficients are calculated by means of

Eq. (2.12). The level population (i.e., how many particles are in the ground level l and how many are in the upper level u) depends, in principle, in a complicated way on the gas temperature and on the density of the collisional partners of the investigated species. In Section 3.5.1 we explain how we calculate it in this work. However, a possible approximation, although not very robust in MCs as we show in Paper I, is to assume that the gas is in Local Thermal Equilibrium. In this case, calculating level populations is trivial as they depend only on the gas temperature and on the statistical weights of the levels:

$$\frac{n_l}{n_u} = \frac{g_l}{g_u} \exp\left(\frac{h\nu}{kT}\right) \, , \tag{2.21}$$

which easily gives n_l and n_u as it must be, in a two-level system, $n = n_u + n_l$. In case the considered species has actually not two, but N levels, this is still solvable as there will be $N - 1$ equations of the type of Eq. (2.21) and the fact that $\sum_{i=1}^{N} n_i = n$.

- *Dust continuum radiative transfer.* Light coming from stars inside and outside a molecular cloud heats the dust grains, which emit light in the far-infrared range. When considering the radiative transfer equation for emitting hot dust, the emission and absorption coefficients are not related with Einstein coefficients, but to the temperature and opacity properties of the dust grains. We will discuss this aspect below in Section 3.5.2.

2.4.2

THE [CII] EMISSION LINE - THEORY AND OBSERVATIONS

Microphysics of the [CII] line emission

The carbon ion has two isotopes, namely $^{12}C^+$ and $^{13}C^+$, with a standard ratio of $^{12}C^+/^{13}C^+ = 67$ (Wakelam & Herbst, 2008). In the following, we will always refer to $^{12}C^+$ (we do not use $^{13}C^+$ in this thesis as we do not expect significantly different observational properties), therefore the ^{12} apex will be omitted from now on. The observed emission line associated with C^+ is a *fine structure* transition. An electronic state in an atom (or ion) is characterized by 4 principal quantum numbers: the main quantum number n, the orbital angular momentum number l, associated with the angular momentum vector $\mathbf{l}$, the magnetic angular momentum number m, associated with the component along one axis of $\mathbf{l}$, and the spin number s, associated with the spin vector $\mathbf{s}$. The resulting total orbital angular and spin momenta for the ion are $\mathbf{L} = \sum \mathbf{l}_i$ and $\mathbf{S} = \sum \mathbf{s}_i$. The total angular momentum of the ion is then the sum of the orbital and the spin vectors and it is indicated with $\mathbf{J} = \mathbf{L} + \mathbf{S}$. The associated quantum number J has values ranging from $L - S$ and $L + S$. The state of a particle is expressed with the following notation:

$$^{2S+1}L_J \, , \tag{2.22}$$

where all the quantum numbers relevant (for line transitions) are expressed.

A carbon ion C^+ has 5 electrons. Two of them are in a state with $n = 1$ and three with $n = 2$. Among those with $n = 2$, two have $l = 0$ and one has $l = 1$. Therefore, the electronic configuration of this ion is $1s^2 2s^2 2p^1$: this means, indeed, two electrons (apex) with $n = 1$ (coefficient) and $l = 1$ (expressed by letter s), two electrons with $n = 2$ ans $l = 0$, and one electron with $n = 2$ and $l = 1$ (letter

p). The total orbital angular momentum of this ion is then $L = 1$ (*P* state, using the same letter convention). Now, each electron has spin $\mathbf{s} = 1/2$ or $\mathbf{s} = -1/2$. However, the sum of the spin of the electrons with $l = 0$ is zero: according to $\mathbf{s}$ of the one electron with $l = 1$, the two possible ion configurations are then ${}^2P_{1/2}$ and ${}^2P_{3/2}$. The transition between the two states is what we observe as the fine structure transition in C^+:

$${}^2P_{3/2} \rightarrow {}^2P_{1/2} \tag{2.23}$$

and it is indicated with the spectroscopic notation [CII]. Such notation means that this line comes from carbon (C) ionised one time (II). Square brackets indicate that this transition is "forbidden" (in the common quantum mechanics language) [3].

The [CII] line has a frequency of $\nu = 1900.5$ GHz, corresponding to $\lambda = 157.741$ μm, and its Einstein emission coefficient is $A_{ul} = 2.6 \times 10^{-6}$ s^{-1} (Mendoza, 1983; Wiese & Fuhr, 2007). This line is easy to excite thermally by collisions with e$^-$, H, and H$_2$. The critical density, defined by the collisional de-excitation rate being equal to the effective spontaneous decay rate, depends on the temperature. According to the collisional partner, it ranges from a few cm^{-3} to several thousands cm^{-3} (Goldsmith et al., 2012; Schneider et al., 2020).

Key [CII] observations in molecular clouds

The [CII] line emission is one of the dominant cooling processes in the ISM (Tielens & Hollenbach, 1985; Klessen & Glover, 2016). It can originate from several phases of the ISM, ranging from molecular (e.g. Langer et al., 2014a) to ionized gas (e.g. Pineda et al., 2013), even though in MC scales the most of the emission is likely to come from atomic regions (Franeck et al., 2018). However, at stages when HII regions, in clouds or even in dwarf galaxies, are young and dense, these can contribute for the majority of the [CII] emission (Bisbas et al., 2021).

Absorption in the atmosphere, mainly because of ozone and atomic oxygen, is particularly effective in the FIR range, and therfore hinders ground-based observations of [CII]. Because of this, telescopes based on balloons, airplanes, or satellites are needed.

After pioneering observations of the [CII] line with the Kuiper airborne observatory in the 1990's and the HIFI instrument on the Herschel satellite, the Stratospheric Observatory for Infrared Astronomy (SOFIA) [4], an airborne observatory mounted on a Boeing 747SP operated by NASA and the Deutsches Zentrum für Luft- und Raumfahrt (DLR), played a major role on [CII] observations. The aircraft flew in the stratoshpere, at altitude as high as 13.7 km (45 000 ft), high above the disturbance of the Earth's atmosphere (Young et al., 2012). It remained in operation from May 2010 till September 29th 2022, when the last observation flight took place. SOFIA performed observations with several instruments. The most relevant for [CII] observations in molecular clouds and HII regions was the German REceiver for Astronomy at Terahertz Frequencies (GREAT) (Heyminck et al., 2012; Walmsley et al., 2012), a modular dual-color heterodyne instrument for high-resolution far-infrared (FIR) spectroscopy. Besides [CII], a large number of other lines were observable with GREAT: HCN, HCO$^+$, CO $(11 - 10)$ and $(12 - 11)$, [OI] 63 μm, etc. With the introduction of the upGREAT array receivers (Risacher et al., 2018), in particular, observations at high resolution ($R = \lambda/\Delta\lambda \gtrsim 107$) of [CII], as well as of [OI] at 63 and 145 μm were possible. A non-exhaustive list of observations of

---

[3]see e.g. Rybicki & Lightman (1979, Chapter 10) for a general explanation of radiative transitions
[4]https://www.dlr.de/content/en/articles/missions-projects/sofia/sofia-infrared-observatory.html
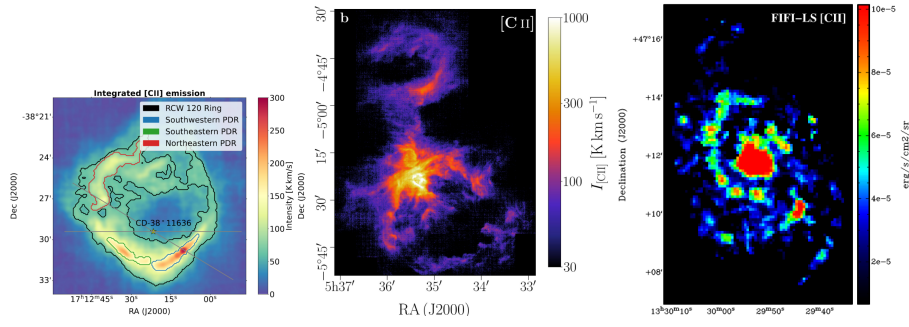
Figure 3: [CII] emission maps obtained with SOFIA upGREAT at different scales. *Left*: the HII region RCW 120 (adapted from Kabanovic et al., 2022). *Center*: the Orion Nebula (Pabst et al., 2020). *Right*: the Whirpool galaxy (M 51a) (Pineda et al., 2018).

[CII] performed with GREAT includes globules and pillars in Cygnus X (Schneider et al., 2012), ionized and hot gas in M17 SW (Pérez-Beaupuits et al., 2012), ionized and photodissociated regions in the IC 342 galaxy (Röllig et al., 2016), the Whirpool galaxy M 51 (Pineda et al., 2018), and Orion A and B molecular clouds (Pabst et al., 2017, 2020). Observations and studies of HII regions have been conducted in recent years within the FEEDBACK Legacy Project (Schneider et al., 2020), aimed to study the interaction of massive stars with their environment in galactic molecular clouds. RCW 49 (Tiwari et al., 2021), NGC 7538 (Beuther et al., 2022), and RCW 120 (Luisi et al., 2021; Kabanovic et al., 2022) are examples of HII regions observed within this project. In Figure 3 we show [CII] maps obtained with (up)GREAT of three different objects at different scales, namely the HII region RCW 120, the Orion Nebula, and the Whirpool galaxy. Both in Paper I and in Paper II the results that we obtain concerning [CII] emission from HII regions are related to the observations performed within this project.

Another important [CII] survey is the Galactic Observations of the Terahertz C+ (GOT C+) survey (Pineda et al., 2013; Langer et al., 2014b, 2017), using Herschel's HIFI (Heterodyne Instrument for the Far-Infrared, de Graauw et al., 2010) instrument. The observations, focused on selected sightlines, aimed to identify the vertical scale height of the disc, which is found to be approximately 73 pc in [CII], as well as to identify the Galactocentric distance at which the [CII] emission peaks, namely between 4 and 11 kpc. Velusamy & Langer (2014) also found, using GOT C+ data, that at galactic scales 62% of the [CII] emission comes from molecular regions, and only 18% from atomic gas. Herschel's HIFI has also been used for observations both at smaller scales, like Orion (Goicoechea et al., 2015), and for extragalactic objects, like the Triangulum galaxy (Mookerjea et al., 2016).

In the near future, the Fred Young Submillimeter Telescope (FYST) ground-based in the Atacama desert in northern Chile, at 5600 m elevation, will be able to detect [CII] emission from star-forming galaxies at the epoch of reionization. At present day, however, observations of [CII] in high redshift galaxies is possible with ALMA.

2.4.3

THE CO EMISSION LINES - THEORY AND OBSERVATIONS

Microphysics of the CO line emissions

Spectroscopy of molecules is extremely complicated and, even limiting our attention to diatomic molecules, considerable quantum physics is required to describe all the possible transitions, and line emission as a consequence. Instead, we will aim here to give only a basic overview of such processes, with particular focus on rotational transitions, which originate the CO lines we work with in this thesis.

Electron in diatomic orbits are characterized by quantum numbers in a way conceptually similar to atom electrons. The total orbital angular momentum along the internuclear axis is indicated with Λ and it is analogous to L in the atomic case. Similarly, the total spin angular momentum Σ is the analogous of S in the atomic case and the total angular momentum is $\Omega = \Lambda + \Sigma$. Molecules have emission and absorption which are the consequence of eletronic transitions between the different states characterised by these quantum numbers, with selection rules similar to the atomic cases. There are, however, also quantum mechanics features of the wave function which do not have an exact equivalent in atoms, like parity under inversion or reflection in the plane containing the two nuclei.

Even if the rules governing them are complicated, it is intuitive to realise that molecules have two possible motions which are not defined for atoms. Indeed, the atoms of which the molecules is composed can oscillate, or "vibrate", along the internuclear axis and rotate around the center of mass. As it always happens in quantum mechanics, the energy associated with such vibrations and rotations is quantized and expressed by means of quantum numbers.

In particular, the rotational energy levels are given by

$$E_{\mathrm{r}} = hcB_{\mathrm{e}}J(J+1) \,, \tag{2.24}$$

where J is the rotational quantum number and B_{e} is the rotational constant, defined by

$$B_{\mathrm{e}} = \frac{h}{8\pi^2 cI} \tag{2.25}$$

being I the momentum of inertia of the molecule respect to its center of mass. We can derive the energy ΔE released, for instance, for a rotational transition from level $J+1$ to level J, which is

$$\Delta E = 2hcB(J+1) \,. \tag{2.26}$$

This is a simple, but relatively robust, approximation to get the energy, and therefore ν and λ, of a certain transition, given J and I.

We are interested in transitions with $\Delta J = 1$ for CO and, in particular, in the $J = 1 \rightarrow 0$ transition. In Table 2.6 we summarise the data relative to some observationally important CO transitions. We note that differenciating between ^{12}CO and ^{13}CO is relevant, as the corresponding lines are located at slightly different frequencies due to the different structure of the molecule. In principle, the same applies for $C^{18}O$ as well, but we do not report the data here as we will not use such isotope in the rest of the thesis.

Molecular hydrogen is also a diatomic molecule like CO, but it is homonuclear and therefore has no permanent dipole moment. Therefore, unlike CO, it also has no allowed dipole vibrational transitions, i.e., those with $\Delta J = 1$ like the ones

Table 2.6: Wavelength (λ) and Einstein spontaneous emission coefficient A_{ul} for some vibrational transitions of ^{12}CO and ^{13}CO particularly relevant in observational works. The notation $N \to N-1$ in the "Transition" column means that the data are referred to the transition from the vibrational level characterised by $J = N$ to the level characterised by $J = N-1$. The data are taken from the Leiden Atomic and Molecular DAtabase (LAMDA) (Schöier et al., 2005)

Species	Transition	λ [μm]	A_{ul} [s^{-1}]
^{12}CO	$1 \to 0$	2600.758	7.203×10^{-8}
	$2 \to 1$	1300.404	6.910×10^{-7}
	$3 \to 2$	866.963	2.497×10^{-6}
	$4 \to 3$	650.252	6.126×10^{-6}
	$7 \to 6$	371.650	3.422×10^{-5}
	$12 \to 11$	216.927	1.735×10^{-4}
^{13}CO	$1 \to 0$	2720.406	6.294×10^{-8}
	$2 \to 1$	1360.228	6.038×10^{-7}
	$3 \to 2$	906.846	2.181×10^{-6}
	$4 \to 3$	680.164	5.353×10^{-6}
	$7 \to 6$	388.743	2.991×10^{-5}
	$12 \to 11$	226.898	1.517×10^{-4}

typically observed for CO. H$_2$ has a weak rotational quadrupole ($\Delta J = 2$), but the temperature at which such transition can occur is too high to allow the presence of H$_2$ in MCs, and therefore can be hardly to identify H$_2$ directly. There are, however, some survey aimed to detect the H$_2$ emission lines in diffuse clouds (Habart et al., 2005; Glover & Mac Low, 2011; Roueff et al., 2019).

CO-to-H$_2$ conversion and key CO observations

The CO emission lines from molecular clouds are usually quite bright and have been observed in various surveys. Probably, the main reason for such extensive observational campaigns is that CO is commonly supposed to be a good tracer of H$_2$ in MCs (we discuss this extensively in Paper I and Chapter 6). As we discussed in the previous paragraph, molecular hydrogen is not directly observable in dense clouds because of the lack of permanent dipole moment. Therefore, astronomers looked for other observable species which shall be abundant in the same regions where also H$_2$ is mainly located. In this way, observing such other species become a way to indirectly trace H$_2$. CO is, indeed, one of such species, and probably the most studied one. A commonly used tool to assess the column density of molecular hydrogen, N_{H_2}, from the measured intensity of the ^{12}CO ($1 \to 0$) line, I_{CO} hereafter, is the X_{CO} factor, defined as

$$X_{CO} = \frac{N_{H_2}}{I_{CO}} \, . \tag{2.27}$$

The typically used value for X_{CO} is 2×10^{20} cm^{-2} K^{-1} km^{-1} s (Bolatto et al., 2013). Such conversion factor is accurate within a factor of a few when applied at least to cloud scales (see e.g. Seifried et al., 2020; Madden et al., 2020; Hu et al., 2022), but does not give meaningful results when applied to single portions of a cloud, as the ^{12}CO ($1 \to 0$) line is optically thick in dense gas, and therefore the relation between it and N_{H_2} breaks (Borchert et al., 2022). In case one deals with resolved clouds,

the useful quantity to roughly assess the column density of H_2 is then the averaged X_{CO} over the entire cloud:

$$\langle X_{CO} \rangle = \frac{\Sigma_i N_{H_2,i}}{\Sigma_i I_{CO,i}} \ , \tag{2.28}$$

where the sum over i is intended over all the pixels of the map.

A primary role in CO observations is definitely played by the 30-meter telescope on Pico Vereta, in the Spanish Sierra Nevada, operated by the Institut de RAdioastronomie Millimétrique (IRAM). Observations performed with this telescope range from extragalactic scales, like the mapping of as much as 532 outer galaxies in CO in recent years (Saintonge et al., 2017), or the HERACLES extragalactic survey (Leroy et al., 2009), to dwarf galaxies (Taylor et al., 1999), to cloud scales: using this telescope, for instance, among many other works, Carlhoff et al. (2013) mapped the molecular cloud W43, located in the Mlky Way in the constellation of Aquila, Berné et al. (2010, 2014) mapped the Orion nebula.

Another important telescope for observations is the Atacama Large Millimeter/submillimeter Array (ALMA), a radiointerferometer composed by 66 antennas located at 5000 m altitude in the Atacama desert, in Chile. It has been used to observe CO emission in high-redshift galaxies (Wardlow et al., 2018, for instance), in resolved, closer galaxies (e.g. Saito et al., 2020), and even in single, resolved GMCs in nearby galaxies, which is possible because of the extremely high resolution achievable (Muraoka et al., 2020).

Also in the Atacama desert, the Atacama Pathfinder EXperiment (APEX) is a 12 meters telescope suitable for observations in the 0.2 - 1.5 mm wavelength range, which include most of the emission lines of CO, excluding $(1-0)$. Indeed, a large number of observational works of e.g. clouds and HII regions in the Mily Way are based on APEX data. Just as an example, this is the case of Kabanovic et al. (2022), who studied ^{12}CO and ^{13}CO $(3-2)$ lines in the HII region RCW 120 and, also very recently, of Leroy et al. (2022), who used the J $(3-2)$ line from APEX and other lines from different telescopes to determine typical ratios between line emission of different transitions. Other telescopes and surveys include the James Clerk Maxewll Telescope at the Mauna Kea Observatory (Hawaii) and the the 1.2 meter Millimeter-Wave Telescope at the Center for Astrophysics within the Smithsonian Astrophysical Observatory, which provided CO observations of the entire northern sky (Dame & Thaddeus, 2022, and references therein).

2.4.4

DUST CONTINUUM EMISSION

In this section we will first give a quick overview of the physical processes regulating the dust IR emission. Then, we will give some examples of dedicated observational telescopes and surveys. The physics of interstellar dust is very complicated. Here, we will limit ourselves to a general description following again Tielens (2005), and in Section 3.5.2 we will describe more in detail how this is practically implemented in this work.

Theory of dust emission

While discussing the basics of radiative transfer (Section 2.4.1) we did not take into account the effects of scattering, and we said that they result in a correction term to the equations presented there. Actually, scattering does play an important role in the heating and cooling processes of dust grains. In cases where the absorp-

tion coefficient is defined, i.e., for line emission, optical depth was defined as in Eq. (2.17). In case of dust, it is rather defined as

$$d\tau(\lambda) = n_{\mathrm{d}}(s)C_{\mathrm{ext}}(\lambda)dx \, , \tag{2.29}$$

where n_{d} is the dust density, and $C_{\mathrm{ext}}(\lambda)$ is the extinction cross section. This term is usually expressed in terms of the extinction efficiency $Q_{\mathrm{ext}}(\lambda)$:

$$Q_{\mathrm{ext}}(\lambda) = \frac{C_{\mathrm{ext}}(\lambda)}{\sigma_d} \, , \tag{2.30}$$

with σ_d being the geometrical cross section. The extinction efficiency is composed by two terms, namely the absorption and the scattering terms:

$$Q_{\mathrm{ext}}(\lambda) = Q_{\mathrm{abs}}(\lambda) + Q_{\mathrm{sca}}(\lambda) \, . \tag{2.31}$$

One can also define $C_{\mathrm{sca}}(\lambda)$ and $C_{\mathrm{abs}}(\lambda)$ accordingly. The ratio

$$\tilde{\omega}(\lambda) = \frac{Q_{\mathrm{sca}}(\lambda)}{Q_{\mathrm{ext}}(\lambda)} \tag{2.32}$$

is called *albedo*. In general, scattering is also function of the scattering angle:

$$C_{\mathrm{sca}}(\lambda) = \int_0^{2\pi} \int_0^\pi \frac{d\sigma(\lambda)}{d\Omega} \sin\theta d\theta d\phi \, , \tag{2.33}$$

where $d\sigma/d\Omega$ is the differential scattering cross section. The average angle at which particles are scattered is called *scattering phase function asymmetry* and is defined as

$$g(\lambda) = <cos\theta> = \frac{1}{C_{\mathrm{sca}}} \int_0^{2\pi} \int_0^\pi \frac{d\sigma(\lambda)}{d\Omega} \cos\theta \sin\theta d\theta d\phi \, . \tag{2.34}$$

The knowledge of C_{sca}, C_{abs}, and g for different values of λ gives, in principle, a generally satisfying picture of the behavior of the dust grains under examination. Such behavior depends on the composition and size of the grains. Anyway, we give no insights of this in this chapter. We just assume to know from literature these values for the type of grains we are interested in. Indeed, we use the values given by Weingartner & Draine (2001) in this thesis.

In presence of a radiation field characterised by the specific intensity I_ν given by Eq. (2.15) we can define the *mean intensity* J_ν as

$$J_\nu = \frac{1}{4\pi} \int_0^{4\pi} I_\nu d\Omega \, . \tag{2.35}$$

We can now define the energy absorbed by a dust grain:

$$\Gamma_{\mathrm{abs}} = 4\pi\sigma_{\mathrm{d}} \int_0^\infty Q(\lambda)J(\lambda)d\lambda \, , \tag{2.36}$$

and analogously the energy emitted by it:

$$\Gamma_{\mathrm{em}} = 4\pi\sigma_d \int_0^\infty Q(\lambda)B(T_{\mathrm{d}}, \lambda)d\lambda \, , \tag{2.37}$$

with T_{d} the dust temperature and $B(T_{\mathrm{d}}, \lambda)$ the Planck spectrum. So, in principle, determining the dust temperature of a certain region requires the following steps:

- Knowledge of the intensity coming from the sources (mostly stars and ISRF for molecular clouds);

- Knowledge of $J(\lambda)$ in the region of interest by solving the radiative transfer equation with the scattering terms. This is done, for example, with Monte Carlo techniques, as we will describe in Section 3.5.2;

- Derivation of T_d by setting $\Gamma_{abs} = \Gamma_{em}$.

The dependence of $Q(\lambda)$ of λ is quite complicated. However, a good approximation, especially at long wavelengths, is to assume that

$$Q(\lambda) = Q_0 \left(\frac{\lambda_0}{\lambda} \right)^\beta . \tag{2.38}$$

For typical interstellar grains, a mixture of silicate and carbonaceous grains, $\beta = 2$ is a good assumption. Integrating Eq. (2.37) with this approximation gives

$$\Gamma_{em} \propto T_d^6 , \tag{2.39}$$

which is indeed used in numerous scientific works (Hildebrand, 1983; André et al., 2010; Palmeirim et al., 2013; Seifried et al., 2017, and many more).

Once T_d is calculated, the radiative transfer equation can be evaluated again to determine the observed intensity from a certain region.

Key dust continuum observations

A primary role in observations of dust FIR emission has been played by the Herschel telescope, a 3.5 meter diameter space telescope orbiting around the Lagrangian point L2. After its launch on May 2009, it remained in operation from late 2009 to 2013 and could observe in the range $55 - 671$ μm (Pilbratt et al., 2010). It included three detectors: the Photodetecting Array Camera and Spectrometer (PACS) was an imaging camera and low resolution spectrometer in the $55 - 210$ μm range (Poglitsch et al., 2010); the Spectral and Photometric Imaging Receiver (SPIRE) was also an imaging camera and low resolution spectrometer, but in a longer $194 - 671$ μm range (Griffin et al., 2010); the Heterodyne Instrument for the Far Infrared (HIFI) was a high resolution spectrometer which could operate in two bands, offering overall a similar wavelength range to the combination of those given by PACS and SPIRE (de Graauw et al., 2010).

Several thousands publications are based on, or include, data obtained by Herschel. Such data range from local clouds scale to external galaxies. Even though Herschel ceased its scientific mission in 2013, the data are still used in very recent works. This is the case, for instance, of Dunne et al. (2022), which used dust continuum data as ancillary data for cross-calibration of molecular gas mass tracers in metal-rich galaxies across cosmic time. Concerning molecular clouds, numerous works with which the results contained in Paper II are compared are based on Herschel's data: Pabst et al. (2022) used Herschel observations of Orion A, Goicoechea et al. (2015) compared dust emission data of the Orion Bar with [CII] data to study the [CII]-deficit, Herrera-Camus et al. (2018) worked on the same relation, but for nearby galaxies.

The extremely vast number of publications with data from Herschel is also due to the lack of other important telescopes covering the same wavelength range. There are other infrared telescopes, but the majority of them cover shorter wavelength

ranges. Among them, an important space telescopes is Spitzer, which remained in operation between 2003 and 2020 and observed in the $3.6 - 180$ μm range. It has been used for a wide range of scientific studies, from the search of exoplanets to the Galactic Legacy Infrared Mid-Plane Survey Extraordinaire (GLIMPSE), the first large-scale mapping of the galaxy in four different wavelengths (Benjamin et al., 2003; Churchwell et al., 2009). The Wide-field Infrared Survey Explorer (WISE) is another relevant telescope for mid-infrared observations (3.4, 4.6, 12, and 22 μm), aimed to map the entire sky in such wavelengths (Wright et al., 2010). Finally, it is worth mentioning that the James Webb Space Telescope, launched on 25th December 2021, is also a visible to mid-infrared telescope and it is expected that images with unprecedented resolution in such wavelength range will be obtained with it. Some initial images, like the famous one of the Creation Pillars in the Orion Nebula, confirm that significant progresses in visible and near-infrared astronomy will be possible with this telescope.

3

METHODOLOGY

In this chapter, we review the methods we use to obtain the results described in Paper I, Paper II, and Chapter 6. In Section 3.1 we describe theoretically the Magneto-hydrodynamics (MHD) equations and the approximations made to obtain them. We then briefly explain the two mostly used numerical techniques to solve such equations in Section 3.2. In Section 3.3 we describe the numerical code that is actually used for our simulations. Then, we highlight the setup and the general features of our simulations in Section 3.4, including the chemical network adopted. We then explain the numerical methods related to the radiative transfer in Section 3.5. We conclude the chapter with Section 3.6, where we describe the post-processing steps we operate in our simulations. In particular, we explain the process necessary to take into account the $C^+ \rightarrow C^{2+}$ photoionization. All these post-processing are also quickly described in Paper I, but, because of their importance in this work, we give here a more exhaustive description.

3.1
THE IDEAL MHD APPROXIMATION

The vast majority of astrophysical systems can be described by means of classical fluid dynamics equations. Indeed, gas velocities and densities are in general low enough not to require a relativistic description. There are, of course, a few exceptions, like black holes, neutron stars, or fast moving relativistic jets, but none of them are simulated in this project. Furthermore, the typical particle separation in the ISM is of the order of a few cm or less, which is many orders of magnitude lower than the maximum resolution of our simulations (a few 0.01 pc). This means that the fluid approximation for the ISM is, in our case, adequate.

The most complete description of a classical fluid is given by the Navier-Stokes equation, which is extremely complex, thus difficult to be solved, even numerically. In order to overcome this, further approximations are made. For instance, bulk viscosity plays in general little role in astrophysics: the ISM is highly turbulent (the Reynolds number has been estimated to be $R_e \sim 10^5 - 10^7$ (Elmegreen & Scalo, 2004)), implying that the viscous dissipation scales are much smaller than the spatial scales of interest and the resolution of all the simulations. This consideration is of great importance, as it allows us to use, instead of the Navier-Stokes equations, the much simpler Euler equation (Choudhuri, 1998). Other assumptions are typically made when magnetic fields are included in the description of the ISM, namely the infinite conductivity of the ISM (Stahler & Palla, 2004) and the perfect collisional coupling between charged and neutral particles.

When all the aforementioned assumptions are made, the combination of the Euler equatione for fluid dynamics and the Maxwell equations for the electromagnetic phenomena lead to the equations of ideal MHD. These can be written in terms of conservation laws of mass, momentum, energy, and magnetic flux. Let us consider a fluid with density ρ, velocity $\mathbf{v}$, total energy e_{tot}, magnetic field strength $\mathbf{B}$,

internal energy u, internal energy input rate $\dot{u}_{\text{heat}}$, thermal pressure P, and a local gravitational potential $\mathbf{g}$. The ideal MHD equations are as follows:

$$\frac{\partial \rho}{\partial t} + \nabla \cdot (\rho \mathbf{v}) = 0 \,, \tag{3.1}$$

$$\frac{\partial \rho \mathbf{v}}{\partial t} + \nabla \cdot \left[\rho \mathbf{v} \otimes \mathbf{v} + \left(P + \frac{B^2}{8\pi} \right) \mathbf{I} - \frac{\mathbf{B} \otimes \mathbf{B}}{4\pi} \right] = \rho \mathbf{g} \,, \tag{3.2}$$

$$\frac{\partial e_{\text{tot}}}{\partial t} + \nabla \cdot \left[\left(e_{\text{tot}} + \frac{B^2}{8\pi} + \frac{P}{\rho} \right) \mathbf{v} - \frac{(\mathbf{B} \cdot \mathbf{v}) \, \mathbf{B}}{4\pi} \right] = \mathbf{v} \cdot \mathbf{g} + \dot{u}_{\text{heat}} \,, \tag{3.3}$$

$$\frac{\partial \mathbf{B}}{\partial t} - \nabla \times (\mathbf{v} \times \mathbf{B}) = 0 \,. \tag{3.4}$$

Here Eqs. (3.1) to (3.4) represent the mass, momentum, energy, and magnetic flux conservation, respectively. We indicated the outer product with $\otimes$.

The total energy and the pressure of the gas are given, respectively, by

$$e_{\text{tot}} = u + \frac{1}{2} \rho v^2 + \frac{1}{8\pi} B^2 \tag{3.5}$$

and

$$P = (\gamma - 1) \, u \,, \tag{3.6}$$

where γ is the adiabatic index. We set t to $\gamma = 5/3$ (Walch et al., 2015).

The gravitational potential $\mathbf{g}$ and the density ρ are related to each other with the Poisson equation:

$$\nabla^2 \Phi = 4\pi G \rho \,, \tag{3.7}$$

$$\mathbf{g} = -\nabla \Phi \,. \tag{3.8}$$

We note that the zero divergence constraint on the magnetic field, i.e.,

$$\nabla \cdot \mathbf{B} = 0 \,, \tag{3.9}$$

is contained in the MHD equations. Maintaining this constraint is, however, one of the main difficulties for numerical solvers and spurious unphysical forces can be generated in case this is not maintained (Derigs et al., 2017).

We mentioned several approximations needed to obtain the ideal MHD equations. There are, however, circumstances where these are not entirely adequate. As an example, the assumption of perfect coupling between gas and charged particles can, in some case, not be fully realistic. This happens when the ionization fraction of the ISM is in general very low, especially in dense environments. For instance, Goicoechea et al. (2009) find the ionization fraction in the Horsehead nebula ranging from 10^{-4} to 10^{-9}. A consequence of this low ionization reaction is that, in very dense regions, charged particles and gas are actually imperfectly coupled (Mathis et al., 1977; Elmegreen, 1979; Nishi et al., 1991). This can result in a situation where the neutral particles have a drift motion respect to the charged particles. In this way, a structure which could not undergo gravitational collapse because of the collisional coupling with the plasma can actually collapse in case this coupling is lost. As this is a deviation from pure MHD physics, this phenomenon is not included in

our simulations.

Other non-ideal MHD effects can, in principle, also happen in the ISM. This is the case, for example, of the ohmic dissipation (e.g. Li et al., 2011) and the Hall effect (Wardle, 2004), both related to the violation of assumption of infinite conductivity of the ISM. For the densities and length scales investigated in our simulations, however, we expect both them to have a negligible effect.

3.2
Smoothed Particle Hydrodynamics and Eulerian approaches

Numerical simulations of the ISM normally use either the so-called *Smooth Particle Hydrodynamics* (SPH) or the Eulerian mesh-based approach. We now briefly describe the essential concepts of these two possible approaches. Another possible approach, which we do not discuss in detail, uses moving mesh (the GIZMO code, for instance, Hopkins, 2014).

Smoothed Particle Hydrodynamics simulations

Initially developed by Lucy (1977) and Gingold & Monaghan (1977), the SPH approach describes a fluid as a collection of particles and each of them represents a certain mass of the fluid. It is a Lagrangian method, i.e., fluid particles are followed as they move through space and time. Solving the aforementioned MHD equations means, in this context, solving the equation of motion for each of the particles and determining the position of such particles at the following time step.

The main advantage of using the SPH approach in simulations is that this approach is intrinsically mesh-free and this makes it easy to simulate problems with complicated boundary dynamics or large boundary displacement. Furthermore, the absence of a mesh structure makes SPH codes relatively easy to parallelize, even for many-cores architectures (Harada et al., 2007; Crespo et al., 2011). On the other hand, treatment of discontinuities in a SPH approach is difficult. This is the case, for instance, of wall boundary conditions and, more interestingly for astrophysical purposes, of evolution of shocks. Therefore, the choice about the approach to use shall be made carefully according to the physical problem which one wants to solve.

As each particle represents a certain fluid mass, the limiting resolution in a SPH approach is defined as a resolution in mass. As a consequence, the spacial resolution increases/decreases automatically in regions of high/low particle densities. In other words, a region with high mass density is, in this approach, a region with a large number of particles per volume unit.

Eulerian mesh-based simulations

The MHD equations can also be solved in an Eulerian reference frame, i.e., by considering a certain region of space and calculating the amount of fluid which flows through in a given time. In this approach, the fluid is distributed in a predefined grid, and the MHD equations are solved for every grid cell.

The basic idea of an Eulerian mesh-based code is that, for each cell, the time rate of change of a quantity of interest q in a fixed volume Ω is equal to the flux $\mathbf{f}$ of q across the boundary of this volume:

$$\frac{\mathrm{d}}{\mathrm{d}t} \int_\Omega q \, \mathrm{d}\mathbf{x} = - \oint_{\partial\Omega} \mathbf{f} \cdot \mathbf{n} \, dS \,, \qquad (3.10)$$

where **n** is the unit vector perpendicular (pointing outwards) to the surface of Ω, and dS is the surface element. With the assumption that **f** is differentiable, Eq. (3.10) can be rewritten in form of a partial differential equation:

$$\frac{\partial q}{\partial t} + \nabla \cdot \mathbf{f} = 0 \ . \tag{3.11}$$

If we imagine now, for notation simplicity, to deal with a 1D problem, this equation can be rewritten as

$$\frac{\partial q}{\partial t} + \frac{\partial f}{\partial x} = 0 \ . \tag{3.12}$$

Once the equations are written in the same form as in Eq. (3.12), the simplest formula to obtain a numerical solution, at the first-order approximation, is

$$q^{n+1} = q^n - \frac{\Delta t}{\Delta x} \left(f_r^n - f_l^n \right) \ , \tag{3.13}$$

where the superscripts n and $n+1$ indicate the quantities evaluated at the n-th and $n+1$-th time step, respectively, and f_r and f_l indicate the values of the flux calculated at the two opposite cell boundaries (the "right" and the "left" boundaries in this 1D model). There are different methods used to evaluate f_r and f_l and the type of physical problem of interest determines which one is more suitable. A commonly-used method is the Lax-Friedrichs scheme (Press et al., 2007, Section 10.1.2), which is particularly suitable for shock (and discontinuity in general) problems, which uses the eigenvalues of the Jacobian matrix of the flux to estimate f_r and f_l.

Although this description may look simple, a real 3D mesh-based MHD solver is complicated, as the role of gravity, magnetic fields and gas heating and cooling have to be taken into account as well. Furthermore, numerical constraints, like limited computational capacity and memory available, typically lead to the usage of non-uniform grids, where the resolution is adjusted according to the complexity of the simulated regions: this technique is called *adaptive mesh refinement* (AMR, Berger & Colella, 1989).

In general, the main advantage of a mesh-based solver is high accuracy, which enables, for instance, simulations of this scheme to easily follow the evolution of shocks. There are, however, critical aspects as well, which need a careful treatment. The most relevant of them is probably the fact that due to the fixed orientation of the grid, there is a preferred direction of travel, which can lead to advection errors of flows, when fluids with large velocity gradients move across grid cells (Hopkins, 2015; Clarke, 2016).

3.3
FLASH 4

The grid structure

The code used for the simulations performed and analyzed in this thesis is FLASH 4.3. It is a highly parallelizable, 3D AMR magneto-hydrodynamic code developed by the FLASH Center for Computational Science[1]. A detailed description of the code can be found in Fryxell et al. (2000) and Dubey et al. (2008). Here, we describe

---

[1] https://flash.rochester.edu/site/about/
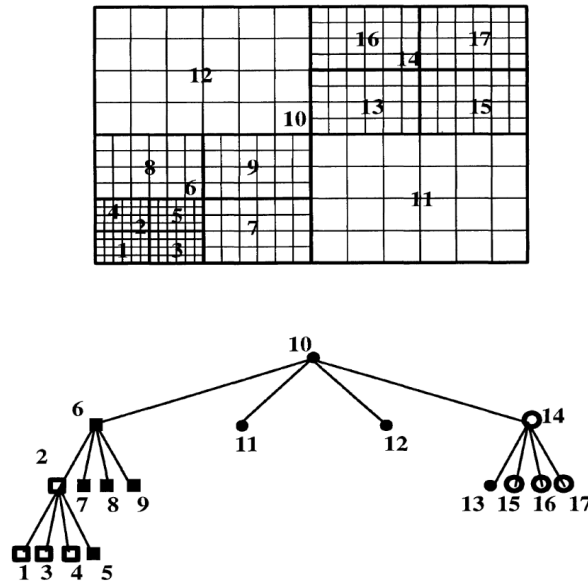
Figure 4: A simple 2D example of a grid block tree covering a rectangular domain. This example represents the AMR structure of FLASH 4. Image taken from MacNeice et al. (2000).

some important modules of the code which are used to performed the simulations analysed in this work.

The general data structure, as we already mentioned, is based on an AMR scheme and is described in detail in MacNeice et al. (2000). This is implemented in terms of *refinement levels*. The largest data block is the refinement level $l = 1$. This block is subdivided into 8 smaller blocks, which are the level $l = 2$. Some, or all, of these blocks in $l = 2$ can be further subdivided in smaller blocks which constitute the level $l = 3$, and so on. The maximum refinement level reached varies according to the simulation settings and, within the same simulation, in different regions according to the local properties of the simulated ISM. Various refinement and derefinement criteria can be chosen; we describe the ones used in our simulations in Section 3.4. The blocks which are not subdivided into smaller blocks contain 8^3 cells. A cell corresponds to the actual simulation resolution, and is the structure which contains the simulation data. This model is schematized in Fig. 4, where a 2D scheme is shown. The FLASH code is, however, a 3D simulation code.

The HD and MHD solvers

We already pointed out in Section 3.2 that, while the basic concept behind a grid (magneto-)hydrodynamic solver is relatively simple, its actual implementation is complicated, especially when electromagnetic phenomena, and not only hydrodynamics, are taken into account. The HD and MHD we analyse are performed by using two different solvers.

The hydrodynamic simulations are run with the directionally split (i.e., the three dimensions are treated as single Riemann problems and solved subsequent to each other) Bouchut 5-wave HLL5R MHD solver, with the magnetic field set to zero (Bouchut et al., 2007; Waagan, 2009; Bouchut et al., 2010; Waagan et al., 2011). It is a stable, approximate Riemann solver which preserves positive density and entropy for highly supersonic flows. Approximate Riemann solvers are those solvers aimed

to solve the so-called *Riemann problem*, i.e., the evolution of a hydrodynamic system whose initial conditions are a density and pressure discontinuity (typically shocks). The Lax-Friedrichs scheme that we mentioned in Section 3.2 is another example of approximate Riemann solver, much less sophisticated than the Bouchut solver used here.

The magneto-hydrodynamic simulations are, instead, run with the ES solver (Derigs et al., 2016, 2017, 2018). This is a solver which keeps the properties of the Bouchut solver (positive density and entropy preserved), but also accomodates minimum possible dissipation and assures that errors in the magnetic field divergence are treated in a way similar to the hyperbolic divergence cleaning method (Dedner et al., 2002). Intuitively, this method consists in transporting the divergence errors to the domain boundaries with the maximal admissible speed, and dumping them at the same time. This method produces overall significantly smaller divergence errors than other methods used in literature.

Gravity

Gravity effects are taken into account in FLASH. The gravitational potential is the sum of three different components: self-gravity, stellar clusters, and external potential.

Self-gravity is simply the potential due to the gas mass itself and it is calculated by means of the Poisson equation (Eqs. (3.7) and (3.8)). The practical implementation is performed using TreeRay (Wünsch et al., 2018), a tool which uses the tree structure of FLASH to calculate the gravitational acceleration.

The potential of stellar clusters is the gravitational potential of the stars which form during the simulations. Each set of formed stars is treated as a point source with a given mass, and the gravitational effects of these sources are then taken into account. In any case, the fraction of the cloud's mass which is converted into stellar mass is low, therefore the stellar cluster potential is not the dominant gravity source in our simulations.

The external potential is, in our simulations, the gravitational potential due to old stars in the galaxy, located outside the boundaries of the simulation. This potential is calculated according to a stellar surface density of 30 $M_\odot$ pc^{-2}, with a scale height of 100 pc, according to Spitzer (1942). Gravitational potential of dark matter is not included in our simulations, as it is supposed to play a negligible role at the scales (a few 100 pc) at which our simulations are performed.

Gas heating and cooling

Our simulations include an interstellar radiation field (ISRF) of strength $G_0 = 1.7$ in Habing units (Habing, 1968; Draine, 1978). The ISRF is attenuated depending on the column density of the gas, thus allowing for dust shielding and H_2 and CO self-shielding. This is implemented by using the OPTICAL DEPTH module of TreeRay (Wünsch et al., 2018). This module calculates the radiation intensity reaching a certain cell from every direction. A pixelized sphere is created around the cell of interest (HEALPIX, Gorski et al., 1999) and the column density of total hydrogen, H_2, and CO (these are the species which play an important role in shielding) are calculated for each of these pixels. Based on this, the average visual extinction, as well as the shielding coefficients for H_2 and CO, are stored. The average visual extinction is a quantity that represents the real extinction experienced by a certain cell, given the 3D structure of the cloud. Observers generally use the (projected)

visual extinction A_V to refer to the column density of an observed region. This is the column density of that region multiplied by a certain factor (see Section 2.2 for details). The average visual $A_{V,3D}$ used here is a 3D generalization of the same concept:

$$A_{V,3D} = -\frac{1}{2.5} \ln \left[\frac{1}{N_{PIX}} \sum_{i=1}^{N_{PIX}} \exp \left(-2.5 \frac{N_{H,tot,i}}{1.87 \times 10^{21}\, cm^{-2}} \right) \right] , \qquad (3.14)$$

where N_{pix} is the number of created pixels, and the total hydrogen column density $N_{H,tot,i}$ is calculated for each pixel. The sum is exponential because intensity of radiation decreases exponentially in presence of gas.

A fixed cosmic rays background is included in our simulation as well. The cosmic ray ionization rate (CRIR) is set to $3 \times 10^{-17}\, s^{-1}$ with respect to atomic hydrogen. Unlike the ISRF, cosmic rays are barely shielded and can penetrate deeply in the ISM and influence essentially its chemistry.

The chemical network is evolved *on-the-fly* in the simulation. The net (positive or negative) heat generated in the chemical reactions contributes to the overall heating or cooling of the ISM. Practically, this contribution is included in the $\dot{u}_{heat}$ term in Eq. (3.3).

3.4
The SILCC and SILCC-Zoom Projects

The SILCC Project is a simulation project aimed to model the entire life-cycle of molecular clouds from the formation in the diffuse ISM to the dispersal by stellar feedback. Simulations within the SILCC Project constitute the basis of those that we analyse in this work. In the following, we first describe the setup of these simulations. Then, we give a description of the SILCC-Zoom simulations, which we analyse in this work.

SILCC

The SILCC simulations (see Walch et al., 2015; Girichidis et al., 2016, for a more detailed description of the setup) aim to investigate the ISM dynamics in relation to the life-cycle of molecular clouds in a portion of galactic disk with solar neighborhood conditions in the present day universe.

The simulation domain is a box of size 500 pc × 500 pc × ± 5 kpc in the vertical direction. Initially, the vertical gas profile (i.e., along the "long" side of the box) has an exponential distribution given by

$$\rho(z) = \max \left[\rho_0 \exp \left(-\frac{1}{2} z^2 / h^2 \right), \, 10^{-28}\, g\, cm^{-3} \right] , \qquad (3.15)$$

where $h = 30$ pc and the mid-plane density $\rho_0 = 9 \times 10^{-24}\, g\, cm^{-3}$. This corresponds to a disc's gas surface density of $\Sigma_{gas} = 10\, M_\odot\, pc^{-2}$. The max condition is intended to prevent the density far away from the galactic plane to drop to arbitrarily low values. The total mass in the simulation domain is $2.5 \times 10^6\, M_\odot$. The temperature of the gas is set initially to 4500 K near the midplane, and to 4×10^8 K in the low density region distant from the midplane, representing hot the gas from the halo. All the hydrogen is set to be initially in atomic form, and all carbon in single ionized form. For runs with magnetic fields (the project includes both runs with and without magnetic fields included), an initial field is set along the *x*-axis.

Its strength varies as a function of the distance from the galactic midplane z:

$$\mathbf{B} = B_x(z)\hat{\mathbf{x}} = B_{x,0} \left[\frac{\rho(z)}{\rho_0} \right]^{-1/2} \hat{\mathbf{x}} , \qquad (3.16)$$

where $\rho(z)$ is as defined in Eq. (3.15) and $B_{x,0} = 3\,\mu$G.

The multi-phase ISM is created by driving supernova explosions in the galactic disk. The rate at which the SNe are injected is given by the Kennicutt-Schmidt (KS) relation (Schmidt, 1959; Kennicutt, 1998), which relates the disc's gas surface density to a typical star formation rate surface density: $\Sigma_{SFR} \propto \Sigma_{gas}^{1.4}$. In a next step, the star formation rate is translated into an SN rate by assuming a standard initial mass function (Chabrier, 2001). A single SN explosion injects an energy of 10^{51} erg into the system in different possible ways, depending on whether the resolution of the simulation in the point where the SN explodes enables to resolve the Sedov-Taylor phase of the SN or not (Gatto et al., 2015; Walch & Naab, 2015; Haid et al., 2016, for details). In any case, this energy injection causes turbulence in the simulated ISM, which leads to the formation of denser regions and, ultimately, of molecular clouds. The SNe are ejected continuously, at a constant rate of 15 Myr^{-1}, in the SILCC simulations. The position where these SNe explode plays a major role in shaping the ISM and, as a consequence, the structures which generate. Several possible configurations have been tested in the first SILCC simulations (Walch et al., 2015; Girichidis et al., 2016). The configuration which better resembles the ISM with solar properties is a mixed driving of SNe: 50 per cent of them are injected in random positions (modulo a weighting of the vertical position) and the other 50 per cent are located in local density peaks. The motivation beyond this choice is to mimic the explosions of massive stars in either their parental cloud (SNe injected in density peaks) or diffuse regions due to runaway massive stars (SNe injected randomly).

SILCC-Zoom

The energy injected by SN explosions in the SILCC simulations, and the consequent turbulence, creates the multi-phase ISM. As a result, portions of the gas, in which hydrogen was initially entirely atomic, create denser structures, and several cold and dense MCs develop from the diffuse ISM. The limited resolution of the SILCC simulations, 3.9 pc, does not allow to follow in detail the evolution of a single MC. In order to do so, it is necessary to run new simulations with a much smaller domain, but much higher achievable resolution. This is is done within the SILCC-Zoom Project. Regions of the SILCC simulations where MCs are forming are identified, and then the simulations are restarted, only for those regions, from a time where the number density inside the "zoom-in" regions do not exceed a few 10 cm^{-3}. This represents the starting time of the SILCC-Zoom simulations. The time passed since the beginning of the zoom-in simulation will be referred to as t_{evol}. External SN explosions are switched off in the SILCC-Zoom simulations.

As we mentioned, the maximum resolution achievable in the SILC-Zoom simulations is much higher compared to the 3.9 pc of the SILCC simulations. There are two criteria do decide which regions need to be refined.

- Variations on gas density are used to refine the simulations up to 0.5 pc, i.e., 3 refinement levels above the base grid. This estimate is based on the approach described by Lohner (1987), which takes into account the second derivative of the density field normalized by the average of the gradient. This allows us to capture low-density fluctuations. This criterion is quite sensitive such that,

practically, the entire region is refined to the maximum possible resolution.

- Considerations on the Jeans length L_{Jeans} are also used as a refinement criterion: L_{Jeans} is computed for all cells and it must be resolved with at least 16 cells in each dimension (Truelove et al., 1997; Federrath et al., 2011). This criterion is used to refine up to 0.122 pc (5 levels above the base grid) or 0.061 pc (6 levels above). We use simulations refined up to 0.122 pc in Paper I and Paper II, and we use both for the discussion on the features of the chemical networks in Chapter 6.

Numerical artifacts may appear if the refinement from the base grid to the maximum level is applied instantaneously. On the other hand, if the refinement is performed in a time scale longer than the free fall time of the cloud, key features of the cloud itself may be affected. A suitable compromise solution, found in Seifried et al. (2017) and used in the simulations we analyse, is to spend around 200 time steps on each intermediate refinement level, corresponding to a total zoom-in time of roughly $1 - 1.5$ Myr. Furthermore, numerical artifacts can also appear if the refinement level of two neighboring blocks differ by more than one level. Therefore, an additional refinement criterion is applied: this prescribes that if a certain block is refined to the n-th level, all the neighboring blocks must be refined either to the same level, or to one level more or less, (i.e., to the $n + 1$-th or the $n - 1$-th level).

Analyzed clouds

Paper I and Paper II use 8 different simulations within the SILCC-Zoom Project. There, we analyse 2 pure HD clouds, i.e., with no external magnetic field included, to which we refer as MC1-HD and MC2-HD, and two MHD clouds, i.e., with the external magnetic field of 3 μG included. Those clouds are labelled MC1-MHD and MC2-MHD. We consider, for all clouds, runs with no stellar formation and feedback included, labelled by the suffix "-noFB", and runs with star formation and stellar feedback, labelled with "-FB". In Chapter 6 we only use clouds without stellar feedback.

3.4.1

Treatment of stellar feedback

The simulations within the the SILCC-Zoom projects can be performed either with or without stellar feedback included. Indeed, in Paper I we explore the effect that stellar feedback has on CO and [CII] emission, and therefore we need to use simulations in both configurations.

In our simulations, stars can form under the following conditions: provided that a certain region of the simulation domain is in the highest refinement level, an accretion radius is set to be $r_{\text{accr}} = 0.31$ pc. Within this radius, the gas must be Jeans unstable (i.e., can collapse via Jeans instability), in a converging flow and representing a local gravitational potential minimum (Federrath et al., 2010). These conditions lead to the definition of a density threshold ρ_{si} above which stars can form:

$$\rho_{\text{si}} = \frac{\pi k_B}{m_p G} \frac{T}{4 r_{\text{accr}}^2} \ , \tag{3.17}$$

where k_B is the Boltzmann constant, m_p the proton mass, and G is the gravitational

constant. Given the r_{accr} set, this is

$$\rho_{\mathrm{si}} \approx 1.1 \times 10^{-20} \left(\frac{T}{100\ \mathrm{K}} \right) \mathrm{g\ cm}^{-3} .\tag{3.18}$$

If a cell satisfied these conditions, a *sink particle* is created in that cell. A sink particle is a simulation object that represents a cluster of stars. It is, thus, a collection of stars, each of them with different properties (temperature, luminosity radiation emitted), but is treated as a single object concerning dynamics in the cloud and gas accretion. Only the massive star ($\geq 9\,M_\odot$) properties are followed and the low mass stars are not sampled.

Sink particles, indeed, accrete gas. One new massive star ($9\ \mathrm{M}_\odot \leq M_\star \leq 120\ \mathrm{M}_\odot$) is randomly sampled for every 120 M$_\odot$ accreted on a sink (Kroupa, 2001). The Salpeter slope of -2.35 (Salpeter, 1955) in the high-mass regime of the IMF is assumed to sample the mass of the newly formed stars. The residual gas accreted is converted into low-mass stars, which are not recorded individually as they provide no feedback (in our simulations) to the surrounding medium.

The transfer of ionizing radiation is calculated by TreeRay (Wünsch et al., 2021). In order to simulate the evolution, and in particular the radiative energy output, of massive stars from the zero-age main sequence to the Wolf–Rayet phase, the prescriptions given in Gatto et al. (2017) and Peters et al. (2017) have been followed. These prescriptions essentially provide temperature, mass, and luminosity of the formed star throughout their life time, which result in information on the rate of emitted photons at their different stages. The photon packages emitted are then propagated in the cloud with TreeRay. More details on this are provided in Haid et al. (2019). The ionization heating rate and number of ionizing photons are provided to the chemistry module of FLASH, where the gas temperature is self-consistently increased by balancing heating and cooling processes, the mean hydrogen ionization state is updated using the photoionization rate which results from the stellar activity (Haid et al., 2018), and CO is dissociated.

3.4.2

Chemical network

A chemical network is implemented in the SILCC and SILCC-Zoom simulations. This network permits to calculate the evolution of some chemical species *on-the-fly*. The simulations used for Paper I and Paper II use the chemical network given in Glover & Mac Low (2007a,b), integrated with the model for CO formation introduced by Nelson & Langer (1997). We refer to this network as NL97, which we describe in the following. The simulations used in Chapter 6 use a more complex network instead, which will be described in that chapter.

The hydrogen chemistry is based on 8 chemical reactions listed in Table 3.1. We refer to Glover & Mac Low (2007a) and references therein for information on the reaction rate.s

Besides these reactions, creation and destruction of CO are modelled as well. This is done by assuming that CO is destroyed by photodissociation and is converted instantly to C^+, as the range of radiation wavelengths that ionize carbon is larger than that which photodissociates CO. In turn, C^+ is destroyed by radiative association:

$$\mathrm{C}^+ + \mathrm{H}_2 \rightarrow \mathrm{CH}_2^+ + \gamma .\tag{3.19}$$
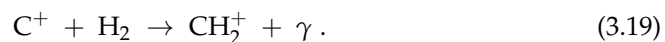
Table 3.1: Set of chemical reactions making up the non-equilibrium hydrogen chemistry model used in the SILCC and SILCC-Zoom simulations which use the NL97 chemical network (Glover & Mac Low, 2007a).

	Hydrogen chemistry	
H + H + grain	$\rightarrow$	H_2 + grain
H_2 + H	$\rightarrow$	3H
H_2 + H_2	$\rightarrow$	2H + H_2
H_2 + γ	$\rightarrow$	2H
H + CR	$\rightarrow$	H^+ + e
H + e	$\rightarrow$	H^+ + 2e
H^+ + e	$\rightarrow$	H + γ
H^+ + e + grain	$\rightarrow$	H + grain

Then, CH_2^+ rapidly converts into CH or CH_2 via ion-molecule reactions with H_2 and dissociative recombination with electrons. At this point, the radicals can form CO via reaction with the oxygen molecule.

These reactions are not modelled in the NL97 network one-by-one. Instead, these considerations lead to an equation which regulates the overall creation and desctruction of CO:

$$\frac{dn_{CO}}{dt} = f\left(n_{C^+}, n_O, G_{0,l}\right) + g\left(n_{CO}, G_{0,l}\right) , \tag{3.20}$$

where $f\left(n_{C^+}, n_O, G_{0,l}\right)$ is a parameter depending on n_{C^+}, n_O, and the local ionization field $G_{0,l}$. More details on these reactions are provided in Nelson & Langer (1997).

The aforementioned chemical reactions are completed with conservation laws, which prescribe that the total abundance of carbon, oxygen, hydrogen, as well as the total charge of the ISM are conserved. Practically, this means that, indicating by x_Y the factional abundance of the species Y respect to total hydrogen, we have that

$$x_{C^+} = x_{C,tot} - x_{CO} , \tag{3.21}$$

$$x_H + 2\,x_{H_2} + x_{H^+} = 1 , \tag{3.22}$$

$$x_O = x_{O,tot} - x_{CO} , \tag{3.23}$$

and

$$x_e = x_{H^+} + x_{C^+} + x_{Si^+} . \tag{3.24}$$

We note that the evolution of Si^+ is not followed in the chemical network. Instead, a constant fractional abundance of it is assumed.

The fractional abundances of total carbon, oxygen, and silicon are taken constant and typical of solar neighborhood conditions: $x_{C,tot} = 1.41 \times 10^{-4}$, $x_{O,tot} = 3.16 \times 10^{-4}$, and $x_{Si,tot} = 1.5 \times 10^{-5}$ (Sembach et al., 2000).

The implementation of this chemical network, together with the calculation of the heating and cooling processes (see Section 3.3) and the stellar feedback (Section 3.4.1) permits to obtain the chemical abundance of all the modelled species at any time in the simulation domain. It is, then, necessary to solve the radiative transfer

equation in order to produce synthetic emission maps of the modelled clouds. The way this is done is discussed in the next section.

3.5
IMPLEMENTATION OF RADIATIVE TRANSFER

In this section, we describe the implementation of radiative transfer in this work. We already discussed the theoretical aspects in Section 2.4.1. Here, we focus instead on how these concepts are implemented. This section is structured as follows. We first explain the treatment of line radiative transfer. Then, we illustrate the implementation of dust continuum emission, which includes the calculations of the dust temperature as a consequence of stellar radiation, and the radiative transfer of light emitted from grains. We leave to Section 3.6 the descrption of the post-processing steps we operate on the simulations before performing the radiative transfer. We discuss the post-process after the radiative transfer because this post-process is performed on the radiative transfer code input files. It is thus easier to first introduce the code, and then explain how these files are post-processed.

All the calculations relative to radiative transfer are performed by using RADMC-3D (Dullemond et al., 2012), a code package for diagnostic radiative transfer calculations in astronomy and astrophysics.

3.5.1
LINE RADIATIVE TRANSFER

Performing the radiative transfer for line emission essentially means solving Eq. (2.16). As we noted in Eqs. (2.13) and (2.14), the emission and absorption coefficients, j_ν and α_ν respectively, depend on the line profile $\phi(\nu)$, which has to be a distribution sharply peaked at the rest frequency ν_0. The (co-moving) line profile assumed $\tilde{\phi}(\nu)$ by RADMC-3D is

$$\tilde{\phi}(\nu) = \frac{c}{a_\text{tot}\nu_0\sqrt{\pi}} \exp\left[-\frac{c^2(\nu-\nu_0)^2}{a_\text{tot}^2\nu_0^2}\right] , \qquad (3.25)$$

where a_tot is the total linewidth. It is composed out of a thermal contribution a_therm an a turbulent term a_turb, such as

$$a_\text{tot} = \sqrt{a_\text{therm}^2 + a_\text{turb}^2} . \qquad (3.26)$$

In our simulations, we set

$$a_\text{turb} = a_\text{therm} = \sqrt{\frac{2k_B T_\text{g}}{\mu m_\text{H}}} , \qquad (3.27)$$

where T_g is the gas temperature, μ is the molecular weight of the emitting particle, and $m_\text{H} \approx m_\text{p}$ is the hydrogen atom mass.

Knowledge of the level populations of the emitting particle is also needed for calculating the emission and absorption coefficients. While they are easily calculated in Local Thermal Equilibrium (LTE), as the level population follows the Maxwell-Boltzmann distribution (Eq. (2.21)), this is not true when LTE is not assumed. Instead, RADMC-3D can calculate the level populations in several ways. We choose to use the so-called *Large Velocity Gradient* (LVG) approximation (Sobolev, 1957; Os-

senkopf, 1997; van der Tak et al., 2007; Shetty et al., 2011). In this approximation, the velocity gradient is used to calculate an optical depth τ_{LVG}:

$$\tau_{\mathrm{LVG}} = \frac{hc}{4\pi} \frac{n_X}{1.064\,|\nabla \cdot \mathbf{v}|} \left(x_l B_{lu} - x_u B_{ul} \right) \,, \tag{3.28}$$

where n_X is the number density of the species of interest, x_l and x_u are the number fraction of the species X in the lower and upper state, respectively (we are here modelling line emission from a two-level system), and B_{lu} and B_{ul} are the Einstein's absorption and stimulated emission, respectively.

After τ_{LVG} (hereafter only τ for notation simplicity) has been calculated, an escape probability β is calculated:

$$\beta = \frac{1 - e^{-\tau}}{\tau} \,. \tag{3.29}$$

With β calculated, the line integrated mean intensity J is

$$J = (1 - \beta)\,S + \beta J^{\mathrm{bg}} \,, \tag{3.30}$$

with $S = j_\nu / \alpha_\nu$ the source function and J^{bg} the background radiation field, which is the CMB in our simulations.

The equations above describe, practically, how to calculate J, provided that the level population of the species of interest is known. Therefore, we need to explain now how to calculate the level population, as long as the Maxwell-Boltzmann distribution cannot be used.

For calculating the level population of the species of our interest, namely C^+ and CO, we need to know the collisional rates with their collisional partners. We consider para-H_2, ortho-H_2, H, and electrons as collisional partners for C^+, and para-H_2, ortho-H_2, H, and He as collisional partners for CO. We do not follow the evolution of helium in the NL97 chemical network; instead, we fix the fractional abundance of helium to 0.1 in respect to total hydrogen. The collisional data are taken from the Leiden Atomic and Molecular DAtabase (LAMDA, Schöier et al., 2005), and we take a constant value for all the temperatures equal or larger than the highest temperature provided in the database Goldsmith et al. (2012). Since the LAMDA database does not provide collisional data for CO with H and He, we use for this the data from Walker et al. (2015) and Cecchi-Pestellini et al. (2002), respectively. The rate coefficient for the species X in the ul transition is

$$C_{ul}^X = \sum_{\mathrm{cp}} n_{\mathrm{cp}}^X R_{ul}^{\mathrm{cp}} \,, \tag{3.31}$$

where R_{ul}^{cp} is the excitation rate for the specific collisional partner "cp" and is read from the collisional data tables, n_{cp}^X is the number density of the collisional partner "cp" of the species X, and the sum is run over all the collisional partners considered. The corresponding rate coefficient for the upward transition is calculated as

$$C_{lu} = C_{ul} \frac{g_u}{g_l} \exp\left(\frac{-h\nu_{ul}}{k_B T} \right) \,. \tag{3.32}$$

Then, the level population is obtain by solving the statistical equilibrium, i.e.,

$$x_l C_{lu} - x_u C_{ul} = x_u A_{ul}\beta + \left(x_u B_{ul} - x_l B_{lu} \right) \beta_{ul} J_{ul}^{\mathrm{bg}} \,. \tag{3.33}$$

We note that Eqs. (3.29) and (3.33) depend on each other, as β appears in the

statistical equilibrium equation, but the definition of β includes x_l and x_u (they appear in τ). Because of this, both equations need to be solved together iteratively.

It might be that the co-moving line width (Eq. (3.25)) becomes narrower than the Doppler shift. If this is the case, some velocity channels do not contribute to the emission. This is, however, a numerical artifact that shall be eliminated. This is done by using a "Doppler-catching" method (Pontoppidan et al., 2009), that ensures a smooth behaviour of the emission in neighbouring velocity channels. This module can be optionally included or excluded in the RADMC-3D calculations, but we include it in all our analysis.

3.5.2

Dust continuum radiative transfer

Dust temperature

The dust temperature in the ISM, and more specifically in MCs, is the consequence of dust heating due to either the external ISRF or the stellar radiation coming from the stars formed in the MC. The radiative transfer modules in FLASH calculate the dust temeprature as a consequence o the ISRF, but do not take into account the effect of formed stars, which, as we show in Paper II, is definitely dominant in MCs respect to the effect of the ISRF. We use RADMC-3D to calculate the dust temperature resulting from stellar radiation, and for each cell we take the maximum between the temperature calculated with RADMC-3D and the temperature given by FLASH, so that we take into account both effects.

In RADMC-3D, the dust temperature is calculated using the Monte Carlo method of Bjorkman & Wood (2001) with various improvements, such as the continuous absorption method described by Lucy (1999). We refer to these paper for a detailed description of the method. Here, we give only a qualitative description of it based on the RADMC-3D's manual.

The total star luminosity is divided into a certain number of photon packages (the number can be chosen by the user). These packages are emitted by the stellar sources one-by-one and, as they move through the grid they may scatter off dust grains and thus change their direction. Besides getting scattered, photons can also be absorbed by dust grains. When this happens, the photon package is immediately re-emitted in another direction and with another wavelength. Each time a photon package enters a cell it increases the dust temperature of that cell. The dust temperature of a cell, conversely, decreases when a photon package leaves the cell. Each photon package moves through the model and never gets lost until it escapes the model through the outer edge of the grid. At this point, another photon package is launched and undergoes the same procedure. The final dust temperature is thus the one resulting after all the photon packages have been launched and escaped the simulation domain.

It is worth noting that the dust temperature calculated in this way is an equilibrium temperature. In principle, this is contradictory with the non-LTE assumption that we make concerning the line radiative transfer. However, this is for most cases presumably a very good approximation, because the heating/cooling time scales for dust grains are typically very short compared to any time-dependent dynamics of the system, including the chemical evolution time scales.

Dust continuum emission maps: treatment of scattering

When discussing photon scattering from dust grains, we have to differentiate between UV photons coming from the stars, and IR photons emitted by the grains.

The UV photons coming from the stars are the heating source of the dust and, as we explained above, their scattering on dust grains is taken into account intrinsically by RADMC-3D when calculating the dust temperature via the Monte Carlo method.

The scattering of IR photons emitted by dust plays a role in changing the shape of the dust continuum emission maps. There are several possible treatments of IR photon scattering in RADMC-3D: it can be either simply neglected, or treated as isotropic, or considered anisotropic, with different levels of approximation. The type of treatment depends both on the dust data that are provided to RADMC-3D and on the settings selected. We use dust data from Weingartner & Draine (2001), which allow for isotropic treatment of scattering. Nevertheless, we switch off such scattering, as its role in affecting emission maps on clouds' scale is negligible. As a consequence, the radiative transfer equation of dust has, with these approximation, the same form as the one for lines (Eq. (2.16)), with

$$\alpha_\nu = \rho_\mathrm{d} k_\mathrm{abs}(\nu) \tag{3.34}$$

and

$$j_\nu = \rho_\mathrm{d} k_\mathrm{abs}(\nu) B(\nu) \,, \tag{3.35}$$

with ρ_d the dust mass density, $k_\mathrm{abs}(\nu)$ the tabulated absorption coefficient, which depends on ν, and $B(\nu)$ the spectral emissive power given by the Planck's law.

The radiative transfer is performed by RADMC-3D by always taking into account both the emission and the absorption term. Nevertheless, we calculated the optical depth τ_ν for several snapshots of our simulations used in Paper II and found that $\tau_\nu > 0.3$ happens rarely, and in the vast majority of the maps it is well below that value. This means that in general the dust emission is optically thin, and the absorption term plays little role in the radiative equation, i.e.,

$$\frac{dI_\nu}{ds} \approx j_\nu \tag{3.36}$$

is in general a good approximation for dust emission in MCs.

3.6
Post-processing of the simulations

We described the main features of the simulations we use, the chemical network implemented, and the treatment of the radiative transfer that we need in order to obtain synthetic emission maps. In order to obtain more realistic results, however, we aim to consider effects which are not included in the physics and chemistry packages of FLASH, and therefore not considered in the original SILCC-Zoom simulations. We include them by post-processing the simulation data before operating the radiative transfer with RADMC-3D. The effects we include are:

- **CO freeze-out**. In dense and cold gas, CO in gas-phase freezes-out on dust grains, and its average residence time on the grains is relatively long. As the fraction of CO which is frozen on dust grains is neither available as a cooling source nor as a reaction reagent, nor emits light, this phenomenon practically

leads to a CO leak in these environments. A good observational example is provided in Bergin et al. (2002), and the mathematical description which we follow in the implementation is given by Glover & Clark (2016).

Cosmic rays, dust temperature, and collision rate between CO and grains, which in turn depends on the gas temperature, are responsible for the CO freeze-out. Their contribution is expressed trough three coefficients k_{cr}, k_{therm}, and k_{ads} which represent the contributions of CRs, thermal desorption, and collisional desorption, respectively. They are defined as (units are omitted)

$$k_{cr} = 5.7 \times 10^4 \times \text{CRIR} \,, \tag{3.37}$$

$$k_{therm} = 1.04 \times 10^{12} \exp\left(-\frac{960\,\text{K}}{T_d}\right) \tag{3.38}$$

$$k_{ads} = 3.44 \times 10^{-18} \sqrt{T_g} \left(2n_{H_2} + n_H\right) \,. \tag{3.39}$$

The number density of frozen CO is then given by

$$n_{CO,f} = n_{CO} \times \frac{k_{cr} + k_{therm}}{k_{cr} + k_{therm} + k_{ads}} \,. \tag{3.40}$$

The calculation of $n_{CO,f}$ is performed cell-by-cell, and the resulting CO density is updated consequently. The script which performs this calculation is included in the pipeline that we use to convert the FLASH simulation data into RADMC-3D input data. This pipeline, written by Pierre C. Nürnberger, is publicly available at https://astro.uni-koeln.de/walch-gassner/downloads/flashpp-pipeline.

- $C^+ \to C^{2+}$ **thermal ionization**. In hot and diffuse regions, particle collision leads to a significant fraction of C^+ being further ionized into C^{2+}. We reduce the C^+ number density in all cells with $T_g \geq 20\,000$ K by a scaling factor $k\left(T_g\right)$ taken from Sutherland & Dopita (1993), such as the new number density $n_{C^+}^{new}$ is

$$n_{C^+}^{new} = k\left(T_g\right) \times n_{C^+} \,, \tag{3.41}$$

where here n_{C^+} is the original C^+ number density. For $T_{gas} \gtrsim 100\,000$ K less than 1 per cent of the original C^+ is preserved. This correction is implemented in the aforementioned pipeline as well.

- $C^+ \to C^{2+}$ **photoionization**. This post-processing step is implemented first in Paper I, and the results shown there are the first one which take into account C^+ photoionization within the work of our group. As this concerns stellar feedback, only simulations which have it included undergo this post-processing step.

Stellar radiation from massive stars can cause further ionization of carbon (Abel et al., 2005, for instance). In particular, O- and B-type stars, which are those whose radiation is taken into account in our simulations, emit a non-negligible amount of photons with energy exceeding the second ionization energy of carbon, equal to 24.4 eV. We expect, therefore, that a significant fraction of the C^+ located in the HII regions created by massive stars is actually converted into C^{2+}. As this phenomenon is not taken into account in the original SILCC-Zoom simulations, the necessity of implementing a post-processing step for this arises.

The quantities that play a major role in determining which fraction of C^+ is converted into C^{2+} are the gas density n_g, the gas temperature T_g, and the number of photons available with $h\nu \geq 24.4$ eV. The first two quantities are directly available as FLASH output data. Conversely, we need to derive the latter from the stellar temperature $T_\star$ and the energy density of photoionizing photons E_{ion} (i.e., the energy density of photons with $h\nu \geq 13.6$ eV). Indeed, given E_{ion} and $T_\star$, we can derive, for instance, the energy density $E_{ion}^{C^+}$ of photons capable of ionizing C^+ by assuming that the stars emit light as a black body. This is also assumed throughout all the other simulation steps, i.e., when calculating the radiation emitted by the stars and the dust temperature. We obtain that

$$E_{ion}^{C^+} = E_{ion} \frac{\int_{24.4\ eV}^{\infty} B_\nu(T_\star) d\nu}{\int_{13.6\ eV}^{\infty} B_\nu(T_\star) d\nu} \ . \tag{3.42}$$

We use CLOUDY (Ferland et al., 2017) to perform the necessary calculations for this post-process. This is a spectral synthesis code designed to simulate conditions in interstellar matter under a broad range of conditions. In practice, it simulates a 1D-slab PDR, with radiation illuminating one side of the slab, and the chemical composition of the PDR, together with other features, is calculated as a function of distance from the illuminated side of the slab. We aim, ideally, to build CLOUDY models of PDRs with the same gas density and temperature of the portion of the cloud we are interested in, illuminated by the rate of ionizing photons we calculate with Eq.(3.42). In this way, CLOUDY determines the chemical composition of that PDR, which we interpret as the correct chemical composition of the region of our interest, and therefore we replace the original n_{C+} with the one given by CLOUDY, which considers the C^+ photoionization. There are, however, a number of relevant implementation difficulties, which we describe in the following.

First of all, CLOUDY requires the bolometric luminosity L_{bol} of a star as an input parameter, and not E_{ion} or $E_{ion}^{C^+}$. Because of this, we first define an "ionizing luminosity" as the luminosity of a star located at a distance d from the region which has the given E_{ion}, in absence of any shielding effects, calculated by considering only those photons with $h\nu \geq 13.6$ eV:

$$L_{ion} = \frac{1}{c} \frac{E_{ion}}{4\pi d^2} \ . \tag{3.43}$$

At this point, we determine the bolometric luminosity of this star following the same idea we used to write Eq. (3.42):

$$L_{bol} = L_{ion} \frac{\int_0^{\infty} B_\nu(T_\star) d\nu}{\int_{13.6\ eV}^{\infty} B_\nu(T_\star) d\nu} \ . \tag{3.44}$$

Using Eqs. (3.43) and (3.44) together we can convert E_{ion}, available as a FLASH output, into L_{bol}. It is crucial to note, here, that d is not the real distance between the cell and the star. If we used the real distance, we would indeed need 5 parameters per cell to perform this post-process, instead of the 4 we declared to use. The reason why it is important to reduce these parameters to a minimum will be clarified in the following. The choice we make, instead, is to set a constant value of $d = 100$ pc for all cells. This means that L_{bol} that we calculate is not the real bolometric luminosity of the star of interest, but the

Table 3.2: Parameter range used for our CLOUDY models. Steps are equally spaced in log-scale.

Quantity	min	max	steps
$n_{\rm g}$ [g cm^{-3}]	10^{-26}	10^{-20}	19
$T_{\rm g}$ [K]	$10^{1.5}$	$10^{4.5}$	19
$T_\star$ [K]	$10^{3.5}$	$10^{5.5}$	21
$E_{\rm ion}$ [erg cm^{-3}]	10^{-18}	10^{-8}	21

bolometric luminosity of an hypothetical star, located at 100 pc from the cell, which produces exactly the same amount of $E_{\rm ion}$ (and therefore also of $E_{\rm ion}^{\rm C^+}$ as the star temperature is the real one) which we have in the simulation. This choice is reasonable since, as we pointed out before, the quantity physically determining the fraction of ionized C^+ is $E_{\rm ion}^{\rm C^+}$.

We cannot run one CLOUDY model for each cell of our simulation domain, for all the analysed snapshots: this would be extremely computationally demanding and thus practically unfeasible with the computational resources available. Instead, we preliminary build a database of CLOUDY models and then we interpolate, for each cell, the data in this database. This approach has already been used in literature, and provided to be sufficiently reliable (Vallini et al., 2015, 2018, 2021; Katz et al., 2017, 2019; Lagache et al., 2018; Pallottini et al., 2019; Leung et al., 2020; Lupi et al., 2020; Liang et al., 2023). We sample $n_{\rm g}$, $T_{\rm g}$, $T_\star$, and $E_{\rm ion}$ within their variability range in our simulations and create the database. Then, we loop for each cell of the snapshot that we post-process and we use LinearNDInterpolator[2], part pf Python's SciPy library, to interpolate the database for the values of the specific cell. Table 3.2 summarizes the parameter range we used. In total, this results in approximately 160 000 CLOUDY models.

It is also important to note that this process is based on the concept that one single star is responsible for the ionization of a given cell. In most cases, this is actually not true. Instead, several stars act together in a certain region, and the presence of a certain $E_{\rm ion}$ is a consequence of all them. We adopt a simplifying assumption that the star whose unattenuated energy flux in the cell of interest is the largest is the only responsible for the ionizing energy in that cell. Therefore, for each cell we loop over all the stars in the simulation domain and for each of them we calculate the flux

$$F = \frac{\widetilde{L_{\rm bol}}}{4\pi \tilde{d}^2} \, , \tag{3.45}$$

where $\widetilde{L_{\rm bol}}$ and $\tilde{d}$ are the real bolometric luminosity (available as simulation data) and the real distance from the cell, respectively. We then select, for the rest of the post-processing, the star which has the largest F. We also check that the selected star is not more than twice as far away from the cell as the closest star, but this never happens in our simulations.

The cells we post-process can have a size of $dx = 0.122$, 0.244, 0.488, or 0.976 pc. We take $dx = 0.976$ as the depth of the PDR in CLOUDY, then we integrate

---

[2]https://docs.scipy.org/doc/scipy/reference/generated/scipy.interpolate.LinearNDInterpolator.html

the results given by CLOUDY (which provides the species abundances as a function of the depth from the illuminated side of the PDR) for each possible dx and we save the results in 4 different database. We select the database to interpolate cell-by-cell, according to the size of the cell itself. In this context, the choice of $d = 100$ pc assures that $dx \ll d$, that is, that the CLOUDY models are essentially a plane-parallel PDR which we can then directly map back to the simulation cell.

We can now summarize the steps we follow for this post-processing step. Concerning the creation of the database, we:

1. run one CLOUDY model for all possible parameter combination. The parameter range is given in Table 3.2. We convert E_{ion} into L_{bol} with Eqs. (3.43) and (3.44) and select $d = 100$ pc;

2. obtain, for each model, the correct fractional abundance of C^+ with respect to total hydrogen $f_{C^+,cloudy}$ as a function of the distance from the illuminated side of the slab;

3. average the collection of $f_{C^+,cloudy}$ that we obtain over the 4 possible dx of our cells and we write them in 4 different databases.

The creation of the database is done only once. After we construct the database, we actually post-process our simulations. We loop over all cells of the snapshot we want to post-process and, for each cell, we:

1. check whether $E_{ion} > 0$. If it is not the case, we do not post-process the cell at all, and skip all the following steps;

2. determine the star responsible for the ionizing radiation by calculating F according to Eq. (3.45) for all the stars and we select the star associated to the largest F;

3. interpolate the appropriate database (depending on dx of the cell) and determine $f_{C^+,cloudy}$;

4. replace the original n_{C^+} with the new one given by

$$n_{C^+,new} = f_{C^+,cloudy}\, n_{H,tot} \,, \tag{3.46}$$

where $n_{H,tot}$ is the total hydrogen number density.

This process replaces the original C^+ number density with the new one given by CLOUDY. In principle, this can lead to inconsistencies, because i) CLOUDY calculates the species abundances assuming chemical equilibrium, whereas we do not make such assumption, and ii) the chemical network embedded in CLOUDY is more complex than NL97, so even given the exactly same conditions, the predicted abundances are slightly different for the two networks.

In order to overcome the issue concerning the diversity in the chemical networks, we test, for a selection of snapshots, another possibility for updating the C^+ abundance. Instead of using Eq. 3.46, we set

$$n_{C^+,new} = \frac{n_{C^+}^C}{n_{C,tot}^C - n_{CO}^C - n_C^C}\, n_{C^+} \,, \tag{3.47}$$

where n_{C^+} is the original number density and $n_X^C = f_{X,cloudy}\, n_{H,tot}$ are the number densities given by CLOUDY for the species X. The carbon-bearing

species included in the chemical network of CLOUDY are CO, C, C^+, C^{2+}, and other further ionized states. The first term in the right hand-side of Eq. (3.47) represents therefore the fraction of single-ionized carbon with respect to all the ionized states of carbon. For instance, if all ionized carbon is in form of C^+, this quantity equals 1, whereas, if all the ionized carbon is e.g. in form of C^{2+}, it equals zero. Applying Eq. (3.47) instead of Eq. (3.46) is thus in principle more accurate as, instead of replacing the C^+ abundance given by NL97 with the one given by CLOUDY in the post-processed cells, it is only a correction which considers the fraction of carbon in highly ionized states as predicted by CLOUDY. In any case, we note that the differences between the two approaches are negligible in all the snapshots we considered, therefore we choose to use Eq. (3.46) for simplicity. The post-process in Paper I and Paper II is thus always performed with Eq. (3.46).

In Appendix A we show the entire code and we give instructions on how to use this post-processing routine.

4

CO AND [CII] LINE EMISSION OF MOLECULAR CLOUDS – THE IMPACT OF STELLAR FEEDBACK AND NON-EQUILIBRIUM CHEMISTRY (PAPER I)

CO and [CII] line emission of molecular clouds – the impact of stellar feedback and non-equilibrium chemistry

S. Ebagezio,[1]★ D. Seifried,[1,2] S. Walch,[1,2] P. C. Nürnberger,[1] T.-E. Rathjen,[1] T. Naab[3]

[1] *Universität zu Köln, I. Physikalisches Institut, Zülpicher Str. 77, 50937 Köln, Germany*
[2] *Center for Data and Simulation Science, University of Cologne, Germany, https://cds.uni-koeln.de*
[3] *Max Planck Institute for Astrophysics, Karl-Schwarzschild-Str. 1, 85748 Garching, Germany*

ABSTRACT

We analyse synthetic ^{12}CO, ^{13}CO, and [CII] emission maps of simulated molecular clouds of the SILCC-Zoom project. We use simulations of hydrodynamical and magnetohydrodynamical clouds, both with and without stellar feedback, including an on-the-fly evolution of seven chemical species including H_2, CO, and C$^+$. We introduce a novel post-processing of the C$^+$ abundance using CLOUDY, necessary in HII regions to account for higher ionization states of carbon due to stellar radiation. With this post-processing routine, we report self-consistent synthetic emission maps of [CII] in and around feedback bubbles. Within the bubbles a consistent fraction of C$^+$ is actually further ionized into C^{2+} and therefore they are largely devoid of emission [CII], as recently found in observations. The C$^+$ mass is only poorly affected by stellar feedback but the [CII] luminosity increases by $50-85$ per cent compared to reference runs without feedback due to the increase of the excitation temperature. Furthermore, we show that, for both ^{12}CO and ^{13}CO, the luminosity ratio, $L_{CO}/L_{[CII]}$, averaged over the entire cloud, does not show a clear trend and can therefore *not* be used as a reliable measure of the H_2 mass fraction or the evolutionary stage of clouds. We note a monotonic relation between the $I_{CO}/I_{[CII]}$ intensity ratio and the H_2 mass fraction for individual pixels of our synthetic maps, but with a too large scatter to reliably infer the mass fraction of H_2. Finally, we show that assuming chemical equilibrium results in an overestimation of H_2 and CO masses by up to 110 and 30 per cent, respectively, and in an underestimation of H and C$^+$ masses by 65 and 7 per cent, respectively. In consequence, L_{CO} would be overestimated by up to 50 per cent, and $L_{C[II]}$ be underestimated by up to 35 per cent. Hence, the assumption of chemical equilibrium in molecular cloud simulations introduces intrinsic errors of a factor of up to ~ 2 in chemical abundances, luminosities and luminosity ratios.

Key words: ISM: molecules – radiative transfer – methods: numerical – ISM: clouds – ISM: HII regions – astrochemistry

1 INTRODUCTION

Molecular clouds (MCs) are defined as those regions of the interstellar medium (ISM) where hydrogen exists predominantly in its molecular form, H_2. Due to the absence of dipole moment and low temperatures, typically of a few 10 K, H_2 is not directly observable in MCs. Nevertheless, information on the abundance and distribution of H_2 are of great importance because they allow us to identify the star formation sites in MCs. H_2 is observed only indirectly by means of dust continuum (see e.g. Bot et al. 2007) and molecules which trace its presence. The most used molecule to trace H_2 in MCs is CO (e.g. Wilson et al. 1970; Scoville & Solomon 1975; Larson 1981; Solomon et al. 1987; Dame et al. 2001; Bolatto et al. 2013; Dobbs et al. 2014). In order to infer the amount of H_2 from

the observations of CO, a conversion factor X_{CO} from the observed CO luminosity into a H_2 column density has been established (see e.g. Scoville et al. 1987; Dame et al. 1993; Strong & Mattox 1996; Melchior et al. 2000; Lombardi et al. 2006; Nieten et al. 2006; Smith et al. 2012; Ripple et al. 2013; Bolatto et al. 2013). The standard value of X_{CO} in the Milky Way is commonly assumed to be $X_{CO} = 2 \times 10^{20}$ cm^{-2} K^{-1} km^{-1} s, but there is plenty of evidence that the actual value strongly depends on the environmental conditions (Glover & Mac Low 2011; Shetty et al. 2011a; Bolatto et al. 2013; Gong et al. 2020; Seifried et al. 2020) or the cloud's evolutionary stage (Borchert et al. 2022). Furthermore, because of this strong dependence, it is used to assess the total amount of H_2 in a cloud, but it cannot be easily used on sub-pc scales (e.g. Bisbas et al. 2021). More in general, CO is not a perfect tracer for H_2 because of (i) the presence of CO-dark areas, which may contain a significant amount of H_2, but almost no CO (see for instance Lada & Blitz

★ E-mail: ebagezio@ph1.uni-koeln.de

2   *S. Ebagezio et al.*

1988; van Dishoeck & Black 1988; Grenier et al. 2005; Glover & Mac Low 2011; Glover & Clark 2016; Seifried et al. 2020), and (ii) the optical thickness of CO in denser regions, which break the quantitative relation between the CO luminosity and the H_2 mass (e.g. Seifried et al. 2020; Bisbas et al. 2021).

Other chemical species are also used to assess the H_2 abundance in the clouds: neutral carbon emission has been studied in this context and an X_C-factor (Papadopoulos et al. 2004; Offner et al. 2014), defined in an analogous way than X_{CO}, has been used to assess the abundance of H_2 in MCs. The value of X_C, however, also depends on the clouds' environment (Offner et al. 2014; Bisbas et al. 2021). C^+ is another frequently abundant form of carbon, which has been studied intensively in MCs and is one of the main coolants of the ISM (Tielens & Hollenbach 1985; Stacey et al. 1991; Stutzki 2001; Röllig et al. 2006; Ossenkopf et al. 2013; Appleton et al. 2013; Lesaffre et al. 2013; Beuther et al. 2014; Pineda et al. 2013, 2014; Klessen & Glover 2016, and many more). It is most abundant in photo-dissociation regions (Ossenkopf et al. 2013) and in shock fronts (Appleton et al. 2013; Lesaffre et al. 2013). Some studies (e.g. Velusamy & Langer 2014; Franeck et al. 2018) suggest that C^+ is a tracer of some CO-dark areas of the clouds. However, a reliable relation between the C^+ emission and the H_2 abundance is difficult to establish, because most of the [CII] emission comes from regions which are predominantly atomic (Franeck et al. 2018).

The formation and evolution of MCs has been studied with numerical simulations in a large number of recent works (e.g. Dobbs & Pringle 2013; Smith et al. 2014a; Gatto et al. 2015; Li et al. 2015; Walch et al. 2015; Ibáñez-Mejía et al. 2016; Padoan et al. 2016; Seifried et al. 2017; Kim & Ostriker 2018, and many more). Chemistry treatment is generally performed in two possible ways: one option is to first run the simulations without considering the chemical composition of the clouds and then post-process the chemistry assuming equilibrium (e.g. Gong et al. 2018; Gong et al. 2020; Li et al. 2018; Keating et al. 2020). Post-processing the chemistry enables the use of complex networks, but the assumption of chemical equilibrium is necessary and,as a consequence, the H abundance is usually underestimated while H_2 is overestimated (Hu et al. 2021; Borchert et al. 2022; Seifried et al. 2022). Conversely, some other simulations include a treatment of molecule formation with a non-equilibrium chemical network (Clark et al. 2012; Smith et al. 2014b,c; Seifried & Walch 2016; Walch et al. 2015; Hu et al. 2016, 2017; Smith et al. 2020; Hu et al. 2021; Valdivia et al. 2016; Lahén et al. 2020). This usually implies the usage of simpler networks but the assumption of chemical equilibrium is avoided. Recently, non-equilibrium chemistry has been joined with high-resolution simulations. For instance, in the SILCC-Zoom project (Seifried et al. 2017, 2020; Haid et al. 2019), the formation of molecular clouds is followed from spatial scales of several hundred parsec down to ~ 0.1 pc. These simulations serve as a basis of this publication.

In this paper, we produce synthetic observations of these simulated MCs using the RADMC-3D radiative transfer code (Dullemond et al. 2012) in order to investigate (i) the usability of the CO/[CII] emission line ratio as an alternative tracer (to X_{CO}) for the prevailing H_2 gas mass, and (ii) its potential of being used as an indicator of MC evolution. We also shed light on the role of the assumption of equilibrium chemistry on the emission of CO and [CII].

This paper is structured as follows: in Section **??** we describe the numerical methods, which we use to run the simulations and the radiative transfer calculations. In Section 4 we describe the overall aspect of the simulations, the corresponding synthetic observations, the X_{CO} factor, and the line ratios, considering both the total lumi-

Table 1. Overview of the simulations giving the run name, the zoom time t_0, the run type (hydrodynamical, HD, or magnetohydrodynamical, MHD), and stellar feedback

run name	t_0 [Myr]	run type	feedback
MC1-HD-noFB	11.9	HD	no
MC1-HD-FB	11.9	HD	yes
MC2-HD-noFB	11.9	HD	no
MC2-HD-FB	11.9	HD	yes
MC1-MHD-noFB	16.0	MHD	no
MC1-MHD-FB	16.0	MHD	yes
MC2-MHD-noFB	16.0	MHD	no
MC2-MHD-FB	16.0	MHD	yes

nosity and the intensity from single pixels. Then, we discuss our results and we analyse the importance of the equilibrium chemistry in Section 5. Finally, we summarise our results in Section 6.

2   SILCC-ZOOM SIMULATIONS

The simulated MCs we use in this paper are part of the SILCC-Zoom project (Seifried et al. 2017). The zoom-in simulations are performed within the SILCC project (see Walch et al. 2015; Girichidis et al. 2016, for details).

The SILCC setup models a region of a stratified galactic disc. The rectangular box measures 500 pc × 500 pc × ± 5 kpc, and uses periodic boundary conditions in *x*- and *y*-direction, while outflow boundary conditions are applied in the *z*-direction. The simulations are performed with the adaptive mesh refinement (AMR) code FLASH 4.3 (Fryxell et al. 2000; Dubey et al. 2008) and use, for the hydrodynamics (HD) runs, a solver described in Bouchut et al. (2007); Waagan (2009), which guarantees positive entropy and density. The magnetohydrodynamical (MHD) runs use an entropy-stable solver (Derigs et al. 2016, 2018). We model the chemical evolution of the ISM using a chemical network for H^+, H, H_2, C^+, O, CO, and e^- (Nelson & Langer 1997; Glover & Mac Low 2007a,b; Glover et al. 2010), hereafter NL97, which also follows the thermal evolution of the gas including the most important heating and cooling processes. We assume solar metallicity with elemental abundances of carbon and oxygen relative to hydrogen of 1.4×10^{-4} and 3.16×10^{-4}, respectively (Sembach et al. 2000). The ISM is embedded in an interstellar radiation field (ISRF) of $G_0 = 1.7$ in units of Habing (1968), that is in line with Draine (1978). The cosmic ray ionization rate (CRIR) is set to 3×10^{-17} s^{-1} with respect to atomic hydrogen. The gas self-gravity as well as the local shielding of the gas from the ISRF is treated with an Octtree-based algorithm described in Wünsch et al. (2018).

For the magnetized runs, we initialize a magnetic field **B** along the *x*-direction as

$$B_x = B_{x,0} \sqrt{\rho(z)/\rho_0} \, , \tag{1}$$

where $B_{x,0} = 3 \, \mu$G is in accordance to recent observations (e.g. Beck & Wielebinski 2013), $\rho_0 = 9 \times 10^{-24}$ g cm^{-3} (see Walch et al. 2015, for more details), and $\rho(z)$ is the initial Gaussian density distribution, with z being the distance from the galactic midplane.

Up to a time t_0 after the beginning of the simulations, supernova explosions drive turbulence. The rate at which the supernovae are injected is based on the Kennicutt – Schmidt relation, relating the disc's surface density (here 10 $M_\odot$ pc^{-2}) with a typical star formation rate surface density. The latter is translated into a supernovae rate by assuming a standard initial mass function. We refer

to Walch et al. (2015) and Girichidis et al. (2016) and references therein for details. At t_0 the further injection of background supernovae is stopped and local gas overdensities, i.e., the regions where MCs are about to form, are already visible. We select a few of these "zoom-in" regions and continue the simulations allowing for a resolution up to 0.12 pc in those regions. The typical side length of the zoom-in regions is about 100 pc. We consider two purely hydrodynamical clouds, which we refer to as MC1-HD and MC2-HD, and two magnetohydrodynamical clouds, MC1-MHD and MC2-MHD. The HD runs are described in detail in Seifried et al. (2017) and the MHD runs in Seifried et al. (2019). We emphasise that HD and MHD runs refer to different clouds, they are not just the same clouds with/without external magnetic field included. In MHD runs t_0 is larger than in the HD runs due to the slower dynamical evolution of the MHD clouds (Walch et al. 2015; Girichidis et al. 2016).

We set $t_0 = 11.9$ Myr for the HD runs and $t_0 = 16.0$ Myr for the MHD runs. We also run these 4 clouds with stellar feedback included. We distinguish throughout the text by indicating, for instance, MC1-HD-noFB and MC1-HD-FB for non-feedback and feedback runs, respectively. An overview of the simulations features is given in Table 1. In the feedback runs (see Haid et al. 2019, for a more detailed description), we use sink particles to model the formation and the evolution of stars and, as a consequence, of the ionizing radiation feedback by massive stars. The sinks form when the gas density exceeds 1.1×10^{-20} g cm^{-3}. Further, the nearby gas has to be in a converging flow, gravitationally bound, Jeans unstable, and in a local gravitational potential minimum. Details on this are provided in Federrath et al. (2010). We also use the sink accretion criteria described there. Next, per 120 M$_\odot$ of accreted mass, a massive star between 9 and 120 M$_\odot$ is created using a random sampling algorithm (Gatto et al. 2017), which follows the initial mass function of Salpeter (1955). The radiative feedback relative to each star is treated with TreeRay (Wünsch et al. 2021). The chemical evolution of all HD clouds, as well as MC1-MHD-noFB and MC2-MHD-noFB, in particular for H$_2$ and CO, is reported in Seifried et al. (2020).

3 POST-PROCESSING AND RADIATIVE TRANSFER

Before the actual synthetic emission maps are produced (Section 3.3) we prepare the necessary input data in two steps. The first step is applied to the entire simulation domain (Section 3.1), the second is only applied to regions affected by stellar feedback (Section 3.2). Unless stated otherwise, all the results shown in the remainder of the paper include the post-processing described in the following.

3.1 Data preparation for the radiative transfer

In the first step we apply a pipeline developed by P. C. Nürnberger[1] to the entire simulation domain. It converts the FLASH simulation data into input files for RADMC-3D (Dullemond et al. 2012, used for the radiative transfer) and incorporates further physical processes: (i) CO freeze-out, (ii) C$^+$ → C^{2+} thermal ionization, (iii) splitting of H$_2$ into para- and orho-H$_2$, and (iv) the generation of a microturbulence file.

(i) The CO density after the freeze-out post-processing, $n_{CO,f}$, is

obtained from the original density n_{CO} following Glover & Clark (2016) and references therein:

$$n_{CO,f} = n_{CO} \times \frac{k_{cr} + k_{therm}}{k_{cr} + k_{therm} + k_{ads}} , \qquad (2)$$

where

$$k_{cr} = 5.7 \times 10^4 \times \text{CRIR} \qquad (3)$$

is the CR-induced desorption rate of CO from dust grains,

$$k_{therm} = 1.04 \times 10^{12} \exp\left(-\frac{960\,\text{K}}{T_d}\right) \qquad (4)$$

is the thermal desorption rate. Here, T_g is the gas temperature and T_d is the dust temperature. Furthermore,

$$k_{ads} = 3.44 \times 10^{-18} \sqrt{T_g} \, (2n_{H_2} + n_H) \qquad (5)$$

is the adsorption rate due to collisions between CO and dust grains.
 (ii) The C$^+$ → C^{2+} ionization due to collisions induced via thermal motions is implemented following Sutherland & Dopita (1993). In cells with a gas temperature $T_g \geq 2 \times 10^4$ K the C$^+$ density is corrected in order to consider such collisions.
(iii) We distinguish between the two nuclear spin states of H$_2$, in which the spins of the nuclei are parallel (ortho $-$ H$_2$) or anti-parallel (para $-$ H$_2$). These are given following, Rachford et al. (2009), by

$$n(\text{para} - \text{H}_2) = \frac{n_{H_2}}{9\, e^{-170.5\,\text{K}/T_g} + 1} \qquad (6)$$

and

$$n(\text{ortho} - \text{H}_2) = n_{H_2} - n(\text{para} - \text{H}_2) . \qquad (7)$$

If Eq. (6) and (7) yield to an ortho-to-para ratio larger than 3, we force $n(\text{ortho} - \text{H}_2)/n(\text{para} - \text{H}_2) = 3$, with $n(\text{ortho} - \text{H}_2) + n(\text{para} - \text{H}_2) = n_{H_2}$.
(iv) Microturbulence is also included in our radiative transfer calculations. We assume that the microturbulence broadening is as strong as the thermal broadening. Therefore, with a being the line width, we have $a^2 = a_{therm}^2 + a_{turb}^2$, with

$$a_{therm} = a_{turb} = \sqrt{\frac{2 k_B T_g}{\mu\, m_p}} , \qquad (8)$$

where k_B is the Boltzmann constant, $\mu = 2.3$ is the assumed mean molecular mass of the gas, and m_p is the proton mass.

3.2 Chemical post-processing of stellar feedback regions

This second data preparation step is only applied to regions affected by stellar feedback to properly model the abundance of C$^+$. The NL97 chemical network does not contain any higher ionized states of carbon than C$^+$ and the ionization to C^{2+} described before only accounts for thermal ionization. Stellar radiation, however, can cause further ionization of carbon (see e.g. Abel et al. 2005): the stars formed in our simulations have masses greater than, or equal to, 9 M$_\odot$ and are therefore O-type or B-type stars. These stars, whose effective temperature equals or exceeds 24 000 K, emit photons with energies larger than the second ionization energy of carbon of 24.4 eV. It is therefore necessary to remove C$^+$, which gets further ionized by this radiation, in order to obtain more realistic emission maps of the feedback runs. For this purpose we use a novel approach based on CLOUDY (Ferland et al. 2017), which we describe in detail in the following.

4   *S. Ebagezio et al.*

3.2.1   CLOUDY *database*

We consider 4 parameters provided by the FLASH simulation data as an input for CLOUDY. The gas density, n_g, the gas temperature, T_g, the energy density of ionizing photons, E_{ion} (converted later to a bolometric luminosity, see below), and the temperature of the star responsible for the ionization, $T_\star$. In order to avoid to run CLOUDY for each simulation cell, we create a database beforehand. To do this, we vary the parameters mentioned above over the range of values found in our simulations, summarized in Table 2. We run one CLOUDY model for each possible combination of values, which corresponds to approximately 160,000 models in total.

CLOUDY requires for a source of ionizing photons its bolometric luminosity, L_{bol}, and not E_{ion}. Therefore, we convert E_{ion} into L_{bol} as follows. Given a defined spectral luminosity L_ν for a star, L_{bol} is defined as

$$L_{bol} = \int_0^\infty L_\nu d\nu . \tag{9}$$

Similarly, we define the ionizing luminosity L_{ion} as the spectral luminosity integrated over the frequencies larger than the ionizing frequency of atomic hydrogen, $\nu_H = 13.6\,eV/h$, where h is the Planck constant:

$$L_{ion} = \int_{\nu_H}^\infty L_\nu d\nu . \tag{10}$$

Furthermore, assuming that the emission spectrum of the chosen star (see below how we choose the star) is equal to that of a black body with its temperature $T_\star$, $B_\nu (T_\star)$, we have

$$L_{bol} = L_{ion} \frac{\int_0^\infty B_\nu (T_\star)\, d\nu}{\int_{\nu_H}^\infty B_\nu (T_\star)\, d\nu} . \tag{11}$$

The energy density of ionizing photons, provided in the FLASH simulation data, is related to the ionizing luminosity (Eq. 10) via

$$E_{ion} = \frac{1}{c} \frac{L_{ion}}{4\pi d^2} , \tag{12}$$

with d being the distance between the star and the investigated point. Therefore, we can convert E_{ion} into L_{bol} via

$$L_{bol} = E_{ion} \times 4\pi d^2 c \times \frac{\int_0^\infty B_\nu (T_\star)\, d\nu}{\int_{\nu_H}^\infty B_\nu (T_\star)\, d\nu} . \tag{13}$$

In our CLOUDY models we now assume a fixed d of 100 pc. Hence, Eq. 13 gives us the luminosity of a *hypothetical* star at a distance of 100 pc, which would provide the exactly same value for E_{ion} as the actual star at its real distance due to the attenuation by gas and dust in between. This approach thus limits the parameter range to be covered by the CLOUDY database to 4 dimensions without loss of generality. Furthermore, the cells in our AMR simulations have a size of $dx = 0.122, 0.244, 0.488$, and 0.976 pc. We take $dx = 0.976$ pc as the depth of the PDR in CLOUDY, which automatically includes the results for all smaller cell sizes (see below). In addition, our choice of $d = 100$ pc assures that $dx \ll d$, that is, the CLOUDY models are essentially a plane-parallel PDR which we can then directly map back to the simulation cell.

CLOUDY provides the fractional abundance $f_{X,cloudy}$ of the chemical species X with respect to the total number of hydrogen nuclei, i.e., $f_{X,cloudy} = n_{X,cloudy}/n_{H,tot}$, as a function of the distance from the edge of the slab. We are interested in the mean value over the cell, to which the slab corresponds. As the length of the (quasi plane-parallel) PDR slab is 0.976 pc, in a next step we average the chemical abundance in the PDR slab from 0 to a depth of $dx =$

Table 2. Parameter range used for CLOUDY models. We run one model for each combination of parameters. Steps are equally spaced in log-scale.

Parameter	min	max	# steps
n_g [g cm^{-3}]	10^{-26}	10^{-20}	19
T_g [K]	$10^{1.5}$	$10^{4.5}$	19
$T_\star$ [K]	$10^{3.5}$	$10^{5.5}$	21
E_{ion} [erg cm^{-3}]	10^{-18}	10^{-8}	21

0.122, 0.244, 0.488, and 0.976 pc, i.e. each CLOUDY model provides now four values of $f_{X,cloudy}$, one for each cell size. Hence, at this point we have a database covering the full range of relevant physical parameters and possible cell lengths.

3.2.2   *Calculation of the new* C^+ *abundance*

In a next step we now post-process the RADMC-3D input file concerning C^+ on a cell-by-cell basis as follows.

• We check whether $E_{ion} > 0$. If this is not the case, we skip the following points and do not post-process the cell. Otherwise,

• In order to estimate which star contributes most to the flux of ionizing photons at the considered cell, we loop over all stars and compute the unattenuated flux F_i from to the i-th star reaching the cell:

$$F_i = L_{bol,i}/4\pi d_i^2 . \tag{14}$$

Here, d_i is the *actual* distance between the cell and the i-th star and $L_{bol,i}$ the *actual* bolometric luminosity of the i-th star obtained directly from the simulation data.

• We select the k-th star, with temperature $T_{\star,k}$, for which $F_k = \max(F_i)$. For consistency, we check that $d_k \leq 2d_{min}$, with $d_{min} = \min(d_i)$. This is always the case in the simulations presented in this paper. In the following we assume that star k is solely responsible for all the ionizing photons.

• Next, we take the input values $n_g, T_g, T_{\star,k}, E_{ion}$, and the cell size dx and interpolate the database for $f_{C^+,cloudy}$ created before using LINEARNDINTERPOLATOR, which is part of PYTHON's NUMPY library, to obtain the updated value f_{C^+} for the given cell.

• Finally, we replace the original C^+ number density of the cell with $f_{C^+} \times n_{H,tot}$, where $n_{H,tot}$ is the total hydrogen nuclei number density.

3.3   Radiative transfer

We create synthetic emission maps of $^{12}CO\,(1 \rightarrow 0)$ at 2600 μm, $^{13}CO\,(1 \rightarrow 0)$ at 2720 μm, and [CII] at 158 μm for all 8 clouds (see Table 1) at three different evolutionary stages separated by 1 Myr for lines of sight (LOS) along the *x*-, *y*-, and *z*-axis. The emission maps have the same resolution as the simulations, i.e. 0.12 pc. The radiative transfer, which is needed to obtain synthetic emission maps of the simulated clouds, is performed using the RADMC-3D software, an open-source, 3D radiative transfer code[2] (Dullemond et al. 2012). We include microturbulence (Eq. 8) and use the Large Velocity Gradient approximation (LVG; Ossenkopf 1997; Shetty et al. 2011a,b) for calculating the level population. In order to capture the contribution of Doppler-shifted emission, we consider a velocity

---

[2] http://www.ita.uni-heidelberg.de/~dullemond/software/radmc-3d/

range of ± 20 km s^{-1}, centred around the selected rest frequency. We divide this range into 201 equally spaced velocity channels, corresponding to a spectral resolution of d$v = 0.2$ km s^{-1}, which is well suited for the studied molecular clouds (Franeck et al. 2018).

Performing the radiative transfer calculations using the LVG approximation means that we do not assume Local Thermal equilibrium (LTE). Therefore, we must specify explicitly the collisional rates for CO and C$^+$. We take the data from the Leiden Atomic and Molecular DAtabase[3] (LAMDA, Schöier et al. 2005). We consider para-H$_2$, ortho-H$_2$, H, and e$^-$, as collisional partners for C$^+$, and para-H$_2$, ortho-H$_2$, H, and He, for CO. As the rates for CO-He and CO-H collisions are not in the LAMDA database, for this we use the rates from Cecchi-Pestellini et al. (2002) and Walker et al. (2015), respectively. We emphasise that it is essential to include also He and H as collisional partners as it increases the CO luminosity by $\sim 20 - 30$ per cent (Borchert et al. 2022).

We also consider the Cosmic Microwave Background (CMB) using an isotropic black body emission at 2.725 K. During the following analysis we subtract this background from the emission maps before any other step. Each emission map is centered on a rest frequency ν_0. The corresponding brightness temperature for the CMB is given by

$$T_{\mathrm{B,CMB}} = \frac{h\nu_0}{k_{\mathrm{B}}} \frac{1}{e^{h\nu_0/kT} - 1} , \tag{15}$$

where h is the Planck constant and $T = 2.725$ K. Considering the CMB background and then subtracting it, has a negligible impact on [CII] emission maps, but it changes the ^{12}CO and ^{13}CO intensity in optically thick areas by up to ~ 20 per cent.

4 RESULTS

4.1 Overview of the simulations

In the following, we refer to the evolution time t_{evol} of the clouds as $t_{\mathrm{evol}} = t - t_0$, where t is the time calculated from the very beginning of the SILCC simulation and t_0 is the time when the zoom-in simulation starts (see also Table 1). As mentioned before, the results shown in the following include the post-processing steps described in Section 3 unless stated otherwise.

In Fig. 1 we show in the top row the H$_{\mathrm{tot}}$, H$_2$, CO, and C$^+$ column densities of MC1-HD-noFB at an evolutionary stage of $t_{\mathrm{evol}} = 4$ Myr along the z-axis. In the bottom row we show MC1-HD-FB together with the formed stars. The impact of stellar feedback is evident: it is possible to identify two regions of star formation where stellar radiation disperses the cloud. This is particularly clear when looking at the H$_2$ and CO maps, since the higher temperature and the stellar radiation lead to the dissociation of these molecules. Stellar radiation has also an impact on C$^+$ by further ionizing it to C^{2+} (see Section 3.2). Furthermore, comparing the H$_2$ column density with the carbon-bearing species maps, shows that the CO distribution is significantly more compact than the H$_2$ distribution, which leads to the presence of CO-dark H$_2$ regions (see Seifried et al. 2020, for details on this). The C$^+$ distribution is significantly more diffuse than the CO distribution, leading to a clearly visible nested CO$-$C$^+$ structure.

Fig. 2 shows the change in CO, C$^+$, and H$_2$ mass as a function of time for the simulated clouds in the zoom-in regions, using selected snapshots separated by 1 Myr in time. In our simulations, $M_{^{13}\mathrm{CO}}$

[3] https://home.strw.leidenuniv.nl/~moldata/

(not shown here) is fixed to 1/69 of $M_{^{12}\mathrm{CO}}$ (Wilson 1999). For runs without feedback, the CO abundance raises with time, and the C$^+$ abundance slowly decreases. The H$_2$ abundance also rises with time, even though at a lower rate than CO. Both the HD and MHD clouds follow the same trend, but the MHD clouds evolve more slowly: this can be seen, for instance, when considering the C$^+$-to-CO ratio (not shown explicitly in Fig. 2), which is much higher and more slowly decreasing in the MHD clouds than in the HD clouds. This is due to the inhibiting effect of the magnetic field on formation of dense structure and thus more H$_2$ and CO (Seifried et al. 2020). Stellar feedback reduces the amount of CO and H$_2$ from the onset of star formation. The total amount of C$^+$ is only marginally affected by stellar feedback (due to a partial conversion into C^{2+}), although feedback results in a different distribution of C$^+$ (see Fig. 1, right column).

4.2 Synthetic emission maps

Next, we analyse the emission maps for the same snapshots as in Fig. 2. In Fig. 3 we show the integrated intensity maps of the ^{12}CO, ^{13}CO, and [CII] lines of MC1-HD-noFB (top row) and MC1-HD-FB (bottom row) at $t_{\mathrm{evol}} = 4$ Myr, which corresponds to the column density maps shown in Fig. 1. Again, a nested CO - [CII] structure is evident, and stellar feedback removes the CO emission from the expanding bubbles and strongly increases the [CII] emission, in particular from the rims of the bubbles.

Next, we calculate the total luminosity L. For this, we first sum the intensity of all pixels to obtain the integrated intensity. Then, L is given by

$$L = 4\pi d^2 F , \tag{16}$$

where d is the distance of the cloud and F is the total flux derived from the integrated intensity map by adding up the contributions from the total number of pixels, n:

$$F = \sum_{i=1}^{n} I_i A_{\mathrm{pixel}} . \tag{17}$$

Here, A_{pixel} is the area of the pixels in steradians given by

$$A_{\mathrm{pixel}} = \left(\arctan\left(\frac{a}{d}\right)\right)^2 , \tag{18}$$

with a being the side length of the pixel. We note that, due to the small angle approximation, for $a/d \ll 1$ the choice of d is practically irrelevant.

We show the values of L calculated for the three different LOS in Fig. 4. Optical thickness plays an important role for $L_{^{12}\mathrm{CO}}$, indicated by the fact that the values for the same cloud, but different LOS, differ by up to a factor of a few, whereas in the optically thin case they should be identical. This is also shown by the fact that changes in M_{CO} (Fig. 2) are not directly reflected in corresponding changes in $L_{^{12}\mathrm{CO}}$ (e.g. for MC1-HD-noFB). Conversely, the measured $L_{^{13}\mathrm{CO}}$ is less affected by optical thickness: the difference in luminosity for the different LOS is lower than for ^{12}CO, and $L_{^{13}\mathrm{CO}}$ changes coherently with M_{CO}.

Stellar feedback significantly increases $L_{[\mathrm{CII}]}$ compared to the noFB runs by a factor of $2 - 7$. Only MC2-MHD-FB, which forms the least stellar mass among the clouds we investigate (41.9 $M_\odot$ at $t_{\mathrm{evol}} = 5$ Myr compared to a maximum of 546.2 $M_\odot$ in MC2-HD-FB at 4 Myr), does not show a significant increase in $L_{[\mathrm{CII}]}$. In contrast, M_{C^+} is practically unchanged between noFB and FB runs (Fig. 2, middle panel). The increase in $L_{[\mathrm{CII}]}$ is a consequence of the

6 *S. Ebagezio et al.*
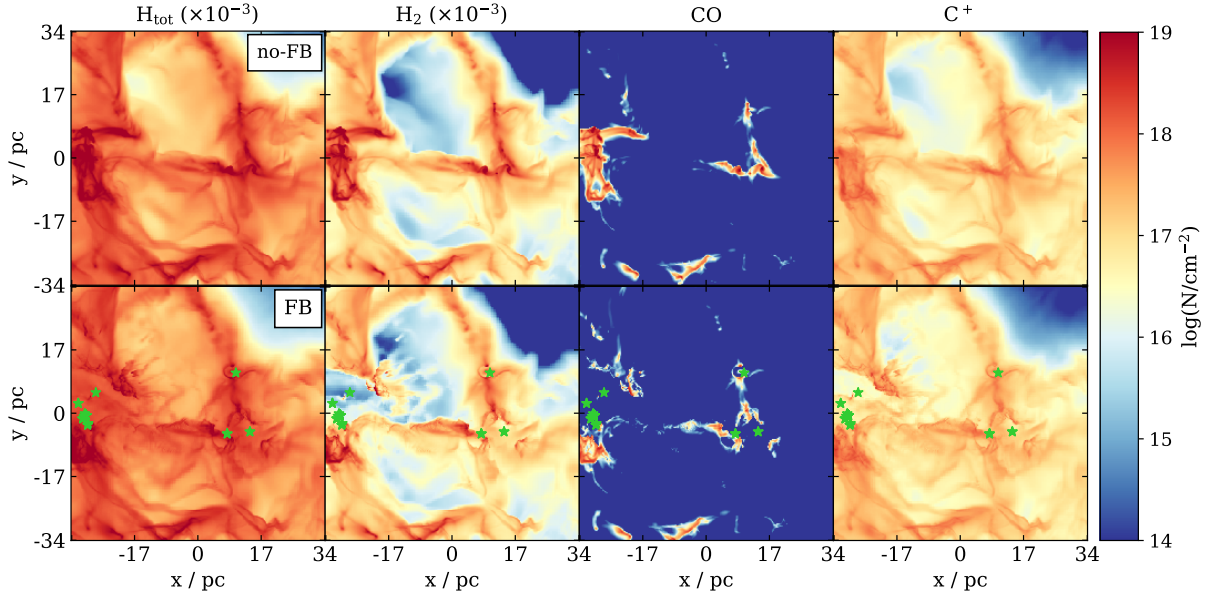
Figure 1. Column density of H_{tot}, H_2, CO, and C^+ (from left to right) of the run MC1-HD-noFB (top row) and MC1-HD-FB (bottom row) at $t_{evol} = 4$ Myr along the z−direction. Green symbols mark the positions where stars form. There is an evident nested CO - C^+ structure. The H_2 distribution is more diffuse than the CO distribution, which leads to a significant CO-dark H_2 region. Conversely, the C^+ distribution is significantly more diffuse than the H_2 distribution. The impact of stellar radiation is evident when comparing particularly dense regions in the noFB run with the corresponding areas in the FB run, as stellar feedback disperses the cloud.

stellar radiation, which heats up the gas and excites the C^+ ions: we find that the excitation temperature of [CII] is overall significantly higher in FB (up to 1000 K) than in noFB runs (hardly more than 50 K). In consequence, $L_{[CII]}$ increases for the FB runs despite a comparable amount of C^+ mass between FB and noFB. Most of the [CII] luminosity in these runs comes from the rims of the HII bubbles, as shown for instance in Fig. 3. Pineda et al. (2013, 2014) claim that $34 - 70$ per cent of the [CII] emission is related to feedback. The factor of $2 - 7$ which we observe for the increase of the [CII] luminosity corresponds to a contribution of $50 - 85$ per cent due to the role of stellar feedback, in rough agreement with the estimate of the aforementioned authors. Moreover, we find that the longer star formation proceeds, the more [CII] increases, thus having an increasingly more important effect on $L_{[CII]}$.

4.3 Feedback-driven [CII] bubbles

As seen in Fig. 3, stellar feedback drives some bubbles also visible in [CII], which we investigate in more detail now. For this purpose, in Fig. 5 we show some examples of HII regions at different evolutionary stages. Stars are superimposed and are characterized with different colors and size according to their age and temperature. In Fig. A1 we also show the emission maps of the same regions obtained without operating the post-processing described in Section 3.2. These exhibit a much higher emission coming from the inner regions supporting the importance of the post-processing. We find that some structures become more evident after the post-processing. This is the case of pillars, which can be easily recognised in the maps of MC2-HD-FB.

In Fig. 6 we summarize the importance of this post-processing step. The total [CII] luminosity decreases by up to 60 per cent if the C^+ within the HII regions is post-processed compared to the less

realistic non-post-processed case. In general, differences are larger at later evolutionary stages, as the stellar mass and thus stellar radiation intensity increase over time. Hence, the consideration of higher ionization states of carbon is crucial to obtain accurate [CII] intensities stemming from HII regions (Spitzer 1978).

We note that the size of the bubble has a positive correlation, at fixed stellar temperature $T_\star$, with the age $t_\star$ of the stars formed inside. Larger bubbles (corresponding to later evolutionary stages) also show a weaker [CII] emission inside them than smaller bubbles (earlier stages). We also observe a correlation between the star temperature and the lack of [CII] emission inside the bubble. For example, the region around the rather cool star on the top of the map for MC1-HD-FB has still some [CII] emission, whereas the regions in the upper part of the maps of MC2-HD-FB and in the centre of MC2-MHD-FB are almost devoid of any emission. In the latter case $T_\star$ is significantly higher, i.e. the star is able to further ionize C^+ as explained in Section 3.2.

At the rims of the bubbles, the [CII] emission is enhanced when compared to even the brightest regions of the noFB runs (Fig. 3). We emphasise that our findings are in excellent agreement with [CII] bubbles with enhanced emission at the rims and a lack of emission inside found recently in a number of observations (see e.g. Pabst et al. 2019; Luisi et al. 2021; Tiwari 2021).

4.4 The X_{CO} and $X_{[CII]}$ factors

The X_{CO} factor has been widely studied in literature (see e.g. Scoville et al. 1987; Dame et al. 1993; Strong & Mattox 1996; Melchior et al. 2000; Lombardi et al. 2006; Nieten et al. 2006; Smith et al. 2012; Ripple et al. 2013; Bolatto et al. 2013). It is defined as

$$X_{CO} = \frac{N_{H_2}}{W_{^{12}CO}} \,, \tag{19}$$
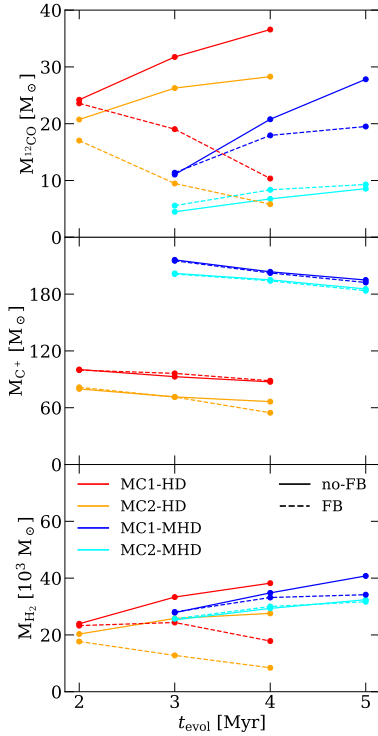
Figure 2. Mass of ^{12}CO, C$^+$, and H$_2$ (from top to bottom) as a function of time for all four clouds, represented in different colors. The noFB runs are plotted with solid lines, and FB runs in dashed lines. The CO mass rises with time, whereas the C$^+$ mass slowly decreases. HD and MHD clouds show the same trend, but the increase (for noFB runs) of H$_2$ and CO is slowed down in MHD runs with respect to HD runs. Stellar feedback disperses the densest parts of the clouds, where stars form, thus decreasing the mass of CO and H$_2$ over time.

where N_{H_2} is the H$_2$ column density, generally expressed in cm^{-2}, and $W_{^{12}CO}$ the line-integrated intensity, summed over the whole image, expressed in K km s^{-1}. Here we calculate X_{CO} as the average quantity over the entire cloud. It allows to assess the H$_2$ mass of a cloud, given the intensity of the ^{12}CO $(1 \rightarrow 0)$ transition. The typical X_{CO} value for the Milky Way is 2×10^{20} cm^{-2} K^{-1} km^{-1} s (e.g. Bolatto et al. 2013). We analogously define the $X_{[CII]}$ factor as

$$X_{[CII]} = \frac{N_{H_2}}{W_{[CII]}} \ . \tag{20}$$

In Fig. 7 we show both factors for our simulations plotted against the mass fraction of H$_2$ (see Seifried et al. 2020, for a plot against t_{evol}). We calculate them under the assumption of unresolved clouds, i.e., we first integrate the H$_2$ column density and the CO, or [CII], intensity over the entire area of the zoom-in regions, no matter whether in some pixels the intensity is beyond a minimum observable threshold, and then take the ratio of both values.

There is a significant scatter of X_{CO} (left panel of Fig. 7) around the reference value for the Milky Way. In our clouds it spans from ~ 0.5 to $\sim 4.5 \times 10^{20}$ cm^{-2} K^{-1} km^{-1} s. This scatter occurs among different clouds, but also to a smaller extent for the same clouds among different LOS and different t_{evol}. It can in parts be attributed to the fact that a larger CO optical thickness leads to a higher X_{CO} factor, as the CO intensity does not increase coherently

with the H$_2$ mass. Furthermore, differences occur between feedback and non-feedback runs, in particular for HD clouds. Stellar feedback lowers the X_{CO} factor, as it both slightly enhances the CO emissivity and reduces the H$_2$ mass (see Figs. 2 and 4).

Moreover, we cannot identify a clear correlation between X_{CO} and the time evolution, respectively the H$_2$ mass fraction of the clouds. We attribute this to the presence of "CO-dark" regions, i.e., molecular gas regions with low or no CO. The amount of CO-dark gas is highly variable in different clouds. As discussed in more detail in Seifried et al. (2020), the CO-dark gas fractions in our MCs range from 40 to 95 per cent. Indeed, we find that the higher the CO-dark gas fraction, the higher is X_{CO}, e.g. for MC1-HD-noFB and MC2-HD-noFB the CO-dark gas fraction is ~ 40 per cent and $X_{CO} = 1 - 2 \times 10^{20}$ cm^{-2} K^{-1} km^{-1} s, whereas for MC1-MHD-noFB and MC2-MHD-noFB the CO-dark gas fraction is $60 - 95$ per cent, and the associated X_{CO} is $1.5 - 4 \times 10^{20}$ cm^{-2} K^{-1} km^{-1} s. We note that the X_{CO} values calculated in Seifried et al. (2020) are slightly different, as there they were calculated considering only the pixel with a CO intensity above a minimum threshold of 0.1 K km s^{-1}.

The $X_{[CII]}$ factor (right panel of Fig. 7) exhibits a lower scatter between the different LOS of the same cloud, which we attribute to the somewhat lower optical depths in the case of [CII]. Nevertheless, the scatter among different clouds is again significant, with $X_{[CII]}$ values ranging from 0.5 to 12×10^{20} cm^{-2} K^{-1} km^{-1} s. This means that such $X_{[CII]}$ is far from being constant and therefore it is difficult to use it as a reliable conversion factor to obtain the H$_2$ mass. Also Franeck et al. (2018) claim that [CII] is not a good tracer of molecular hydrogen, as most of the [CII] intensity comes indeed from atomic hydrogen gas, and not from molecular part. Hence, the monotonic increase in $X_{[CII]}$ for the noFB runs is mainly due to the increase in H$_2$ mass, while the [CII] luminosity stemming from the outskirts of the clouds remains largely constant (see Figs. 2 and 4). The FB runs, conversely, do not exhibit a clear relation because the stellar feedback both inhibits the formation of H$_2$ (Fig. 2) and enhances the [CII] intensity (Fig. 4).

4.5 The global CO/[CII] line ratio

The large scatter in X_{CO} makes it difficult to use it to reliably estimate the H$_2$ mass for individual clouds (Bolatto et al. 2013; Seifried et al. 2020; Madden et al. 2020; Hu et al. 2022). We therefore consider another possible estimator: We take the total luminosities integrated over the entire cloud, $L_{^{12}CO}$, $L_{^{13}CO}$, and $L_{[CII]}$, and investigate the relation between $L_{^{12}CO}/L_{[CII]}$, $L_{^{13}CO}/L_{[CII]}$, and the H$_2$ mass fraction of the clouds, $M_{H_2}/M_{H,tot}$.

Fig. 8 shows $L_{^{12}CO}/L_{[CII]}$ and $L_{^{13}CO}/L_{[CII]}$ as a function of time (top row) and as a function of the H$_2$ mass fraction $M_{H_2}/M_{H,tot}$ (bottom row). In the Appendix (Figs. A2 and A3) we also show the line ratios as a function of the H$_2$ mass and the [CII]/CO ratio calculated with luminosities given in units of erg s^{-1} cm^{-2} in order to allow for an easier comparison with observational literature. We note that we relate the luminosity ratio to $M_{H_2}/M_{H,tot}$ rather than M_{H_2}, as the latter depends on the size of the cloud, i.e. it is an extensive quantity and not an intensive one as the mass fraction.

We find that different LOS of the same cloud typically have significantly different $L_{^{12}CO}/L_{[CII]}$ values with the exception of MC2-MHD (for both FB and noFB). The scatter is of the order of a factor of a few in some snapshots: for instance, in MC2-HD-noFB at t_{evol} = 4 Myr, $L_{^{12}CO}/L_{[CII]}$ is ~ 1.5 for the LOS along the z-axis, but it is ~ 4.3 along the x-axis. Considering ^{13}CO instead of ^{12}CO
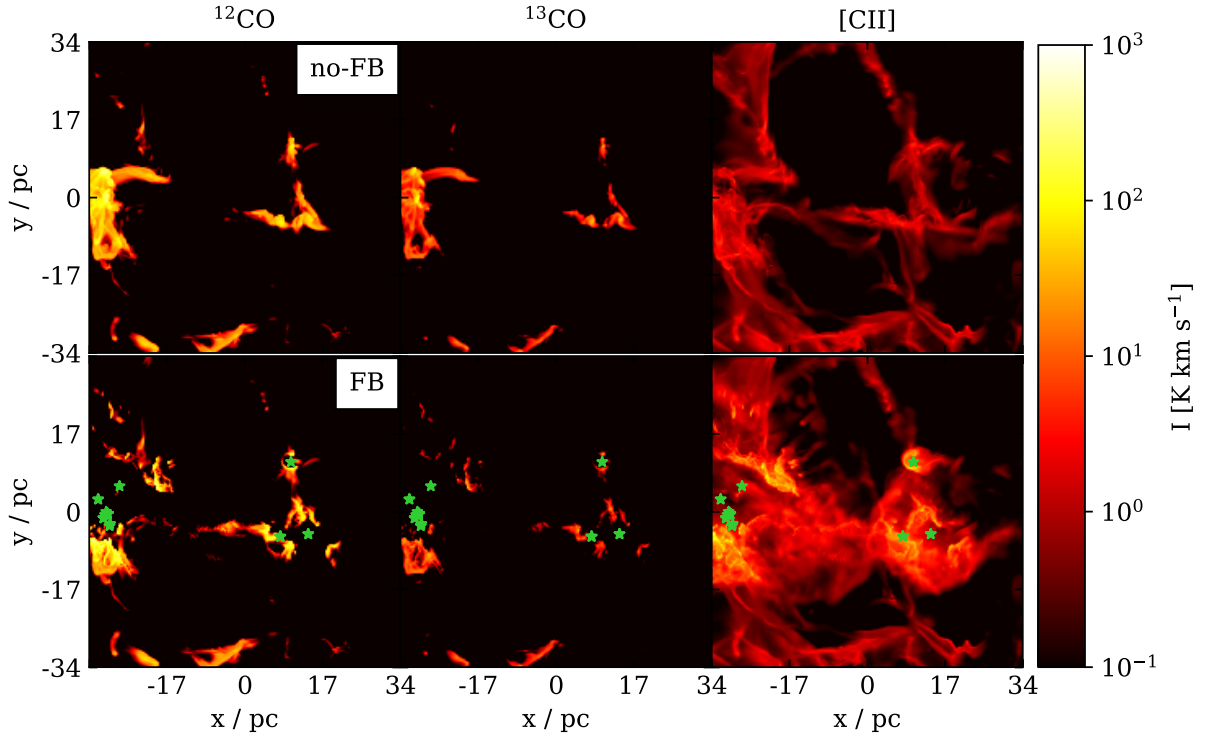
Figure 3. From left to right: integrated emission maps of ^{12}CO $(1 \rightarrow 0)$, ^{13}CO $(1 \rightarrow 0)$, and [CII] of MC1-HD without feedback (top row) and with feedback (bottom row) at $t_{evol} = 4$ Myr. The CMB background has been subtracted. A nested CO - [CII] is evident in both clouds. HII regions around stars devoid of any or most of the emission are visible in both the [CII] and in CO maps. [CII] intensity is enhanced by an order of magnitude in the rims of the HII regions with respect to the brightest areas in the non-feedback map.

considerably reduces the scatter between different LOS. The same snapshot gives $L_{13CO}/L_{[CII]} \simeq 0.4$ along the z-axis and 0.5 along the x-axis. As discussed, this is due to the lower optical depth of ^{13}CO with respect to ^{12}CO (Borchert et al. 2022). Indeed, we would expect identical values for different LOS if the lines were completely optically thin. To a good approximation, this is the case for the snapshots which have very low CO column densities, i.e. MC2-MHD, which is a more diffuse cloud, and MC1-HD-FB and MC2-HD-FB at $t_{evol} = 4$ Myr (see Fig. 2), where stellar feedback has dispersed most of the dense regions.

We also observe a relevant scatter of a factor of up to a few in the line ratios among different clouds for a selected H_2 mass fraction. This is a consequence of the different structures and properties of the clouds and does not change significantly when considering ^{12}CO or ^{13}CO. For instance, for $M_{H_2}/M_{H,tot} \simeq 0.3$, $L_{12CO}/L_{[CII]}$ ranges from 2 to 6 and $L_{13CO}/L_{[CII]}$ from 0.2 to 0.8. As we discuss in detail in the following, we do not observe a systematic relation between higher/lower line ratios (at fixed H_2 mass fraction) and the presence/absence of magnetic fields or stellar feedback.

Stellar feedback has an impact on the evolution of the line ratio: if no feedback is considered, the line ratios increase with t_{evol}: this can be seen clearly for the HD runs, and, even though less evidently, also in the MHD runs. Conversely, including stellar feedback causes a decreasing ratio over time for the same clouds. This trend is less pronounced for MC2-MHD because it is less developed and therefore the stellar feedback has a smaller impact.

The luminosity ratios as a function of $M_{H_2}/M_{H,tot}$ exhibit an overall increasing relation for noFB runs (apart from optical

thickness effects). On the other hand, for the FB clouds, there is no clear trend any more. This is a consequence of the fact that both the H_2 mass fraction (Fig. 2) and the CO/[CII] luminosity ratio (Fig. 8, left hand-side plot) decrease with t_{evol}, but with different slopes, making their reciprocal relation non-trivial.

In summary, there is no clear trend of the luminosity ratios with both t_{evol} and $M_{H_2}/M_{H,tot}$. This implies that it is not possible to quantitatively assess an age or evolutionary stage of a cloud by measuring a certain line ratio value. Moreover, there is a large scatter among different LOS and different clouds. We refer to Section 5.1 for a further discussion about the implications of these findings and a comparisons with recent observational works.

4.6   Analysis of single pixels

4.6.1   *The intensity - column density relation*

Next, we investigate – pixel by pixel – the relation between the intensity I (in K km s^{-1}) of ^{12}CO, ^{13}CO and [CII] and the column density N of ^{12}CO, ^{13}CO, C$^+$, and H_2. This is shown in Fig. 9, where in the top row I_{12CO} (left panel), I_{13CO} (middle panel), and $I_{[CII]}$ (right panel) are plotted as a function of N_{H_2}. Each line represents the mean value of I for a given N_{H_2}-bin for the selected snapshot. The bottom row shows the cumulative distribution of the intensity arising from regions with H_2 column densities lower or equal to the threshold of N_{H_2} given on the x-axis. Snapshots corresponding to different t_{evol} for the same cloud are plotted with the same color, and therefore are not distinguished here. We plot
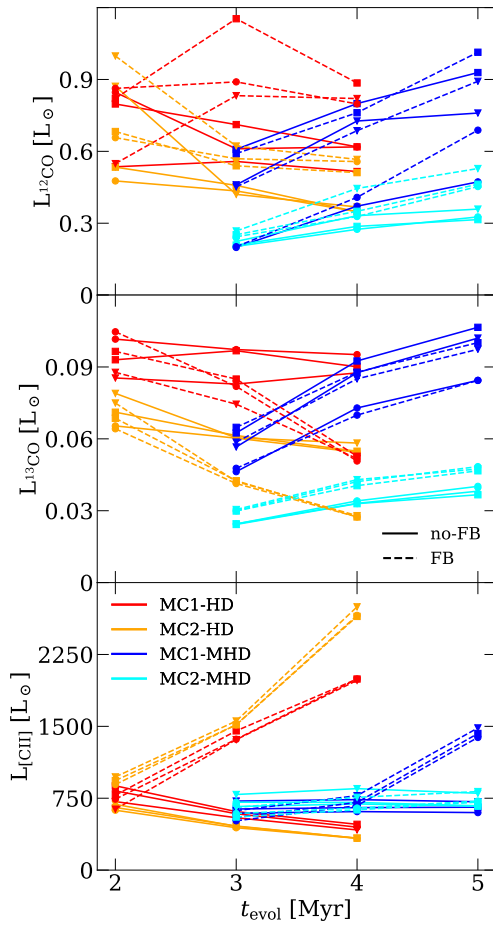
Figure 4. Total luminosity of ^{12}CO, ^{13}CO, and [CII] for the investigated clouds. Circles, squares, and triangles indicate values along $z-$, $y-$, and $x-$axis, respectively. The differences in the evolution of $L_{^{12}CO}$ and $L_{^{13}CO}$, together with the smaller scatter of $L_{^{13}CO}$ among the different LOS for the same cloud, indicate that ^{12}CO is more affected from optical thickness than ^{13}CO. The significant increase of $L_{[CII]}$ in the feedback runs is a consequence of the enhanced excitation temperature of C$^+$ due to stellar feedback. This is not the case for MC2-MHD as the stellar feedback plays a minor role for this cloud.

intensity of a few K km s^{-1} coming from non-irradiated optically thick regions.

The values of N_{H_2} at which I_{CO} and $I_{[CII]}$ become optically thick are in a good agreement with, for instance, the simulations of Bisbas et al. (2021), in particular regarding the $I_{^{12}CO}$ - N_{H_2} relation, whereas the $I_{[CII]}$ - N_{H_2} is more dependent on the environmental conditions of the simulated clouds. Moreover, Beuther et al. (2014) find an $I_{[CII]}$ - N_{H_2} relation in the G48.66 cloud in good agreement with our curve, whereas a study of the Perseus Giant Molecular Cloud by Hall et al. (2020) shows an overall lower $I_{[CII]}$ for given N_{H_2}. Finally, comparing the $I_{^{12}CO} - N_{H_2}$ with the typical X_{CO} of $N_{H_2}/I_{^{12}CO} = 2 \times 10^{20}$ cm^{-2} K^{-1} km^{-1} (Bolatto et al. 2013, green line) shows that a linear relation between the two quantities does not hold on local scales, as already pointed out in Seifried et al. (2020).

In Fig. 4 we have already shown that the [CII] luminosity is enhanced by stellar feedback. Next, we analyse the column density regimes where the majority of luminosity comes from. For $N_{H_2} \gtrsim 10^{22}$ cm^{-2} we report typical $I_{[CII]}$ values of 1 - 10 K km s^{-1} for noFB runs and up to a few $\sim 10^2$ K km s^{-1} for feedback runs (right panel of Fig. 9). Stellar feedback increases the [CII] excitation temperature, which causes a stronger emission for a given density. In general, areas with the highest N_{C^+} are those closer to the star-forming regions (see Fig. 1). Therefore, this is also the regime where the difference between FB and noFB runs are most evident. In addition, for the HD clouds (red and orange lines) at late evolutionary stages, stellar feedback affects even larger parts of the clouds, such that the enhancement in $I_{[CII]}$ is visible also in lower column density regimes.

The cumulative distribution of the intensity (bottom row of Fig. 9) reveals the column density range from which the line emission comes from. We have no CO emitting regions with $N_{H_2} < 10^{21}$ cm^{-2}, whereas 5 - 20 per cent of the [CII] emission comes from these areas. Despite this, we still argue that a significant fraction of [CII] comes from the atomic phase (Franeck et al. 2018) as also pixels with high N_{H_2} still do have a significant amount of atomic hydrogen mixed in (and thus a high N_H) (Seifried et al. 2022). In general, the lines in the plot corresponding to the different clouds differ as each cloud has a different maximum N_{H_2} value. The role of feedback on the [CII] emission is particularly evident: a large part of the emission comes from the rims of the bubbles, which typically regions with $N_{H_2} \gtrsim 10^{22}$ cm^{-2}. This is reflected in the steep ascent of the corresponding curves at $N_{H_2} > 10^{22}$ cm^{-2} for MC1-HD-FB and MC2-HD-FB, the clouds which are most affected by stellar feedback.
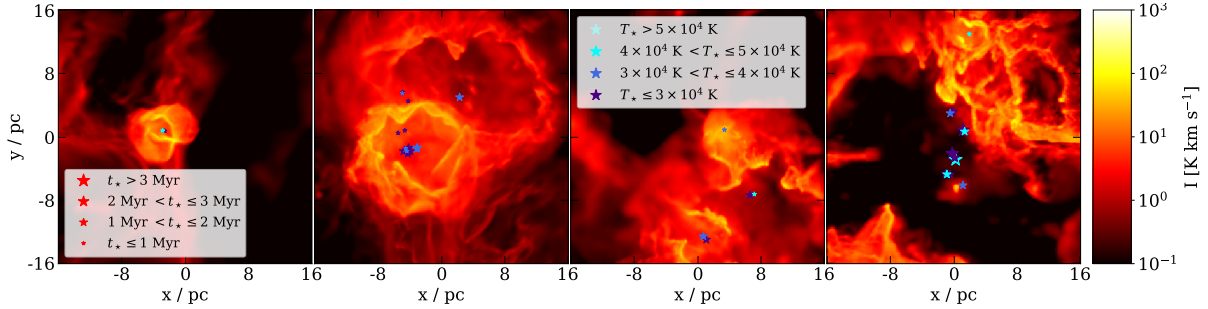
4.6.2 $I_{CO} / I_{[CII]}$ and H_2 mass fraction

In Section 4.5 we show that there is no clear relation between the CO/[CII] luminosity ratio and the H_2 mass fraction. Now, we consider the intensity ratio $I_{^{12}CO}/I_{[CII]}$ as a function of $N_{H_2}/N_{H,tot}$ for each pixel of the maps. We need to be sure that we consider the same portion of the cloud for both, CO and C$^+$. For this purpose, we loop over the 201 velocity channels of the maps and indicate with $\{k\}$ the set of channels for which both specific intensities, $I_{\nu,k,^{12}CO}$ and $I_{\nu,k,[CII]}$, are above the specific intensity of the Cosmic Microwave Background, corresponding to 0.84 and 2.69 $\times$ 10^{-13} K for ^{12}CO and [CII], respectively. (Eq. 15). We define

$$I_{^{12}CO} = \sum_k I_{\nu,k,^{12}CO} \Delta \nu \,, \tag{21}$$

where $\Delta \nu$ is the width of a velocity channel, $I_{[CII]}$ is obtained analogously. The result is shown in Fig. 10, where the mean values

only the data resulting from the integration along the z-direction. However, we obtain qualitatively and quantitatively similar results when considering the x- or the y-direction. We note that the large scatter at very low and very high N_{H_2} is due to the low number of pixels in these regimes.

The column density at which $I_{^{12}CO}$ and $I_{[CII]}$ become optically thick is around $N_{H_2} \simeq 10^{21}$ cm^{-2} in both cases. The $I_{^{13}CO}$ values (middle panel of Fig. 9) show a similar behaviour, but the effect of optical thickness is less evident: deviations from the optically thin behaviour occur at $N_{H_2} \gtrsim 10^{21}$ cm^{-2}, but the change of slope is less pronounced than in the ^{12}CO case. The kink in the $I_{[CII]}$ - N_{H_2} relation does not appear to happen for most of the FB runs. We attribute it to the fact that the regions, where $N_{H_2} > 10^{21}$ cm^{-2}, are essentially the rims of the expanding bubbles (see Fig. 1). In these regions [CII] emission is enhanced by the effect of stellar radiation (see Section 4.3) and – even if optically thick – is thus larger than the

Figure 5. HII regions at different evolutionary stages as seen in [CII]. The individual snapshots are taken from different clouds: from left to right, i) MC2-MHD-FB, t_{evol} = 5 Myr, LOS along the $z-$axis; ii) MC1-MHD-FB, t_{evol} = 5 Myr, LOS along the $y-$axis; iii) MC1-HD-FB, t_{evol} = 4 Myr, LOS along the $y-$axis, and (iv) MC2-HD, t_{evol} = 4 Myr, LOS along the $x-$axis. The bubbles are ordered, from left to right, from the youngest to the oldest evolutionary stage. Stars formed are superimposed and plotted with different sizes and colors according to their age and temperature. We find than the largest and [CII]-darker bubbles are associated with older stars, whereas smaller and brighter bubbles correspond to younger stars.
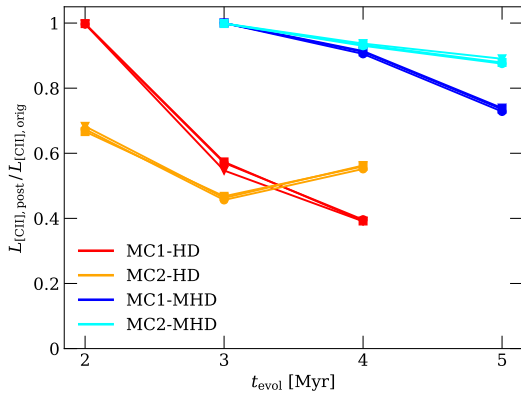
Figure 6. Ratio between the total luminosity of [CII] of the post-processed data, $L_{[CII],post}$, and the original data, $L_{[CII],orig}$. Circles, squares, and triangles indicate values along $z-$, $y-$, and $x-$axis, respectively. Post-processing the simulation data removes up to 60 per cent of the [CII] luminosity, especially at later stages where feedback becomes more important. Hence, it is essential to obtain reliable [CII] emission maps.

of the distribution of $I_{CO}/I_{[CII]}$ for a given N_{H_2} are shown using again the same color for snapshots referring to different t_{evol}. We show here the data referring to the LOS along the z-axis, but we obtain analogous results for the integration along the other LOS. The $I_{12CO}/I_{[CII]}$ ratio increases with increasing $N_{H_2}/N_{H,tot}$. However, different clouds and snapshots show significantly different line ratios for given $N_{H_2}/N_{H,tot}$ with a typical scatter of up to two orders of magnitude. At very low values of $N_{H_2}/N_{H,tot}$ the scatter is even larger due to the low statistics. Furthermore, the presence of CO-dark and CO-bright pixels for the same N_{H_2} (as shown in detail in Seifried et al. 2020, see their figure 8) also contributes to enlarge such scatter.

Hence, the variability for a given $N_{H_2}/N_{H,tot}$ value is so large that the ratio $I_{12CO}/I_{[CII]}$ cannot be reliably used to determine $N_{H_2}/N_{H,tot}$. This is also shown in the example given in Fig. 11, where we show a map of $I_{12CO}/I_{[CII]}$ for MC1-HD-noFB at t_{evol} = 4 Myr. We overplot isocontour lines corresponding to H_2 mass fractions of 0.1, 0.3, 0.5, 0.7, and 0.9. There is a general correspondence between high line ratios and high H_2 mass fractions, but there are still significant variations in the line ratio within regions

of similar H_2 mass fraction, especially for mass fraction regimes between 0.3 and 0.7.

Our results for the *pixel-by-pixel* approach are thus similar to that for the global luminosity ratio shown in Fig. 8, which also does not allow for a determination of the global H_2 mass fraction. However, we cannot directly compare the relation between $I_{12CO}/I_{[CII]}$ and $N_{H_2}/N_{H,tot}$ with the one between $L_{12CO}/L_{[CII]}$ and $M_{H_2}/M_{H,tot}$. For the pixel-by-pixel approach we also find H_2 column density fractions close to 0 and 1 and corresponding $I_{12CO}/I_{[CII]}$ values spanning 8 orders of magnitude. On the other hand, when analysing $L_{12CO}/L_{[CII]}$, we average over the entire cloud and, as a consequence, both the mass fraction and the luminosity ratio span over a considerably lower range.

5   DISCUSSION

5.1   Intrinsic variability of line ratios

The ^{12}CO/[CII] and ^{13}CO/[CII] line ratios shown in Fig. 8 are characterized by a large dispersion due to the difference in the structure and evolutionary stage of the clouds themselves only, but not to different environments or external factors. In fact, all clouds form in a portion of a galactic disc with the same CRIR, G_0, and metallicity and with turbulence driven by supernovae. Furthermore, all MHD runs have the same initial magnetic field strength. Despite that, $L_{12CO}/L_{[CII]}$ varies by up to a factor of 5 for a given $M_{H_2}/M_{H,tot}$. The same applies for ^{13}CO, although the scatter among different LOS for the same snapshot is reduced because of the reduced optical depth.

This scatter is also found in other works. For instance, Röllig et al. (2006) use the luminosity ratio to assess the environmental conditions like the cloud metallicity, density, and FUV field intensity[4]. Their models also exhibit large difference in the line ratio up to a factor of a few, even when leaving environmental conditions like the metallicity, FUV, and cloud density unchanged. Furthermore, also observational results at similar metallicities quoted in their work, e.g. for the LMC and 30 Doradus, show a similar scatter

---

[4]   In order to compare values from observational works with our simulations, it might be necessary to convert the intensity from K km s^{-1} to erg s^{-1} cm^{-2} and recalculate the luminosity and luminosity ratio (see Fig. A3). Note that we plot [CII]/CO there, whereas Fig. 8 shows CO/[CII].
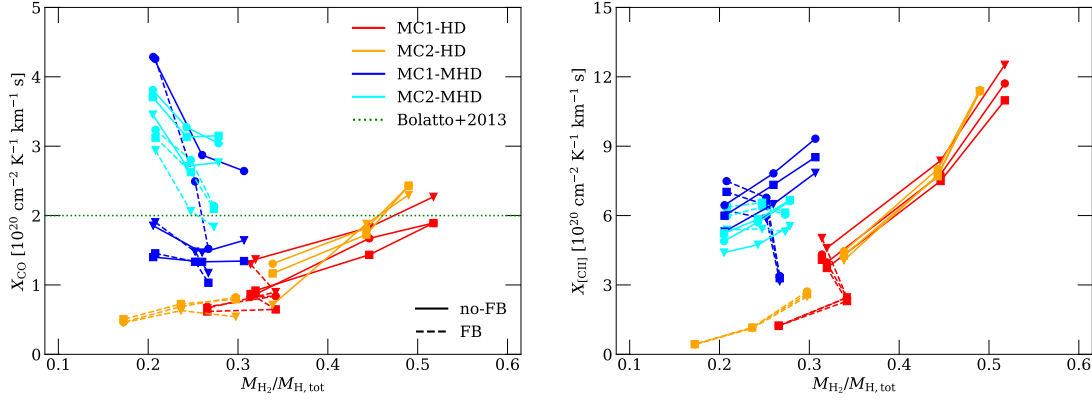
Figure 7. X_{CO} (left) and $X_{[CII]}$ (right) of our simulated clouds as a function of the H_2 mass fraction. Circles, squares, and triangles indicate values along $z-$, $y-$, and $x-$axis, respectively. Regarding X_{CO}, we find a significant scatter among the different clouds and in time around the reference value for the Milky Way of 2×10^{20} cm^{-2} K^{-1} km^{-1} s (dotted line). A similar scatter is found for $X_{[CII]}$ as well. We see an increase of $X_{[CII]}$ with $M_{H_2}/M_{H,tot}$ for the non-FB runs, whereas the FB runs show no clear trend.
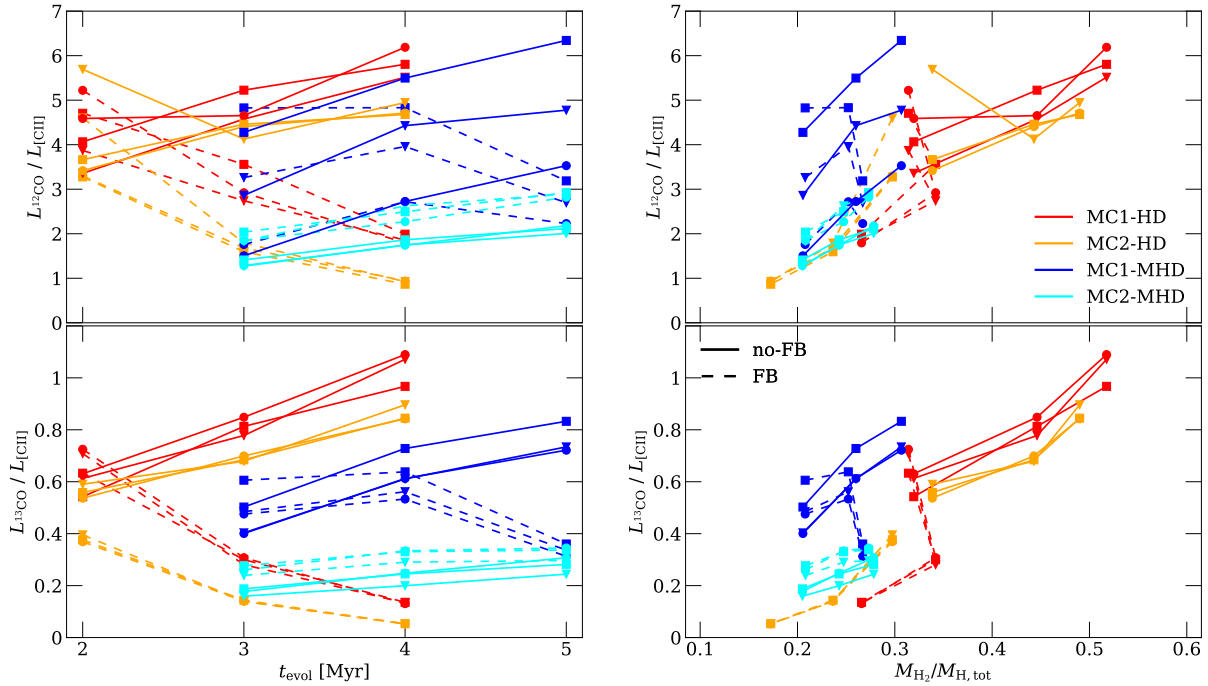

Figure 8. $L_{^{12}CO}/L_{[CII]}$ (top row) and $L_{^{13}CO}/L_{[CII]}$ (bottom row) as a function of t_{evol} (left column) and $M_{H_2}/M_{H_{tot}}$ (right column). For all noFB runs the line ratio increases with t_{evol}. For all FB runs it decreases, with the only exception of MC2-MHD-FB, which has less dense gas. Altogether, there is no clear trend of the luminosity ratio with either t_{evol} and $M_{H_2}/M_{H,tot}$. In addition, there is a large scatter for a given evolutionary stage. The scatter among different LOS is reduced when considering ^{13}CO, due to its smaller optical thickness.

of 5 - 10 in the [CII]/^{12}CO line ratio. In summary, as already stated by Röllig et al. (2006), we do not recommend to use $L_{^{12}CO}/L_{[CII]}$ to infer physical properties of the clouds.

Furthermore, Madden et al. (2020) analyse the ^{12}CO and [CII] emission in a variety of environments. For normal galaxies and galactic star-forming regions, they find $L_{[CII]}/L_{^{12}CO} \approx 4000$, with a large scatter covering values from 300 to 25 000. Our simulation results are thus in good agreement with their findings, although they consider a much larger variety of environments.

Recently, Hall et al. (2020) analysed the ^{12}CO (1 → 0) and [CII] emission from two regions of the Perseus Giant Molecular Cloud. As their observations refer to a resolved portion of a cloud, this corresponds to our *pixel-by-pixel* analysis shown in Fig. 10. In general, we find that their reported values of $I_{^{12}CO}/I_{[CII]}$ of 2 − 100 agree well with ours. They also show that the highest values of the line ratio are reached where H_2 (obtained via a comparison of the optical depth, obtained from dust continuum measurements,
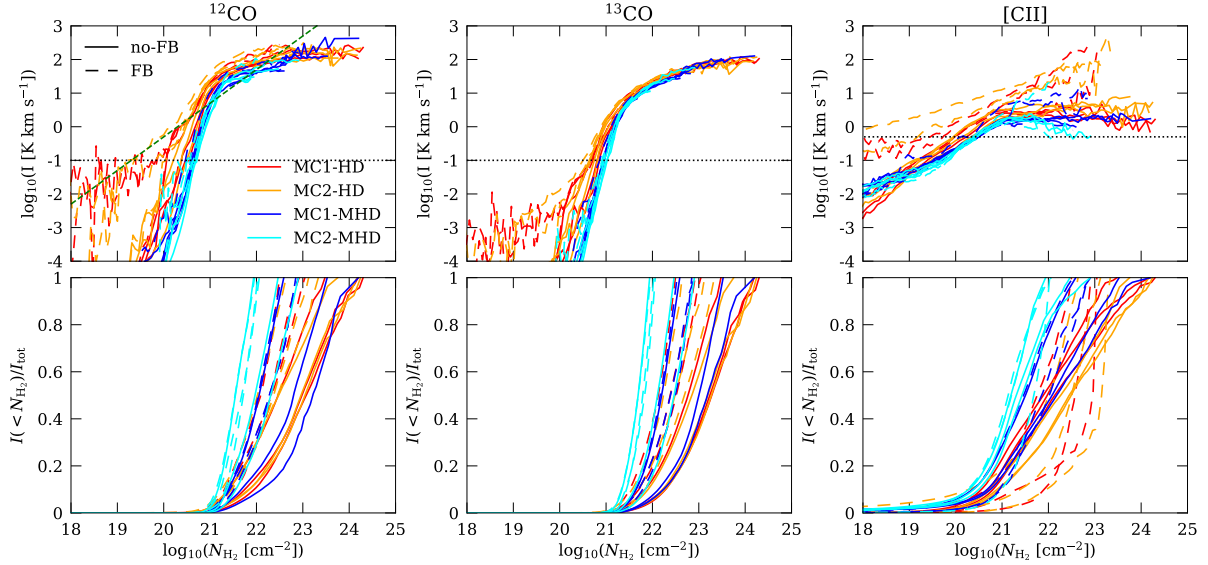
Figure 9. *Top row:* $I_{^{12}CO}$, $I_{^{13}CO}$, and $I_{[CII]}$ (from left to right) as a function of the column density of H_2 column density see along the z-axis. Lines (solid for noFB r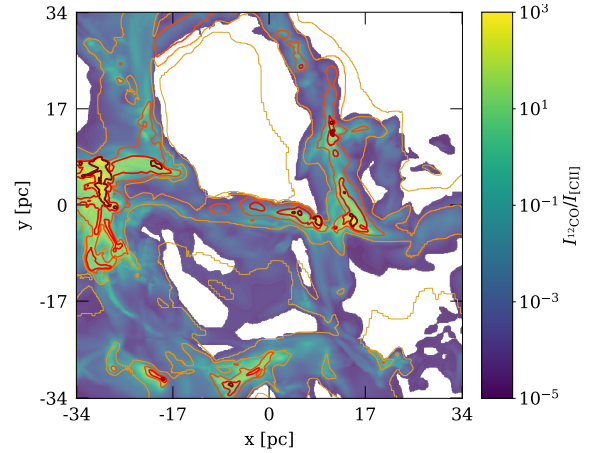uns and dashed for FB runs) represent the mean values for each N_{H_2}-bin. Snapshots at different t_{evol}, for a given cloud, are plotted with the same color. The dotted, horizontal lines represent realistic observable limits for CO and [CII], which we set to 0.1 and 0.5 K km s^{-1}, respectively. The dashed, green line in the top-left panel represents the X_{CO} reference value given by Bolatto et al. (2013). Optical thickness effects play a role for $N_{H_2} \gtrsim 10^{21}$ cm^{-2}. *Bottom row:* cumulative distribution of the intensity of ^{12}CO, ^{13}CO, and [CII] (from left to right) as a function of a N_{H_2} threshold value. Regions with $N_{H_2} < 10^{21}$ cm^{-2} are associated with a negligible CO emission, but they correspond to 5 - 20 per cent of the [CII] emission. The role of feedback is evident in MC1-HD and MC2-HD, where the most of [CII] emission comes from regions with $N_{H_2} > 10^{22}$ cm^{-2}, corresponding to the rims of the bubbles.
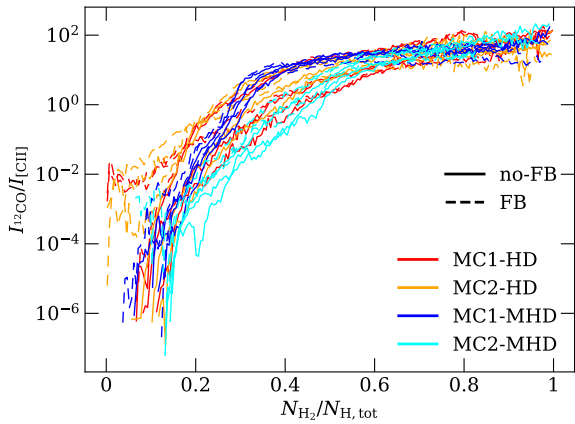
Figure 10. CO/[CII] intensity ratio plotted as a function of the H_2 mass fraction $N_{H_2}/N_{H,tot}$. We plot the snapshots at different t_{evol} with the same color. The line ratio increases with $N_{H_2}/N_{H,tot}$, although there is a large scatter, which is particularly relevant at high $N_{H_2}/N_{H,tot}$ as the relation is much shallower in this regime than at lower mass fraction. This prevents the usage of $I_{^{12}CO}/I_{[CII]}$ to determine $N_{H_2}/N_{H,tot}$.

Figure 11. Map of $I_{^{12}CO}/I_{[CII]}$ for MC1-HD at $t_{evol} = 4$ Myr. Contour lines indicate an H_2 mass fraction $N_{H_2}/N_{H,tot}$ of 0.1, 0.3, 0.5, 0.7 and 0.9, respectively. We note a general correspondence between higher intensity ratio and higher $N_{H_2}/N_{H,tot}$ values. There are, however, significant differences in the line ratio for a given $N_{H_2}/N_{H,tot}$ value, especially in moderate $N_{H_2}/N_{H,tot}$ regimes.

and the HI column density, see their Eq. 1) is more abundant, which is in agreement with our results.

Finally, Bisbas et al. (2021) analysed the line emission of several species from two different, simulated clouds with different environmental parameters. For comparable CRIR, G_0, and metallicity, they find ^{12}CO/[CII] line ratios larger by up to one order of magnitude compared to our work. We tentatively attribute this difference to two main factors. First, our clouds are somewhat more

diffuse than the clouds used by Bisbas et al. (2021) (priv. communication). Indeed, when going to later evolutionary states, i.e. denser clouds, our line ratios increase (Fig. 8). Second, their work assumes chemical equilibrium, while we use non-equilibrium chemistry, a difference whose effects we will discuss in detail in the following.

5.2 Equilibrium vs. Non-equilibrium chemistry

A large number of MC simulation works post-process their results to obtain chemical abundances by assuming that the chemical state is in equilibrium (see e.g. Gong et al. 2018; Li et al. 2018; Keating et al. 2020; Bisbas et al. 2021). As an example, Gong et al. (2020) study the X_{CO} factor for a wide range of environments. They evolve the chemical network for 50 Myr, i.e. equilibrium is roughly reached at that point (Joshi et al. 2019), before analysing synthetic CO observations and the X_{CO} factor. However, the presence of phenomena like e.g. the turbulent mixing (see e.g. Glover & Mac Low 2007c; Valdivia et al. 2016; Seifried et al. 2017) suggests that this approach can determine inaccurate estimations at least for hydrogen and directly related quantities like e.g. X_{CO}.

Here, we aim to assess how much the assumption of equilibrium chemistry affects synthetic emission maps. In order to do so, we first select the snapshots of MC1-HD-noFB and MC2-HD-noFB at t_{evol} = 2 and 3 Myr and only evolve the chemistry with the NL97 network for additional 120 Myr while the hydrodynamical state (total gas density, etc.) remains frozen. In the following, t_{chem} refers to the time for which the chemistry of the snapshot was evolved. We also define $M_{no-eq} = M(t_{chem} = 0)$ and $L_{no-eq} = L(t_{chem} = 0)$.

Fig. 12 shows the evolution of H_2, H, H^+, CO, C^+, and e^- as a function of t_{chem}. The CO and H_2 masses (left column) increase with t_{chem} by up to 30 and 120 per cent, respectively, in rough agreement with e.g. Gong et al. (2018). The masses of H^+ and e^- (right column) also increase over time but the increase is less pronounced (between 3 and 12 per cent). The masses of C^+ and H decrease with t_{chem} by 7 and 60 per cent, respectively. In summary, these results once again confirm that the assumption of chemical equilibrium is – in particular for hydrogen-bearing species – questionable (Glover & Mac Low 2007c; Valdivia et al. 2016; Seifried et al. 2017; Seifried et al. 2022; Hu et al. 2021).

Furthermore, we find that CO and C^+ reach equilibrium at $t_{chem} \sim 10$ Myr, whereas H_2, H, and H^+ reach it after $\gtrsim 40$ Myr. In all cases, however, we can assume that at $t_{chem} = 50$ Myr (used in the following) equilibrium is roughly reached, as the relative changes with respect to later times are $\lesssim 5$ per cent.

The significant changes of the chemical abundances by up to 120 per cent also affect the synthetic emission maps. In Fig. 13 we show the difference in total luminosity between the equilibrium (defined here as the state at $t_{chem} = 50$ Myr) and non-equilibrium state ($t_{chem} = 0$) for ^{12}CO and [CII]. The luminosity of CO increases in equilibrium by up to 50 per cent with respect to the non-equilibrium case. This increase is only marginally larger than the respective increase of the CO mass (up to 30 per cent), indicating that the increase in M_{CO} in chemical equilibrium is responsible for this luminosity change. Furthermore, due to the different gain in M_{H_2} (top left panel of Fig. 12) and L_{CO}, the value of X_{CO} determined for the chemical equilibrium case is about 50 per cent larger than the actual value for the non-equilibrium state. However, this deviation is within the typical scatter of X_{CO} of a factor of a few found here (see Section 4.4) as well as in Gong et al. (2020) using equilibrium chemistry. Hence, differences caused by the equilibrium approach can hardly be assessed by comparing the values for X_{CO} obtained in both works.

On the other hand, the change in [CII] luminosity (right panel of Fig. 13) is considerably larger than the corresponding change in mass (as shown in Fig. 12), e.g. for MC1-HD-noFB at 2 Myr for one LOS we have $\Delta L / L_{non-eq} \simeq -30$ per cent and $\Delta M / M_{non-eq} \simeq -7$ per cent.

One element contributing to explain the changes in mass and luminosity are the collisional partners, which in our case are H_2, H, and electrons. We find that the H_2 abundance increases with t_{chem}, whereas H decreases. Although the electron abundance increases for the equilibrium case and the $C^+ - e^-$ de-excitation rates rates are in general larger than those of H and H_2, this does not lead to an increase in $L_{[CII]}$. We attribute this to the fact that the relative change of the electron abundance is significantly lower ($\lesssim 12$ per cent) than for the other two collisional partners. Additionally, there is little C^+ in the low-density/high-temperature regime where the e^- collisional rate is high. Hence, as the [CII] emission is dominated by atomic gas (Franeck et al. 2018), the drop in H mass is mainly responsible for the drop in $L_{[CII]}$.

The impact of the collisional partners affecting $L_{[CII]}$ can also be expressed by the excitation temperature (see Fig. A4 in the appendix). We find that T_{ex} is overall lower for the equilibrium case. This contributes to explain the larger decrease in luminosity than in mass when moving to equilibrium for C^+.

Another factor explaining why the relative changes of mass and luminosity for C^+ do not directly correlate is connected to the detailed distribution of C^+ in the density – temperature phase space. The majority of C^+ mass is contained in the Warm Neutral Medium (WNM), where the C^+ abundance is already quite close to chemical equilibrium. Thus, evolving the chemistry to equilibrium does not imply a major change in this region and then the overall change in M_{C^+} is rather moderate. However, for observations towards MCs, the C^+ in the WNM – despite existing in this environment – contributes only little to the total [CII] luminosity. Rather, most of the [CII] luminosity from MCs comes from the Cold Neutral Medium (CNM) (Franeck et al. 2018). In the CNM, however, the C^+ abundance is further away from equilibrium, hence evolving the chemistry to equilibrium produces a significant change in the C^+ mass in this region, and in consequence on the total [CII] luminosity. The total change in C^+ mass (being dominated by the WNM) is, however, minor.

We emphasise that the values for $t_{evol} = 2$ Myr (solid lines in Figs. 12 and 13) change more, both in terms of mass and luminosity, than the values for $t_{evol} = 3$ Myr (dashed lines). Hence, early evolutionary stages appear to be further away from a chemical equilibrium state, as the overall densities are still lower and thus, the chemical timescales longer. As a result, we argue that the chemical post-processing of MC simulations up to equilibrium, in particular at an early evolutionary state, is questionable and should be considered with great caution.

Given the luminosity changes shown in Fig. 13, the values of $L_{CO}/L_{[CII]}$ (not shown) increase by up to 100 per cent for the equilibrium case with respect to the non-equilibrium case. Assuming chemical equilibrium can therefore lead to a relative error of up to a factor of ~ 2 when calculating such line ratios. As pointed out before, this error is generally larger at early evolutionary stages of the clouds. This effect can thus contribute to the differences seen in line ratios when compared to e.g. the work of Bisbas et al. (2021).

Finally, we investigate the change in the relation between N_{H_2} and N_{CO} assuming chemical equilibrium. In Fig. 14 we show an example for MC2-HD-noFB at $t_{evol} = 2$ Myr. The red-shaded area represents the 2D-PDF for the original, non-equilibrium snapshot, whereas the blue-shaded area represents the equilibrium case. The two lines indicate the mean values. We observe a shift towards higher N_{H_2} for a given N_{CO} for chemical equilibrium, which we mainly attribute to the more pronounced increase in M_{H_2} than in M_{CO} in case of chemical equilibrium (see Fig. 12). We note that this is in excellent agreement with results of Hu et al. (2021), who
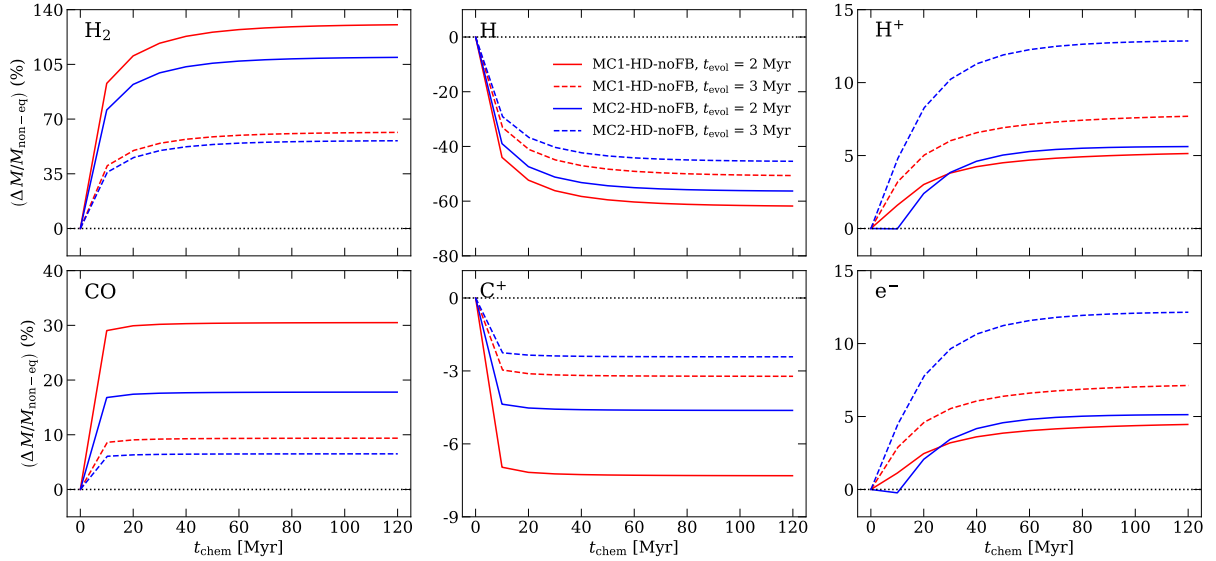
Figure 12. Relative mass changes of H_2, H, H^+, CO, C^+, and e^- (from top left to bottom right) for a selection of snapshots, obtained by freezing the evolution of the physics in the simulation and only evolving the chemistry for a time t_{chem}. CO and C^+ reach equilibrium after ~ 10 Myr, whereas H and H_2 reach equilibrium at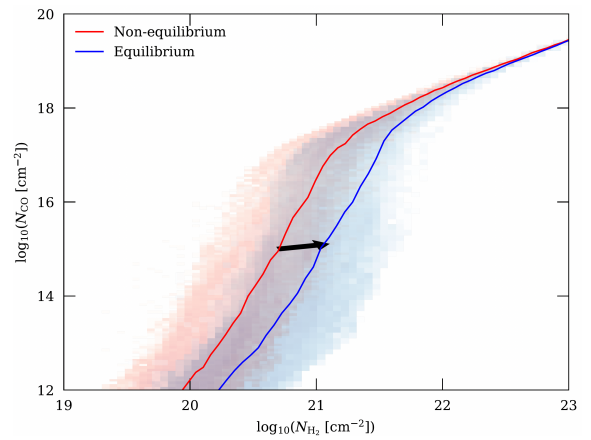 $\gtrsim 40$ Myr. The mass variations at equilibrium are particularly important for H (decreasing by up to 60 per cent) and for H_2 (increasing by up to 120 per cent), making the assumption of equilibrium for these species questionable. Changes for carbon-bearing species, H^+, and e^- are smaller than for H and H_2.
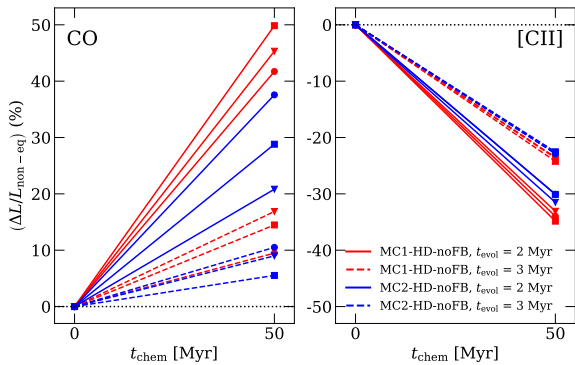
Figure 13. Relative luminosity changes of L_{CO} (left) and $L_{[CII]}$ (right) between $t_{chem} = 0$ and $t_{chem} = 50$ Myr for the same selection of snapshot as in Fig. 12. The three different LOS are indicated with different markers. We note that the the luminosity decreases for [CII] up to ~ 30 per cent, while the corresponding mass decreases of ~ 7 per cent. The changes in the CO luminosity are comparable with the changes in the CO mass.

Figure 14. N_{CO} as a function of N_{H_2} for MC2-HD at $t_{evol} = 2$ Myr, considering the chemical state in non-equilibrium (red) and at equilibrium (blue). Shaded areas represent the 2D-PDFs and solid lines represent the mean values. The change is due to the larger increase in the H_2 mass than in the CO mass when moving from non-equilibrium to equilibrium chemistry (120 per cent vs. 30 per cent for the considered snapshot). The black arrow qualitatively indicates the change of the abundances for this transition.

find a similar difference in mass changes for H_2 and CO concerning equilibrium and non-equilibrium states.

To summarize, we consider it as crucial to use non-equilibrium chemistry to simulate the H/H_2 content of MCs, as cloud evolution and molecule formation go hand in hand. Because of this, using chemical equilibrium for simulated MCs should be considered with great caution, in particular at early evolutionary stages, as it can significantly effect both the masses and luminosities of the various species.

6   CONCLUSIONS

We present an analysis of the abundance and luminosity of ^{12}CO, ^{13}CO and C^+ for 8 simulated MCs within the SILCC-Zoom project (Seifried et al. 2017), in which the chemical network is evolved *on-the-fly*. In particular, we investigate two clouds with and two without magnetic fields under solar neighborhood conditions at different evolutionary stages. For each simulation we consider a reference case without stellar feedback and one including radiative

feedback in the form of ionizing radiation by massive stars. For this purpose, we have developed a novel post-processing routine (based on CLOUDY) to account for higher ionization states of carbon. We show that this post-processing is essential to obtain reliable [CII] emission maps in feedback-dominated regions.

Our conclusions can be summarised as follows:

- The [CII] emission maps of the runs with radiative feedback show expanding HII regions/bubbles, where carbon is largely in form of C^{2+} and thus devoid of [CII] emission inside, but with significant emission at the rims. This is in good agreement with recent [CII] surveys.

- We estimate that radiative feedback increases the [CII] luminosity by $\sim 50-85$ per cent compared to the non-feedback case due to an enhancement of the excitation temperature. The CO luminosity decreases by up to a factor of 3 at late evolutionary stages of the clouds due to the dispersal of dense regions.

- The line luminosity ratios $L_{12CO}/L_{[CII]}$ and $L_{13CO}/L_{[CII]}$, integrated over the entire maps, show an increase with increasing H_2 mass fraction in noFB runs, but no clear relation in FB runs. We obtain values for $L_{12CO}/L_{[CII]}$ from 1 to 6 and for $L_{13CO}/L_{[CII]}$ from 0.1 to 1.1. We argue that due to the large spread, these line ratios *cannot* be used as a reliable tracer of the cloud's H_2 mass fraction. Similarly, this spread makes it difficult to use them to assess environmental parameters like the CRIR, the IRSF, or the metallicity, which we kept fixed in our simulations.

- A pixel-by-pixel analysis of $I_{12CO}/I_{[CII]}$ as a function of $N_{H_2}/N_{H, tot}$ shows an increase of the ratio with $N_{H_2}/N_{H, tot}$. However, as for the total luminosity ratio, also here the scatter is so significant that $I_{12CO}/I_{[CII]}$ cannot reliably be used to predict the mass fraction of H_2 along the LOS.

- Evolving the chemistry to equilibrium as done in various works results in significant differences in terms of species abundance with respect to a self-consistent non-equilibrium approach used *on-the-fly* during the simulation. Hence, in particular for early evolutionary stages an equilibrium approach is questionable. We find that for the equilibrium case, the H_2 mass is increased and the H mass is decreased by up to a factor of about 2. Other species abundances such as CO, C^+ and electrons change by a few 10 per cent.

- Assuming chemical equilibrium also affects the inferred luminosities of CO and [CII], with relative changes of up to +50 and −30 per cent, respectively. These luminosity changes cause an overestimate of the $L_{CO}/L_{[CII]}$ line ratios by up to 100 per cent if equilibrium chemistry is assumed. Similarly, the X_{CO} factor would be overestimated by up to 50 per cent in this case.

- In general, the X_{CO} factor ranges between 0.5 and 4.5×10^{20} cm^{-2} K^{-1} km^{-1} s, showing no clear trend with respect to time evolution or the H_2 mass fraction. Feedback runs in general have a lower X_{CO} than the corresponding non-feedback runs. The similarly defined $X_{[CII]}$ factor ranges between 0.5 and 12×10^{20} cm^{-2} K^{-1} km^{-1} s, also not showing a clear trend with evolutionary time or H_2 mass fraction.

In summary, we show that it is crucial to take into account the effects (i) of stellar radiation in further ionizing C^+ within HII regions, and (ii) an *on-the-fly*, non-equilibrium chemistry treatment to accurately model CO and [CII] line emission in simulated MCs. We thus strongly suggest to consider both effects for future and more detailed comparisons with observations (e.g. Ebagezio et al., in prep.).

REFERENCES

Abel N. P., Ferland G. J., Shaw G., van Hoof P. A. M., 2005, ApJS, 161, 65
Appleton P. N., et al., 2013, ApJ, 777, 66
Beck R., Wielebinski R., 2013, in Oswalt T. D., Gilmore G., eds, , Vol. 5, Planets, Stars and Stellar Systems. Volume 5: Galactic Structure and Stellar Populations. p. 641, doi:10.1007/978-94-007-5612-0_13
Beuther H., et al., 2014, A&A, 571
Bisbas T. G., Tan J. C., Tanaka K. E. I., 2021, MNRAS, 502, 2701
Bolatto A. D., Wolfire M., Leroy A. K., 2013, ARAA, 51, 207
Borchert E. M. A., Walch S., Seifried D., Clarke S. D., Franeck A., Nürnberger P. C., 2022, MNRAS, 510, 753
Bot C., Boulanger F., Rubio M., Rantakyro F., 2007, A&A, 471, 103
Bouchut F., C. K., K. W., 2007, Numerische Mathematik., 108
Cecchi-Pestellini C., Bodo E., Balakrishnan N., Dalgarno A., 2002, ApJ, 571, 1015
Clark P. C., Glover S. C. O., Klessen R. S., Bonnell I. A., 2012, MNRAS, 424, 2599
Dame T. M., Koper E., Israel F. P., Thaddeus P., 1993, ApJ, 418, 730
Dame T. M., Hartmann D., Thaddeus P., 2001, ApJ, 547, 792
Derigs D., Winters A. R., Gassner G. J., Walch S., 2016, Journal of Computational Physics, 317, 223
Derigs D., Winters A. R., Gassner G. J., Walch S., Bohm M., 2018, Journal of Computational Physics, 364, 420
Dobbs C. L., Pringle J. E., 2013, MNRAS, 432, 653
Dobbs C. L., et al., 2014, Protostars and Planets VI, pp 3–26
Draine B. T., 1978, ApJS, 36, 595
Dubey A., Reid L. B., Fisher R., 2008, Phys. Scr., 132
Dullemond C. P., Juhasz A., Pohl A., Sereshti F., Shetty R., Peters T., Commercon B., Flock M., 2012, Astrophysics Source Code Library
Federrath C., Banerjee R., Clark P. C., Klessen R. S., 2010, ApJ, 713, 269
Ferland G. J., et al., 2017, Rev. Mex. Astron. Astrofis., 53, 385
Franeck A., et al., 2018, MNRAS, 481, 4277
Fryxell B., et al., 2000, ApJS, 131, 273
Gatto A., et al., 2015, MNRAS, 449, 1057
Gatto A., et al., 2017, MNRAS, 466, 1903
Girichidis P., et al., 2016, MNRAS, 456, 3432
Glover S. C. O., Clark P. C., 2016, MNRAS, 456, 3596
Glover S. C. O., Mac Low M.-M., 2007a, ApJS, 169, 239
Glover S. C. O., Mac Low M.-M., 2007b, ApJ, 659, 1317
Glover S. C. O., Mac Low M.-M., 2007c, ApJ, 659, 1317
Glover S. C. O., Mac Low M. M., 2011, in Röllig M., Simon R., Ossenkopf V., Stutzki J., eds, EAS Publications Series Vol. 52, EAS Publications Series. pp 147–150 (arXiv:1101.3157), doi:10.1051/eas/1152023

Glover S. C. O., Federrath C., Mac Low M. M., Klessen R. S., 2010, MNRAS, 404, 2

Gong M., Ostriker E. C., Kim C.-G., 2018, ApJ, 858, 16

Gong M., Ostriker E. C., Kim C.-G., Kim J.-G., 2020, ApJ, 903

Grenier I. A., Casandjian J.-M., Terrier R., 2005, Science, 307, 1292

Habing H. J., 1968, Bull. Astron. Inst. Netherlands, 19, 421

Haid S., Walch S., Seifried D., Wünsch R., Dinnbier F., Naab T., 2019, MNRAS, 482, 4062

Hall K. P., Stanimirović S., Lee M.-Y., Wolfire M., Goldsmith P., 2020, ApJ, 899

Hu C.-Y., Naab T., Walch S., Glover S. C. O., Clark P. C., 2016, MNRAS, 458, 3528

Hu C.-Y., Naab T., Glover S. C. O., Walch S., Clark P. C., 2017, MNRAS, 471, 2151

Hu C.-Y., Sternberg A., van Dishoeck E. F., 2021, arXiv e-prints, p. arXiv:2103.03889

Hu C.-Y., Schruba A., Sternberg A., van Dishoeck E. F., 2022, ApJ, 931, 28

Ibáñez-Mejía J. C., Mac Low M.-M., Klessen R. S., Baczynski C., 2016, ApJ, 824, 41

Joshi P. R., Walch S., Seifried D., Glover S. C. O., Clarke S. D., Weis M., 2019, MNRAS, 484, 1735

Keating L. C., et al., 2020, MNRAS, 499, 837

Kim C.-G., Ostriker E. C., 2018, ApJ, 853, 173

Klessen R. S., Glover S. C. O., 2016, Saas-Fee Advanced Course, 43, 85

Lada E. A., Blitz L., 1988, ApJ, 326, L69

Lahén N., Naab T., Johansson P. H., Elmegreen B., Hu C.-Y., Walch S., Steinwandel U. P., Moster B. P., 2020, ApJ, 891, 2

Larson R. B., 1981, MNRAS, 194, 809

Lesaffre P., Pineau des Forêts G., Godard B., Guillard P., Boulanger F., Falgarone E., 2013, A&A, 550, A106

Li M., Ostriker J. P., Cen R., Bryan G. L., Naab T., 2015, ApJ, 814, 4

Li Q., Narayanan D., Davè R., Krumholz M. R., 2018, ApJ, 869, 73

Lombardi M., Alves J., Lada C. J., 2006, A&A, 454, 781

Luisi M., et al., 2021, Science Advances, 7, eabe9511

Madden S. C., et al., 2020, A&A, 643

Melchior A. L., Viallefond F., Guélin M., Neininger N., 2000, MNRAS, 312, L29

Nelson R. P., Langer W. D., 1997, ApJ, 482, 796

Nieten C., Neininger N., Guélin M., Ungerechts H., Lucas R., Berkhuijsen E. M., Beck R., Wielebinski R., 2006, A&A, 453, 459

Offner S. S. R., Bisbas T. G., Bell T. A., Viti S., 2014, MNRAS, 440, L81

Ossenkopf V., 1997, New Astron., 2, 365

Ossenkopf V., Röllig M., Neufeld D. A., Pilleri P., Lis D. C., Fuente A., van der Tak F. F. S., Bergin E., 2013, A&A, 550, A57

Pabst C., et al., 2019, Nature, 565, 618

Padoan P., Pan L., Haugbølle T., Nordlund Å., 2016, ApJ, 822, 11

Papadopoulos P. P., Thi W. F., Viti S., 2004, MNRAS, 351, 147

Pineda J. L., Langer W. D., Velusamy T., Goldsmith P. F., 2013, A&A, 554

Pineda J. L., Langer W. D., Goldsmith P. F., 2014, A&A, 570

Rachford B. L., et al., 2009, ApJS, 180, 125

Ripple F., Heyer M. H., Gutermuth R., Snell R. L., Brunt C. M., 2013, MNRAS, 431, 1296

Röllig M., Ossenkopf V., Jeyakumar S., Stutzki J., Sternberg A., 2006, A&A, 451, 917

Salpeter E. E., 1955, ApJ, 121, 161

Schöier F. L., van der Tak F. F. S., van Dishoeck E. F., Black J. H., 2005, A&A, 432, 369

Scoville N. Z., Solomon P. M., 1975, ApJ, 199, L105

Scoville N. Z., Yun M. S., Clemens D. P., Sanders D. B., Waller W. H., 1987, ApJS, 63, 821

Seifried D., Walch S., 2016, MNRAS, 459, L11

Seifried D., et al., 2017, MNRAS, 472, 4797

Seifried D., Walch S., Reissl S., Ibáñez-Mejía J. C., 2019, MNRAS, 482, 2697

Seifried D., Haid S., Walch S., Borchert E. M. A., Bisbas T. G., 2020, MNRAS, 492, 1465

Seifried D., Beuther H., Walch S., Syed J., Soler J. D., Girichidis P., Wünsch R., 2022, MNRAS, 512, 4765

Sembach K. R., Howk J. C., Ryans R. S. I., Keenan F. P., 2000, ApJ, 528, 310

Shetty R., Glover S. C., Dullemond C. P., Klessen R. S., 2011a, MNRAS, 412, 1686

Shetty R., Glover S. C., Dullemond C. P., Ostriker E. C., Harris A. I., Klessen R. S., 2011b, MNRAS, 415, 3253

Smith M. W. L., et al., 2012, ApJ, 756, 40

Smith R. J., Glover S. C. O., Clark P. C., Klessen R. S., Springel V., 2014a, MNRAS, 441, 1628

Smith R. J., Glover S. C. O., Clark P. C., Klessen R. S., Springel V., 2014b, MNRAS, 441, 1628

Smith R. J., Glover S. C. O., Klessen R. S., 2014c, MNRAS, 445, 2900

Smith R. J., et al., 2020, MNRAS, 492, 1594

Solomon P. M., Rivolo A. R., Barrett J., Yahil A., 1987, ApJ, 319, 730

Spitzer L., 1978, Physical processes in the interstellar medium, doi:10.1002/9783527617722.

Stacey G. J., Geis N., Genzel R., Lugten J. B., Poglitsch A., Sternberg A., Townes C. H., 1991, ApJ, 373, 423

Strong A. W., Mattox J. R., 1996, A&A, 308, L21

Stutzki J., 2001, Astrophysics and Space Science Supplement, 277, 39

Sutherland R. S., Dopita M. A., 1993, ApJS, 88, 253

Tielens A. G. G. M., Hollenbach D., 1985, ApJ, 291, 722

Tiwari M., 2021, in American Astronomical Society Meeting Abstracts. p. 137.03

Valdivia V., Hennebelle P., Gérin M., Lesaffre P., 2016, A&A, 587, A76

Velusamy T., Langer W. D., 2014, A&A, 572, A45

Waagan K., 2009, J. Comput. Phys., 228

Walch S., et al., 2015, MNRAS, 454, 238

Walker K. M., Song L., Yang B. H., Groenenboom G. C., van der Avoird A., Naduvalath B., Forrey R. C., Stancil P. C., 2015, American Astr. Soc.

Wilson T. L., 1999, Reports on Progress in Physics, 62, 143

Wilson R. W., Jefferts K. B., Penzias A. A., 1970, ApJ, 161, L43

Wünsch R., Walch S., Dinnbier F., Whitworth A., 2018, MNRAS, 475, 3393

Wünsch R., Walch S., Dinnbier F., Seifried D., Haid S., Klepitko A., Whitworth A. P., Palouš J., 2021, MNRAS, 505, 3730

van Dishoeck E. F., Black J. H., 1988, ApJ, 334, 771

APPENDIX A: SUPPLEMENTARY FIGURES

In the following, we show some additional plots which help in clarifying several aspects of the paper. In Fig. A1 we show the same expanding bubbles as in Fig. 5, but now for the case with and without the post-processing for C^{2+} (see Section 3.2) to allow for a direct comparison. The importance of the post-processing in removing the [CII] intensity coming from the interior of the bubbles is evident, in particular for bubbles associated with older and hotter stars.

In Fig. A2 we show $L_{12CO}/L_{[CII]}$ (left side) and $L_{13CO}/L_{[CII]}$ (right side) as a function of the H_2 mass, instead of the H_2 mass fraction (see Fig. 8). The correspondence of the line ratio with the H_2 mass is even weaker than with the H_2 mass fraction. This is due to the fact that the mass is an extensive quantity, whereas line ratios and mass fractions are intensive quantities.

In Fig. A3 we show the line ratios using units of erg s^{-1} for the luminosity. This allows an easier comparison with some observational results e.g. by Röllig et al. (2006) (see Section 5.1).

In Fig. A4 we show a 2D-PDF of the gas temperature and the excitation temperature for MC1-HD-noFB at $t_{evol} = 2$ Myr. The upper plot refers to the non-equilibrium (i.e., $t_{chem} = 0$), and the bottom plot refer to the equilibrium state ($t_{chem} = 50$ Myr) as discussed in Section 5.2. Due to the changes in the collisional partners (see Fig. 12), the excitation temperature is lower at equilibrium, which explains why the [CII] luminosity decreases when evolving the chemistry to equilibrium.
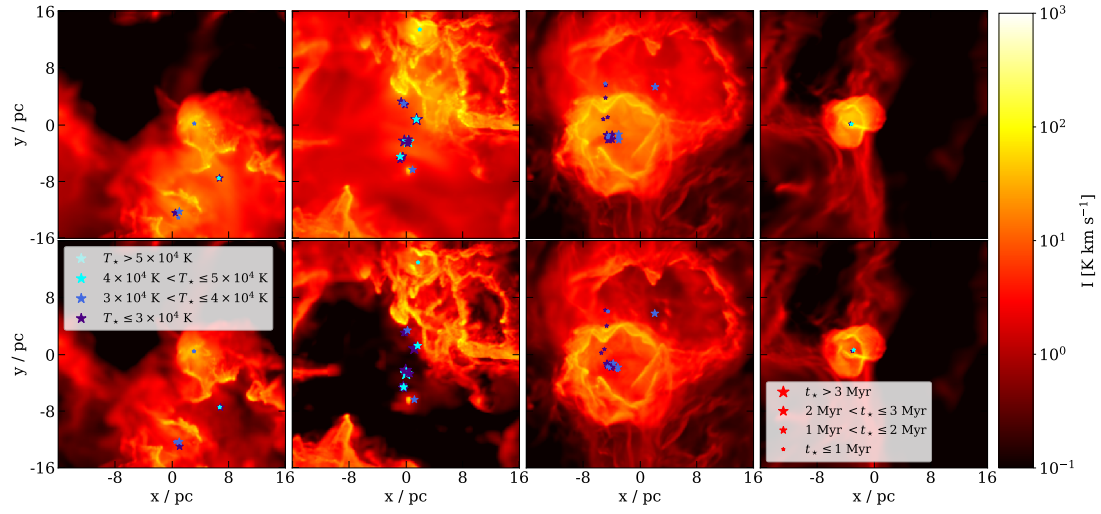
Figure A1. Examples of synthetic [CII] emission maps of expanding feedback bubbles, before (top row) and after the post-processing described in Section 3.2 to account for the conversion of C^+ into C^{2+} (bottom row). The importance of the post-processing in reducing the [CII] intensity coming from the interior of the bubbles is evident, in particular for bubbles associated with older and hotter stars.
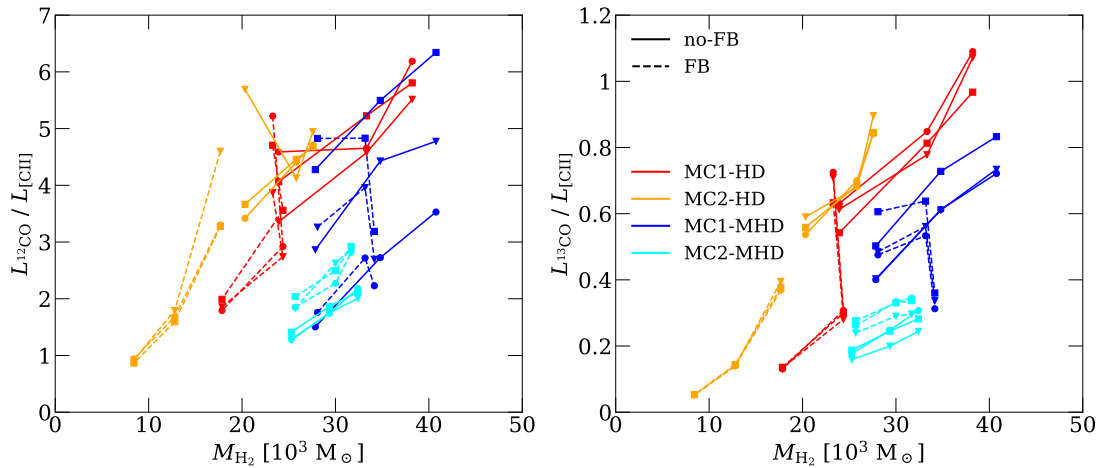
Figure A2. $L_{12CO}/L_{[CII]}$ (left panel) and $L_{13CO}/L_{[CII]}$ (right panel) as a function of the H_2 mass as opposed to Fig. 8 where it is plotted against $M_{H_2}/M_{H,tot}$. As the luminosity ratio is an intensive property of the clouds, while the H_2 mass is extensive, the relation shows an even larger scatter than the one against the H_2 mass fraction (see Fig. 8).

This paper has been typeset from a TEX/LATEX file prepared by the author.

18   *S. Ebagezio et al.*
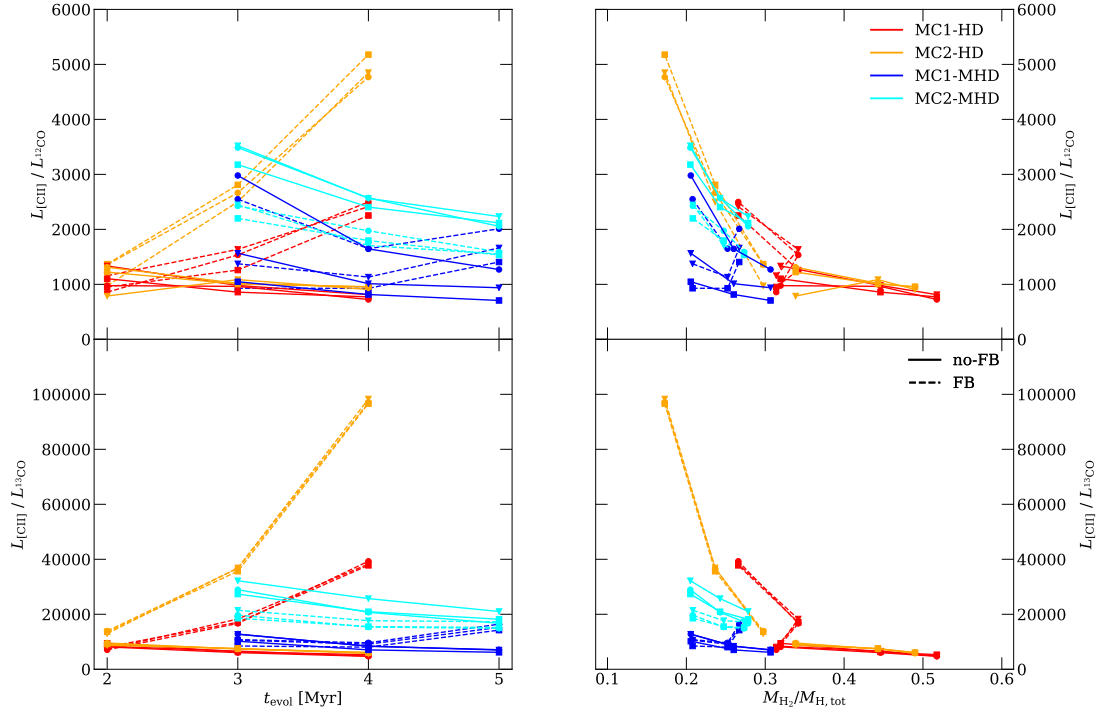
Figure A3. $L_{[\text{CII}]}/L_{^{12}\text{CO}}$ (top row) and $L_{[\text{CII}]}/L_{^{13}\text{CO}}$ (bottom row) as a function of t_{evol} (left column) and $M_{\text{H}_2}/M_{\text{H,tot}}$ (right column). Luminosities are expressed in erg s^{-1} as opposed to the usage of K km s^{-1} in the main body of the paper.
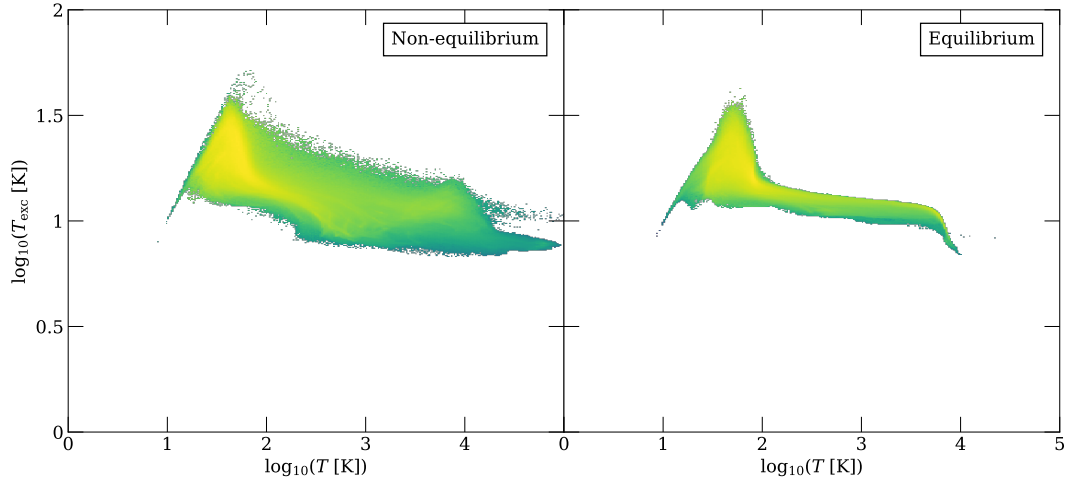
Figure A4. 2D-PDF of excitation temperature T_{ex} as a function of the gas temperature. The left-hand side plot represents MC1-HD-noFB at $t_{\text{evol}} = 2$ Myr with the chemistry evolved *on-the-fly*, the right-hand side plot represents the same snapshot at steady state, i.e. at $t_{\text{chem}} = 50$ Myr.

5

THE ORIGIN OF THE [CII]-DEFICIT IN HII REGIONS AND STAR FORMING MOLECULAR CLOUDS (PAPER II)

The origin of the [CII]-deficit in HII regions and star forming molecular clouds

S. Ebagezio,[1][*] D. Seifried,[1,2] S. Walch,[1,2]

[1]*Universität zu Köln, I. Physikalisches Institut, Zülpicher Str. 77, 50937 Köln, Germany*
[2]*Center for Data and Simulation Science, University of Cologne, Germany, https://cds.uni-koeln.de*

ABSTRACT

We produce and analyse synthetic emission maps of [CII] and FIR continuum of simulated molecular clouds within the SILCC-Zoom Project. We use both hydrodynamical and magnetohydrodynamical simulations. All simulations include stellar radiative feedback and the chemical evolution of hydrogen species, CO, and C^+ is calculated on-the-fly. The further ionization of C^+ into C^{2+} is also included in a post-processing step to obtain reliable results. We study the relation of the [CII]-deficit, i.e., the drop of the [CII]/FIR intensity ratio caused by stellar activity, within individual HII regions, as well as of entire star forming molecular clouds. We find that, in young HII regions, the [CII]-deficit is mainly caused by the strong FIR emission produced by hot and dense dust, and the contemporary saturation of the [CII] line. In more evolved HII regions, the main cause of the deficit is the second ionization of carbon. The [CII]/FIR ratio integrated over entire clouds decreases for increasing total stellar luminosity. We show that this correlation can be fitted with a power-law. The relation found breaks when the total FIR luminosity starts decreasing as an effect of the cloud dispersal caused by stellar feedback. This happens in evolved clouds. In general, the aspect of HII regions in MCs strongly depends on the geometry of the cloud, and on the line of sight. A certain HII region can have significantly different properties when observed from different lines of sight.

Key words:

1 INTRODUCTION

Molecular clouds (MCs) are the densest regions of the insterstellar medium (ISM) and, as the name suggests, they are defined as those regions where hydrogen exists mainly in molecular form. Such environments are also the regions where dense cores and stars form. The formation and evolution of MCs has been studied with numerical simulations in a large number of recent works (see e.g. the reviews by Chevance et al. 2022; Henshaw et al. 2022; Hacar et al. 2022, and references therein).

The life-cycle of MCs is complex. Essentially, the gas first undergoes a collapse phase, which creates very dense cores within the molecular gas. Part of the mass of such cores, by further collapsing, creates stars. Once stars have formed, they exert feedback on the MC they are embedded in. Such feedback ultimately has the effect of dispersing the cloud. The three most important forms of stellar feedback are supernova explosions, stellar winds, and ionizing radiation. For details on the life-cycle of MCs we refer, for instance, to the review by Chevance et al. (2020) and references therein. In particular, ionizing radiation has two main effects on the cloud. First of all, it mechanically contributes to the cloud dispersal as it determines a decrease of the density of the cloud in proximity of the star formation sites. As a consequence, this also inhibits further star formation, contributing to the low star formation efficiency generally observed

(e.g. Krumholz et al. 2014). Besides this, photons emitted by stars dissociate or ionize the surrounding medium. A first theoretical study of this phenomenon, performed by Strömgren (1939) showed that, under the assumption of uniform density and isotropic conditions, stellar radiation produces a shell where hydrogen is ionized ad the radius r of such shell is $r \propto Q_0^{1/3} n^{-2/3}$, where Q_0 is the ionizing flux and n the gas density. These portions of MCs are called *HII regions*. Later on, Spitzer (1978) calculated the expansion velocity of the ionization fronts, finding $r \propto t^{4/7}$. Besides these two fundamental works, ionizing radiation and its role in MCs have been extensively studied (Hosokawa & Inutsuka 2006; Krumholz & Matzner 2009; Fall et al. 2010; Murray et al. 2010; Dale et al. 2012; Walch et al. 2012; Girichidis et al. 2016; Gatto et al. 2017; Haid et al. 2019, and many more). Although it is known that stellar feedback has dramatic effects on the evolution MCs, with profound consequences on the star formation (Naab & Ostriker 2017; Ostriker & Kim 2022) and on the structure of the cloud (Haid et al. 2019), the relative importance of the different feedback sources is still controversial, especially in relation to the competition between ionizing radiation and stellar winds (Geen et al. 2020; Ali et al. 2022, for instance).

One of the brightest emission lines originating from star-forming regions is the [CII] line at 157.7 μm (e.g. Stacey et al. 1991; Brauher et al. 2008): indeed, it is one of the main coolants in MCs and in the ISM in general (Tielens & Hollenbach 1985; Stacey et al. 1991; Hollenbach & Tielens 1999; Stutzki 2001; Röllig et al. 2006; Wolfire et al. 2003; Ossenkopf et al. 2013; Beuther et al. 2014; Pineda et al.

---

[*] E-mail: ebagezio@ph1.uni-koeln.de

2013, 2014; Klessen & Glover 2016). The [CII] emission line has been extensively observed in HII regions (Schneider et al. 2012; Goicoechea et al. 2015; Röllig et al. 2016; Pabst et al. 2017, 2020; Tiwari et al. 2021; Luisi et al. 2021; Beuther et al. 2022; Kabanovic et al. 2022), generally highlighting a bubble structure with very little emission from the inner part and bright rims.

Besides the [CII] line, the far infrared (FIR) dust continuum emission is also a meaningful quantity to understand HII regions, as it is intimately associated with stellar activity, as shown in numerous recent studies (Brauher et al. 2008; Graciá-Carpio et al. 2011; De Looze et al. 2011; Casey et al. 2014; Herrera-Camus et al. 2018; Pabst et al. 2022; Dunne et al. 2022; Bisbas et al. 2022, and many more).

The ratio between [CII] and FIR emission is of particular interest for understanding stellar feedback in MC. In general, such ratio is of of the order of $10^{-2} - 10^{-3}$ in the ISM, but decreases with increasing infrared luminosity (Malhotra et al. 1997; Luhman et al. 1998; Malhotra et al. 2001; Luhman et al. 2003; Casey et al. 2014). This phenomenon is called the "[CII]-deficit" and there are different hypotheses about its origin, including AGN contributions to FIR emission (Sargsyan et al. 2012), further ionization of C^+ into C^{2+} (Abel et al. 2005), and fine-structure lines overcoming [CII] as coolants (Luhman et al. 2003, for instances) , and saturation of the [CII] line (Muñoz & Oh 2016; Rybak et al. 2019). Relations between the [CII]-deficit and the star formation rate (SFR) have also been proposed, both under a theoretical (Narayanan & Krumholz 2017) and observational (Stacey et al. 2010; Smith et al. 2017; Hu et al. 2019) point of view. Furthermore, some recent observational works, for instance those of Goicoechea et al. (2015) and Pabst et al. (2021), analyse the relation between [CII] and FIR emission on MC scales, inspecting the properties of the clouds which can be inferred by these observables.

This work aims to provide a simulation counterpart to such observations, enabling comparisons between real and simulated data, as well as to take advantage of the knowledge of the simulation input to give more detailed insights on the physical phenomena which cause the [CII]-deficit. The paper is organised as follows. In Section 2 we present the numerical simulations of the MCs which serve as basis for the analysis, as well as the post-processing and analysis techniques that we use. Next, in Sec. 3 we describe our results: we first investigate the dust temperature sey by the heading of nearby stars, before we present our [CII] and FIR emission maps. This enables us to calculate their ratio, i.e., to analyse the phenomenon of the [CII]-deficit: we first look at its radial dependence from the stars which create HII regions and then consider the global behavior in the entire clouds. These results are discussed in Sec. 4, where we investigate more in detail the cause of the [CII]-deficit, and compare this with real observational data. Furthermore, we highlight the role played in this context by projection effects. In Sec. 5 we summarise our work and draw our conclusions.

2 NUMERICAL METHODS

This work is a further analysis of the simulations described in Ebagezio et al. (2022), unless differently specified. Therefore, we refer to this paper for a detailed description of the numerical simulations, the post-processing routines, and the radiative transfer. Here, we summarize briefly the most important concepts and describe the differences and the processes which are not present in the aforementioned work.

2.1 SILCC-Zoom simulations

The simulated MCs that we use in this work are part of the SILCC-Zoom Project (Seifried et al. 2017). This consists of zoom-in simulations of specific regions of the larger-scale simulations within the SILCC project (see Walch et al. 2015; Girichidis et al. 2016, for details).

The SILCC Project aims to simulate the life-cycle of molecular clouds in typical solar neighborhood conditions. To do so, it models a region of a stratified galactic disc of 500 pc × 500 pc × 5 kpc in size using the adaptive mesh refinement code FLASH 4.3 (Fryxell et al. 2000; Dubey et al. 2008). The maximum allowed resolution is 3.9 pc. Both hydrodynamics (HD) and magnetohydrodynamics (MHD) runs are simulated within the project. The chemistry is modelled using a chemical network for H^+, H, H_2, C^+, O, CO, and e^- (Nelson & Langer 1997; Glover & Mac Low 2007a,b; Glover et al. 2010), also including the most important heating and cooling processes of the gas. This chemical network is applied *on-the-fly* in the simulations, i.e., the chemistry is evolved together with the hydrodynamical evolution. In Ebagezio et al. (2022) we showed that having an *on-the-fly* chemical network permits to obtain significantly more accurate chemical abundance respect to post-processed chemical networks which assume chemical equilibrium, in agreement with findings, for instance, of Glover & Mac Low (2007b); Seifried et al. (2017); Hu et al. (2021); Seifried et al. (2022). We assume solar metallicity, corresponding to an elemental abundance of carbon and oxygen of 1.4×10^{-4} and 3.16×10^{-4}, respectively, relative to total hydrogen. The interstellar radiation field (ISRF) is set to $G_0 = 1.7$ in Habing units (Habing 1968) and the cosmic ray ionization rate to CRIR = 3×10^{-17} s^{-1} with respect to atomic hydrogen. We also consider the attenuation of the ISRF using TreeCol (Wünsch et al. 2018). The magnetized runs also have a magnetic field $\boldsymbol{B}$ initialized to be parallel to the x-direction with an amplitude of $B_{x,0} = 3$ μG in the galactic plane. The dust-to-gas ratio is fixed to be 1/100 everywhere in the simulations. We refer to Walch et al. (2015) for further details concerning the initial conditions.

At the beginning of the SILCC simulations and up to a given time t_0 (see Table 1), supernovae explosions drive turbulence. At t_0, further explosions are stopped and local overdensities are already visible. At this point, some of these overdensity regions are chosen and the zoom-in (i.e., those which are part of the SILCC-Zoom project) simulations are continued in such regions allowing for a resolution up to 0.12 pc. In this paper we use two HD and two MHD clouds. We refer to them as MC1-HD, MC2-HD, MC1-MHD, and MC2-MHD, respectively (see Table 1). All runs include stellar feedback. We use sink particles to model the formation and evolution of stars and refer to Federrath et al. (2010); Gatto et al. (2017) for more details. The radiative feedback relative to each star is treated with TreeRay (Wünsch et al. 2018; Haid et al. 2019; Wünsch et al. 2021). We note that our stellar feedback includes stellar radiation, but not stellar winds. We plan to run simulations including stellar winds in the next future.

2.2 Chemical post-processing

Before the actual synthetic emission maps are produced, we post-process the data in order to model physical phenomena which are not included in the simulation itself. In particular, we include: (i) CO freeze-out, (ii) splitting of H_2 into para- and ortho-H_2, (iii) microturbulence, (iv) $C^+ \rightarrow C^{2+}$ thermal ionization, and (v) $C^+ \rightarrow C^{2+}$ ionization in regions affected by stellar feedback as a consequence of stellar radiation. We use the pipeline developed by Pierre C. Nürn-

Table 1. Overview of the simulations and snapshots used in this paper: run name, start time of the zoom-in, t_0, run type (purely hydrodynamical, HD, or magnetohydrodynamical, MHD), and time $t_{\rm evol} = t - t_0$ when synthetic emission maps are produced.

run name	t_0 [Myr]	run type	$t_{\rm evol}$ [Myr]
MC1-HD	11.9	HD	2, 3, 4
MC2-HD	11.9	HD	2, 3, 4
MC1-MHD	16.0	MHD	3, 4, 5
MC2-MHD	16.0	MHD	3, 4, 5

berger[1] As pointed out in Ebagezio et al. (2022), the non-thermal ionization has a large impact on the abundance of C^+ within the HII regions that stars create and, as a consequence, also on the synthetic [CII] maps of those regions. It is thus essential to operate this post-processing in order to accurately model the [CII] within the HII regions.

For this purpose, we sample the gas density, gas temperature, star temperature, and ionizing flux over the typical ranges occurring in our simulations, and for each possible parameter combination we build a PDR model with CLOUDY (Ferland et al. 2017), from which we obtain the fractional abundance of C^+ that takes into account the $C^+ \rightarrow C^{2+}$ ionization and then replace the original abundance given by FLASH. More details on this post-processing routine are provided in Ebagezio et al. (2022).

2.3 Radiative transfer

We use the RADMC-3D (Dullemond et al. 2012) code to do the radiative transfer calculations of the simulated clouds and to obtain synthetic emission maps. RADMC-3D is an open-source, 3D radiative transfer code, capable of performing both line and dust continuum radiative transfer calculations. In this work, we use it to obtain synthetic emission maps of the [CII] 158 μm line and of FIR emission between 3 and 1100 μm. We define t as the simulation time since the very beginning of the SILCC simulations and $t_{\rm evol}$ as $t_{\rm evol} = t - t_0$. We consider the evolutionary stages at $t_{\rm evol} = 2, 3$, and 4 Myr for the HD simulations, and $t_{\rm evol} = 3, 4$, and 5 Myr for the MHD simulations as the MHD clouds generally evolve somewhat slower (Seifried et al. 2020; Ebagezio et al. 2022). Table 1 gives an overview of the simulations and the $t_{\rm evol}$ at which the synthetic emission maps produced. All emission maps are produced for lines of sight (LOS) along the x-, y-, and z-axis. Furthermore, for MC1-HD and MC2-HD we produce maps at intervales of 100 kyr along the z-axis. We will use these highly time-refined emission maps in Section 3.4 in order to better study the evolution of the considered characteristics.

2.3.1 Line radiative transfer

In order to accurately model the [CII] line emission with RADMC-3D, we include microturbulence assuming that microturbulent broadening is as strong as the thermal broadening (see Ebagezio et al. 2022, Section 3.1, for details). Furthermore, we use the Large Velocity Gradient (LVG) approximation (Ossenkopf 1997; Shetty et al. 2011a,b) to calculate the level population. We consider 201 equally spaced velocity channels for a velocity range of ± 20 km s^{-1} around the [CII] rest frequency, which results in a spectral resolution of

---

[1] https://astro.uni-koeln.de/walch-gassner/downloads/flashpp-pipeline

d$v = 0.2$ km s^{-1}. This velocity range and spectral resolution enable us to capture the contribution of Doppler-shifted emission (Franeck et al. 2018). As we us the LVG approximation, we need to specify the collisional rates for C^+. For this, we rely on the Leiden Atomic and Molecular DAtabase (LAMDA, Schöier et al. 2005). We consider para-H_2, ortho-H_2, H, and e^- as collisional partners for C^+. We also model the effect of the Cosmic Microwave Background (CMB) by assuming a background black body radiation at $T = 2.725$ K (Fixsen 2009). Such temperature corresponds to a brightness temperature of

$$T_{\rm B,CMB} = \frac{h\nu_0}{k_B} \frac{1}{e^{h\nu_0/k_B T} - 1} \, , \tag{1}$$

where ν_0 is the [CII] rest frequency, h the Planck constant, and k_B the Boltzmann constant. We obtain $T_{\rm B,CMB} \simeq 2.8 \times 10^{-13}$ K, which is many orders of magnitude lower than the obtained [CII] intensities, The contribution of the CMB to the [CII] emission maps is therefore negligible. At most, it gives a slight contribution to the level population of C^+.

2.3.2 Dust continuum radiative transfer

In order to calculate the dust continuum emission, the dust temperature $T_{\rm d}$ must be known. The FLASH simulation data contain information about dust temperature, but this is calculated by considering only the external radiation field (ISRF), and not the effect of stars. Therefore, in a first step we use RADMC-3D to calculate the dust temperature resulting from the presence of stars. In a second step, we consider, for each simulation cell, the maximum between the dust temperature given by FLASH and the one given by RADMC-3D. In this way, we properly consider both effects in our $T_{\rm d}$ calculation.

RADMC-3D calculates the dust temperature using a Monte Carlo method described in Bjorkman & Wood (2001) with the continuous absorption method of Lucy (1999). In order to do so, information on absorption and scattering coefficients for different wavelengths are needed. These coefficients depend mainly on the chemical composition and size of the grains. In general, the extinction coefficient κ is roughly $\kappa \propto \lambda^{-2}$ at long wavelengths, but varies significantly at shorter wavelengths. We use the coefficients from Weingartner & Draine (2001), which aim to model a mixture of carbonaceous and silicate grains typical of solar neighborhood conditions. The total stellar luminosity is divided by RADMC-3D in a variable number of photon packages, which can be set by the user. Such photon packages are emitted by the stars one-by-one and may scatter off dust grains and thus change their direction, as well as get absorbed by the dust. If that happens, the photon package is immediately re-emitted in another direction and with another wavelength. This calculation is done assuming that dust is in chemical equilibrium, i.e., that the energy absorbed equals the energy released: this is normally a very good approximation, as the typical dust heating and cooling processes are very fast compared to the other time scales of the system, but in extreme cases, like in the vicinity of shock waves or in very optically thick regions, this assumption might no longer be appropriate (Bjorkman & Wood 2001).

We perform a convergence study in order to determine the appropriate number of photon package to use. To do so, we consider MC2-HD at $t_{\rm evol} = 4$ Myr, as this is the snapshot which contains the largest number of stars. Because of this, the number of photons that we find to be appropriate here is also appropriate for all other snapshots. In Fig. 1 we show the distribution of $T_{\rm d}$ (calculated by RADMC-3D) for different numbers of photon packages. We note that with a low number of photon packages ($10^5 - 10^6$) the distribution is clearly not yet converged, whereas the distributions for 10^9

4   *S. Ebagezio et al.*
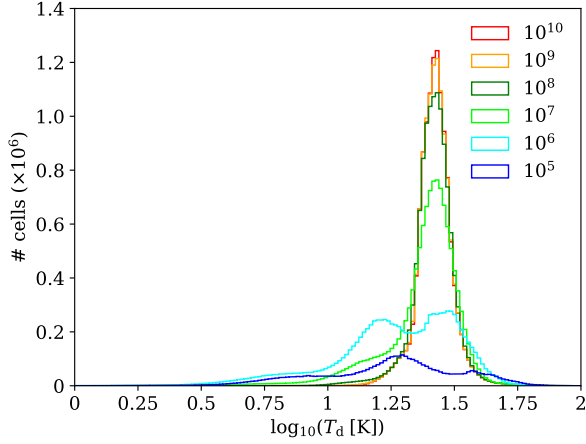
Figure 1. Dust temperature distribution calculated with RADMC-3D of MC2-HD at $t_{\rm evol} = 4$ Myr for different numbers of photon packages. Differences between the distribution for 10^9 and 10^{10} photon packages are less than 1 per cent for all dust temperature bins, therefore we choose to use 10^{10} photon packages for all dust temperature calculations.

and 10^{10} photon packages are almost identical (they vary for less than 1 per cent). We thus choose to use 10^{10} photon packages in the Monte Carlo dust temperature calculation.

Once the dust temperature is calculated, we use RADMC-3D to calculate the FIR dust continuum emission. We produce maps of 101 wavelengths between 3 and 1100 μm, equally spaced in logarithmic space. We then compute the integrated FIR luminosity by integrating in the range $40 - 500$ μm as this is used in different observational works (e.g. Sanders & Mirabel 1996; Goicoechea et al. 2015; Pabst et al. 2021), allowing us a straightforward comparison with observations. Even if we do not use the maps produced at $\lambda < 40$ μm and $\lambda > 500$ μm in this work, we save those data and have them available for future work.

3 RESULTS

3.1 Dust temperature

We first analyse the dust temperature $T_{\rm d}$ of our molecular clouds. This is important in order to understand the characteristics of the FIR continuum that we will analyse later on. In Fig. 2 we show 4 examples of $\langle T_{\rm d} \rangle$ maps. Specifically, we show the mass-weighted average $\langle T_{\rm d} \rangle$ along the line of sight (LOS). The 4 snapshots correspond to different stages of star formation in MCs. Moving from top left to bottom right, we show snapshots with progressively longer star formation times and thus also higher numbers of formed stars. In general, $\langle T_{\rm d} \rangle \simeq 15$ K in regions not affected by stellar feedback, and $\langle T_{\rm d} \rangle \lesssim 50$ K in regions where stellar feedback is relevant. Feedback-affected regions are confined to a small area of a few pc when star formation has set in recently (≤ 1 Myr), and are extended to a large portion of the cloud (a few 10 pc) when star formation has set in for a few Myr and several massive stars have been formed. We emphasize that the actual dust temperature in vicinity of stars can be considerably larger than $\langle T_{\rm d} \rangle$. Indeed, the maximum $T_{\rm d}$ we obtain in our simulations is $T_{\rm d} \simeq 220$ K: LOS effects significantly reduce the observed range of dust temperatures.
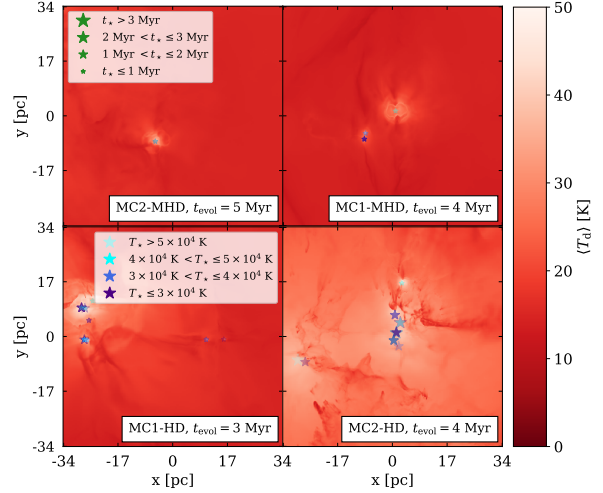
Figure 2. Maps of the mass-weighted dust temperature average, $\langle T_{\rm d} \rangle$, along the LOS for 4 snapshots of the simulated clouds. We show, from top left to bottom right, MCs with progressively longer star formation time. We overplot the stars present in the simulations, where the size and color indicate the age and temperature of the star. In general, regions not affected by stellar feedback have $\langle T_{\rm d} \rangle \simeq 15$ K, and regions where stellar feedback is important have $\langle T_{\rm d} \rangle \simeq 50$. These regions are small (a few pc) and limited to the vicinity of the stars in the early stages of star formation (e.g. MC2-MHD, top left), but involve larger parts of the cloud (a few 10 pc) on a later stage (e.g. MC2-HD, bottom right).

3.2 [CII] and dust continuum emission maps

In this section, we analyse the [CII], the FIR maps and the [CII]/FIR ratio. We show that this ratio is particularly low in regions affected by star formation, and we highlight two different mechanisms which lead to this low ratio. We show in Fig. 3 two examples of such maps. The left column contains the [CII] moment 0 maps, $I_{\rm [CII]}$, the central column contains the FIR intensity, $I_{\rm FIR}$, maps, and the right column shows $I_{\rm [CII]}/I_{\rm FIR}$. Stars are overlaid on the figure with the same size and color coding as in Fig. 2. The top row corresponds to MC2-MHD at $t_{\rm evol} = 5$ Myr and the bottom row corresponds to MC2-HD at $t_{\rm evol} = 4$ Myr.

The [CII] maps (left column) are, in general, characterized by $I_{\rm [CII]} \sim 10^{-6}$ erg s^{-1} cm^{-2} sr^{-1} in the diffuse regions (external parts of the maps), and much brighter regions ($I_{\rm [CII]} \gtrsim 10^{-4}$ erg s^{-1} cm^{-2} sr^{-1}) in dense regions, i.e., in the central parts of the maps. Furthermore, MC2-HD also shows a central region with low [CII] emission, surrounded by bright rims. The FIR maps (central column) show bright, localized spots with $I_{\rm FIR} \gtrsim 1$ erg s^{-1} cm^{-2} sr^{-1}, and more diffuse areas (a few pc in MC2-MHD, a few 10 pc in MC2-HD) with moderate emission ($\sim 10^{-2} - 10^{-1}$ erg s^{-1} cm^{-2} sr^{-1}), surrounded by regions with very little emission.

We focus, now, on specific regions of these maps and aim to highlight the different properties of the [CII]/FIR ratio. Concerning the top row, we note there that the area close to the central star is very bright in FIR ($\simeq 5$ erg s^{-1} cm^{-2} sr^{-1}), which is approximately three orders of magnitude above the values obtained for the surrounding cloud. Conversely, $I_{\rm [CII]}$ in that area is only larger of a factor of a few than in the rest of the dense filament (the [CII]-bright T-shaped structure) of MC2-MHD. As a result, $I_{\rm [CII]}/I_{\rm FIR}$ drops in the vicinity of the central star.

A similar behaviour can be noted in proximity of the stars at the
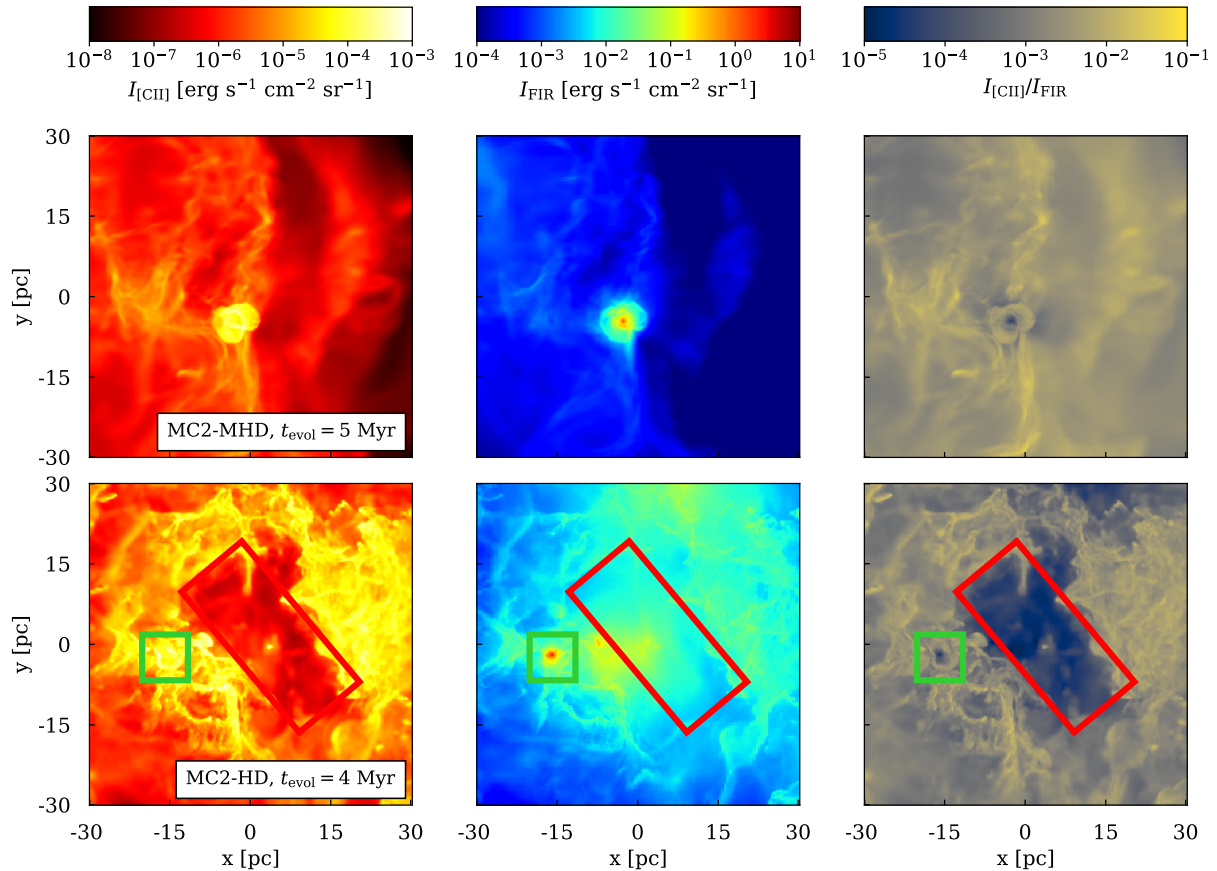
Figure 3. Emission maps of $I_{[CII]}$ and I_{FIR}, and maps of $I_{[CII]}/I_{FIR}$, for MC2-MHD, t_{evol} = 5 Myr (top), and MC2-HD, t_{evol} = 4 Myr (bottom). In the HII regions located in the center of MC2-MHD and in the region highlighted with a green rectangle in MC2-HD, the low [CII]/FIR ratio is mostly due to the high I_{FIR}. Conversely, the red rectangle highlights a more developed HII region, where the [CII]-deficit is mainly caused by the C+ → C²⁺ ionization due to stellar radiation.

left side of MC2-HD (bottom row, green rectangle), where again $I_{[CII]}$ is comparable to the emission coming from the neighboring regions, and I_{FIR} is significantly higher. Again, this leads to a lower $I_{[CII]}/I_{FIR}$ in that area than in the rest of the cloud. Overall, however, $I_{[CII]}$ in MC2-HD is roughly an order of magnitude higher than in MC2-MHD. This is likely due to the excitation determined by radiation coming from the other stars of the cloud (see Section 3.3).

In the central part of MC2-HD (red rectangle) there is another region, corresponding to an evolved HII region, with low $I_{[CII]}/I_{FIR}$. Unlike for the other two aforementioned regions, here this low ratio is due to the lack of [CII] emission coming from the HII region, and not to the enhancement of I_{FIR}. Indeed, we only note a moderately enhanced FIR emission, of the order of a few 10^{-1} erg s^{-1} cm^{-2} sr^{-1}, in the vicinity of stars, and the rest of the highlighted region is not distinguishable in FIR with respect to the other parts of the cloud. This is due to the ionising radiation coming from the more evolved, bright stars in the central part of the highlighted area, which sweep up the surrounding area, reducing therefore the total column density. This means that even though $\langle T_d \rangle$ is large in that area (see Fig. 2, bottom-right plot), I_{FIR} is relatively low. Furthermore, $I_{[CII]}$ is very faint in this area ($\simeq 10^{-6}$ erg s^{-1} cm^{-2} sr^{-1}, comparable to the emission coming from the surrounding medium), not only due

to the aforementioned sweep-up, but mainly as a consequence of the second ionization C$^+$ → C^{2+} determined by stellar radiation (see Ebagezio et al. 2022, for details). The [CII] intensity in this region would be, indeed, significantly higher if we excluded the post-process for the second ionization of carbon.

We claim that the mechanisms listed above are general features of [CII]/FIR ratio in HII regions: at early stages, it occurs at small scales because of the enhancement in I_{FIR} in regions with newly formed stars. At later stages, and thus in more evolved HII regions, it involves larger scales and is mainly due to the further ionization of C$^+$. In order to investigate this more in detail, we now analyse the $I_{[CII]}/I_{FIR}$ ratio systematically in all HII regions that we have in our simulated clouds.

3.3 [CII]-FIR ratio within HII regions

In this section we study $I_{[CII]}$, I_{FIR}, and $I_{[CII]}/I_{FIR}$ as a function of distance from the center of the HII regions in order to analyse radial trends of the [CII]-FIR ratio and their possible dependence on the age of the HII regions and on the kind of stellar population which create them.

In Fig. 4 we show an example of the procedure we follow. The top
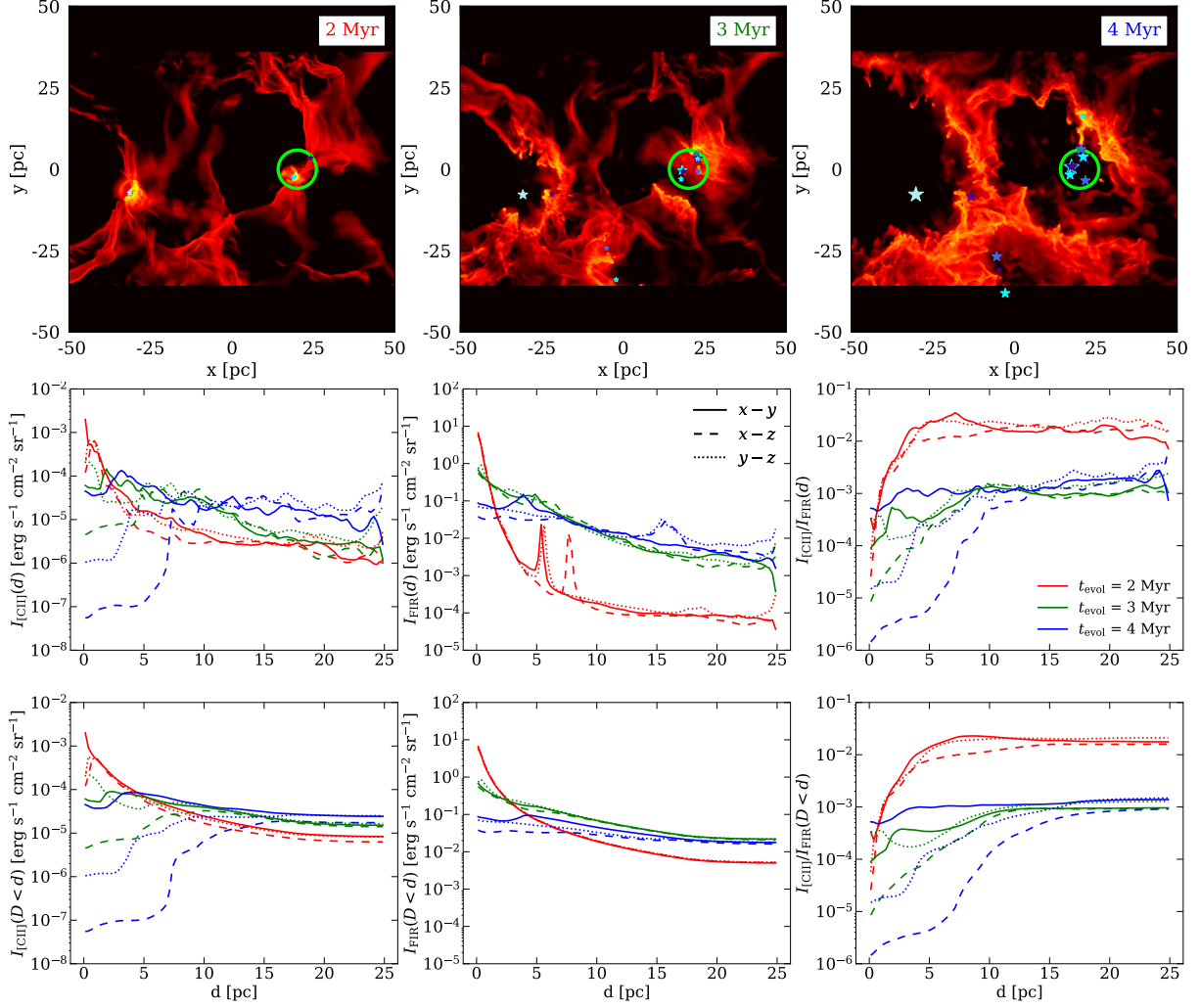
Figure 4. *Upper row*: maps of $I_{\rm [CII]}$ for MC2-HD ($x - z$ plane) at $t_{\rm evol} = 2$, 3, and 4 Myr (from left to right). Stars are represented using the same symbols as in Fig. 2. The green circles represent the region inspected in the central and bottom rows. *Middle row:* $I_{\rm [CII]}$, $I_{\rm FIR}$, and $I_{\rm [CII]}/I_{\rm FIR}$ as a function of the distance d from the main star of the HII region highlighted by the green circles in the upper row. Solid, dashed, and dotted lines represent the values for the $x - y$, $x - z$, and $y - z$ planes, respectively. *Bottom row:* same as in middle row, but the values plotted are an average of all the points with distance $D < d$, instead of the average of a single distance bin centered in d.

row shows, from left to right, the [CII] emission map of MC2-HD at $t_{\rm evol} = 2$, 3, and 4 Myr, respectively, in the $x - z$ plane. The star symbols have the same meaning as in Fig. 2. We highlight with a green circle the HII regions we are interested in. The middle row shows, from left to right, $I_{\rm [CII]}$, $I_{\rm FIR}$, and $I_{\rm [CII]}/I_{\rm FIR}$ as a function of the distance from the center of the bubble: we define the origin of our system as the position of the "main" star of the HII region and we construct a number of radial bins. The "main" star is defined as the hottest star in the oldest sink particle associated with the HII region. This definition is motivated by the consideration that the size of the bubble is mainly determined by the time available for the expansion (this is the reason why we choose the oldest sink) and that the hottest star produces the most of the radiation. We point out, however, that such "main" stars may not be the stars which constitute the main source of ionizing radiation for all cells in their HII regions. This can happen when a bright star forms later on. Furthermore, it has been

recently shown that the hottest and brightest stars may even not be associated with the largest bubbles in a MC in presence of significant density gradients (Beilis et al. 2022). Hence, our definition of a main star mainly is useful to define the center of each bubble and to characterize it. In the central row, the values shown are averages on the radial bins. The bottom row shows the same quantities, but for each distance bin we average over all the pixels at a distance $D \leq d$:

$$I(D < d) = \frac{1}{N} \sum_{i=1}^{N} I_i \,, \tag{2}$$

where the sum is run over all pixels located at a distance $D \leq d$. Solid, dashed, and dotted lines represent the calculation performed on the $x - y$, $x - z$, and $y - z$ planes, respectively.

We note, by looking both at the emission maps (Fig. 3) and at the $I_{\rm [CII]}(d)$ plot (Fig. 4, middle row), that at an early evolutionary stage

$I_{\rm [CII]}$ decreases uniformly with increasing d. When going to later evolutionary stages, $I_{\rm [CII]}$ is low at small d (a few pc), then rapidly increases and eventually slightly decreases again at large d. This is a direct consequence of the expansion of the HII regions with time, as well as of the further ionization of C^+ inside such regions (lowering $I_{\rm [CII]}$) and its high excitation in the rims (enhancing $I_{\rm [CII]}$). The distance within which such a lack of [CII] is observed depends not only on the age of the HII region, but also on the LOS considered (see e.g. the various blue lines for $t_{\rm evol} = 4$ Myr). We will discuss this aspect in more detail in Section 4.4.

The FIR intensity ($I_{\rm FIR}$, central panel of middle row) at early evolutionary stages is very high, reaching ~ 0.1 erg s^{-1} cm^{-2} sr^{-1}, in proximity of the formed stars and then rapidly decreases with increasing d due to the colder and less dense medium. At later stages, the dust density is less peaked around the star and hotter at large distance due to the presence of other stars: this turns out in a less pronounced (but still existing) decreasing trend of $I_{\rm FIR}$ with increasing d. The additional peaks in $I_{\rm FIR}$ (those at $d = 5 - 7$ pc) are due to other neighbouring stars.

The features of $I_{\rm [CII]}$ and $I_{\rm FIR}$ together lead to a $I_{\rm [CII]}/I_{\rm FIR}$ overall progressively increasing with d. Such increase is sharp at early stage, reaching a roughly constant value of $\simeq 10^{-2}$ at $d \simeq 5$ pc. At later stages, we find a central region where $I_{\rm [CII]}/I_{\rm FIR}$ spans between $\lesssim 10^{-3}$ and $\sim 10^{-6}$, depending on the snapshot and the LOS, followed by an increase up to values of $\simeq 10^{-3}$. These are consequences of the lack of [CII] inside the HII region and of the enhanced $I_{\rm FIR}$ in the part of the cloud surrounding it, respectively.

The profiles of $I_{\rm [CII]}$, $I_{\rm FIR}$, and $I_{\rm [CII]}/I_{\rm FIR}$ averaged over areas with $D \leq d$ (bottom row of Fig. 4) follow approximately the same trend as those averaged in radial bins. This is due to the fact that, in the averaging process, the outer bins contribute with more points than the inner bins as they contain more pixels. However, really high values in the inner bins can still lead to values at high d much larger than those obtained by averaging in radial bins (this is the case, for instance, of $I_{\rm FIR}$ at $t_{\rm evol} = 2$ Myr).

The behavior of $I_{\rm [CII]}$, $I_{\rm FIR}$, and $I_{\rm [CII]}/I_{\rm FIR}$ described above is referred to a specific HII region within MC2-HD. However, the same physical phenomena, namely the dust heating, the clearing of the HII regions due to ionizing radiation, the C^+ excitation and ionization, produce similar trends in the other HII regions as well. Differences in stellar population and surrounding environment produce, however, quantitative differences among different HII regions.

For this reason, in Fig. 5 we now show $I_{\rm [CII]}/I_{\rm FIR}$ as a function of d for all HII regions identified in our simulations. Each bubble is characterized by a different stellar population. For each snapshot, we identify the main star of the HII region with the procedure described above. Table 2 presents the association of each snapshot with the corresponding main star. In the table, the temperature $T_\star$ and the age $t_\star$ of the main star at each snapshot are also shown. Comparing this table with the $I_{\rm [CII]}/I_{\rm FIR}$ plots in Fig. 5 we identify the following results:

- At small d, $I_{\rm [CII]}/I_{\rm FIR}$ drops, as we anticipated already in Fig. 4, to very small values. The lowest reached values, however, is not dependent on the main star temperature: for instance, in their earliest snapshot in MC1-MHD, bubbles 2 and 3 have the lowest $I_{\rm [CII]}/I_{\rm FIR}$ equal to 10^{-4} and 10^{-6}, respectively, but very similar star temperatures. Vice versa, both MC1-HD, bubble 1, and MC2-HD, bubble 2 reach $I_{\rm [CII]}/I_{\rm FIR} \simeq 10^{-5}$, but the main star temperatures are of about 2.8×10^4 and 4.6×10^4 K, respectively. The spatial extension of the low $I_{\rm [CII]}/I_{\rm FIR}$ regime is somewhat related, at early evolutionary stages, to the extension of the ionization front of the HII region. This

Table 2. Cloud name and bubble name, evolutionary time, as well as the temperature and age of the main star (see main text for its definition) for all bubbles and snapshots analysed. The main star is defined as the most luminous (therefore also the hottest) star within the oldest sink particle in a given bubble.

cloud	bubble	$t_{\rm evol}$ [Myr]	$T_\star$ [Myr]	$t_\star$ [Myr]
MC1-HD	1	2	27853	0.139
		3	46064	0.956
		4	45988	1.956
MC1-HD	2	3	25552	0.150
		4	42959	0.734
MC1-HD	3	4	33551	0.310
MC2-HD	1	2	50137	0.317
		3	51357	1.317
		4	53643	2.317
MC2-HD	2	2	45983	0.152
		3	44513	1.152
		4	44202	2.152
MC1-MHD	1	4	39970	0.276
		5	40934	0.965
MC1-MHD	2	4	39498	0.330
		5	38795	1.330
MC1-MHD	3	4	40115	0.924
		5	39391	1.924
MC2-MHD	1	5	40085	0.33

does not hold at later stages, where the ionizing radiation permeates large portions of the cloud.

- A robust relation between stellar age and $I_{\rm [CII]}/I_{\rm FIR}$ is not recognisable. We can associate, in some cases, a very low [CII]/FIR ratio with particularly young stars: this is the case, for instance, in MC2-HD, bubble 2, or MC1-HD, bubble 1. Also, HII regions at later stages have in general a higher $I_{\rm [CII]}/I_{\rm FIR}$ at small d as the dust density, and thus the FIR intensity, is lower (see the discussion above). In any case, we cannot determine, for a given stellar temperature, an reliable relationship between $I_{\rm [CII]}/I_{\rm FIR}$ and $t_\star$. Moreover, we do not fine a clear correlation between $I_{\rm [CII]}/I_{\rm FIR}$ and the luminosity of the main star nor the local column density evaluated within a radius of 2 pc.

- The low [CII]/FIR ratio extending up to a radius of $5 - 10$ pc shown in Fig. 3 is clearly visible only in MC2-HD, bubbles 1 and 2 and, to a smaller extent, in MC1-HD, bubble 1. These bubbles are characterized by an extremely hot star ($45\,000 - 50\,000$ K) and a large number of stars in the HII region. This causes an extended HII region with a lack of [CII] emission, which is the reason of the low $I_{\rm [CII]}/I_{\rm FIR}$ ratio on such scale (Sec. 3.2). However, the geometry and the LOS from which we observe have a great impact on whether this feature is observable or not (see also Section 4.4 for a more detailed discussion).

- The value of $I_{\rm [CII]}/I_{\rm FIR}$ at $d > 5 - 10$ pc depends neither on the main star temperature, nor on its age. In general, this value decreases within approximately the first Myr of an HII region's lifetime, transiting from $\sim 10^{-2}$ to $\sim 10^{-3}$. This is a consequence not only of the ionizing radiation of the main star, but also of the presence, at late stages, of numerous other stars in the investigated HII regions, as well as in other parts of the cloud. The progress in star formation

8   *S. Ebagezio et al.*
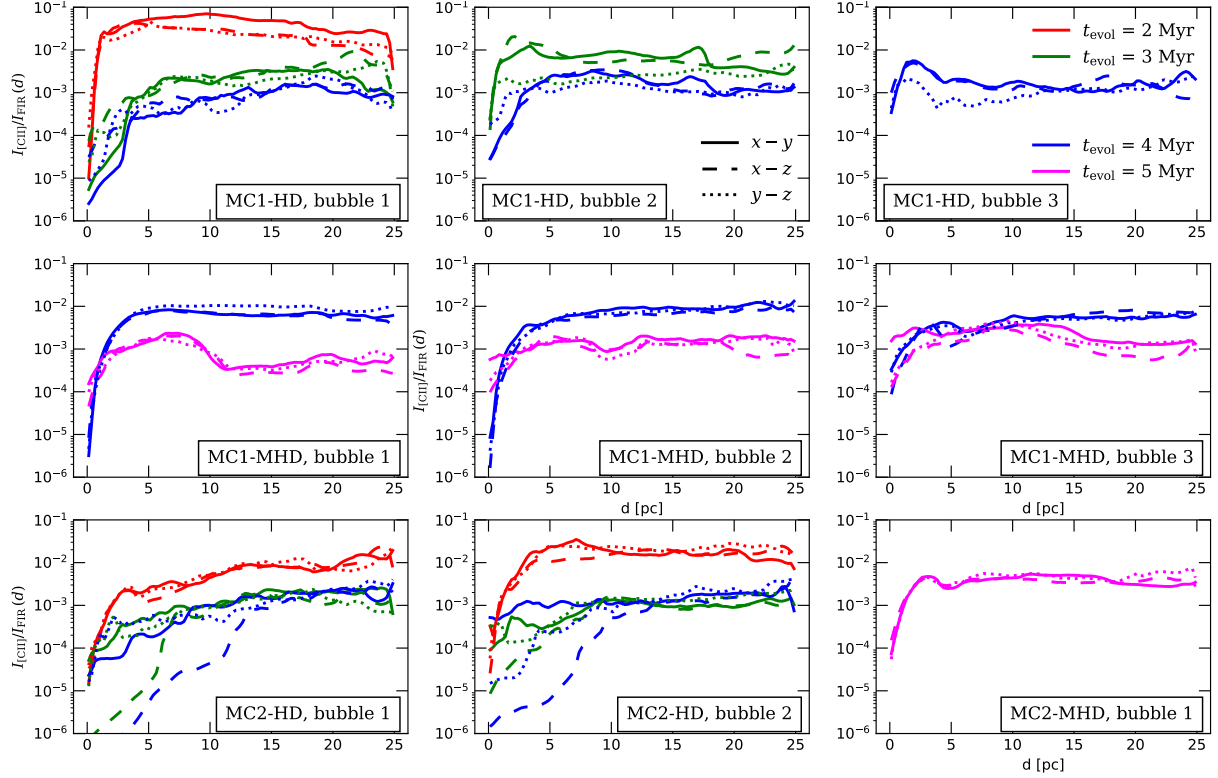
Figure 5. $I_{[CII]}/I_{FIR}$ as a function of the distance d from the main star of all HII regions in the investigated clouds. At small d, $I_{[CII]}/I_{FIR}$ drops to $10^{-6} - 10^{-4}$, depending on the regions and snapshots. At larger radii, this ratio is $\sim 10^{-2}$ at early stages, and $\sim 10^{-3}$ at later stages. The drop of this ratio at later stages is mostly due to the overall dust heating in the entire cloud determined by the various stars which have already formed.

thus leads to an increased dust heating, increasing the FIR emission and thus lowering the $I_{[CII]}/I_{FIR}$ ratio.

In Fig. 6 we show the distribution of $I_{[CII]}$ and I_{FIR} for all pixels of an image, color-coded according to the distance of the main star, motivated by the analysis of Orion A presented by Pabst et al. (2021). In all 3 panels we can identify a "main branch", characterized by a high $I_{[CII]}$ for a given I_{FIR}. At early stages ($t_{evol} = 2$ Myr), the pixels at small distance constitute the portion of this branch with largest I_{FIR} and $I_{[CII]}$. When moving to later evolutionary stages, however, the pixels at small distance are not on the "main branch" any more: they form a sort of separate branch which is located, in this diagram, below the main one.

This corresponds to the drop of the $I_{[CII]}/I_{FIR}$ ratio over time discussed before. The reasons for this are, as stated before, the stellar ionizing radiation and the consequent second ionization of carbon. The ionizing radiation disperses the cloud: therefore, the density of both dust and C^+ drop at small d, and also I_{FIR} and $I_{[CII]}$ as a consequence. The second ionization of carbon causes an extra reduction of $I_{[CII]}$, because the C^+ which is still present is converted into C^{2+}. Therefore, at small d, $I_{[CII]}$ is reduced more than I_{FIR}, and this creates the separated branch, characterized by a lower $I_{[CII]}$ for a given I_{FIR}.

The example we show in Fig. 6 is particularly evident, but for other bubbles and/or LOS we reproduce these two branches only partially. This is mostly due to projection effects (see also Sec. 4.4), i.e., to other parts of the MC located on the same LOS.

Table 3. Conversion between t_{evol} and t_{sf}. Note that for the MC1-MHD the first snapshot, at $t_{evol} = 3$ Myr, is before the onset of star formation.

cloud	t_{sf} [Myr]
MC1-HD	$t_{evol} - 1.837$
MC2-HD	$t_{evol} - 1.684$
MC1-MHD	$t_{evol} - 3.363$
MC2-MHD	$t_{evol} - 2.104$

3.4 The [CII]-deficit on molecular clouds scales

In this section we explore the relations between the [CII] and FIR luminosity in the entire clouds (which we refer to as $L_{[CII]}$ and L_{FIR}, respectively) their ratio, $L_{[CII]}/L_{FIR}$, and the time evolution of the clouds, their total mass and their total stellar luminosity.

In order to better compare different clouds, we introduce the new variable t_{sf}, defined as the time passed since the onset of star formation in a specific cloud. In this way, $t_{sf} = 0$ has the same physical meaning for all clouds, whereas t_{evol} is only a simulation parameter. Table 3 shows the relation between t_{evol} and t_{sf} for our clouds.

In Fig. 7 we show the relation of $L_{[CII]}$, L_{FIR}, and $L_{[CII]}/L_{FIR}$ with t_{sf}. The [CII] luminosity generally increases with time, as already pointed out in Ebagezio et al. (2022). This is consistent with the common usage of $L_{[CII]}$ as a star formation tracer. For MC1-HD and MC2-HD we note that, in both cases, $L_{[CII]}$ is constant at low values till the onset of star formation. Then, it increases with time.
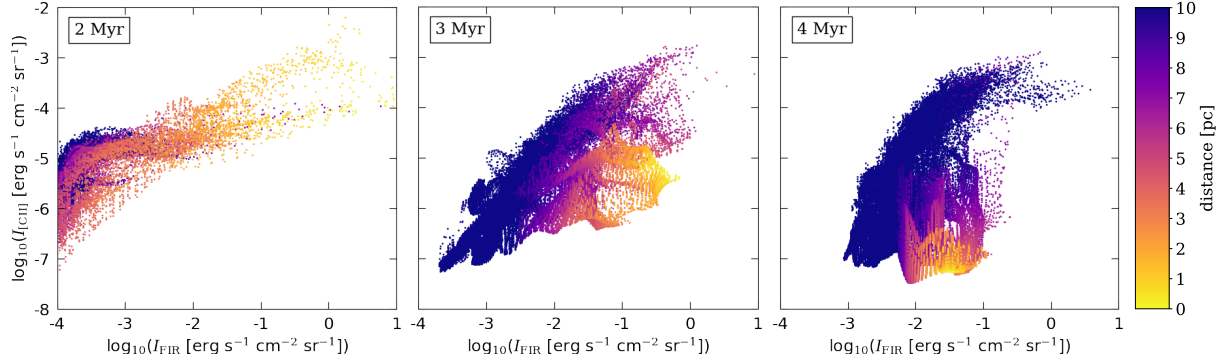
Figure 6. Distribution of $I_{[CII]}$ as a function of I_{FIR} for all pixels within 10 pc from the main star of MC2-HD, bubble 2, on the $x - z$ plane. The color bar indicates the distance from the main star. Time evolution is associated with a decrease in both $I_{[CII]}$ and I_{FIR}, leading to a clear separation, in this diagram, between a "main branch", formed by distant pixels, and a branch of close pixels, located below the main one.
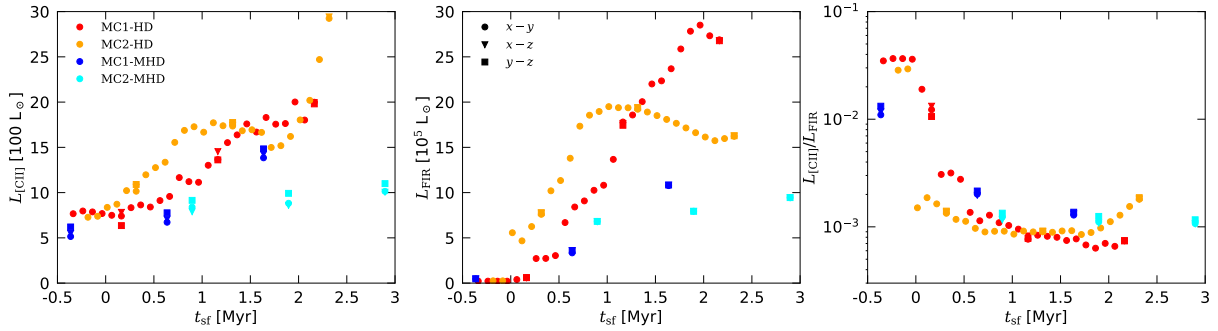
Figure 7. Evolution of $L_{[CII]}$ (left), L_{FIR} (center), and $L_{[CII]}/L_{FIR}$ (right) as a function of t_{sf}. The 4 clouds are represented with different colors and the 3 LOS with different symbols. Overall, we observe a general tendency of a decreasing $L_{[CII]}/L_{FIR}$ with increasing t_{sf}. There is, in any case, a large scatter in the values for different clouds at given t_{sf}.

The increase is monotonic for MC1-HD, with a smaller slope after $t_{sf} \simeq 1.5$ Myr. In MC2-HD, we note that $L_{[CII]}$ reaches a plateau at $t_{sf} \simeq 1$ Myr, and then slowly decreases up to $t_{sf} \lesssim 2$ Myr, when it sharply increases again. This is due to the excitation of C^+ ions in larger regions of the cloud. This diffuse excitation is possible since the stellar radiation permeates now larger portions of the cloud because of the fractal structure of the cloud. There are, in other words, low-density areas where the radiation can easily penetrate (Seifried et al. 2020, Fig. 20). A new star formation phase contributes to this late increase of $L_{[CII]}$ as well. For MC1-MHD and MC2-MHD the increase is monotonic with time, although with different slopes.

Concerning the relation between L_{FIR} and t_{sf}, we first note that it is monotonically increasing for the two MHD clouds, with different slopes in the same way we noted for $L_{[CII]}$. For both HD clouds, L_{FIR} reaches a maximum and then starts decreasing again. This maximum occurs at approximately $t_{sf} \simeq 2$ Myr for MC1-HD and approximately 1 Myr for MC2-HD. Furthermore, L_{FIR} increases again after $t_{sf} \gtrsim 2$ Myr in MC2-HD, as a consequence of the new star formation phase.

Now, we consider the $L_{[CII]}/L_{FIR}$ ratio. Due to the stronger increase of L_{FIR} compared to that of $L_{[CII]}$, this results in an initial decrease of $L_{[CII]}/L_{FIR}$ with t_{sf}, up to a roughly constant value of $\simeq 10^{-3}$, with a scatter of a factor of a few. In MC2-HD, at $t_{sf} \gtrsim 1.5$ Myr, $L_{[CII]}/L_{FIR}$ increases again and this is due to the aforementioned sharp increase of $L_{[CII]}$. Concerning MC1-HD, we note a

very slight increase of $L_{[CII]}/L_{FIR}$ for $t_{sf} \geq 2$ Myr as a consequence of the decrease in L_{FIR}.

The different behavior of the MHD clouds with respect to the HD clouds, at given t_{sf}, is due to the more rapid evolution that the HD clouds experience: magnetic fields, indeed, slow down the evolution of MCs as they act against gravitational collapse (Girichidis et al. 2018; Seifried et al. 2020; Ebagezio et al. 2022). Therefore, the entire star formation process is slower in MHD clouds than in HD clouds. As a consequence, a given t_{sf} is representative of an earlier evolutionary stage in a MHD cloud than in a HD cloud.

Next, we investigate the dependence on $L_{[CII]}/L_{FIR}$ on the total hydrogen ionization fraction. This is defined as

$$x_{H^+} = \frac{M_{H^+}}{M_{H,tot}} , \qquad (3)$$

where M_{H^+} is the total mass of H^+ in the cloud, and $M_{H,tot}$ is the total hydrogen mass. he dependence of $L_{[CII]}$, L_{FIR}, and $L_{[CII]}/L_{FIR}$ on x_{H^+} is shown in Fig. 8. Symbols and colors have the same meaning as in Fig. 7.

As a preliminary note, we point out that for each cloud t_{sf} and x_{H^+} are correlated: because of the stellar ionizing radiation, x_{H^+} increases with t_{sf}. The relations of $L_{[CII]}$, L_{FIR}, and $L_{[CII]}/L_{FIR}$ with x_{H^+} are thus qualitatively similar for each cloud to those with t_{sf}. However, the differences among the clouds are much smaller when x_{H^+}, instead of t_{sf}, is used.

We note that $L_{[CII]}$ increases with x_{H^+} up to $x_{H^+} \lesssim 10^{-1}$. Then,

10   *S. Ebagezio et al.*
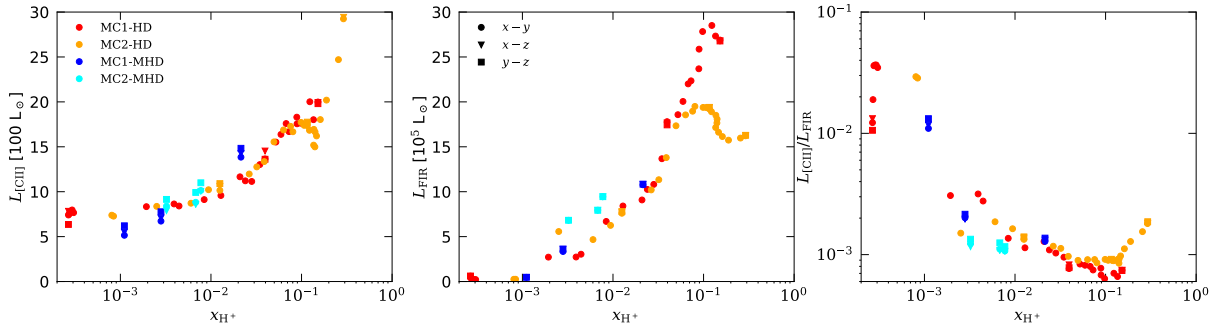
Figure 8. Same as Fig. 7, but as a function of x_{H^+}. We note a general increase of $L_{[CII]}$ with increasing x_{H^+} and a maximum in L_{FIR} at $x_{H^+} \simeq 10^{-1}$ in the two HD clouds. As a consequence, $L_{[CII]}/L_{FIR}$ decreases for increasing x_{H^+} up to this point, and then increases again.

the values for MC1-HD remain roughly constant, and for MC2-HD there is first a slight decrease followed by a sharp increase again due the excitation of the C^+ ions and the formation of new stars. The MHD clouds do not reach $x_{H^+} = 0.1$ within the simulated time.

The evolution of L_{FIR} increases with x_{H^+} up to $x_{H^+} \lesssim 10^{-1}$ as well. At that point, both MC1-HD and MC2-HD exhibit a decrease in L_{FIR}, which is then followed, in MC2-HD, by a slight increase in the last snapshots.

The evolution of $L_{[CII]}/L_{FIR}$ with x_{H^+} is qualitatively similar to the relation with t_{sf}, but now for both MC1-HD and MC2-HD the minimum of $L_{[CII]}/L_{FIR}$ is reached at a similar value of $x_{H^+} \simeq 0.1$. Furthermore, all three relations ($L_{[CII]}$, L_{FIR}, and $L_{[CII]}/L_{FIR}$ with x_{X^+}) have a significantly smaller scatter than the analogous relations with t_{sf}.

This suggests that x_{H^+} is indeed a better parameter to describe the evolution of $L_{[CII]}$, L_{FIR}, and of $L_{[CII]}/L_{FIR}$, than t_{sf}. This is due to the fact that all these quantity depend in turn on the effectiveness of stellar feedback: stellar radiation excites the C^+ ion, leading to a brighter [CII] line, heats the dust, determining more FIR emission, and ionizes hydrogen, leading to a larger x_{H^+}.

The amount of stellar feedback is determined, to some extent, by the stellar luminosity. We now define $L_{\star,tot}$ as the sum of the bolometric luminosity of all stars with a mass $M_\star > 8 M_\odot$ and we use it as the quantity to use for studying the evolution of $L_{[CII]}$, L_{FIR}, and $L_{[CII]}/L_{FIR}$. This is done in Fig. 9.

The relation of $L_{[CII]}$ with $L_{\star,tot}$ is qualitatively similar to the relations with t_{sf} and x_{H^+}: there is a first monotonic increase followed by, in the case of MC2-HD, a slight decrease and a last sharp increase. However, the values for different clouds are more scattered, for a given $L_{\star,tot}$, than in the case of x_{H^+}. The relation between L_{FIR} and x_{H^+} is similar to the ones already discussed, as well. Here, MC1-HD reaches the maximum of L_{FIR} at $L_{\star,tot} \simeq 5 \times 10^6$ $L_\odot$ and MC2-HD does so at $L_{\star,tot} \simeq 4 \times 10^6$ $L_\odot$.

The relation between $L_{[CII]}/L_{FIR}$ and $L_{\star,tot}$ shows an initial decrease of $L_{[CII]}/L_{FIR}$ for increasing $L_{\star,tot}$ for all clouds. Then, in the case of MC2-HD there is an increase for $L_{\star,tot} \gtrsim 4 \times 10^6$ $L_\odot$, which corresponds to the high C^+ excitement and new star formation phase already mentioned. Apart from the data points associated to this phase, however, the scatter of $L_{[CII]}/L_{FIR}$ as a function of $L_{\star,tot}$ is reduced respect to the cases of x_{H^+} and t_{sf}. This relation can be well modelled with a power-law, as shown in the figure. We fit this relation, taking into account all the snapshots apart from those at very late stages of MC1-HD and MC2-HD, i.e., those after L_{FIR} reaches its maximum ($t_{sf} = 1$ Myr for MC2-HD and $t_{sf} = 2$ Myr for

MC1-HD). The best fit we obtain is

$$L_{[CII]}/L_{FIR} = 4.15 \times \left(\frac{L_{\star,tot}}{L_\odot}\right)^{-0.56}. \tag{4}$$

This fit provides a potential method to assess the total stellar luminosity of a cloud by using [CII] and FIR luminosity measurements. This relation holds up to when L_{FIR} increases. As we will discuss in detail in Section 4.1, this corresponds to the phase of life of MCs when the stellar feedback heats the dust in the dense regions close to the star formation sites, but has not dispersed these regions enough to move a significant fraction of the dust towards colder regions of the MC.

4 DISCUSSION

4.1 Time evolution of dust luminosity

The FIR luminosity of a HII region does not change monotonically with time. Shortly after a sink particle forms, the area in the vicinity of the formation site is very bright in FIR. We showed two examples of this in Fig. 3, where the HII region in MC2-MHD (top) and one in MC2-HD (bottom, green rectangle) are associated with newly-formed stars and show a compact, but bright peak in I_{FIR}. In the same figure, the bubble highlighted with the red rectangle shows a more evolved HII region, where there is diffuse FIR emission, but at a much lower intensity than at earlier stages. As we will show in detail in the following, this is essentially due to the fact that T_d remains roughly constant with time in the HII regions, but the density drops, leading to an overall decrease in L_{FIR}, even though it becomes more extended.

We explicitly show such evolution in Fig. 10, where we show the LOS-averaged, mass-weighted dust temperature $\langle T_d \rangle$, the dust column density N_d, and I_{FIR} for MC2-HD, bubble 2 (see Tab. 2) at $t_{evol} = 2$, 3, and 4 Myr. As speculated before, $\langle T_d \rangle$ in the bubble is, indeed, roughly constant over time, remaining around $\langle T_d \rangle \lesssim 50$ K. The size of the bubble (i.e., of the "hot" region with $\langle T_d \rangle \lesssim 50$ K) increases with time (top row), but the bubble becomes less dense (middle row), as the stellar feedback pushes the dust towards the shell of the bubble, where $\langle T_d \rangle$ is much lower. There are thus two phenomena which act in opposition to each other: (i) the enlargement of the hot regions leads to an increase of L_{FIR}, and (ii) the redistribution of dust towards cooler areas leads to a decrease.

The net result of these two processes is shown in the bottom row: there is a first phase when L_{FIR} increases, as the enlargement of the
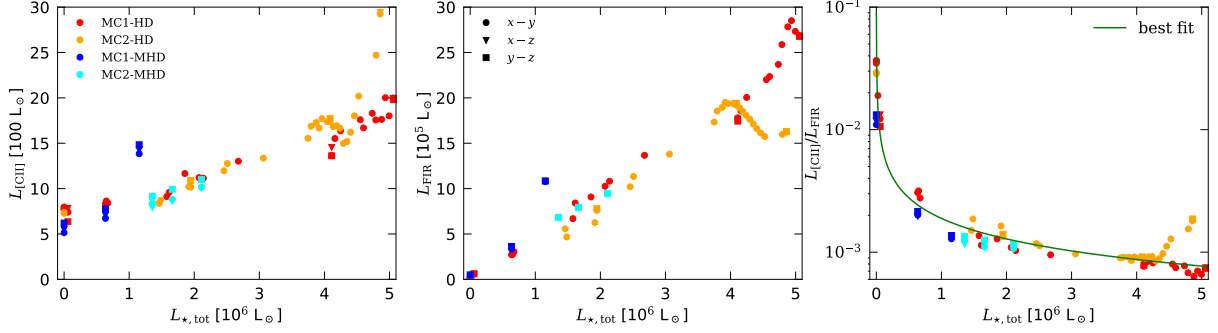
Figure 9. Same as Fig. [7](), but as a function of $L_{\star,\text{tot}}$. We fitted a power-law (green line) for te relation of $L_{[\text{CII}]}/L_{\text{FIR}}$ with $L_{\star,\text{tot}}$. The relation holds as long as L_{FIR} increases (middle panel). After reaching its maximum, the decrease of L_{FIR}, which has no counterpart in $L_{[\text{CII}]}$, breaks this relation, which we therefore do not consider in the fit.
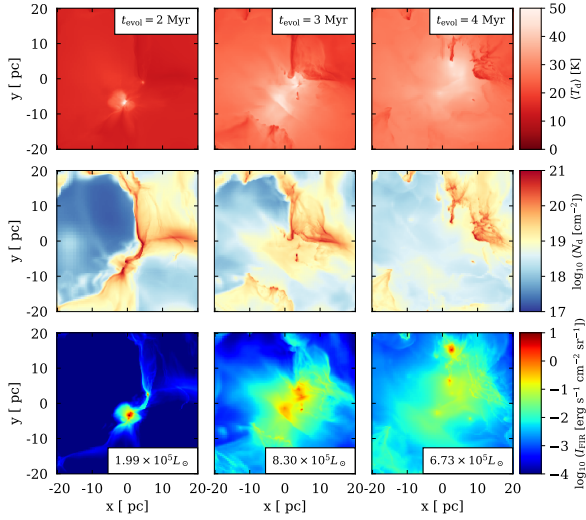
Figure 10. Mass-weighted dust temperature along the LOS ($< T_d >$, *top*), dust column density (N_d, *center*), and FIR intensity (I_{FIR}, *bottom*) of a portion of MC2-HD centered around bubble 2 (see Tab. [2]()) at $t_{\text{evol}} = 2$ (*left*), 3 (*center*), and 4 (*right*), respectively. The expansion of the bubble progressively enlarges the region with warm dust, characterised by $\langle T_d \rangle \lesssim 50$ K. However, the dust density N_d in the warm region is reduced by the expansion of the bubble, which pushes the dust towards the much cooler shell of the bubble. As a consequence, I_{FIR} arises from a progressively larger, but less FIR-bright, area. This is also reflected in the total L_{FIR}, reported for each snapshot in the I_{FIR} maps.

hot areas overcomes the decrease of N_d, and a second phase when L_{FIR} decreases again, as the redistribution of dust now takes over.

This explanation and the maps of Fig. [10]() refer to a single bubble. The evolution of L_{FIR} of an entire cloud can, however, be explained as the combined effect of several bubbles evolving in the manner described above. Indeed, the first phase when L_{FIR} increases (see Figs.[7](), [8](), and [9]()) corresponds to a phase when, i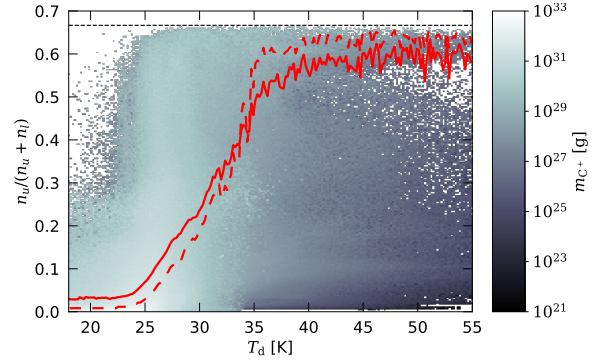n average over all the bubbles present in the cloud, the phenomenon (i) is dominant. Then, the phase when L_{FIR} decreases is the phase when, in average, the phenomenon (ii) dominates. The final of MC2-HD, when L_{FIR} increases again, is the consequence of a new star formation phase, thus the formation of new bubbles, which cause the phenomenon (i) to be dominant again.

Figure 11. Mass-weighted 2D histogram of the fraction of C^+ ions in the $^2P_{3/2}$ level ($n_u/(n_u + n_l)$) as a function of the dust temperature T_d. The color bar is in logarithmic scale. The solid red line represents the mass-weighted average of $n_u/(n_u + n_l)$ for a given T_d bin, and the dashed line represents the median. The thin, dotted black line represents $n_u/(n_u + n_l) = 2/3$, i.e., the maximum possible value. We represent the cells of MC2-HD, at $t_{\text{evol}} = 4$ Myr, with 18 K $\leq T_d \leq 55$ K. On average, C^+ saturates at $T_d \simeq 40$ K. This confirms that, in vicinity of stars, the [CII] line is saturated, causing, in part, the [CII]-deficit.

4.2 Saturation of [CII] in HII regions

The origin of the [CII]-deficit has been often attributed to the saturation of [CII] ([Kaufman et al. 1999](); [Muñoz & Oh 2016](); [Rybak et al. 2019](); [Bisbas et al. 2022]()) caused by stellar radiation, which prevents the [CII] emissivity from increasing above a certain amount, no matters how strong the radiation field becomes. On the other hand, the stellar radiation, reprocessed by dust and emitted in the FIR, keeps increasing with stellar radiation.

In order to test this hypothesis, we use RADMC-3D to calculate the level population of the C^+ ions and analyse its dependence on the dust temperature. More specifically, let n_u be the number density of C^+ ions in the upper level, $^2P_{3/2}$, and n_l the number density of those in the lower level, $^2P_{1/2}$. Then, we investigate the fraction of ions in the upper level, $n_u/(n_u + n_l)$ as a function of T_d. This is done in Fig. [11](), where we show this relation for MC2-HD at $t_{\text{evol}} = 4$ Myr. We consider here only the cells with 18 K $\leq T_d \leq 55$ K and we plot $n_u/(n_u + n_l)$ and T_d in a mass-weighted 2D histogram. We overplot the mean and the median (solid and dashed red line, respectively). We choose to restrict the plot in this temperature range as for $T_d < 18$

K the main heating source is the ISRF, in which we are not interested now. The number of cells with $T_d > 55$ K is low, making the mean and median very noisy.

The fraction of ions in the excited state remains very low $(n_u/(n_u + n_l) \simeq 0.03)$ up to $T_d \simeq 23$ K, then slowly increases till $T_d \simeq 40$ K, where saturation is reached. We point out that $\max(n_u/n_l) = 2$, because of the statistical weights of the upper and lower level, and therefore $(n_u/(n_u + n_l))_{\max} = 2/3$. The [CII] line, therefore, saturates for $T_d \geq 40$ K. Since the regions with this T_d are those close to bright stars (Figs. 2 and 10, top row), we conclude that in vicinity of bright stars the [CII] line is saturated.

4.3 Origin of the [CII]-deficit

We now use our results about the evolution of the dust luminosity (Sec. 4.1) and the saturation of the [CII] line to explain the evolution of $L_{[CII]}/L_{FIR}$ with $L_{\star,tot}$ and the onset of the [CII]-deficit. We distinguish between three evolutionary stages of MCs as follows.

(i) *Recently formed HII regions*: The dust temperature and density are large in the regions surrounding the newly formed stars. Thus, I_{FIR} is very large in these regions. There, $I_{[CII]}$ is saturated. As a consequence, the $I_{[CII]}/I_{FIR}$ is low close to the newly-formed stars. The other regions of the clouds have low $I_{[CII]}$ and low I_{FIR} values. The $I_{[CII]}/I_{FIR}$ ratio is, in these other regions, higher than in vicinity of the stars. The overall $L_{[CII]}/L_{FIR}$ ratio in the clouds is $\sim 10^{-2}$.

(ii) *Evolved HII regions*: The $L_{[CII]}/L_{FIR}$ decreases in this phase, and the main reasons are the [CII] saturation and the second carbon ionization. In this phase, the [CII] emission from within the HII regions is very weak because a significant fraction of the C^+ is converted into C^{2+}, and the remaining [CII] is saturated. The [CII] emission from the other regions of the clouds increases because of the excitation due to stellar radiation. Overall, $L_{[CII]}$ moderately increases. The dust luminosity keeps increasing (more sharply than $L_{[CII]}$) in the first part of this phase, and then starts decreasing (see Section 4.1). The combined evolution of [CII] and FIR lead first to a decrease of $L_{[CII]}/L_{FIR}$ and then to roughly constant values, when L_{FIR} stops increasing. In this phase, $L_{[CII]}/L_{FIR} \sim 10^{-3}$.

(iii) *Larger scale [CII] excitation and formation of new stars*: In this last phase, the stellar radiation, which now permeates the entire cloud, excites the C^+ lines also in regions of the cloud distant from the HII regions. This leads to an increase of $L_{[CII]}$. Furthermore, the eventual onset of a new star formation leads to an increase of $L_{[FIR]}$ because of the sharp increase of T_d in these new, still dense, star formation regions. The increase of $L_{[CII]}$ is, however, dominant, therefore $L_{[CII]}/L_{FIR}$ slightly increases in this phase. We encounter this phase in the latest snapshots of MC2-HD.

4.4 Projection effects

Molecular clouds and their substructures do not have, in general, a spherical geometry. Instead, they present often a filamentary or sheet-like structure (Bally et al. 1987; André et al. 2014; Kainulainen et al. 2022). This is verified for the simulations analysed in this paper, too (Ganguly et al., in prep.). This means that the aspect ratio of a cloud is, in general, very different according to the LOS trough which it is observed. As a consequence, HII regions also have different shapes depending on the LOS. For instance, a star-forming region in a sheet-like structure exhibits a ring shape when observed face-on, with the formed stars approximately in the center. If the same HII region is observed edge-on, it may even be not observable at all due to the

attenuation by the gas in the sheet (sitting in the foreground). We showed already a consequence of this in Fig. 5, where the profiles of I_{FIR}, $I_{[CII]}$, and $I_{[CII]}/I_{FIR}$ are different for different LOS. In some cases, for instance in MC2-HD, bubbles 1 and 2, these profiles strongly differ for different LOS, mostly at late evolutionary stages.

The impact of projection effects is evident in Fig. 12, where we draw the $I_{[CII]}$ emission maps of MC2-HD for all LOS. With green and light blue circles, we highlight the stars responsible for the creation of bubble 1 and bubble 2 and we note that, indeed, the shape of these bubbles is significantly different along the three LOS. In particular, bubble 2 (light blue circle) cannot be seen at all in the $x - y$ plane, but is evident in the $x - z$ and $y - z$ planes. The bubble has a diameter of ~ 40 pc and is deeply devoid of [CII] emission inside, due to the large amount or radiation coming from the several hot stars contained. Bubble 1 (green circle) exhibits different shapes when observed from different LOS as well, even if there no LOS where the bubble is not visible. Nevertheless, the apparent size of the bubble changes significantly for different LOS. This explains the variations in the profiles, for different LOS, shown in Fig. 5.

Projection effects can also cause apparent bubbles, similar to those associated to expanding HII regions, with no stars inside. Such an apparent bubble could be "created" by a dense fore/background layer which "separates" the part of the bubble containing the driving stars from a more distant region of the same bubble. An example of such an apparent bubble is given in Fig. 13, a zoom-in of the rightmost panel of Fig. 12. In the center of the figure there is a region with very low $I_{[CII]}$ surrounded by a much brighter ring, which in combination resemble the structure of the other actual HII regions shown in this paper. However, there are no stars embedded in this structure: the apparent bubble is a result of the extensive stellar radiation coming from the stars of the large HII region left to it, which also ionize that region of the cloud.

Apparent bubbles with no stellar counterparts are also found in real observations of MCs and HII regions: for instance, Beuther et al. (2022) find several of such bubbles in [CII] emission maps of NGC 7538. In general, we point out that apparent bubbles should be a reason of caution when attempting to identify bubble structures on intensity maps of regions affected by stellar feedback.

4.5 Comparison with real observations reporting [CII]-deficit

A very well studied MC in solar neighborhood is the Orion Molecular Cloud 1 (OMC 1): it lies, in our LOS, beyond the Orion Nebula cluster and is at a distance of $\simeq 414$ pc from us (Genzel & Stutzki 1989). It is an actively star forming cloud, similar to ours despite being more massive (about one order of magnitude). A study of the [CII]-deficit in this MC has been performed by Goicoechea et al. (2015), which used Herschel HIFI data to obtain, among other results, a $I_{[CII]}/I_{FIR}$ map of such cloud. They measure the radial change of $I_{[CII]}/I_{FIR}$ with distance to their reference center (the HII region around the Trapezium cluster). On the smallest scale of 0.1 pc they obtain $L_{[CII]}/L_{FIR} = 9.3 \times 10^{-4}$. This ratio increases to $L_{[CII]}/L_{FIR} = 3.8 \times 10^{-3}$ when averaged over the entire cloud. We can compare this values with the same analysis we performed for our simulated clouds, shown in Fig. 5. As discussed already in Sec. 3.3, there is a large scatter in values both at small and at large radii due to different stellar population, geometry, and global characteristics of the clouds. Nevertheless, the general behavior of an increasing $I_{[CII]}/I_{FIR}$ with larger portions of clouds considered is in agreement with the OMC 1 results of Goicoechea et al. (2015). Our typical
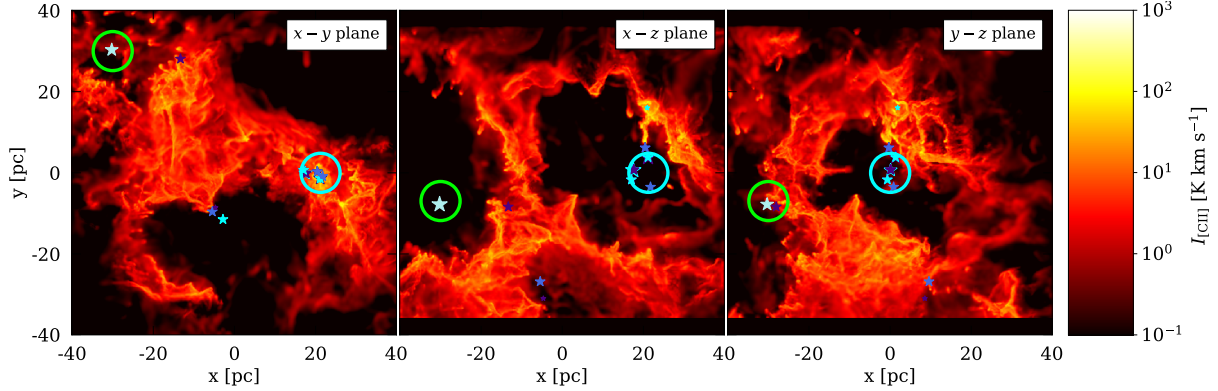
Figure 12. [CII] emission map of MC2-HD at t_{evol} = 4 Myr for 3 different LOS. The green circle highlights the stars responsible for the formation of "bubble 1" and the light blue circles highlight the stars responsible for "bubble 2". Because of the complex structure of the cloud, the shape of such HII regions is very different for different LOS. As an example, "bubble 2" is not visible at all when looking along the LOS perpendicular to the $x - y$ plane. This explains the variations of the [CII]-deficit as a function of the bubble radius (Fig. 5) for different LOS

.
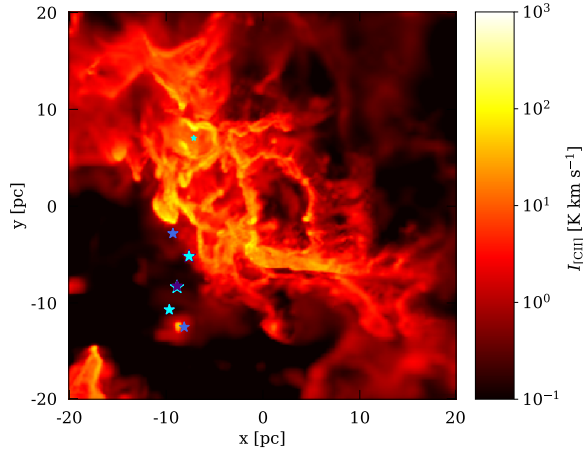
Figure 13. [CII] emission map of a portion of MC2-HD at t_{evol} = 4 Myr, centered on an apparent cavity in the [CII] emission, which does not contain any star. Projection effects can cause apparent bubbles similar to expanding HII regions.

values of $10^{-5} - 10^{-4}$ at small radii, and $10^{-3} - 10^{-2}$ at large radii are in rough agreement with their results as well.

Values of $L_{[CII]}/L_{FIR}$ ranging between 10^{-3} and 10^{-2} have also been found by Suzuki et al. (2021) in the star-forming region RCW 36. In particular, they observe a decreasing $L_{[CII]}/L_{FIR}$ value for increasing L_{FIR}, which is consistent with the model of saturation of the [CII] line as the reason of the [CII]-deficit as we discussed before. Somewhat lower values are measured by Jackson et al. (2020) in the analysis of 4 star-forming clumps in the Milky way. They measure $L_{[CII]}/L_{FIR} \simeq 10^{-4} - 10^{-3}$, apart from one clump characterized by a very low, atypical ratio of $\simeq 10^{-6}$ because of the extremely low $L_{[CII]}$ measured, for which several possible explanations are given. The lower values observed are probably due to the fact that they observe at smaller scales ($\sim$ 1 pc): we typically obtain smalelr values for smaller scales as well (Fig. 5).

The relation between $L_{[CII]}$ and L_{FIR} has been analysed for extragalactic observations as well. Several works, like Smith et al.

(2017); Herrera-Camus et al. (2018); Pineda et al. (2018), find $L_{[CII]}/L_{FIR} \simeq 10^{-3} - 10^{-2}$. This is the case, for instance, of the study of M 51 performed by Pineda et al. (2018), who found $L_{[CII]}/L_{FIR} \simeq 0.003$ in the center of the galaxy, and somehow larger values in the interarm regions. Observations of dwarf galaxies from Smith et al. (2017); Herrera-Camus et al. (2018) show $L_{[CII]}/L_{FIR}$ between a few 10^{-4} and 10^{-2} as well. Such observations highlight a correlation between $L_{[CII]}/L_{FIR}$ and the SFR, following the prescription of Muñoz & Oh (2016). Recent numerical simulations (Smith et al. 2017; Bisbas et al. 2022) fit the relation between $L_{[CII]}/L_{FIR}$ and the star formation rate surface density Σ_{SFR} by means of a power-law with an exponent of $-1/4.7$. We could not find, however, a robust correlation with the SFR in our simulations. Conversely, we find $L_{[CII]}/L_{FIR}$ being much strongly correlated with the total stellar mass within the cloud and, even more, with the stellar luminosity (see Fig. 9). Indeed, we find that $L_{[CII]}/L_{FIR}$ and $L_{\star,tot}$ are related by a power-law (Eq. 4). We plan to benchmark this relation against real data in a subsequent work.

5 CONCLUSIONS

In this paper we present an analysis of simulations of star-forming MCs including stellar feedback and an *on-the-fly* chemical network. In particular, we consider 4 MCs within the SILCC-Zoom Project (Seifried et al. 2017) and analyse the [CII] 158 μm line and the FIR dust continuum emission. Two of the 4 clouds include an external magnetic field. The aim of this paper is to investigate the origin and the evolution of the so-called [CII]-deficit, i.e., the observed drop in the $I_{[CII]}/I_{FIR}$ ratio in vicinity of star formation regions. We summarise our main results as follows.

- At an early evolutionary stage of the HII regions, i.e., when the cloud has not been significantly dispersed yet, I_{FIR} is very large in proximity of the newly-formed stars because of the high dust temperature and density. The [CII] line is saturated in these regions, and $I_{[CII]}$ cannot thus increase beyond a certain limit, no matter how strong the stellar radiation is. This causes a particularly low $I_{[CII]}/I_{FIR}$ in these regions.
- At late evolutionary stages, HII regions are characterised by

14   *S. Ebagezio et al.*

a lower dust and gas density respect to earlier stages because stellar radiation disperses the cloud. Therefore, I_{FIR} is diminished with respect to earlier stages, even though the dust temperature is comparable. In any case, $I_{[CII]}$ is also strongly diminished, not only because of general drop in gas density, but also since C^+ is largely converted into C^{2+} by stellar radiation. This is then the main reason of the observed low $I_{[CII]}/I_{FIR}$ in developed HII regions.

• The evolution of L_{FIR} is a consequence of the evolution of single HII regions. It increases as long as the dust heating dominates over the cloud dispersal. Later on, the dispersal of HII regions determines an overall decrease in L_{FIR}.

• The [CII] luminosity monotonically increases with time. As long as MCs evolve, the [CII] emission coming from the HII regions progressively reduces, and the emission coming from the other regions of the clouds increases because of the C^+ excitation provided by stellar radiation.

• The evolution of $L_{[CII]}/L_{FIR}$ can be divided in three phases. The first phase (young HII regions) is characterized by $L_{[CII]}/L_{FIR} \simeq 10^{-2}$, with peaks of I_{FIR} close to the newly formed stars. The second phase is characterized by a mild increase of $L_{[CII]}$ and a sharper increase of L_{FIR}, which leads to a decrease of $L_{[CII]}/L_{FIR}$ down to $\simeq 10^{-3}$. In the third phase, several combined phenomena (dust pushed towards colder regions, larger excitation of C^+, and onset of new star formation) lead to a slight increase of $L_{[CII]}/L_{FIR}$.

• The $L_{[CII]}/L_{FIR}$ ratio as a function of the total star luminosity $L_{\star,tot}$ follows a relation that can be fitted with a power-law (Eq. (4)). This relation is valid before the stellar radiation disperses the hot HII regions, and L_{FIR} decreases consequently.

• Projection effects significantly change the appearance of HII regions and quantities connected to them significantly. Depending on the geometry of the cloud and on the LOS, a certain HII region may be not visible at all, or, conversely, apparent bubbles which are, however, not associated to any massive stars, can be observed.

DATA AVAILABILITY

The data underlying this article will be shared on reasonable request to the corresponding author.

REFERENCES

Abel N. P., Ferland G. J., Shaw G., Troland T. H., O'Dell C. R., 2005, in American Astronomical Society Meeting Abstracts. p. 81.17
Ali A. A., Bending T. J. R., Dobbs C. L., 2022, MNRAS, 510, 5592
André P., Di Francesco J., Ward-Thompson D., Inutsuka S. I., Pudritz R. E., Pineda J. E., 2014, in Beuther H., Klessen R. S., Dullemond C. P., Henning T., eds, Protostars and Planets VI. p. 27 (arXiv:1312.6232), doi:10.2458/azu_uapress_9780816531240-ch002
Bally J., Langer W. D., Stark A. A., Wilson R. W., 1987, ApJ, 312, L45
Beilis D., Beck S., Lacy J., 2022, MNRAS,
Beuther H., et al., 2014, A&A, 571, A53
Beuther H., et al., 2022, A&A, 659, A77
Bisbas T. G., et al., 2022, ApJ, 934, 115
Bjorkman J. E., Wood K., 2001, ApJ, 554, 615
Brauher J. R., Dale D. A., Helou G., 2008, ApJS, 178, 280
Casey C. M., Narayanan D., Cooray A., 2014, Phys. Rep., 541, 45
Chevance M., et al., 2020, Space Sci. Rev., 216, 50
Chevance M., Krumholz M. R., McLeod A. F., Ostriker E. C., Rosolowsky E. W., Sternberg A., 2022, arXiv e-prints, p. arXiv:2203.09570
Dale J. E., Ercolano B., Bonnell I. A., 2012, MNRAS, 424, 377
De Looze I., Baes M., Bendo G. J., Cortese L., Fritz J., 2011, MNRAS, 416, 2712
Dubey A., Reid L. B., Fisher R., 2008, Physica Scripta Volume T, 132, 014046
Dullemond C. P., Juhasz A., Pohl A., Sereshti F., Shetty R., Peters T., Commercon B., Flock M., 2012, RADMC-3D: A multi-purpose radiative transfer tool, Astrophysics Source Code Library, record ascl:1202.015 (ascl:1202.015)
Dunne L., Maddox S. J., Papadopoulos P. P., Ivison R. J., Gomez H. L., 2022, MNRAS, 517, 962
Ebagezio S., Seifried D., Walch S., Nürnberger P. C., Rathjen T. E., Naab T., 2022, arXiv e-prints, p. arXiv:2206.06393
Fall S. M., Krumholz M. R., Matzner C. D., 2010, ApJ, 710, L142
Federrath C., Banerjee R., Clark P. C., Klessen R. S., 2010, ApJ, 713, 269
Ferland G. J., et al., 2017, Rev. Mex. Astron. Astrofis., 53, 385
Fixsen D. J., 2009, ApJ, 707, 916
Franeck A., et al., 2018, MNRAS, 481, 4277
Fryxell B., et al., 2000, ApJS, 131, 273
Gatto A., et al., 2017, MNRAS, 466, 1903
Geen S., Pellegrini E., Bieri R., Klessen R., 2020, MNRAS, 492, 915
Genzel R., Stutzki J., 1989, ARA&A, 27, 41
Girichidis P., et al., 2016, MNRAS, 456, 3432
Girichidis P., Seifried D., Naab T., Peters T., Walch S., Wünsch R., Glover S. C. O., Klessen R. S., 2018, MNRAS, 480, 3511
Glover S. C. O., Mac Low M.-M., 2007a, ApJS, 169, 239
Glover S. C. O., Mac Low M.-M., 2007b, ApJ, 659, 1317
Glover S. C. O., Federrath C., Mac Low M. M., Klessen R. S., 2010, MNRAS, 404, 2
Goicoechea J. R., et al., 2015, ApJ, 812, 75
Graciá-Carpio J., et al., 2011, ApJ, 728, L7
Habing H. J., 1968, Bull. Astron. Inst. Netherlands, 19, 421
Hacar A., Clark S., Heitsch F., Kainulainen J., Panopoulou G., Seifried D., Smith R., 2022, arXiv e-prints, p. arXiv:2203.09562
Haid S., Walch S., Seifried D., Wünsch R., Dinnbier F., Naab T., 2019, MNRAS, 482, 4062
Henshaw J. D., Barnes A. T., Battersby C., Ginsburg A., Sormani M. C., Walker D. L., 2022, arXiv e-prints, p. arXiv:2203.11223
Herrera-Camus R., et al., 2018, ApJ, 861, 95
Hollenbach D. J., Tielens A. G. G. M., 1999, Reviews of Modern Physics, 71, 173
Hosokawa T., Inutsuka S.-i., 2006, ApJ, 648, L131
Hu C.-Y., Zhukovska S., Somerville R. S., Naab T., 2019, MNRAS, 487, 3252
Hu C.-Y., Sternberg A., van Dishoeck E. F., 2021, ApJ, 920, 44
Jackson J. M., et al., 2020, ApJ, 904, 18
Kabanovic S., et al., 2022, A&A, 659, A36
Kainulainen J., Rezaei K. S., Spilker A., Orkisz J., 2022, A&A, 659, L6
Kaufman M. J., Wolfire M. G., Hollenbach D. J., Luhman M. L., 1999, ApJ, 527, 795
Klessen R. S., Glover S. C. O., 2016, Saas-Fee Advanced Course, 43, 85
Krumholz M. R., Matzner C. D., 2009, ApJ, 703, 1352
Krumholz M. R., et al., 2014, in Beuther H., Klessen R. S., Dullemond C. P., Henning T., eds, Protostars and Planets VI. pp 243–266 (arXiv:1401.2473), doi:10.2458/azu_uapress_9780816531240-ch011
Lucy L. B., 1999, A&A, 344, 282
Luhman M. L., et al., 1998, ApJ, 504, L11

Luhman M. L., Satyapal S., Fischer J., Wolfire M. G., Sturm E., Dudley C. C., Lutz D., Genzel R., 2003, ApJ, 594, 758

Luisi M., et al., 2021, Science Advances, 7, eabe9511

Malhotra S., et al., 1997, ApJ, 491, L27

Malhotra S., et al., 2001, ApJ, 561, 766

Muñoz J. A., Oh S. P., 2016, MNRAS, 463, 2085

Murray N., Quataert E., Thompson T. A., 2010, ApJ, 709, 191

Naab T., Ostriker J. P., 2017, ARA&A, 55, 59

Narayanan D., Krumholz M. R., 2017, MNRAS, 467, 50

Nelson R. P., Langer W. D., 1997, ApJ, 482, 796

Ossenkopf V., 1997, New Astron., 2, 365

Ossenkopf V., Röllig M., Neufeld D. A., Pilleri P., Lis D. C., Fuente A., van der Tak F. F. S., Bergin E., 2013, A&A, 550, A57

Ostriker E. C., Kim C.-G., 2022, ApJ, 936, 137

Pabst C. H. M., et al., 2017, A&A, 606, A29

Pabst C. H. M., et al., 2020, A&A, 639, A2

Pabst C. H. M., et al., 2021, A&A, 651, A111

Pabst C. H. M., et al., 2022, A&A, 658, A98

Pineda J. L., Langer W. D., Velusamy T., Goldsmith P. F., 2013, A&A, 554, A103

Pineda J. L., Langer W. D., Goldsmith P. F., 2014, A&A, 570, A121

Pineda J. L., et al., 2018, ApJ, 869, L30

Röllig M., Ossenkopf V., Jeyakumar S., Stutzki J., Sternberg A., 2006, A&A, 451, 917

Röllig M., Simon R., Güsten R., Stutzki J., Israel F. P., Jacobs K., 2016, A&A, 591, A33

Rybak M., et al., 2019, ApJ, 876, 112

Sanders D. B., Mirabel I. F., 1996, ARA&A, 34, 749

Sargsyan L., et al., 2012, ApJ, 755, 171

Schneider N., et al., 2012, A&A, 542, L18

Schöier F. L., van der Tak F. F. S., van Dishoeck E. F., Black J. H., 2005, A&A, 432, 369

Seifried D., et al., 2017, MNRAS, 472, 4797

Seifried D., Haid S., Walch S., Borchert E. M. A., Bisbas T. G., 2020, MNRAS, 492, 1465

Seifried D., Beuther H., Walch S., Syed J., Soler J. D., Girichidis P., Wünsch R., 2022, MNRAS, 512, 4765

Shetty R., Glover S. C., Dullemond C. P., Klessen R. S., 2011a, MNRAS, 412, 1686

Shetty R., Glover S. C., Dullemond C. P., Ostriker E. C., Harris A. I., Klessen R. S., 2011b, MNRAS, 415, 3253

Smith J. D. T., et al., 2017, ApJ, 834, 5

Spitzer L., 1978, Physical processes in the interstellar medium, doi:10.1002/9783527617722.

Stacey G. J., Geis N., Genzel R., Lugten J. B., Poglitsch A., Sternberg A., Townes C. H., 1991, ApJ, 373, 423

Stacey G. J., Hailey-Dunsheath S., Ferkinhoff C., Nikola T., Parshley S. C., Benford D. J., Staguhn J. G., Fiolet N., 2010, ApJ, 724, 957

Strömgren B., 1939, ApJ, 89, 526

Stutzki J., 2001, Astrophysics and Space Science Supplement, 277, 39

Suzuki T., et al., 2021, A&A, 651, A30

Tielens A. G. G. M., Hollenbach D., 1985, ApJ, 291, 722

Tiwari M., et al., 2021, ApJ, 914, 117

Walch S. K., Whitworth A. P., Bisbas T., Wünsch R., Hubber D., 2012, MNRAS, 427, 625

Walch S., et al., 2015, MNRAS, 454, 238

Weingartner J. C., Draine B. T., 2001, ApJ, 548, 296

Wolfire M. G., McKee C. F., Hollenbach D., Tielens A. G. G. M., 2003, ApJ, 587, 278

Wünsch R., Walch S., Dinnbier F., Whitworth A., 2018, MNRAS, 475, 3393

Wünsch R., Walch S., Dinnbier F., Seifried D., Haid S., Klepitko A., Whitworth A. P., Palouš J., 2021, MNRAS, 505, 3730

This paper has been typeset from a TeX/LaTeX file prepared by the author.

6

A COMPARISON BETWEEN SIMULATIONS WITH NL97 AND NL99 CHEMICAL NETWORK

In Paper I and Paper II we analysed numerical simulations which include a chemical network, which we referred to as "NL97". This network is based on the chemical reactions described in Glover & Mac Low (2007a,b), integrated with the model for CO formation of Nelson & Langer (1997). In this chapter, we compare those simulations with other ones of the same clouds, but performed with a different, more complex chemical network, which we to refer with "NL99".

The goal of this chapter is to highlight the differences that the two chemical networks produce on the simulated clouds and to assess the reliability of the implementation of the NL99 network in our simulations.

We first explain the characteristics of the NL99 network in Section 6.1. We then analyse the abundance of the carbon-bearing species in the simulations with this chemical network included and we compare with the corresponding simulations performed with NL97 and with data from real observations (Section 6.2). After this, we study the emission maps resulting from these simulations, again with comparisons with other simulations and real data (Section 6.3).

We only use simulations of molecular clouds without stellar feedback for this analysis, i.e., MC1-HD-noFB, MC2-HD-noFB, MC1-MHD-noFB, and MC2-MHD-noFB, according to the nomenclature criterion we explained in Section 3.4. This is sufficient to understand the differences that the two chemical networks lead to and, as we will show, to motivate the choice of using NL97 in Paper I and Paper II. We point out that the work described in this chapter has been actually been done before starting the analysis of the simulations which lead to Paper I and Paper II.

6.1
SIMULATION WITH THE NL99 CHEMICAL NETWORK

6.1.1
THE NL99 CHEMICAL NETWORK

Our NL99 chemical network is largely based on the network described in Glover & Clark (2012), with which combines a model for hydrogen chemistry taken from Glover & Mac Low (2007a,b) and a model for CO chemistry introduced by Nelson & Langer (1999). We introduce some modifications, such as the grain-surface reactions, to these networks based on more recent works (e.g., Gong et al., 2017). The X-ray reactions and rates are taken largely from Yan (1997) and Meijerink & Spaans (2005). The entire network is described in detail in Mackey et al. (2019): we refer to this paper for a more comprehensive description of the network. Here, we focus on the main aspects and differences respect to the NL97 network.

The NL99 network models the evolution of 18 chemical species: H^+, H, H_2, OH_x, C, C^+, CO, CH_x, HCO^+, He, He^+, M, M^+, O, O^+, H_2^+, H_3^+, and e^-. Some of them

Table 6.1: Elemental abundances in the gas phase by number with respect to hydrogen nuclei, Y_R

Species	Y_R
H	1
He	0.1
C	1.4×10^{-4}
O	3.1×10^{-4}
M	1×10^{-5}

are not physical species, but proxies for several different physical species with similar chemical properties and reactions, which are therefore considered as a single one for simplicity. This is the case for CH_x, which represents simple hydrocarbons such as CH, CH_2, CH_3, and so on, as well as OH_x, which includes OH, H_2O,... In addiction, ions, such as CH^+ and OH^+, are included in CH_x and OH_x, respectively. All metals which do not appear explicitly in the above list are treated with a proxy, M, which is supposed to have two possible states of ionization: M and M^+. There are several methods applied to calculate the abundance of the aforementioned species in this network. The evolution of some of them is calculated by numerically solving an ordinary differential equation of the same type of Eq. (3.20), that is, for these species the production and destruction rates are tabulated and the changes in their abundance can be calculated depending on the physical parameters of a given cell (gas temperature, density, ionizing photons...) and on the abundance of the other reactants. Conversely, the abundance of other species is inferred by the total abundance conservation principle. This is the case, for instance, foe neutral He and neutral M, whose abundances are calculated as the difference between the total abundance of helium and metals, which is constant, and the abundance of the ionized species He^+ and M^+. Finally, the abundance of other species is tracked by assuming equilibrium abundances or instantaneous further reactions. A description of the treatment of each modelled species is summarized in Mackey et al. (2019), Table 1.

The total abundance of H, He, C, O, and M is constant. Table 6.1 summarizes these elemental abundances, Y_R, with respect to total hydrogen. These are particle fractional abundances, i.e., there are, for instance, 0.1 helium nuclei for each hydrogen nucleus.

Some of the reactions included in the network take place on the surface of dust grains, which act as catalysts for these reactions. We will explore the differences which including/excluding these grain-assisted reactions produce in the chemical abundance of the species of our interest.

6.1.2

OVERVIEW OF THE SIMULATIONS

As a first step in our analysis, we look at the column density maps of CO, C, and C^+ of the clouds simulated with the NL99 network, in order to understand how these species are spatially distributed. This is done in Fig. 5, where we show the column density maps in the $x - y$ plane of CO, C, and C^+ (N_{CO}, N_C, and N_{C^+}, respectively, from left to right) for MC1-HD at t_{evol} =2, 3, and 4 Myr (from top to bottom). We overlay, with black lines, the H_2 column density contour plot, where

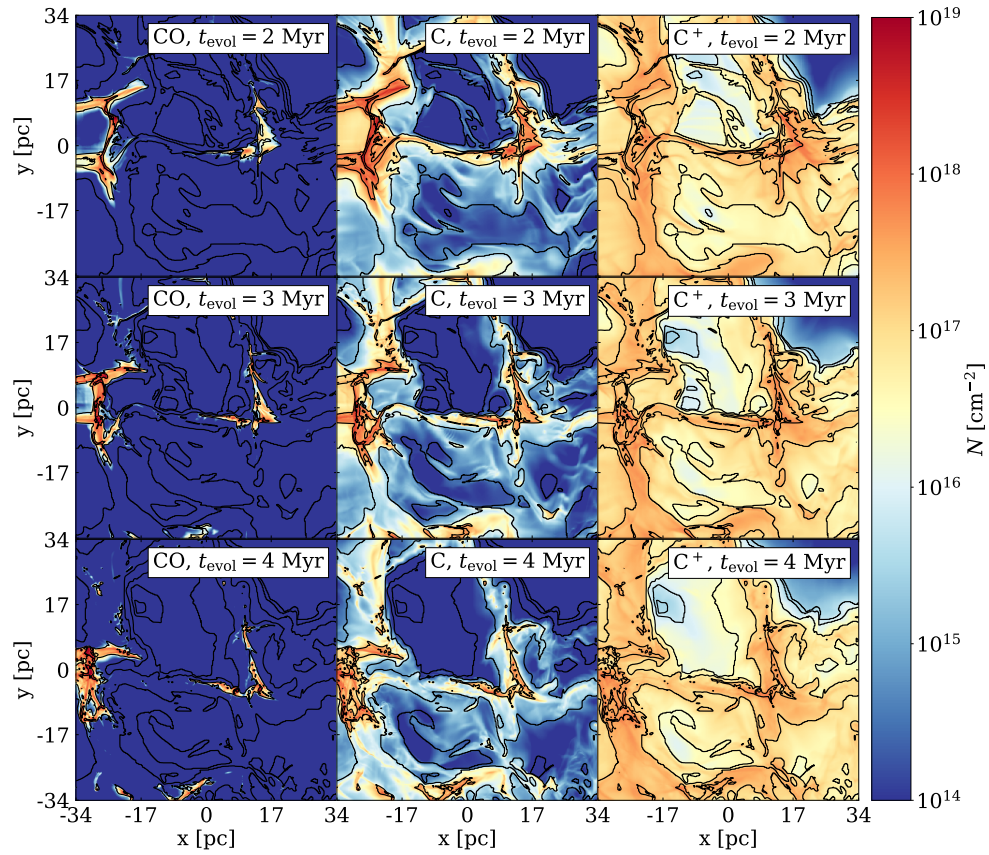Figure 5: Column density maps of CO, C, and C^+ (from left to right) of MC1-HD at t_{evol} =2, 3, and 4 Myr (from top to bottom), simulated with the NL99 chemical network. The black lines represent isocontour lines of H_2 column density for N_{H_2} = 10^{17}, 10^{18}, 10^{19}, 10^{20}, 10^{21}, and 10^{22} cm^{-2}.

we draw isocontour lines for $N_{H_2} = 10^{17}$, 10^{18}, 10^{19}, 10^{20}, 10^{21}, and 10^{22} cm^{-2}.

A nested CO - C - C$^+$ structure is evident when looking at these column density plots. The regions with a significant CO column density are rich in C and C$^+$ as well. There are, however, large portions of the cloud where N_{CO} is negligible, whereas N_C and N_{C^+} are much larger. In the same way, there are regions where N_C is small, but there is a moderate amount of C$^+$ instead. This is the case, for instance, of the two cavities located in the center of the image, on the top and bottom sides, separated by a denser bridge filament.

If we now compare these column density maps with the H$_2$ column density, whose isocontour lines are drawn in black in the figure, we note that the CO, C, and C$^+$ are associated with different H$_2$ densities. The CO column density is $N_{CO} \leq 10^{14}$ cm^{-2} in the vast majority of the cloud, and only sharply increases to $10^{17} - 10^{19}$ cm^{-2} in those regions with the largest H$_2$ column density. This confirms the well-known fact that the CO does not trace the entire H$_2$ present in a cloud, but only the regions with very high density. This is essentially a consequence of the higher energy required to photodissociate H$_2$ (14.16 or 14.68 eV, Allison & Dalgarno, 1969, for ortho- and para-H$_2$, respectively) than CO (11.09 eV, Visser et al., 2009). This feature is well-known in literature, both in simulational and observational works (e.g. van Dishoeck & Black, 1988; Lada & Blitz, 1988; van Dishoeck et al., 1992; Wolfire et al., 2010; Glover & Mac Low, 2011; Ackermann et al., 2012; Duarte-Cabral et al., 2015; Glover & Clark, 2016; Donate & Magnani, 2017; Seifried et al., 2020, and many more) and the fraction of molecular gas with no CO counterpart is called "CO-dark" gas fraction, as there is no CO emission coming from those regions.

Neutral carbon is present in vaster areas of the cloud. Its column density peaks where N_{H_2} peaks as well, but there are regions which contain molecular hydrogen with no (or very little) CO, and a moderate N_C instead. This is the case, for instance, of the leftmost part of the cloud at $t_{evol} = 2$ and 3 Myr. Indeed, neutral carbon has been proposed in the literature as an alternative tracer to CO for atomic hydrogen, for instance by Gerin & Phillips (2000); Papadopoulos & Greve (2004); Offner et al. (2014); Glover et al. (2015); Clark et al. (2019).

Ionized carbon is widespread in the cloud. The maximum column density values in the simulation shown reach $N_{C^+} \lesssim 10^{18}$ cm^{-2}, i.e., somehow lower than the highest column densities of CO and C. Furthermore, a comparison with the N_{H_2} isocontour lines shows that the regions with the largest N_{H_2} cannot be effectively identified in the C$^+$ column density maps. Instead, N_{C^+} seems to be roughly constant above a certain N_{H_2} threshold. On the other hand, N_{C^+} is non-negligible in diffuse regions with low H$_2$ column density and very little amount of CO and C (e.g., the bottom-right region of the map shown). Again, numerous literature works (e.g. Langer et al., 2010, 2014b; Pineda et al., 2013; Franeck et al., 2018) describe this behavior and emphasize that, at cloud scale, most of the [CII] emission (which is strictly correlated with the C$^+$ column density) comes from the atomic regions of the cloud, and only a small fraction comes from the molecular part (Franeck et al., 2018).

We can appreciate these properties more quantitatively by looking at N_{CO}, N_C, and N_{C^+} as a function of N_{H_2}. This is done in Fig. 6, where we show these quantities for MC1-HD at $t_{evol} = 2$, 3, and 4 Myr. We consider all pixels with $N_{H_2} \geq 10^{17}$ cm^{-2} and we divide the resulting range value of N_{H_2} in 100 bins, equally spaced in logspace. Then, we take the mean value of the column density of the carbon-bearing species for each N_{H_2} bin.
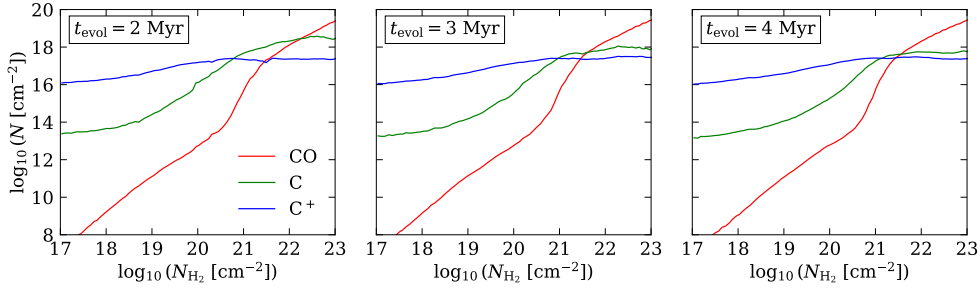
Figure 6: Column density of CO, C, and C^+ as a function of the H_2 column density N_{H_2} for MC1-HD at t_{evol} = 2, 3, and 4 Myr (from left to right). We consider the column density maps pixels with $N_{H_2} \geq 10^{17}$ and we divide them in bins equally large in log-space. The values on the y-axis are the mean values for each of these bins.

As we anticipated, N_{CO} is the species which traces high H_2 column densities most effectively, as N_{CO} keeps increasing for increasing N_{H_2} in high-density regime and drops to very low levels for $N_{H_2} \lesssim 10^{21}$ cm^{-2}. On the other hand, both N_C and N_{C^+} are roughly constants for $N_{H_2} \gtrsim 10^{21}$ cm^{-2}. Moreover, as we noted already when analysing the column density maps before, C^+ is also present in regions with very little H_2: indeed, we note that N_{C^+} only drops by about two orders of magnitude (from $\sim 10^{18}$ to $\sim 10^{16}$ cm^{-2}) where N_{H_2} drops by about 4 orders of magnitude (from $\sim 10^{21}$ to $\sim 10^{17}$ cm^{-2}).

Furthermore, we note that the relation between N_{H_2} and the column density of C^+, C, and CO has only a weak dependence on the evolutionary stage of the cloud. If we compare the plots for 2, 3, and 4 Myr (left, center, and right plot of Fig. 6, respectively), we realize that the profiles of N_{CO} and N_{C^+} are essentially the same for all the evolutionary stages. Nevertheless, the profile of N_C does change at high N_{H_2}: the average C column density at t_{evol} = 4 Myr is approximately one order of magnitude lower than at t_{evol} = 2 Myr.

We point out that, for $N_{H_2} \sim 10^{21} - 10^{22}$ cm^{-2}, the column density of neutral carbon is (depending on the snapshot considered) either the highest among the carbon-bearing species, or at least comparable with those of CO and C^+. We will get back to this consideration in Section 6.2, where we discuss the abundance of the carbon-bearing species.

These general considerations, even if already well-known in literature, are useful foe us to have a first overview of the regions traced by CO, C, and C^+ and give us a confirmation that, at least at a general, qualitative level, the NL99 network reproduces the known features of these three elements.
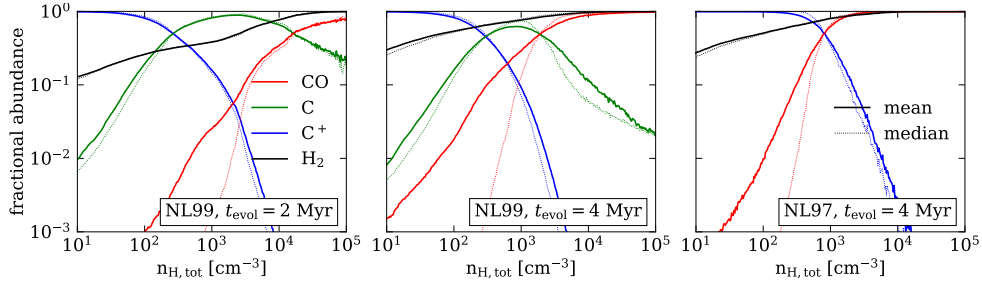
Figure 7: Fractional abundance of CO, C, C^+ (with respect to total carbon), and H_2 (with respect to total hydrogen) as a function of the total gas density $n_{H,tot}$. The plots refer to MC1-HD simulated with the NL99 network at $t_{evol} = 2$ (left) and 4 Myr (center), as well as to the same cloud simulated with the NL97 network at $t_{evol} = 4$ Myr (right), for comparison. The solid and the dotted lines represent the mean and the median values of the distributions for each $n_{H,tot}$ bin. Neutral carbon is the dominant species around $n_{H,tot} \sim 10^3$ cm^{-3}. A comparison between the plots for $t_{evol} = 2$ myr and $t_{evol} = 4$ Myr also shows the late formation of CO and H_2 in the cloud.

6.2

ABUNDANCE OF THE CARBON-BEARING SPECIES

6.2.1

RESULTS FROM THE NL99 SIMULATIONS

In the previous section we analysed the column density of CO, C, and C^+ as a function of the H_2 column density. The column density N is a projected quantity:

$$N = \int_{s_0}^{s_1} n(s')ds' \,, \tag{6.1}$$

where n is the number density, s' is the path length, and s_0 and s_1 are the limits of the column considered. The column density is thus an useful parameter, as information on projected quantities are in general the most straightforward to obtain from real observations. Nevertheless, it is worth to consider the number density n instead of the column density N in the analysis of the NL99 chemical network.

We show this analysis in Fig. 7, where we plot the mean (solid lines) and the median (dashed lines) of the fractional abundances of CO, C, C^+, and H_2 as a function of the total hydrogen number density. The left and the middle plots represent MC1-HD simulated with NL99 at $t_{evol} = 2$ and 4 Myr, respectively, and the right plot represents, for comparison, the cloud simulated with NL97 at $t_{evol} = 4$ Myr. The fractional abundances of the carbon-bearing species are intended with respect to total carbon, while the fractional abundance of H_2 is with respect to total hydrogen. We followed a similar binning procedure as we described for Fig. 6. All cells of the simulation have the same weight in this process, i.e., we did not mass-weighted, or volume-weighted, the quantities.

The most important information that we can obtain from Fig. 7 can be summarized as follows:

- The distributions are in general, for a given $n_{H,tot}$ bin, highly asymmetric: this is proved by the large differences between the mean and median values.

- C^+ is by far the dominant carbon-bearing species at low density, namely for $n_{\text{H,tot}} \lesssim 10^2$ cm^{-3}.

- CO is the dominant species at high density, namely for $n_{\text{H,tot}} \gtrsim 10^4$ cm^{-3}.

- The overall abundance CO and H$_2$, which are mostly present in dense regions of MCs, increases with t_{evol}. The time scale for the formation of H$_2$ and CO in MCs is of the order of several Myr.

- Neutral carbon is the dominant species for $n_{\text{H,tot}} \sim 10^3$ cm^{-3}. This is the case both for $t_{\text{evol}} = 2$ Myr and 4 Myr, but for $t_{\text{evol}} = 2$ Myr, C actually constitutes more than 80 per cent of total carbon for $n_{\text{H,tot}} \approx 2 \times 10^3$ cm^{-3}, and is the dominant species for a $n_{\text{H,tot}}$ range larger than an order of magnitude. At $t_{\text{evol}} = 4$ Myr, this phenomenon is mitigated by the larger amount of CO formed, but C nevertheless constitutes, in this density regime, about 50 per cent of total carbon. We discuss this aspect in detail in Section 6.2.2.

- The abundances of CO and C^+ in the NL97 network are higher than in the NL99, as the total carbon fractional abundance is the same (it is equal to 1.4×10^{-4} with respect to total hydrogen) and there is no neutral carbon. The neutral carbon modelled in NL99 is "distributed" between both CO and C^+ in NL97.

- The fractional abundance of H$_2$ presents, as a function of $n_{\text{H,tot}}$, a much shallower increase than CO. In other words, there are regions (those with $n_{\text{H,tot}} \lesssim 10^3$ cm^{-3}) which contain a non-negligible amount of H$_2$, but practically no CO. This is a confirmation of the existence of the aforementioned "CO-dark" areas in MCs.

Next, we look at the *cumulative fractional mass* of the carbon-bearing species as a function of $n_{\text{H,tot}}$. We define the cumulative fractional mass of the species X, $M_X/M_{X,\text{tot}}$, as

$$M_X/M_{X,\text{tot}} \left(n_{\text{H,tot}}^{\text{crit}} \right) = \frac{\sum_i m_{X,i}}{M_{X,\text{tot}}} \, , \tag{6.2}$$

where the sum runs over all the cells with $n_{\text{H,tot}} \leq n_{\text{H,tot}}^{\text{crit}}$, and $m_{X,i}$ is the mass of the species X in the i-th cell. Practically, this means that we calculate how much mass of a certain species X (with respect to the total mass of X in the cloud) comes from those regions of the cloud with a total density lower or equal than a given density threshold. This is done in Fig. 8, where we show the cumulative fractional masses of CO, C, C^+, and H$_2$ for MC1-HD with NL99 at $t_{\text{evol}} = 2$ and 4 Myr, as well as for the cloud with NL97 at $t_{\text{evol}} = 2$ Myr, for comparison.

We note that all the C^+ mass is located in regions with $n_{\text{H,tot}} \lesssim 10^3$ cm^{-3}, and all the C mass comes from regions with $n_{\text{H,tot}} \lesssim 10^4$ cm^{-3}. On the other hand, $M_{\text{CO}}/M_{\text{CO,tot}}$ keeps increasing up to $n_{\text{CO}}^{\text{crit}} = 10^6$ cm^{-3}, which means that the densest regions of the cloud still contribute significantly to the total CO mass.

This result is consistent with the column density profiles as a function of N_{H_2} that we showed in Fig. 6 and, in particular, with the fact that only N_{CO} keeps increasing for the highest N_{H_2} values. Both results indicate, indeed, that CO is the only tracer (among the carbon-bearing species) of the densest parts of the cloud. Furthermore, the cumulative fractional mass plots of Fig. 8 highlight once more that C is mostly associated with an intermediate $n_{\text{H,tot}}$ regime between those traced by C^+ and CO, confirming the considerations we made for the fractional abundance profiles of Fig. 7.
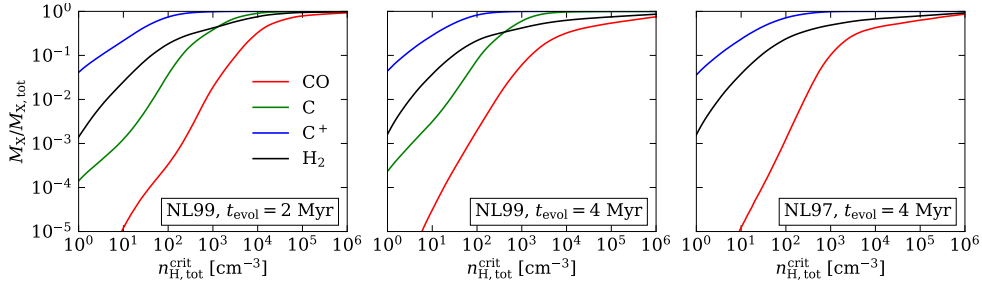
Figure 8: Cumulative fractional mass, $M_X/M_{X,\mathrm{tot}}$, of CO, C, C$^+$, and H$_2$ for MC1-HD simulated with the NL99 network at $t_{\mathrm{evol}} = 2$ and 4 Myr, and with the NL97 at $t_{\mathrm{evol}} = 4$ Myr, for comparison. All the C$^+$ and C mass are located in regions with $n_{\mathrm{H,tot}} \lesssim 10^3$ and 10^4 cm^{-3}, respectively. A non-negligible contribution to the mass of CO is given by regions with density up to $n_{\mathrm{H,tot}} \approx 10^6$ cm^{-3}. Atomic hydrogen does not follow precisely any of the profiles of the simulated carbon-bearing species.

It is also interesting to note here that $M_{\mathrm{H_2}}/M_{\mathrm{H_2,tot}}$ does not closely follow any of the profiles of the carbon-bearing species. Although CO is the best tracer for H$_2$ at high density, this is not true in lower density regime, where the abundance of H$_2$ is not closely associated with any of the simulated carbon-bearing species (see also Fig. 7).

As a final remark, we note that the relations between the different M_X and $n_{\mathrm{H,tot}}^{\mathrm{crit}}$ do not change in general significantly with t_{evol}. Nevertheless, while at $t_{\mathrm{evol}} = 2$ Myr we have $M_{\mathrm{CO}} \approx 1$ for $n_{\mathrm{H,tot}}^{\mathrm{crit}} = 10^6$ cm^{-3}, there is a few 10 per cent of the CO and H$_2$ mass coming from regions with $n_{\mathrm{H,tot}} > 10^6$ cm^{-3} at $t_{\mathrm{evol}} = 4$ Myr (note the log-scale on the y-axis). This is an immediate consequence of the fact that more very dense structures are present in the cloud at late stages than at early stages.

6.2.2

Comparison with other simulations and observations

A first, simple check of the reliability on the NL99 in giving the correct amount of CO, C, and C$^+$ can be performed by comparing the total mass of these species in our simulated clouds with the total mass of the same species in real MCs. To do so, we use the data of Beuther et al. (2014), where 4 different infrared-dark clouds (IRDCs) are analysed. Two of the clouds, namely G11.11 (Henning et al., 2010; Kainulainen et al., 2013) and G48.66 (Ossenkopf et al., 2011; Pitann et al., 2013) are relatively isolated clouds, with modest star formation activity. The third source, IRDC18223, is an infrared dark filament that has already formed a high-mass protostellar object with $\sim 10^4$ L$_\odot$ at one end (Beuther et al., 2010), and the last one, IRDC18454, is a starless dark cloud (Beuther et al., 2013). We remind that our simulated clouds with NL99 do not have any stellar feedback included, so the fact that some of these real clouds to which we are comparing the carbon-bearing abundances do have some ongoing star formation is a caveat to take into account. In any case, as they are still infrared-dark, we assume that the star formation process is at an early stage and, because of this, that the stellar feedback has not changed the chemical composition of those clouds dramatically yet.

In Table 6.2 we show the $m_{\mathrm{CO}}/m_{\mathrm{C^+}}$ and $m_{\mathrm{C}}/m_{\mathrm{C^+}}$ for MC1-HD and MC2-HD, both with NL97 and NL99, as well as the 4 IRDCs mentioned before. It is worth

Table 6.2: Total C/CO, CO/C$^+$, and C/C$^+$ mass ratio for the 4 clouds analyzed in Beuther et al. (2014) and for MC1-HD and MC2-HD at different t_{evol}, both with NL97 and NL99.

Cloud	network	t_{evol} [Myr]	$m_{\text{C}}/m_{\text{CO}}$	$m_{\text{CO}}/m_{\text{C}^+}$	$m_{\text{C}}/m_{\text{C}^+}$
G11.11			0.07	47.65	3.29
G48.66			0.08	1.76	0.14
IRDC18223			0.11	2.45	0.28
IRDC18454			0.12	0.65	0.08
MC1-HD	NL99	1.5	12.06	0.04	0.45
MC1-HD	NL99	2	1.78	0.3	0.53
MC1-HD	NL99	2.5	0.61	0.69	0.42
MC1-HD	NL99	3	0.38	0.89	0.34
MC1-HD	NL99	3.5	0.27	1.05	0.28
MC1-HD	NL99	4	0.21	1.18	0.24
MC1-HD	NL99	4.4	0.17	1.29	0.22
MC2-HD	NL99	1.5	5.00	0.07	0.37
MC2-HD	NL99	2	0.93	0.42	0.39
MC2-HD	NL99	2.5	0.42	0.72	0.31
MC2-HD	NL99	3	0.28	0.91	0.25
MC2-HD	NL99	3.5	0.21	1.01	0.21
MC2-HD	NL99	3.8	0.18	1.07	0.19
MC1-HD	NL97	2		0.57	
MC1-HD	NL97	3		0.80	
MC1-HD	NL97	4		0.98	
MC2-HD	NL97	2		0.61	
MC2-HD	NL97	3		0.86	
MC2-HD	NL97	4		0.99	

noting that Beuther et al. (2014) point out that the mass estimation is not extremely accurate (especially for C^+), as it depends on the emitting as temperature which is, in turn, the result of a somewhat rough estimation. Therefore, while the values reported in the table are definitely useful for a qualitative comparison with our simulated clouds, they should not be used as an exact comparison due to the relatively large margin of uncertainty.

We first discuss the m_C/m_{CO} ratio. The 4 observed clouds have this mass ratio in the range $0.07 - 0.12$, which is much smaller than the ranges in which the other two ratios vary. Furthermore, this ratio does not depend on the measurements of m_{C^+}, which are the most uncertain. Therefore, it is, among the three ratios, the most robust quantity to compare our simulations with. The values of m_C/m_{CO} that we obtain in our simulated clouds are all higher than the observed ones. This ratio decreases for increasing t_{evol} (as a consequence of the late formation of CO, see the discussion relative to Fig. 8) and at the latest time steps it is less than a factor of 2 larger than the average of the observed values, for both MC1-HD and MC2-HD. However, if the star formation process were not artificially switched off, stellar feedback would have started having an effect on the clouds much before than these last snapshots (we can realize it by comparing the non-feedback runs with the corresponding feedback runs, see Paper I, e.g. Fig. 2).

The other mass ratios are scattered over a much larger value range in the IRDCs observations. In particular, G11.11 presents really high m_{CO}/m_{C^+} and m_C/m_{C^+} values. Even if we exclude G11.11, however, we obtain values with a scatter of a factor of $3 - 4$. The m_{CO}/m_{C^+} values in our simulated clouds are scattered over a large value range as well and, apart from the values obtained for the first two snapshots of both MC1-HD and MC2-HD, they fall in the range covered by the values relative to the real observations. The m_C/m_{C^+} that we obtain are on average somewhat larger than those coming from real observations (excluding G11.11), but only of a factor 2 or less.

In conclusion, both the m_C/m_{CO} and m_C/m_{C^+} ratios of our simulations are larger than the values measured in the 4 IRDCs analyzed by Beuther et al. (2014), with the excess in the m_C/m_{CO} more significant than the other one because of the larger difference between the simulated and observed values and the smaller scatter in the observed values. This suggests than the NL99 network overpredicts the amount of neutral carbon in the MCs by a factor of a few. This is, however, only a primary suggestion, and robust conclusions cannot be drawn yet, because of the small number of real observations considered and, more importantly, because this comparison only considers the clouds as a whole, and ignores other factors (structure of the cloud, ISRF, and CRIR, for instance) which play a role in determining the relative abundance of the various chemical species.

In order to investigate this suggested overproduction of neutral carbon, we compare now our results with other simulations which use the same, or similar, chemical network. In particular, it is interesting to make a comparison with the various networks analyzed in Glover & Clark (2012) (hereafter GC12). There, a number of different networks are used to run the same simulation, and therefore can be directly compared. We are particularly interested in the network that they refer to "G10": that is the one described in detail in Glover et al. (2010) with grain-surface reactions included. It is the most similar to the network used in our simulations. It is worth noting that GC12 also use the chemical network of Nelson & Langer (1999), which they refer to as NL99 in their work. However, that network does not include any extra reactions that we have in our simulations (see Mackey et al., 2019,
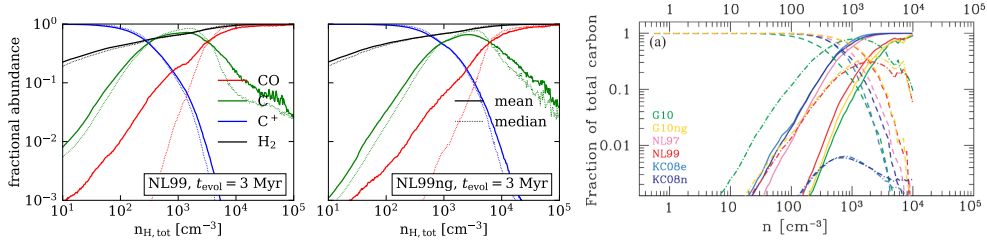
Figure 9: *Left and central panel*: Same as Fig. 7 for MC1-HD at t_{evol} = 3 Myr with (NL99) and without (NL99ng) grain-surface reactions included. *Right panel*: results of Glover & Clark (2012) (GC12) for different chemical network. Comparing our NL99 with G10 and our NL99ng with G10ng we note that the reduction in the amount of C is larger in GC12 than in our simulations.

for details) (in particular the dust-surface reactions). This is why the G10 network is actually the most similar to ours.

The G10 network overproduces neutral carbon with respect to what is observed: indeed, this gives $N_C/N_{CO} = 9.3$ in the GC12 simulation (N_X is the column density for the entire cloud), whereas the typical observed values are between 0.1 and 3 (Ingalls et al., 1997; Ikeda et al., 2002; Bensch et al., 2003; Beuther et al., 2014). This confirms the larger C/CO ratio with respect to real observations that we notice in our simulations, as well.

The excess of C is attributed by GC12 mostly to the grain-surface reactions. Indeed, simulations run excluding these reactions ("G10ng" network) have a significantly lower amount of neutral carbon: the C/CO ratio is, in this case, 2.2, which is closer to the observed values, although still in the upper range.

In order to check whether the grain-surface reactions are responsible for the overproduction of neutral carbon in our simulation as well, we run a simulation of MC1-HD with a modified chemical network, where we exclude the grain-surface reactions. We refer to it as "NL99ng". Then, we compare the fractional abundances of the carbon-bearing species obtained with the two networks and with the values obtained by GC12.

The result is shown in Fig. 9. In the left and center plot we show the fractional abundances of the carbon-bearing species as a function of $n_{\text{H,tot}}$ for MC1-HD at $t_{\text{evol}} = 3$ Myr with (left) and without (center) grain-surface reactions included, analogously to what we did in Fig. 7. The right plot is adapted from GC12 and shows the fractional abundances as a function of $n_{\text{H,tot}}$ for their simulations. The different colors represent the different network (see legend in the plot), and the different line styles represent the different species. In particular, solid lines represent CO, dashed lines represent C$^+$, and dash-dotted lines represent C. We are interested in comparing their run with the G10 (green) network with ours with NL99 (left), and their run with G10ng (yellow) with ours NL99ng (center). We summarize the relevant points as follows:

- **CO**: in our simulations, excluding grain-surface reactions leads to a decrease in the fractional abundance of CO at $n_{\text{H,tot}} \sim 10^3$ cm^{-3} and, to a small extent, also at $n_{\text{H,tot}} \gtrsim 10^4$ cm^{-3}. The differences between G10g and G10ng in this density regime are negligible. Overall, GC12 find a lower CO fractional abundance at low $n_{\text{H,tot}}$.

- **C$^+$**: Our simulations show a larger C$^+$ fractional abundance at $n_{\text{H,tot}} \sim 10^3$ cm^{-3} if grain-surface reactions are excluded. The same happens for GC12 as

well.

- **C**: Excluding dust-grain reduces the fractional abundance of about one order of magnitude at $n_{\text{H,tot}} \leq 10^2$ cm^{-3}. The fractional abundance is reduced to a progressively lower extent up to $n_{\text{H,tot}} \approx 2 \times 10^3$ cm^{-3}. The peak of the fractional abundance is slightly shifted towards higher $n_{\text{H,tot}}$. In high-density regions, $n_{\text{H,tot}} > 10^4$ cm^{-3}, the fractional abundance of C is slightly larger when grain-surface reactions are excluded. GC12 obtain a much larger reduction of the fractional abundance of C even at $n_{\text{H,tot}} \sim 10^3$ cm^{-3}, and their peak is slightly shifted to the right, too.

- **C/CO**: The $N_{\text{C}}/N_{\text{CO}}$ integrated over all the cloud that we obtain is 0.89 in NL99, and 0.75 with NL99ng. It is 9.3 and 2.2, respectively, in GC12.

The results obtained with the KOSMA-τ PDR models (Röllig et al., 2006) confirm a scenario where neutral carbon is not the clearly dominant carbon-bearing species at any $n_{\text{H,tot}}$. In those models, indeed, the fractional abundance at C is at most similar to the abundance of CO and C$^+$. The extinction coefficient A$_{\text{V}}$ at which the C fractional abundance peaks depends on the value of G_0 assumed, but the behavior described does not change. Similar results have also been recently found by Bisbas et al. (2023) with the novel PDFchem tool (with relevant differences for different ISRF and CRIR values).

From these considerations we conclude that excluding the grain-surface reactions leads to a reduction of the amount of C in our simulations, but to a lower extent than in GC12. Neutral carbon is particularly abundant in density regimes of $n_{\text{H,tot}} \sim 10^3$ cm^{-3}, where it is clearly the dominant species with up to approximately 80 per cent of total carbon in form of C at early evolutionary stages. The amount of C in our simulations is in excess with respect to what generally observed in MCs at these density regimes. However, the $N_{\text{C}}/N_{\text{CO}}$ values that we obtain are more in agreement with observations than the value obtained by GC12.

We use our NL99 network (with grain-surface reactions) for the synthetic emission maps that we describe in the next section.

6.3
CO, [CI], and [CII] emission maps

6.3.1
Overview of the emission maps

We now present the synthetic emission maps that we obtain with the NL99 simulations and analyse some of their properties.

We produce the emission maps using the same procedure described in Section 3.5. The collisional partners we used are again para-H$_2$, ortho-H$_2$, H, and He for CO and para-H$_2$, ortho-H$_2$, H, and electrons for C$^+$. Furthermore, we use para-H$_2$, ortho-H$_2$, H, H$^+$, He, and electrons as collisional partners for C. The collisional data concerning neutral carbon are all taken from the LAMDA database (Schöier et al., 2005).

In Fig. 10, we show the ^{12}CO $(1-0)$ (hereafter only CO), [CI] $(1-0)$ (hereafter only [CI]), and [CII] emission maps for MC1-HD at $t_{\text{evol}} = 2$, 3, and 4 Myr, in the same way we showed the column density maps in Fig. 5 (from left to right: CO, [CI], [CII]; from top to bottom: $t_{\text{evol}} = 2$, 3, 4 Myr). We recognise the nested CO-[CI]-[CII] structure that we already pointed out when analysing the corresponding
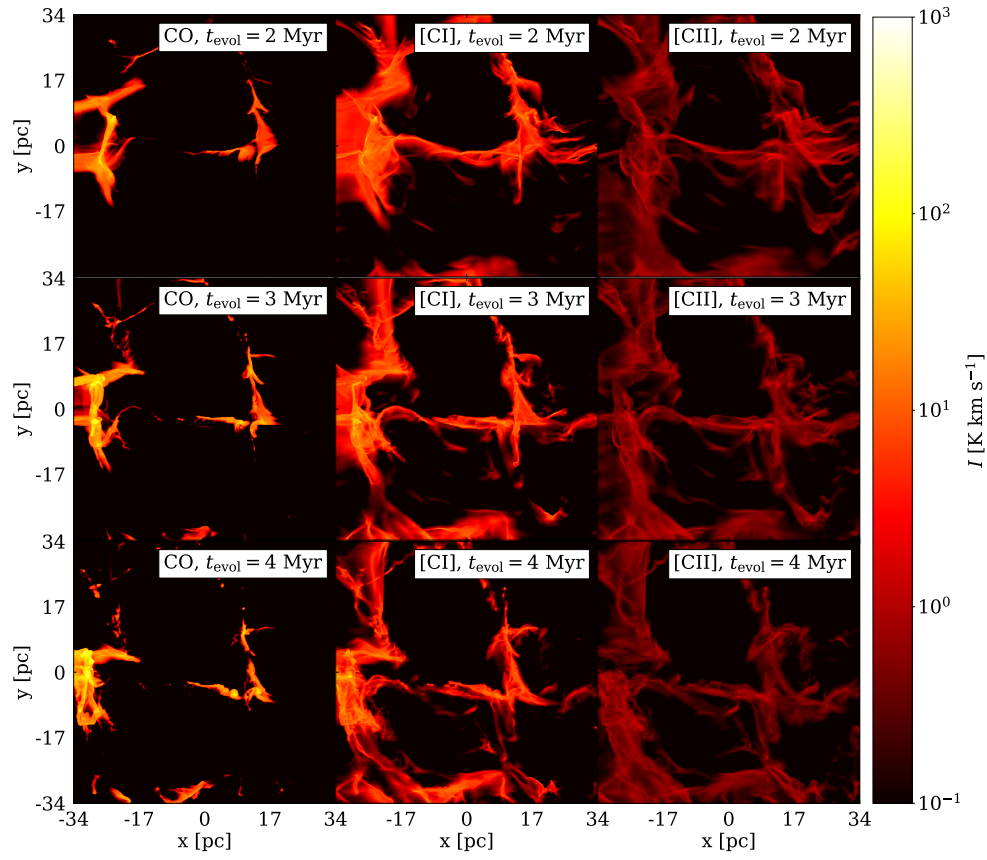
Figure 10: Synthetic emission maps of ^{12}CO $(1-0)$, [CI] $(1-0)$, and [CII] (from left to right) of MC1-HD at $t_{\mathrm{evol}} = 2$, 3, and 4 Myr (from top to bottom), simulated with the NL99 chemical network. The intensity is expressed in K km s^{-1}.

column density maps. However, in the case of the emission maps this structure seems less evident. This is a consequence of the fact that the the intensity of [CI] is in general lower than the intensity of CO, and, even more, the [CII] intensity is much lower than those of [CI] and CO. We point out, however, that given two species A and B, I_A can be larger than I_B in one unit system (e.g., K km s^{-1}), but not in another unit system (e.g., erg s^{-1} cm^{-2} sr^{-1}). In any case, the following analysis permits us to assess from which parts of the clouds the emission of CO, [CI], and [CII] come.

6.3.2

Origin of the CO, [CI], and [CII] emission

We are, now, interested in understanding which density regimes in MCs are associated with emission of CO, [CI], and [CII]. In order to do so, we use a procedure similar to that used to produce Fig. 8:

1. We select a number of density thresholds $n_{\mathrm{H,tot}}^{\mathrm{crit}}$.

2. For each $n_{\mathrm{H,tot}}^{\mathrm{crit}}$ we create a new collection of RADMC-3D input files where we set the density of all cells which have a "real" density $n_{\mathrm{H,tot}} > n_{\mathrm{H,tot}}^{\mathrm{crit}}$ to zero. Practically, we eliminate all the emission coming from regions with $n_{\mathrm{H,tot}} > n_{\mathrm{H,tot}}^{\mathrm{crit}}$.

3. We create emission maps for CO, [CI], and [CII] for each $n_{\mathrm{H,tot}}^{\mathrm{crit}}$ and calculate the total luminosity of the three species.

4. We produce cumulative luminosity plots, where the fraction of the total luminosity which comes from regions with $n_{\mathrm{H,tot}} < n_{\mathrm{H,tot}}^{\mathrm{crit}}$, to which refer as $L_X/L_{X,\mathrm{tot}}$, where X is the species of interest, is shown as a function of $n_{\mathrm{H,tot}}^{\mathrm{crit}}$.

This process is extremely computationally onerous, as it requires 3 separate RADMC-3D runs for each density threshold (one for each species), and the procedure is repeated for all the snapshots that we investigate. Therefore, we only do this operation for MC2-HD, $t_{\mathrm{evol}} = 2$ Myr and for MC1-MHD, $t_{\mathrm{evol}} = 4$ Myr. The analysis in Section 6.2, and in particular Fig. 8, showed that the species abundances as a function of $n_{\mathrm{H,tot}}$ changes only marginally for different clouds and t_{evol}. Therefore, we are expect the general trend not to change, at least in its fundamental features. The result of this operation is shown in Fig. 11 for MC2-HD at $t_{\mathrm{evol}} = 2$ Myr, and MC1-MHD at $t_{\mathrm{evol}} = 5$ Myr. the dashed, vertical lines represent the $n_{\mathrm{H,tot}}^{\mathrm{crit}}$ associated to $L_X/L_{X,\mathrm{tot}} = 0.5$. The colored areas represent the interquartile range, i.e., the $n_{\mathrm{H,tot}}^{\mathrm{crit}}$ region where $0.25 \leq L_X/L_{X,\mathrm{tot}} \leq 0.75$, so, practically, the density regime from which most of the emission of the species X comes. The values of $n_{\mathrm{H,tot}}^{\mathrm{crit}}$ associated to a specific $L_X/L_{X,\mathrm{tot}} = 0.5$ are achieved through interpolation.

We clearly recognise that [CII], [CI], and CO are associated, in this order, with progressively denser areas, as suggested already by looking at the column density and emission maps (Figs. 5 and 10) and the fractional abundance plots (Figs. 7 and 9). More specifically, we note in Fig. 11 that the [CII] emission is associated with $n_{\mathrm{H,tot}} \lesssim 10^2$ cm^{-3}, the [CI] emission is associated with $n_{\mathrm{H,tot}} \sim 10^2 - 10^3$ cm^{-3}, and CO is associated with $n_{\mathrm{H,tot}} \sim 10^3$ cm^{-3}. The position of the interquartile range, however, changes by a factor of a few between MC2-HD and MC1-MHD: the values given above about the typical density regimes associated with the different species are thus only a general indication. The interquartile ranges are different
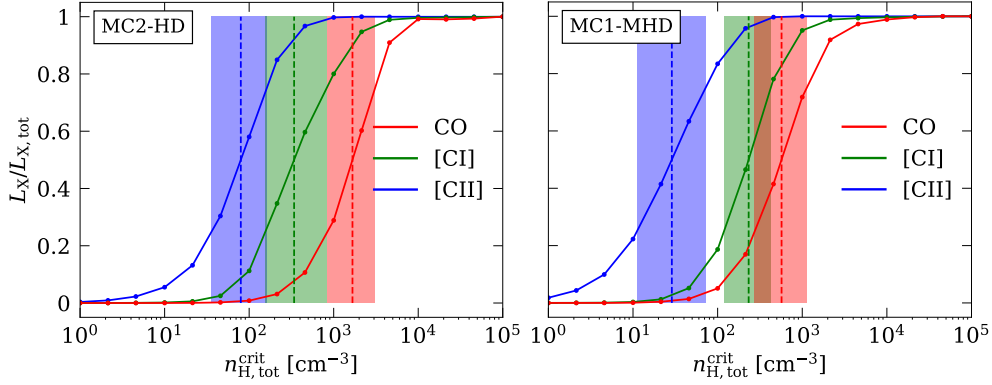
Figure 11: Cumulative luminosity $L_X/L_{X,\text{tot}}$ as a function of $n_{\text{H,tot}}^{\text{crit}}$ for CO, [CI], and [CII] for MC2-HD and MC1-MHD at $t_{\text{evol}} = 2$ and 5 Myr, respectively. Each data poin represents the traction of the total luminosity coming from the regions of the clouds with $n_{\text{H,tot}} < n_{\text{H,tot}}^{\text{crit}}$. The shaded areas represent the interquartile ranges, and the dashed lines represent the $n_{\text{H,tot}}^{\text{crit}}$ associated with 50 per cent of the total luminosity. The nested CO-[CI]-[CII] structure is recognisable, with differences in values of a factor of a few between the two clouds.

for different clouds mostly as a consequence of the overall density and structure of the cloud: in our case, MC2-HD is more compact than MC1-MHD (because there is no magnetic field, see Seifried et al., 2020; Ganguly et al., 2022). Therefore, the emission of all these species comes, on average, from denser regions, especially that of species which trace high-density regimes (CO, in our case). In any case, these changes are of a factor of a few at most, and do not change the picture of the nested CO-[CI]-[CII] emission.

This analysis is conceptually similar to the one performed in Fig. 8, where we showed the cumulative mass, instead of the luminosity, as a function of $n_{\text{H,tot}}^{\text{crit}}$. Indeed, the values that we obtain, for a given species, of $M_X/M_{X,\text{tot}}$ are comparable, within a factor of a few, to the values of $L_X/L_{X,\text{tot}}$ at the same $n_{\text{H,tot}}^{\text{crit}}$. This can intuitively be explained by the fact that the emission coefficient j_ν depends on the number density of emitters in the upper level n_u (Eq. (2.13)), which depends in turn, on LTE, the gas temperature and the total density n (Eq.(2.21)). Assuming that the temperature where the emitters of a certain species are located within the cloud is roughly constant (as they trace gas with similar properties), we can approximate $j_\nu \propto n_u$. This approximation is not valid any more if the gas is far from equilibrium or if the temperature range within which the emitters find themselves is large. For instance, we expect that the similarities between Fig. 8 and Fig. 11 would break down if we considered runs with stellar feedback included.

As a final remark, we note that optical thickness can, in principle, have an impact on the results coming from the procedure described above: if a line is optically thick above a certain $\tilde{n}_{\text{H,tot}}^{\text{crit}}$, the total luminosity calculated with two different $n_{\text{H,tot}}^{\text{crit}} > \tilde{n}_{\text{H,tot}}^{\text{crit}}$ will be very similar as a consequence of optical thickness, and not because of the lack of emitters at high $n_{\text{H,tot}}$. A method to estimate the effect of optical thickness is described in Franeck et al. (2018). There, the same analysis we performed is made also by considering, for each $n_{\text{H,tot}}^{\text{crit}}$, the cells with $n_{\text{H,tot}} > n_{\text{H,tot}}^{\text{crit}}$, i.e., using the reverse logic. Then, by comparing the results obtained with the two methods, the impact of optical thickness can be estimated. However, onlythe [CII] is investigated there. Franeck et al. (2018) find that this impact is limited for [CII].
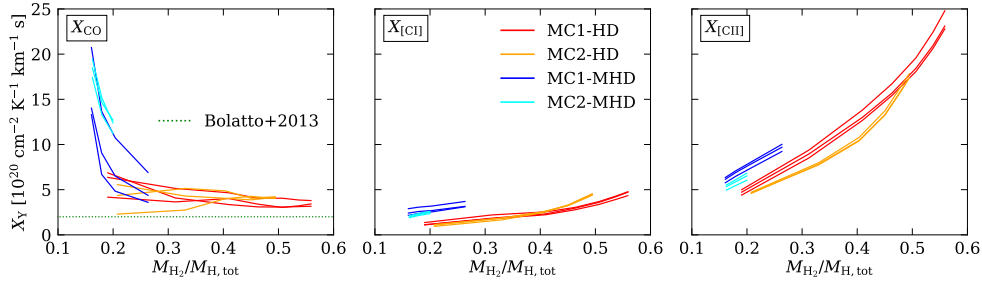
Figure 12: X_{CO}, $X_{[CI]}$, and $X_{[CII]}$ (from left to right, respectively) as a function of the H_2 mass fraction, $M_{H_2}/M_{H,tot}$, for 4 MCs simulated with NL99. We analyse, for each cloud, several snapshots at different t_{evol}. The lines join the values for the different snapshots. Three different LOS (x-, y-, and z-axis) are shown for each cloud. The green, dotted line represents the X_{CO} factor for the MW determined by Bolatto et al. (2013).

We speculate, however, that it can be somewhat larger for CO, as it is more optically thick in our clouds than [CII] (see Paper I).

6.3.3

The X_{CO}, $X_{[CI]}$, and $X_{[CII]}$ factors

In this section and in the following one we use the simulations with NL99 to reproduce some of the results of Paper I and highlight the most important differences.

In Paper I, we find that the X_{CO} factor for the simulated clouds ranges from $0.5 - 4.5 \times 10^{20}$ cm^{-2} K^{-1} km $^{-1}$ s (feedback runs are included in Paper I). We show in Fig. 12, left panel, the results obtained for the simulations with NL99. Although the dependence of X_{CO} on $M_{H_2}/M_{H,tot}$ does not change in general (roughly constant values for the HD clouds, and much larger values for the MHD clouds at low $M_{H_2}/M_{H,tot}$), the X_{CO} factor with NL99 is overall $4 - 5$ times larger than in the simulations with the NL97 network. Because of this, we always obtain values larger than the commonly used "standard" X_{CO} for the MW, equal to 2×10^{20} cm^{-2} K^{-1} km^{-1} s (Bolatto et al., 2013). This reference value is, on the other hand, within the range obtained in our simulations with NL97.

Similar considerations apply for the $X_{[CII]}$ factor as well (Fig. 12, right panel), especially at low $M_{H_2}/M_{H,tot}$. Indeed, we find values within the range $0.5 - 12$ cm^{-2} K^{-1} km^{-1} s with NL97, and higher of a factor $2 - 4$ with NL99. The increase in $X_{[CII]}$ for increasing $M_{H_2}/M_{H,tot}$ is evident with both networks, as well as the slightly higher values for the MHD runs than for HD runs, at a given $M_{H_2}/M_{H,tot}$.

With NL99 we can calculate the $X_{[CI]}$ as well, which is not possible in NL97. This is shown in Fig. 12, central panel. The values we obtain range from 1 to 5 cm^{-2} K^{-1} km^{-1} s, with only a shallow dependence on $M_{H_2}/M_{H,tot}$ ($X_{[CI]}$ slightly increases with increasing H_2 fractional abundance), and somewhat larger values for MHD runs than for HD runs at given $M_{H_2}/M_{H,tot}$. The $X_{[CI]}$ is therefore, according to the simulations with NL99, a more robust estimator of the amount of molecular hydrogen in a MC than X_{CO} and $X_{[CII]}$, as the values obtained cover a smaller range than for the other two conversion factors (we refer to Paper I for more details on the usage of the X factors). However, this result needs to be considered with great caution, since an analysis of runs with stellar feedback included would be necessary as well, and the accuracy of the NL99 in modelling the abundance of C is, as we already discussed, questionable. Possibly because of the overproduction
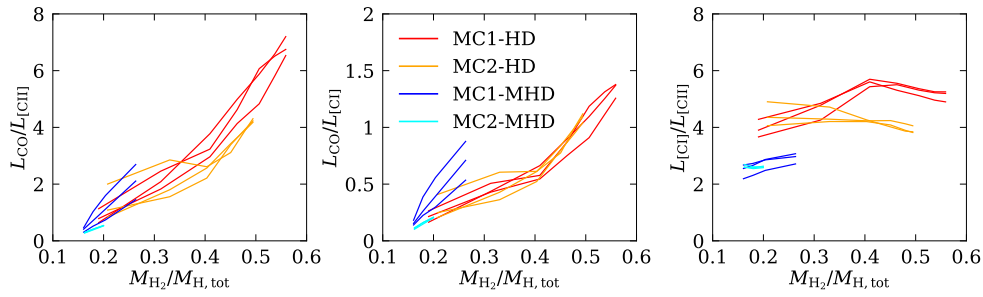
Figure 13: Total luminosity ratios as a function of $M_{H_2}/M_{H,tot}$ for 4 MCs simulated with NL99. From left to right: $L_{CO}/L_{[CII]}$, $L_{CO}/L_{[CI]}$, and $L_{[CI]}/L_{[CII]}$. The meaning and the color coding of the plotted lines are the same as in Fig. 12

.

of C, the values of $X_{[CI]}$ that we obtain are significantly lower than those found in other similar works: as an example, Offner et al. (2014) find $X_{[CI]} = 1.1 \times 10^{21}$ cm^{-2} K^{-1} km^{-1} s for simulated Galactic clouds. They also find $X_{CO} = 3 \times 10^{20}$ cm^{-2} K^{-1} km^{-1} s for the same cloud, which is fairly close to the reference value of Bolatto et al. (2013). This suggests that the post-processing with 3D-PDR used in Offner et al. (2014) might be more accurate in determining the abundance of the carbon-bearing species than our NL99 network. This is, anyway, only a speculation, and more detailed analysis should be performed to draw more robust conclusions.

6.3.4

LINE RATIOS AS TRACERS OF MOLECULAR HYDROGEN

Next, we investigate the capability of total luminosity ratios to trace the H_2 mass fraction $M_{H_2}/M_{H,tot}$ in MCs. In Paper I, we analyse the $L_{CO}/L_{[CII]}$ ratio for clouds simulated with NL97, we motivate the reason why we choose to use this quantity as a diagnostic tool for $M_{H_2}/M_{H,tot}$, and comment on the result obtained, including some comparison with real data of observed MCs. We refer to Paper I for more details on this aspect. Here, we repeat this analysis with the NL99 network, and highlight the relevant differences. In Fig. 13, left panel, we show $L_{CO}/L_{[CII]}$ as a function of $M_{H_2}/M_{H,tot}$ for the 4 simulated clouds. The luminosity ratio monotonically increases with the H_2 mass fraction. The $L_{CO}/L_{[CII]}$ values obtained, for any given $M_{H_2}/M_{H,tot}$, have a scatter within a factor ~ 2. We do not note evident differences in the behavior of the MHD clouds with respect to the HD clouds, at least within the available data. In Paper I, Fig. 7, the same relation is shown for NL97. The values of $L_{CO}/L_{[CII]}$, for given $M_{H_2}/M_{H,tot}$, are comparable within the two networks. However, even excluding the feedback runs (present in Paper I, but not here), we note that the scatter is larger in NL97 than in the runs analyzed here.

The NL99 network permits to calculate $L_{CO}/L_{[CI]}$ and $L_{[CI]}/L_{[CII]}$ as well. These are shown, as a function of $M_{H_2}/M_{H,tot}$, in the central and right plot of Fig. 13, respectively. The $L_{CO}/L_{[CI]}$ ratio increases with increasing $M_{H_2}/M_{H,tot}$ in similar manner to $L_{CO}/L_{[CII]}$, described before. The values obtained for MC1-MHD are significantly different from the values obtained for the HD clouds, and this suggests that the CO/[CI] ratio might be a less robust tracer of the molecular content of a MC than the CO/[CII] ratio, which does not exhibit significant differences between HD and MHD clouds. In any case, a more quantitative analysis and the inclusion of feedback runs, would be needed to draw more reliable conclusions on this aspect.

The $L_{[CI]}/L_{[CII]}$ ratio, shown in the right panel of Fig. 13, does not present any visible correlation with the H_2 mass fraction, and there is not a common trend among the different clouds. Therefore, it is unlikely that this line ratio can be meaningfully used as an H_2 mass fraction tracer in MCs.

6.4
SUMMARY ON THE COMPARISON BETWEEN NL97 AND NL99

In this chapter, we analysed the relative abundance of the carbon-bearing species in our simulations performed with the NL99 chemical network, namely CO, C, and C^+, as well as some quantities related to the line emission maps associated with these carbon-bearing species. We compared our results with the analogous ones obtained with simulations which include the simpler NL97 network instead (most of these results are described in detail in Paper I) and to other simulation and observational works, in order to assess the reliability of NL99.

We find that NL99 qualitatively reproduces the general properties of CO, C, and C^+ in molecular clouds well: a nested CO-C-C^+ structure is easily recognizable in column density maps (Fig. 5), in fractional abundance plots (Fig. 7), in synthetic emission maps (Fig. 10), and in cumulative luminosity plots (Fig. 11).

Even if the distribution of CO, C, and C^+ qualitatively matches this well-known nested structure, the abundance of neutral carbon in our simulated clouds is probably overpredicted by a factor of a few. It is difficult to draw concrete conclusions about this, because the relative abundance of the various carbonaceous species changes between different (real) clouds as a consequence of numerous factors: metallicity, CRIR, ISRF, magnetic fields, density and structure of the clouds. Therefore, comparisons between our simulated clouds and real observations should be made with great caution. In any case, the reasons we claim that C is actually overpredicted can be summarized as follows:

- The m_C/m_{CO} and the N_C/N_{CO} ratios in our clouds are by a factor of a few larger than in several different Galactic clouds;

- This discrepancy is observed (even to a larger extent) for other simulations, by other authors, which use chemical networks similar to our NL99;

- Neutral carbon is, in our simulations, the dominant carbon-bearing species at $n_{H,tot} \sim 10^3$ cm^{-3}, with even up to 80 per cent of total carbon in form of C. Several PDR models show a lower carbon abundance in this density regime.

- The X_{CO} factor, calculated in the NL99 simulations, is several times larger than the observed typical Galactic value, even though our simulations are performed in solar neighborhood conditions. The same simulations, run with NL97, provide X_{CO} values closer to the observed Galactic value.

Since C is overpredicted, CO and C^+ are necessarily underpredicted in our NL99 simulations, since the total amount of carbon is fixed. Therefore, it is likely that the simulations performed with NL97 provide more reliable abundances of CO and C^+, which are the two carbon-bearing species used for the research work of Paper I and Paper II. The simulations used in those papers are, indeed, performed with the NL97 chemical network.

7

SUMMARY AND CONCLUSION

7.1
Summary

In this work, we produce and analyse synthetic emission maps of simulated molecular clouds in order to determine a correspondence between observable quantities and important characteristics of the clouds, which are not directly measurable. In particular, we focus our attention on the fraction of molecular gas in the clouds and on the impact of stellar feedback on the structure of the clouds. To do so, we use some of the simulations performed within the SILCC-Zoom project, which study formation of dense, molecular gas in a supernova-driven, turbulent interstellar medium in a stratified galactic disc with the size of a few hundred parsecs in solar neighborhood conditions. Feedback from stellar ionizing radiation, external magnetic fields, interstellar radiation fields, cosmic rays, and a chemical network for some of the most relevant species observed in the interstellar medium are included. The chemical evolution of the clouds is calculated *on-the-fly*.

In Chapter 6 we study the accuracy of one possible chemical network, available for our simulations, in reproducing some observed features of the carbon-bearing species in molecular clouds. This network, which we refer to as "NL99", includes 18 chemical species, among which, crucially, carbon monoxide (CO), neutral carbon (C), and ionized carbon (C^+).

We analyse the abundance of these three species in several simulations and we find that this network qualitatively reproduces the distribution of such species observed in real clouds and in other simulation works. In particular, we find a clear nested CO-C-C^+ structure in our cloud, i.e., CO is mostly present in the diffuse regions of the cloud, C in denser regions, and CO is mostly located in the densest cores of the clouds. We note this by looking at column density maps of our simulated clouds (Fig. 5), and, more quantitatively, at the fractional abundance of these species as a function of the total hydrogen density (Fig. 7). This structure is reflected in the resulting ^{12}CO $(1-0)$, [CI], and [CII] synthetic emission maps (Fig. 10).

These emission maps enable to calculate the X_{CO}, $X_{[CI]}$, and $X_{[CII]}$ conversion factors, i.e., to investigate the correspondence between a measured line luminosity and the amount of molecular hydrogen in the cloud. We find $X_{CO} \sim 3 - 20 \times 10^{20}$ cm^{-2} K^{-1} km^{-1} s, therefore, on average, a factor of a few larger than the typical Galactic value. We also find $X_{[CI]} \sim 1 - 5 \times 10^{20}$ cm^{-2} K^{-1} km^{-1} s, and $X_{[CII]}$ values strongly dependent the evolutionary stages of the cloud. This leads us to identify, in principle, the $X_{[CI]}$ factor as the most reliable one. We also associate the $L_{CO}/L_{[CII]}$, $L_{CO}/L_{[CI]}$, and $L_{[CI]}/L_{[CII]}$ with the H$_2$ mass fraction of the clouds, and we find that $L_{CO}/L_{[CII]}$ and $L_{CO}/L_{[CI]}$ trace, to some extent, the molecular fraction of the clouds (at least in the simulations without feedback considered here), although with significant uncertainty.

A comparison between the total CO, C, and C^+ mass in our simulated clouds

with data from real clouds, as well as between our data, other simulated clouds and PDR models, shows that C is overproduced in our simulations, and CO and C^+ are consequently underproduced. Overall, there is a probable excess in C mass of a factor of a few. The overproduction mostly happens in regions where $n_{H,tot} \sim 10^3$ cm^{-3}. This overproduction is reflected in the higher values of X_{CO} obtained (as CO is underproduced) with respect to the standard Galactic value.

In Paper I, we repeat the analysis performed in Chapter 6 including, now, also simulated clouds with stellar feedback included. We use the simpler NL97 chemical network, which provides more reliable abundances for CO nd C^+ (but it does not include neutral carbon). In order to accurately model the amount of C^+ in the HII regions, we post-process the simulations with a novel tool based on CLOUDY models which calculates the amount of C^+ converted into C^{2+} by the stellar ionizing radiation. We find that this post-processing step is relevant, as it reduces the total C^+ luminosity by up to 60 per cent (Paper I, Fig. 6).

We find that the presence of stellar feedback undermines the correlation between $L_{CO}/L_{[CII]}$ and the H_2 mass fraction that we find in Chapter 6 (and in Paper I as well for non-feedback runs). Therefore, we cannot use this line ratio as a tracer of the molecular content of a cloud. An analysis of a *pixel-by-pixel* correlation between $I_{CO}/I_{[CII]}$ and the column density ratio $N_{H_2}/N_{H,tot}$ leads to analogous conclusions.

Our results also show that evolving the chemistry to equilibrium leads to significant differences in terms of species abundance with respect to a non-equilibrium, *on-the-fly* during the simulations (Paper I, Fig. 12). This is particularly true for clouds at early evolutionary stages. At equilibrium, the H mass decreases and the H_2 increases by up to a factor of 2. The changes for CO and C^+ are somewhat lower. Significant differences between equilibrium and non-equilibrium cases are present for the total CO and [CII] luminosity as well (Paper I, Fig. 13).

In Paper II, we focus our attention on clouds with included stellar feedback and study the [CII] and the FIR continuum emission from within the HII regions. Then, we enlarge our view to the entire clouds, and investigate how $L_{[CII]}$, L_{FIR}, and their ratio $L_{[CII]}/L_{FIR}$ change with the evolution of the clouds as a consequence of the stellar feedback.

We find that, with some simplification, the evolution of a HII region, when observed in [CII] and in FIR emission, can be divided in two phases. The first phase is characterized by small HII regions with very high I_{FIR} as a consequence of the dust heating, determined by the stellar radiation, and the high dust density in the region. The [CII] line is bright, but is saturated, and this leads to $I_{[CII]}/I_{FIR} \sim 10^{-5} - 10^{-4}$, well below the values obtained for the rest of the cloud. The second phase, which corresponds to a later evolutionary stage, is characterized by larger HII regions with moderate FIR emission, and very little [CII] emission. This is due to the redistribution of gas and dust towards colder regions because of the stellar feedback (causing a decrease both in $I_{[CII]}$ and I_{FIR}) and the further ionization of C^+, converted then into C^{2+}, causing a further reduction of $I_{[CII]}$.

The evolution of $L_{[CII]}$, L_{FIR}, and their ratio on entire clouds is essentially a consequence of the evolution of the various HII regions present in the cloud. A first phase, where the low $I_{[CII]}/I_{FIR}$ ratio is only observed in the small, young clouds, is characterized by overall $L_{[CII]}/L_{FIR} \sim 10^{-2}$. Then, a second phase corresponds to the enlargement of the HII regions: most of the [CII] emission comes from the excited C^+ ions in the regions far from the formed stars, and the dust is progressively pushed towards the colder regions of the cloud. In this phase, typic-

ally $L_{\text{[CII]}}/L_{\text{FIR}} \sim 10^{-3}$. A last phase can be identified with the excitation of most of the C^+ present in the cloud, which leads to an increase of $L_{\text{[CII]}}/L_{\text{FIR}}$. New star formation phases in the cloud can also affect the evolution of $L_{\text{[CII]}}/L_{\text{FIR}}$. Overall, this leads to a relation between $L_{\text{[CII]}}/L_{\text{FIR}}$ and $L_{\star,\text{tot}}$ which can be fitted with a power-law. This relation holds up to a point where a significant part of the dust is pushed towards cold regions of the cloud, and most of the C^+ ions are excited because of the stellar radiation.

Furthermore, we note that projection effects can change the shape of the HII regions significantly, and even create apparent HII regions, i.e., cavities devoid of [CII] emission in the center, and very [CII]-bright in the rims, which are actually the result of the complex geometry of the clouds and not of the presence of massive stars in their center.

7.2

Conclusion

This project arises from the necessity to build bridges between numerical simulations and real observations of the ISM and molecular clouds. To pursue this goal, we first investigate the characteristics of the chemical networks adopted in our simulations; then, we produce synthetic emission maps, whose features we try to associate with specific properties of the clouds.

The complexity of molecular clouds is the characteristic which most prominently emerges from the work described in this thesis. Complexity is a feature of the simulations analyzed in this work as well: indeed, the initial onset of instabilities in the simulated interstellar medium by means of turbulence produced by SN explosions, the detailed treatment of heating and cooling processes, self-gravity, chemistry, and stellar feedback make the simulations we analysed very rich in terms of phenomena reproduced. This must be considered an advantage of these simulations, as it permits to face with the real complexity of the clouds, and therefore makes it unlikely to find, for instance, a certain relation which holds in a simplified model, but does not for more realistic ones.

A primary consequence of this complexity is the difficulty in finding observable quantities which can be clearly and unambiguously associated with some properties of the clouds. The large scatter in the X_{CO} or the $L_{\text{CO}}/L_{\text{[CII]}}$ values that we found for given H_2 mass fraction (Paper I) is a good example of this, as it indicates that the CO and the [CII] emission are not only a function of the H_2 abundance, but of a lot of other factors as well. In other words, that the chemical and the dynamical evolution of the cloud do depend on each other in a complex interplay. Indeed, most of the results of this work are, more than precise laws which associate a certain quantity with another one, trends which highlight some of the physics of the interstellar medium. This is the case, for instance, of the nested CO-C-C^+ structure in MCs and the changes in $L_{\text{[CII]}}$, L_{FIR}, and $L_{\text{[CII]}}/L_{\text{FIR}}$ with the evolution of the clouds.

There are, however, some important take-home messages from this work. We list them in the following, in form of answers to the scientific questions we posed at the very beginning of this work (Chapter 1). We refer to Section 7.1 for a more detailed summary of all the results obtained.

- *To which extent the chemical networks we use are reliable in predicting the observed abundances and properties of the species of our interest?*

  We performed our simulations with two different chemical networks: a simpler NL97 and a more complex NL99 network. For us, the most relevant difference is that NL99 includes neutral carbon, while NL97 does not. Both networks qualitatively reproduce the known typical distributions of the carbon-bearing species in MCs, but NL99 gives abundances quantitatively inaccurate by a factor of a few, and more in specific density regimes. The NL97 is likely to reproduce the abundances of CO and C^+ more accurately.

- *How can be the molecular hydrogen in the interstellar medium be traced adequately by the other chemical species that we model?*

  The distribution of molecular hydrogen is not well traced by any of the carbon-bearing species we analyzed in the entire clouds. Instead, each of the used carbon-bearing species traces a different density regime of the cloud, and therefore the molecular hydrogen present in those density regimes. We could not find a line ratio capable of accurately tracing molecular hydrogen in molecular clouds, especially when we consider the effects of stellar feedback.

- *Which physical phenomena must be taken into account to accurately reproduce the observed [CII] line emission coming from HII regions?*

  The reactions modelled in the chemical network used are essential to reproduce the correct abundance of C^+. Besides this, the HII regions are permeated by strong radiation coming from the massive stars that they contain. This radiation can further ionize C^+ into C^{2+}. It is essential to model this phenomenon when considering the [CII] emission from HII regions. Otherwise, the emission could be strongly overestimated.

- *Which information can be obtained about the evolution of HII regions and star-forming molecular clouds by analysing their [CII] and FIR continuum emission?*

  Stellar feedback has a primary role in determining the evolution of the [CII] and FIR luminosity of a molecular cloud across its life cycle in a quite complex way, with different phases and different phenomena involved. However, we identify a relation between $L_{[CII]}/L_{FIR}$ and the total stellar luminosity of the cloud, which is valid for the first part of the life cycle of the cloud. This relation can be fitted by means of a power-law.

7.3

OUTLOOK

We propose that this work can be extended in three different ways: by increasing the number of simulated and analyzed clouds, by considering more chemical species in the analysis, and by investigating more in detail the dynamics of the clouds.

We considered 8 MCs in this work, of which 4 are with stellar feedback included and the other 4 are with no feedback. In both cases, 2 of the clouds are simulated with an external magnetic field, and 2 of them without it. This means that we analyzed 4 pairs of clouds with the same characteristics. Since our simulations are very complex in terms of modelled physical phenomena, even the clouds with the same characteristics are actually quite different to each other. As an example, the

average density of MC2-MHD is much lower than the density of MC1-MHD, which leads to a much lower star formation rate in MC2-MHD. Similarly, star formation in MC2-HD is faster than in MC1-HD, and more massive stars are formed. Therefore, the evolution of MC2-HD is faster and the HII regions cover, in the last steps of our simulations, a much larger portion of MC2-HD than in MC1-HD. This means that it is somewhat difficult to identify which are the typical properties of MCs, which are common to most of them, and those which are, instead, the result of the peculiar configuration of a specific cloud. In this context, a larger number of clouds to analyse, even if really expensive in terms of both computational and analysis time, would be beneficial.

The analysis of the distribution and the emission of other chemical species would also throw new light on the thermal and chemical phases of MCs. For instance, OH could be a good tracer of the CO-dark areas, and possibly a gas thermometer as well. Furthermore, other molecules and molecular ions, like ArH^+, HCO^+, HF, HCl, HCN, and many more, could efficiently trace the densest parts of the clouds, for which the CO lines easily become optically thick. A large number of observational works have been published in recent years concerning these species, so a comparison with real observations would be potentially doable as well.

In this work, we only considered the moment 0 maps of our synthetic emission maps. In other words, when studying line emission we neglected the information about the velocity of the gas along the LOS. This kind of information, however, can help in distinguishing between different emitting sources along the same LOS, and can provide useful information about the dynamics of the clouds. This is particularly true for the HII regions, for which velocity information provide important insights on their evolution.

A

APPENDIX: THE C$^+$ → C^{2+} PHOTOIONIZATION POST-PROCESSING PIPELINE

In this Appendix, we provide the technical description of the post-processing pipeline used to model the second ionization of carbon in regions affected by stellar radiation. We refer to Section 3.6 for the theoretical description of the physics beyond it.

These script must be used after creating the RADMC input file with the pipeline mentioned in Section 3.6[1]. It is very important to make sure to use the version of this pipeline which also writes down the E_{ion} values for each cell (*ionizing_flux.inp*), as well as the cell size (*cell_size.inp*) and the position of the cell centers (*cell_centers.inp*), otherwise these scripts do not work.

This pipeline is composed of 5 files. We describe them in the order they shall be used.

1. CREATION OF THE CLOUDY INPUT FILES (CREATE_CLOUDY_INPUT.PY)

The first part of the post-processing routine consists in the creation of the CLOUDY input files. The user defines the range of E_{ion} (euve), n_{gas} (gdens), T_g (temp_cell), and $T_\star$ (temp_star) and the number of steps in which the range should be divided. The routine then creates one input file for each possible parameter combination. The elemental abundance and the CRIR are, in this version of the routine, hard-coded.

```python
import numpy as np
import math
import astropy.constants as const
import os

#The first term is the minimum value, the second is the
 #maximum value, and the last one is the number of steps.
#Ranges are given in log-scale:
#euve = np.linspace(-18, -8, 21) means
#10^-18 <= euve <= 10^-8 in 21 log-spaced steps.

euve = np.linspace(-18, -8, 21)  #Ionizing density energy
#as given in flash
gdens = np.linspace(-26, -20, 19)  #Gas density in g/cm^3
temp_cell = np.linspace(1.5, 4.5, 19) #in K
temp_star = np.linspace(3.5, 5.5, 21) #in K

#This is the assumed star-cell distance.
```

```python
#It has to be >> than the size of the cell.
#By default it is 100 pc.
sc_dist = 100


def Planck_function(x):

    return x**3 / (math.exp(x) - 1.)


#This returns the bolometric flux, given the ionizing
#flux (>13.6 eV), a temperature T and blackbody assumption.
def compute_bol_flux(ion_flux, T):

    from scipy.integrate import quad
    nu_ion = 3290034591619891    #in Hz corresponds to 13.6 eV
    import astropy.constants as const
    h = const.h.value*1e7
    c = const.c.value*1e2
    k_B = const.k_B.value*1e7
    expo = h*nu_ion/(k_B*T)

    const_value = (2./c**2)*((k_B*T)**4 /(h**3))

    small, small_err = quad(lambda x: Planck_function(x), 0, expo)
    small = const_value*((math.pi)**4/15. - small)
    large = const_value*((math.pi)**4/15.)

    return ion_flux/(small/large)


#This returns the luminosity of a star with given temperature
#which produces the given euve (=ionizing energy density)
#when located at sc_dist (see above).
def give_luminosity_from_flux(flux, temp):

    real_flux = flux * const.c.value*1e2
    bol_flux = compute_bol_flux(real_flux, temp)
    distance = sc_dist*const.pc.value*1e2
    lum = bol_flux*4*math.pi*distance*distance

    return lum


#hdens is the total number hydrogen density and it is based
#on the givan total gas density
hdens = []
for i in range(0, len(gdens)):
    gdens[i] = math.pow(10, gdens[i])
    gdens[i] = (gdens[i]/(const.m_p.value*1e3))/1.4
    hdens.append(math.log10(gdens[i]))
```

```python
#Cloudy needs the star temperature in linear value.
for i in range(0, len(temp_star)):
    temp_star[i] = math.pow(10, temp_star[i])



#HERE THE CLOUDY INPUTS ARE WRITTEN DOWN
#One file per every possible paramter combination is created.
import glob

try:
    os.mkdir('./Cloudy_input')
except:
    print ('Cloudy_input directory exists')

input_done = glob.glob("Cloudy_input/*.in")
count = 0

for i in range(0, len(euve)):
    for j in range(0, len(hdens)):
        for k in range(0, len(temp_cell)):
            for t in range(0, len(temp_star)):

                id = str(count)
                name = 'Cloudy_input/cell_' + id + '.in'


                #If i-th input file is already in the
                #directory, it is not overwritten.
                skip = False
                for x in range(0, len(input_done)):
                    if input_done[x] == name:
                        skip = True
                        print count
                #Here the instruction for CLOUDY are
                #written in each input file
                if skip == False:
                    f = open(name, 'w')

                    #This is the ''title'' of each input file
                    title = 'cell_' + id
                    f.write('title ')
                    f.write(title)
                    f.write ('\n')

                    #We assume that stars emit as a blackbody
                    f.write('blackbody ')
                    f.write(str(temp_star[t]))
                    f.write(' K')
                    f.write('\n')
```

```python
#The ionizing flux (euve) is converted into
#bolometric luminosity
this_flux = math.pow(10, euve[i])
lum = give_luminosity_from_flux(this_flux, temp_star[t])
luminosity = math.log10((lum/1e7)/const.L_sun.value)
f.write('luminosity ')
f.write(str(luminosity))
f.write(' solar')
f.write('\n')

#We include the CMB (although it probably
#has very little effect)
f.write('CMB')
f.write('\n')

#The temperature of the cell is the T_gas
#that we use
f.write('constant temperature ')
f.write(str(temp_cell[k]))
f.write('\n')

#The distance from the star to the cell
#is set to 100 pc
distance = math.log10(99.5*const.pc.value*1e2)
f.write('radius ')
f.write(str(distance))
f.write('\n')

#The density of the cell is the n_gas
#that we use
h_density = hdens[j]
f.write('hden ')
f.write(str(h_density))
f.write('\n')

#This is a stop instruction to CLOUDY
#(stop when temerature drops below 10 K)
f.write('stop temperature 1')
f.write('\n')

#The depth of a cell is fixed to 1 pc
depth = math.log10(const.pc.value*1e2)
f.write('stop depth ')
f.write(str(depth))
f.write('\n')

#CRIR, carbon and helium abundances
cr = math.log10(3.*1e-17)
cab = math.log10(1.4*1e-4)
```

```python
heab = math.log10(1e-1)

carb = str(cab)
f.write('element_abundance_carbon_')
f.write(carb)
f.write('\n')

hel = str(heab)
f.write('element_abundance_helium_')
f.write(hel)
f.write('\n')

#oxygen abundance
f.write('element_abundance_oxygen_-3.49485\n')

cosmic = str(cr)
f.write('cosmic_ray_rate_')
f.write(cosmic)
f.write('\n')

#This regulates the accuracy of the calculation
f.write('iterate_to_convergence')
f.write('\n')

#This reduces the amount of output generated
f.write('print_quiet')
f.write('\n')

#This makes cloudy save all the "good"
#values, an not all the iterations
#prior to convergence
f.write('save_last_iteration')

nameovr = 'cell_' + id + '.ovr'
#This determines the type of output generated
f.write('_overview_"')
f.write(nameovr)
f.write('"')
f.write('\n')

f.close()

count += 1
```

2. RUN CLOUDY MODELS (RUN_CLOUDY.PY)

This script runs CLOUDY for each input filed constructed. It uses a variable number of cores, which can be set by the user, to speed the process up.

```python
#This script runs Cloudy for each .in file present
```

```python
#in the directory.
#This file must therefore be in the same directory
#where the .in files are.

import numpy as np
import math
from joblib import Parallel
from joblib import delayed
from scipy.special import zeta
import astropy.constants as const
import sys
import os

num_of_cores = 16

def run(files):
    os.system('cloudy -r %s' % files)

def run_cloudy(num_of_cores):

    import os
    import glob

    files = []
    filesout = []
    rawin = glob.glob("*.in")
    rawout = glob.glob("*.out")
    print len(rawin)
    print len(rawout)
    #sys.exit()
    for x in rawin:
        files.append(x[:-3])
    for x in rawout:
        filesout.append(x[:-4])

    files_to_process = []
    for i in range(0, len(files)):
        skip = False
        for j in range(0, len(filesout)):
            if files[i] == filesout[j]:
                skip = True
                #print (files[i], '    ', filesout[j])
        if skip == False:
            files_to_process.append(files[i])


    total = len(files_to_process)
    print('Got %d models' % total)

    del files
```

```python
    files = files_to_process

    # do it in parallel
    if num_of_cores == 1:
        for i in range(0, len(files)):
            run(files_to_process[i])

    elif num_of_cores > 1:
        Parallel(n_jobs=num_of_cores, verbose=100)(delayed(run)(files)
        for files in files)

    #os.chdir(dpath)


run_cloudy(num_of_cores)
```

3. Database creation (make_table_of_results.py)

This routine reads the raw CLOUDY output files and creates the database to be
used in the next steps. The database consists in different files, each of them is a
table containing the fractional abundance of the different species. When using this
file, it is important to note that:

- The parameter range has to be specified by the user in the first lines of the
  file. These have to be **identical** to those specified in create_cloudy_input.py,
  described before.

- The length of the cell has to be specified as well. Therefore, this file has to be
  run 4 times if, like in our case, one wants to create 4 different databases for
  cells with a size of 0.12, 0.24, 0.48, or 0.96 pc.

```python
import numpy as np
import math
import astropy.constants as const

#ATTENTION: Make sure that the following 4 lines are identical to
#the corrisponding ones in Create_cloudy_input.py
euve = np.linspace(-18, -8, 21)      #Ionizing density energy as given in flash
gdens = np.linspace(-26, -20, 19)       #Gas density in g/cm^3
temp_cell = np.linspace(1.5, 4.5, 19) #in K
temp_star = np.linspace(3.5, 5.5, 21) #in K

#This is the cell size for which you want to create the database.
this_cell_size = 0.96    #in pc

#The following routine reads an output file from cloudy
#and returns the c+ and c++ abundances. This is done by
#averaging the abundances given by cloudy, which are as
# a function of the depth of the pdr,
#up to the required depth  (thic_cell_size)
```

```python
def get_cii_ciii(file, final_depth):
    final_depth = final_depth*const.pc.value*100
    depth, hden, co, ci, cii, ciii =
    np.loadtxt(file, unpack=True, comments='#',
    usecols=(0, 3, 11, 12, 13, 14))
    depthnew = []
    hdennew = []
    conew = []
    cinew = []
    ciinew = []
    ciiinew = []

    for i in range(0, len(depth)):

        #1.4e-4 is the total carbon fractional abundance
        #respect to carbon. In a following version, this should
        #be modified so that it is not hard-coded any more

        conew.append((co[i]*1.4e-4)*hden[i])
        cinew.append((ci[i]*1.4e-4)*hden[i])
        ciinew.append((cii[i]*1.4e-4)*hden[i])
        ciiinew.append((ciii[i]*1.4e-4)*hden[i])


    mean_co = conew[0]
    mean_ci = cinew[0]
    mean_cii = ciinew[0]
    mean_ciii = ciiinew[0]
    dx = depth[0]

    #The following loop calculates the average
    i = 1
    while dx < final_depth and i < len(depth):
        mean_co += conew[i]*(depth[i] - depth[i-1])
        mean_ci += cinew[i]*(depth[i] - depth[i-1])
        mean_cii += ciinew[i]*(depth[i] - depth[i-1])
        mean_ciii += ciiinew[i]*(depth[i] - depth[i-1])
        dx += (depth[i] - depth[i-1])

        i += 1

    mean_co = mean_co/dx
    mean_ci = mean_ci/dx
    mean_cii = mean_cii/dx
    mean_ciii = mean_ciii/dx

    return mean_co, mean_ci, mean_cii, mean_ciii

#The table is constructed: the first 4 columns
#are the 4 quantities given as input (euve,
```

```python
#n_g , T_gas, T_star)

#The hydrogen number density is actually written in the
#database, not the total gas mass density

hdens = []
for i in range(0, len(gdens)):
    gdens[i] = math.pow(10, gdens[i])
    hdens.append((gdens[i]/(const.m_p.value*1e3))/1.4)


int_length = int(this_cell_size*100)
str_length = str(int_length)
name = 'results_table_'+str_length+'.dat'
f = open(name, 'w')
f.write('euve     hdens     T_cell     T_star     ndens_CO
ndens_CI     ndens_CII     ndens_CIII')
f.write('\n')

count = 0

#This is the loop over all the input parameters, each of them
#associated to one cloudy output.

for i in range(0, len(euve)):
    for j in range(0, len(hdens)):
        for k in range(0, len(temp_cell)):
            for t in range(0, len(temp_star)):

                name = 'Cloudy_input/cell_' + str(count) + '.ovr'
                try:
                    co, ci, cii, ciii = get_cii_ciii(name, this_cell_size)

                    f.write(str(euve[i]))
                    f.write('   ')
                    f.write(str(hdens[j]))
                    f.write('   ')
                    f.write(str(temp_cell[k]))
                    f.write('   ')
                    f.write(str(temp_star[t]))
                    f.write('   ')
                    f.write(str(co))
                    f.write('   ')
                    f.write(str(ci))
                    f.write('   ')
                    f.write(str(cii))
                    f.write('   ')
                    f.write(str(ciii))
                    f.write('\n')
```

```
            #This is a warning in case some cells are missing
            #or have invalid values
            except:
                print ('Warning:␣file␣', count, '␣with␣euve␣=␣',
                euve[i], ',␣hdens␣=␣', hdens[j], ',␣t_cell␣=␣',
                temp_cell[k], ',␣t_star␣=␣', temp_star[t], '
␣␣␣␣␣␣␣␣␣␣␣␣␣␣␣␣␣␣␣failed')
                count += 1


f.close()
```

4. INTERPOLATION OF THE DATABASE (WRITE_NEW_INPUT_FILE.PY)

The creation of the database, which is done by using the files described above, should be done only once. Provided that the typical variability range of the sampled parameters is the same, or similar, for all the clouds of interest, the database can be created once and then used for all the clouds and snapshots for which the post-processing is required. This is, indeed, the procedure we followed for post-processing the feedback runs analyzed in this thesis work.

On the other hand, the file described here has to be run for each snapshot that one wants to post-process. This file reads the original RADMC input files and, for each cell with with $E_{ion} \neq 0$, interpolates the database and determines the new number density of C^+. The command which runs the methods in this file is at the very end of the file, and it has 5 important options, which we describe now:

- **method**: it can be either "simple" or "full". We refer to Section 3.6 for the differences. It determines, however, the method used to calculate the new C^+ density, after interpolating the database.

- **star_file**: it is the star file given from FLASH with the information on the stars in the investigated snapshot. It is normally named "stars_xxxx.dat".

- **id_number**: It determines the name of the output file. For instance, if "method" is set to "simple" and "id_number" is set to "1", the output file is named "numberdens_co_simple_1.inp". This is done because it takes very long to post-process one entire snapshot. Therefore, this process can be somehow parallelized by launching multiple scripts, each of them post-processing one portion of the original "numberdens_cp.inp" (see next point).

- **begin** and **end** Indicate the start and the end point of the post-processing, in fraction of the total file.

An example clarifies the mechanism. If we are interested in splitting the post-processing of a certain snapshot in 4 parts, we launch this script 4 times. The 4 scripts will have the following parameters:

1. id_number = 1; begin = 0; end = 0.25;

2. id_number = 2; begin = 0.25; end = 0.5;

3. id_number = 3; begin = 0.5; end = 0.75;

4. id_number = 4; begin = 0.75; end = 1;

This creates 4 output files named "numberdens_cp_simple_X.inp", where X goes from 1 to 4.

```python
import numpy as np
import math
from joblib import Parallel
from joblib import delayed
from scipy.special import zeta
import astropy.constants as const
import sys

#This creates the new .inp file. It needs 4 databases, respectively
 for 0.12, 0.24, 0.48, and 0.96 pc.
#This is hard-coded in the write_new_cp_file_nd_interpolator method.
#See the end of this file fro the command description.

#This calculates, for each cell, which star has the
#larger flux, i.e., which one should be considered
#for the database interpolation
def find_closest_star(x, y, z, sx, sy, sz, l, t):

    min_distance = 1e50
    max_flux = 0

    index = 0
    index2 = 0
    lum = 0
    temp = 0
    dist_from_max_flux = 0
    for i in range(0, len(sx)):
        d = math.sqrt((x-sx[i])**2 + (y-sy[i])**2 + (z-sz[i])**2)

        l_W = l[i]*const.L_sun.value
        l_erg = l_W*1e7
        flux = l_erg/(4.*math.pi*d**2)


        if flux > max_flux:
            max_flux = flux
            index = i
            lum = l_erg
            temp = t[i]
            dist_from_max_flux = d

        if d < min_distance:
            min_distance = d
            index2 = i
            lum2 = l_erg
            temp2 = t[i]
```

```
    return index, lum, temp, dist_from_max_flux
```

This **is** the ''main'' function of this script
```python
def write_new_cp_file_nd_interpolator(method, star_file, id_number,
begin, end):

    import glob
    import os
    import astropy.constants as const
    from scipy.interpolate import LinearNDInterpolator

    try:
        os.rename('numberdens_cp.inp', 'numberdens_cp_nocloudy.inp')
    except:
        print ('')

    #Here all the relavant files are loaded
    cp_old = np.loadtxt('numberdens_cp_nocloudy.inp', unpack=True,
    skiprows=2)
    print ('cp loaded')

    hdens = np.loadtxt('gas_density.inp', unpack=True, skiprows=2)
    for i in range(0, len(hdens)):
        hdens[i] = (hdens[i]/1.4)/(const.m_p.value*1e3)
    print ('hdens loaded')

    euve = np.loadtxt('ionizing_flux.inp', unpack=True, skiprows=2)
    print ('euve loaded')

    tcell = np.loadtxt('gas_temperature.inp', unpack=True, skiprows=2)
    print ('tcell loaded')

    star_x, star_y, star_z, luminosity, T_eff = np.loadtxt(star_file,
    skiprows=1, unpack=True, usecols=(0, 1, 2, 4, 5))
    print ('stars loaded')

    x, y, z = np.loadtxt('cell_centers.inp', skiprows=2,
    unpack=True, usecols=(0, 1, 2))
    print ('cell centers loaded')

    cellsize = np.loadtxt('cell_size.inp', skiprows=2, unpack=True)
    print ('cell centers loaded')

    d_euve12, d_hdens12, d_tcell12, d_tstar12, d_co12, d_ci12,
    d_cii12, d_ciii12 = np.loadtxt('results_table_12.dat',
    skiprows=1, unpack=True)
    d_euve24, d_hdens24, d_tcell24, d_tstar24, d_co24, d_ci24,
    d_cii24, d_ciii24 = np.loadtxt('results_table_24.dat',
    skiprows=1, unpack=True)
    d_euve48, d_hdens48, d_tcell48, d_tstar48, d_co48, d_ci48,
```

```python
d_cii48, d_ciii48 = np.loadtxt('results_table_48.dat',
skiprows=1, unpack=True)
d_euve96, d_hdens96, d_tcell96, d_tstar96, d_co96, d_ci96,
d_cii96, d_ciii96 = np.loadtxt('results_table_96.dat',
skiprows=1, unpack=True)

print ('database_loaded')

for i in range(0, len(d_hdens12)):
    d_hdens12[i] = math.log10(d_hdens12[i])

for i in range(0, len(d_hdens24)):
    d_hdens24[i] = math.log10(d_hdens24[i])

for i in range(0, len(d_hdens48)):
    d_hdens48[i] = math.log10(d_hdens48[i])

for i in range(0, len(d_hdens96)):
    d_hdens96[i] = math.log10(d_hdens96[i])


#f and fstar are combinations of the quantities given in
#the database. 12, 24, 48, 96 refer to the cell size.
#f_interpXX and f_starinterp are the output of the
#interpolation routine
fstar12 = []
f12 = []
for i in range(0, len(d_cii12)):
    fstar12.append(d_cii12[i]/(1.4e-4*math.pow(10, d_hdens12[i])
    - d_co12[i] - d_ci12[i]))
    f12.append(d_cii12[i]/(1.4e-4*math.pow(10, d_hdens12[i])))
if method=='full':
    fstar_interp12 = LinearNDInterpolator(list(zip(d_euve12,
    d_hdens12, d_tcell12, d_tstar12)), fstar12)
elif method =='simple':
    f_interp12 = LinearNDInterpolator(list(zip(d_euve12,
    d_hdens12, d_tcell12, d_tstar12)), f12)

fstar24 = []
f24 = []
for i in range(0, len(d_cii24)):
    fstar24.append(d_cii24[i]/(1.4e-4*math.pow(10, d_hdens24[i])
    - d_co24[i] - d_ci24[i]))
    f24.append(d_cii24[i]/(1.4e-4*math.pow(10, d_hdens24[i])))
if method=='full':
    fstar_interp24 = LinearNDInterpolator(list(zip(d_euve24,
    d_hdens24, d_tcell24, d_tstar24)), fstar24)
elif method=='simple':
    f_interp24 = LinearNDInterpolator(list(zip(d_euve24,
    d_hdens24, d_tcell24, d_tstar24)), f24)
```

```python
fstar48 = []
f48 = []
for i in range(0, len(d_cii48)):
    fstar48.append(d_cii48[i]/(1.4e-4*math.pow(10, d_hdens48[i])
    - d_co48[i] - d_ci48[i]))
    f48.append(d_cii48[i]/(1.4e-4*math.pow(10, d_hdens48[i])))
if method=='full':
    fstar_interp48 = LinearNDInterpolator(list(zip(d_euve48,
    d_hdens48, d_tcell48, d_tstar48)), fstar48)
elif method=='simple':
    f_interp48 = LinearNDInterpolator(list(zip(d_euve48,
    d_hdens48, d_tcell48, d_tstar48)), f48)


fstar96 = []
f96 = []
for i in range(0, len(d_cii96)):
    fstar96.append(d_cii96[i]/(1.4e-4*math.pow(10, d_hdens96[i])
    - d_co96[i] - d_ci96[i]))
    f96.append(d_cii96[i]/(1.4e-4*math.pow(10, d_hdens96[i])))
if method=='full':
    fstar_interp96 = LinearNDInterpolator(list(zip(d_euve96,
    d_hdens96, d_tcell96, d_tstar96)), fstar96)
elif method=='simple':
    f_interp96 = LinearNDInterpolator(list(zip(d_euve96,
    d_hdens96, d_tcell96, d_tstar96)), f96)



read = open('numberdens_cp_nocloudy.inp', 'r')
str1 = read.readline()
str2 = read.readline()
read.close()


min_euve = min(d_euve12)
max_euve = max(d_euve12)
min_hdens = min(d_hdens12)
max_hdens = max(d_hdens12)
min_tcell = min(d_tcell12)
max_tcell = max(d_tcell12)
min_tstar = min(d_tstar12)
max_tstar = max(d_tcell12)

if method=='full':
    name = 'numberdens_cp_full_'+id_number+'.inp'
    write_full = open(name, 'w')
    write_full.write(str1)
    write_full.write(str2)

elif method=='simple':
```

```python
        name = 'numberdens_cp_simple_'+id_number+'.inp'
        write_simple = open(name, 'w')
        write_simple.write(str1)
        write_simple.write(str2)

nanc_s = 0
yesc_s = 0
nanc_f = 0
yesc_f = 0
warning = 0

#Here the original numberdens_cp.inp file is read
#in the portion post-processed by this script.
for i in range(int(begin*len(cp_old)), int(end*len(cp_old))):
    warning = 0
    #if the cell is empty or euve \simeq 0, the cell
    #is not interpolated
    if cp_old[i] < 1e-40 or euve[i] < 1e-40:

        if method=='full':
            write_full.write(str(cp_old[i]))
            write_full.write('\n')

        elif method=='simple':
            write_simple.write(str(cp_old[i]))
            write_simple.write('\n')

    else:
        star_number, lum, temp, dist = find_closest_star(x[i],
        y[i], z[i], star_x, star_y, star_z, luminosity, T_eff)


        euvelog = math.log10(euve[i])
        tcelllog = math.log10(tcell[i])
        hdenslog = math.log10(hdens[i])
        templog = math.log10(temp)

        #This assures that the values are within the database
        #limits. Otherwise, errors appear.
        if euvelog < min_euve:
            euvelog = min_euve+1e-4
            warning = 1

        if euvelog > max_euve:
            euvelog = max_euve-1e-4
            warning = 1

        if hdenslog < min_hdens:
            hdenslog = min_hdens+1e-4
            warning = 1
```

```python
if hdenslog > max_hdens:
    hdenslog = max_hdens-1e-4
    warning = 1


if tcelllog < min_tcell:
    tcelllog = min_tcell+1e-4
    warning = 1


if tcelllog > max_tcell:
    tcelllog = max_tcell-1e-4
    warning = 1


if templog < min_tstar:
    templog = min_tstar+1e-4
    warning = 1


if templog > max_tstar:
    temp = max_tstar-1e-4
    warning = 1



if warning == 1:
    print ('Limit at i = ', i)



size = cellsize[i]/(const.pc.value*100)

#Here the interpolation is actually performed.
#f_interp or fstar_interp are the interpolated
#values suitable for the cell unter examination
if size < 0.18:
    if method=='simple':
        f_interp = f_interp12(euvelog, hdenslog, tcelllog,
        templog)
    elif method=='full':
        fstar_interp = fstar_interp12(euvelog, hdenslog,
        tcelllog, templog)

elif size >= 0.18 and size < 0.36:
    if method=='simple':
        f_interp = f_interp24(euvelog, hdenslog, tcelllog,
        templog)
    elif method=='full':
        fstar_interp = fstar_interp24(euvelog, hdenslog,
        tcelllog, templog)

elif size >= 0.36 and size < 0.72:
    if method=='simple':
        f_interp = f_interp48(euvelog, hdenslog, tcelllog,
```

```
                        templog)
                elif method=='full':
                    fstar_interp = fstar_interp48(euvelog, hdenslog,
                    tcelllog, templog)

            else:
                if method=='simple':
                    f_interp = f_interp96(euvelog, hdenslog, tcelllog,
                    templog)
                elif method=='full':
                    fstar_interp = fstar_interp96(euvelog, hdenslog,
                    tcelllog, templog)


            #Here the output file is written
            if method=='simple':
                towrite_simple = f_interp*1.4e-4*hdens[i]
                write_simple.write(str(towrite_simple))
                write_simple.write('\n')

            elif method=='full':
                towrite_full = fstar_interp*cp_old[i]
                write_full.write(str(towrite_full))
                write_full.write('\n')

    if method=='simple':
        write_simple.close()
    elif method=='full':
        write_full.close()


write_new_cp_file_nd_interpolator(method=method, star_file=star_file,
 id_number='1', begin=0, end=0.05)


#method --> 'simple' or 'full'
#star_file --> the filw where to get information about the stars in
 the simulation
#id_number --> the created file will be called for example
 numberdens_cp_simple_3.inp, if id_number = '3'
#begin and end --> where to start and finish with respect of the
original .inp file. If begin = 0 and end = 1
#it processes the entire file. The idea is that varying id_number,
 begin and end you can parallelize the job.
```

5. JOINING THE POST-PROCESSED FILES (JOIN_INPUT.PY)

This routine is needed in case the post-processing has been parallelized and several
files have been created. This routine simply joins them together in one single file,
which has exactly the same format as the original, unprocessed, numberdens_cp.inp

```python
import numpy as np
from glob import glob

#This creates an unique .inp file in case you parallelized the
previous step by creating several files.

minimum = 1
maximum = 20
method = 'simple'

files = []

for i in range(1, maximum+1):
    number = str(i)
    str_simple = 'numberdens_cp_simple_'+number+'.inp'
    str_full = 'numberdens_cp_full_'+number+'.inp'

    if method=='simple':
        files.append(str_simple)
    elif method=='full':
        files.append(str_full)

if method=='simple':
    tot = open('numberdens_cp_simple.inp', 'w')
elif method=='full':
    tot = open('numberdens_cp_full.inp', 'w')

for i in range(0, len(files)):
    if i == 0:
        read = np.loadtxt(files[i], unpack=True)
        for j in range(0, len(read)):
            if j == 0 or j == 1:
                tot.write(str(int(read[j])))
                tot.write('\n')
            else:
                tot.write(str(read[j]))
                tot.write('\n')

    else:
        read = np.loadtxt(files[i], unpack=True, skiprows=2)
        for j in range(0, len(read)):
            tot.write(str(read[j]))
            tot.write('\n')

    print (i+1, ' done')
```

BIBLIOGRAPHY

Abel, N. P., Ferland, G. J., Shaw, G., & van Hoof, P. A. M., The H II Region/PDR Connection: Self-consistent Calculations of Physical Conditions in Star-forming Regions. 2005, ApJS, 161, 65

Ackermann, M., Ajello, M., Allafort, A., et al., Gamma-Ray Observations of the Orion Molecular Clouds with the Fermi Large Area Telescope. 2012, ApJ, 756, 4

Ali, A. A., Bending, T. J. R., & Dobbs, C. L., Stellar winds and photoionization in a spiral arm. 2022, MNRAS, 510, 5592

Allison, A. C. & Dalgarno, A., Photodissociation of Vibrationally Excited H_2, HD, and D_2 by Absorption into the Continua of the Lyman and Werner Systems. 1969, Atomic Data, 1, 91

Ambartsumian, V. A., Stellar Associations. 1949, AZh, 26, 3

André, P., Men'shchikov, A., Bontemps, S., et al., From filamentary clouds to pres-tellar cores to the stellar IMF: Initial highlights from the Herschel Gould Belt Survey. 2010, A&A, 518, L102

Arzoumanian, D., André, P., Peretto, N., & Könyves, V., Formation and evolution of interstellar filaments. Hints from velocity dispersion measurements. 2013, A&A, 553, A119

Bakes, E. L. O. & Tielens, A. G. G. M., The Photoelectric Heating Mechanism for Very Small Graphitic Grains and Polycyclic Aromatic Hydrocarbons. 1994, ApJ, 427, 822

Ballesteros-Paredes, J. & Hartmann, L., Remarks on Rapid vs. Slow Star Formation. 2007, Rev. Mexicana Astron. Astrofis., 43, 123

Beck, R. & Wielebinski, R. 2013, in Planets, Stars and Stellar Systems. Volume 5: Galactic Structure and Stellar Populations, ed. T. D. Oswalt & G. Gilmore, Vol. 5, 641

Becklin, E. E. & Neugebauer, G., Observations of an Infrared Star in the Orion Nebula. 1967, ApJ, 147, 799

Benjamin, R. A., Churchwell, E., Babler, B. L., et al., GLIMPSE. I. An SIRTF Legacy Project to Map the Inner Galaxy. 2003, PASP, 115, 953

Bensch, F., Leuenhagen, U., Stutzki, J., & Schieder, R., [C I] 492 GHz Mapping Observations of the High-Latitude Translucent Cloud MCLD 123.5+24.9. 2003, ApJ, 591, 1013

Berger, M. J. & Colella, P., Local Adaptive Mesh Refinement for Shock Hydro-dynamics. 1989, Journal of Computational Physics, 82, 64

Bergin, E. A., Alves, J., Huard, T., & Lada, C. J., N_2H^+ and $C^{18}O$ Depletion in a Cold Dark Cloud. 2002, ApJ, 570, L101

Berné, O., Marcelino, N., & Cernicharo, J., Waves on the surface of the Orion molecular cloud. 2010, Nature, 466, 947

Berné, O., Marcelino, N., & Cernicharo, J., IRAM 30 m Large Scale Survey of ^{12}CO(2-1) and ^{13}CO(2-1) Emission in the Orion Molecular Cloud. 2014, ApJ, 795, 13

Beuther, H., Henning, T., Linz, H., et al., From high-mass starless cores to high-mass protostellar objects. 2010, A&A, 518, L78

Beuther, H., Linz, H., Tackenberg, J., et al., Fragmentation and dynamical collapse of the starless high-mass star-forming region IRDC 18310-4. 2013, A&A, 553, A115

Beuther, H., Ragan, S. E., Ossenkopf, V., et al., Carbon in different phases ([CII], [CI], and CO) in infrared dark clouds: Cloud formation signatures and carbon gas fractions. 2014, A&A, 571, A53

Beuther, H., Schneider, N., Simon, R., et al., FEEDBACK from the NGC 7538 H II region. 2022, A&A, 659, A77

Binney, J. & Tremaine, S. 2008, Galactic Dynamics: Second Edition

Bisbas, T. G., Tan, J. C., & Tanaka, K. E. I., Photodissociation region diagnostics across galactic environments. 2021, MNRAS, 502, 2701

Bisbas, T. G., van Dishoeck, E. F., Hu, C.-Y., & Schruba, A., PDFCHEM: A new fast method to determine ISM properties and infer environmental parameters using probability distributions. 2023, MNRAS, 519, 729

Bjorkman, J. E. & Wood, K., Radiative Equilibrium and Temperature Correction in Monte Carlo Radiation Transfer. 2001, ApJ, 554, 615

Black, J. H. & Dalgarno, A., Models of interstellar clouds. I. The Zeta Ophiuchi cloud. 1977, ApJS, 34, 405

Bolatto, A. D., Wolfire, M., & Leroy, A. K., The CO-to-H_2 Conversion Factor. 2013, ARA&A, 51, 207

Bondi, H., On spherically symmetrical accretion. 1952, MNRAS, 112, 195

Borchert, E. M. A., Walch, S., Seifried, D., et al., Synthetic CO emission and the X_{CO} factor of young molecular clouds: a convergence study. 2022, MNRAS, 510, 753

Bouchut, F., Klingberg, C., & Waagan, K., A multiwave approximate Riemann solver for ideal MHD based on relaxation I: theoretical framework. 2007, Numer. Math., 108, 7

Bouchut, F., Klingberg, C., & Waagan, K., A multiwave approximate Riemann solver for ideal MHD based on relaxation II: numerical implementation with 3 and 5 waves. 2010, Numer. Math., 115, 647

Carlhoff, P., Nguyen Luong, Q., Schilke, P., et al., Large scale IRAM 30 m CO-observations in the giant molecular cloud complex W43. 2013, A&A, 560, A24

Cecchi-Pestellini, C., Bodo, E., Balakrishnan, N., & Dalgarno, A., Rotational and Vibrational Excitation of CO Molecules by Collisions with ^{4}He Atoms. 2002, ApJ, 571, 1015

Chabrier, G., The Galactic Disk Mass Budget. I. Stellar Mass Function and Density. 2001, ApJ, 554, 1274

Chevance, M., Krumholz, M. R., McLeod, A. F., et al., The Life and Times of Giant Molecular Clouds. 2022, arXiv e-prints, arXiv:2203.09570

Choudhuri, A. R. 1998, The physics of fluids and plasmas : an introduction for astrophysicists /

Churchwell, E., Babler, B. L., Meade, M. R., et al., The Spitzer/GLIMPSE Surveys: A New View of the Milky Way. 2009, PASP, 121, 213

Clark, P. C., Glover, S. C. O., Ragan, S. E., & Duarte-Cabral, A., Tracing the formation of molecular clouds via [C II], [C I], and CO emission. 2019, MNRAS, 486, 4622

Clarke, S. D. C. H. 2016, PhD thesis, Cardiff University, UK

Crespo, A. C., Dominguez, J. M., Barreiro, A., Gómez-Gesteira, M., & Rogers, B. D., GPUs, a New Tool of Acceleration in CFD: Efficiency and Reliability on Smoothed Particle Hydrodynamics Methods. 2011, PLoS ONE, 6, e20685

Dame, T. M. & Thaddeus, P., A CO Survey of the Entire Northern Sky. 2022, ApJS, 262, 5

de Graauw, T., Helmich, F. P., Phillips, T. G., et al., The Herschel-Heterodyne Instrument for the Far-Infrared (HIFI). 2010, A&A, 518, L6

Dedner, A., Kemm, F., Kröner, D., et al., Hyperbolic Divergence Cleaning for the MHD Equations. 2002, Journal of Computational Physics, 175, 645

Derigs, D., Winters, A. R., Gassner, G. J., & Walch, S., A novel high-order, entropy stable, 3D AMR MHD solver with guaranteed positive pressure. 2016, Journal of Computational Physics, 317, 223

Derigs, D., Winters, A. R., Gassner, G. J., & Walch, S., A novel averaging technique for discrete entropy-stable dissipation operators for ideal MHD. 2017, Journal of Computational Physics, 330, 624

Derigs, D., Winters, A. R., Gassner, G. J., Walch, S., & Bohm, M., Ideal GLM-MHD: About the entropy consistent nine-wave magnetic field divergence diminishing ideal magnetohydrodynamics equations. 2018, Journal of Computational Physics, 364, 420

Donate, E. & Magnani, L., Sensitive CO(1-0) survey in Pegasus-Pisces reduces CO-dark gas inventory by a factor of 2. 2017, MNRAS, 472, 3169

Draine, B. T., Photoelectric heating of interstellar gas. 1978, ApJS, 36, 595

Draine, B. T. 2011, Physics of the Interstellar and Intergalactic Medium

Draine, B. T. & Bertoldi, F., Structure of Stationary Photodissociation Fronts. 1996, ApJ, 468, 269

Duarte-Cabral, A., Acreman, D. M., Dobbs, C. L., et al., Synthetic CO, H_2 and H I surveys of the second galactic quadrant, and the properties of molecular gas. 2015, MNRAS, 447, 2144

Dubey, A., Fisher, R., Graziani, C., et al. 2008, in Astronomical Society of the Pacific Conference Series, Vol. 385, Numerical Modeling of Space Plasma Flows, ed. N. V. Pogorelov, E. Audit, & G. P. Zank, 145

Dullemond, C. P., Juhasz, A., Pohl, A., et al. 2012, RADMC-3D: A multi-purpose radiative transfer tool, Astrophysics Source Code Library, record ascl:1202.015

Dunne, L., Maddox, S. J., Papadopoulos, P. P., Ivison, R. J., & Gomez, H. L., Dust, CO, and [C I]: cross-calibration of molecular gas mass tracers in metal-rich galaxies across cosmic time. 2022, MNRAS, 517, 962

Elmegreen, B. G., Magnetic diffusion and ionization fractions in dense molecular clouds: the role of charged grains. 1979, ApJ, 232, 729

Elmegreen, B. G., Star Formation in a Crossing Time. 2000, ApJ, 530, 277

Elmegreen, B. G. & Scalo, J., Interstellar Turbulence I: Observations and Processes. 2004, ARA&A, 42, 211

Federrath, C., Banerjee, R., Clark, P. C., & Klessen, R. S., Modeling Collapse and Accretion in Turbulent Gas Clouds: Implementation and Comparison of Sink Particles in AMR and SPH. 2010, ApJ, 713, 269

Federrath, C., Sur, S., Schleicher, D. R. G., Banerjee, R., & Klessen, R. S., A New Jeans Resolution Criterion for (M)HD Simulations of Self-gravitating Gas: Application to Magnetic Field Amplification by Gravity-driven Turbulence. 2011, ApJ, 731, 62

Ferland, G. J., Chatzikos, M., Guzmán, F., et al., The 2017 Release Cloudy. 2017, Rev. Mexicana Astron. Astrofis., 53, 385

Ferrière, K. M., The interstellar environment of our galaxy. 2001, Reviews of Modern Physics, 73, 1031

Field, G. B., Thermal Instability. 1965, ApJ, 142, 531

Field, G. B., Goldsmith, D. W., & Habing, H. J., Cosmic-Ray Heating of the Interstellar Gas. 1969, ApJ, 155, L149

Fixsen, D. J., The Temperature of the Cosmic Microwave Background. 2009, ApJ, 707, 916

Franeck, A., Walch, S., Seifried, D., et al., Synthetic [C II] emission maps of a simulated molecular cloud in formation. 2018, MNRAS, 481, 4277

Fryxell, B., Olson, K., Ricker, P., et al., FLASH: An Adaptive Mesh Hydrodynamics Code for Modeling Astrophysical Thermonuclear Flashes. 2000, ApJS, 131, 273

Ganguly, S., Walch, S., Clarke, S. D., & Seifried, D., SILCC-Zoom: the dynamic balance in molecular cloud substructures. 2022, arXiv e-prints, arXiv:2204.02511

Gatto, A., Walch, S., Low, M. M. M., et al., Modelling the supernova-driven ISM in different environments. 2015, MNRAS, 449, 1057

Gatto, A., Walch, S., Naab, T., et al., The SILCC project - III. Regulation of star formation and outflows by stellar winds and supernovae. 2017, MNRAS, 466, 1903

Geen, S., Pellegrini, E., Bieri, R., & Klessen, R., When H II regions are complicated: considering perturbations from winds, radiation pressure, and other effects. 2020, MNRAS, 492, 915

Gerin, M. & Phillips, T. G., Atomic Carbon in Galaxies. 2000, ApJ, 537, 644

Gingold, R. A. & Monaghan, J. J., Smoothed particle hydrodynamics: theory and application to non-spherical stars. 1977, MNRAS, 181, 375

Girichidis, P., Walch, S., Naab, T., et al., The SILCC (SImulating the LifeCycle of molecular Clouds) project - II. Dynamical evolution of the supernova-driven ISM and the launching of outflows. 2016, MNRAS, 456, 3432

Glassgold, A. E. & Langer, W. D., Heating of Molecular-Hydrogen Clouds by Cosmic Rays and X-Rays. 1973, ApJ, 186, 859

Glover, S. C. O. & Clark, P. C., Approximations for modelling CO chemistry in giant molecular clouds: a comparison of approaches. 2012, MNRAS, 421, 116

Glover, S. C. O. & Clark, P. C., Is atomic carbon a good tracer of molecular gas in metal-poor galaxies? 2016, MNRAS, 456, 3596

Glover, S. C. O., Clark, P. C., Micic, M., & Molina, F., Modelling [C I] emission from turbulent molecular clouds. 2015, MNRAS, 448, 1607

Glover, S. C. O., Federrath, C., Mac Low, M. M., & Klessen, R. S., Modelling CO formation in the turbulent interstellar medium. 2010, MNRAS, 404, 2

Glover, S. C. O. & Mac Low, M.-M., Simulating the Formation of Molecular Clouds. I. Slow Formation by Gravitational Collapse from Static Initial Conditions. 2007a, ApJS, 169, 239

Glover, S. C. O. & Mac Low, M.-M., Simulating the Formation of Molecular Clouds. II. Rapid Formation from Turbulent Initial Conditions. 2007b, ApJ, 659, 1317

Glover, S. C. O. & Mac Low, M. M., On the relationship between molecular hydrogen and carbon monoxide abundances in molecular clouds. 2011, MNRAS, 412, 337

Goicoechea, J. R., Pety, J., Gerin, M., Hily-Blant, P., & Le Bourlot, J., The ionization fraction gradient across the Horsehead edge: an archetype for molecular clouds. 2009, A&A, 498, 771

Goicoechea, J. R., Teyssier, D., Etxaluze, M., et al., Velocity-resolved [CII] Emission and [CII]/FIR Mapping along Orion with Herschel. 2015, ApJ, 812, 75

Goldsmith, P. F., Molecular Depletion and Thermal Balance in Dark Cloud Cores. 2001, ApJ, 557, 736

Goldsmith, P. F. & Langer, W. D., Molecular cooling and thermal balance of dense interstellar clouds. 1978, ApJ, 222, 881

Goldsmith, P. F., Langer, W. D., Pineda, J. L., & Velusamy, T., Collisional Excitation of the [C II] Fine Structure Transition in Interstellar Clouds. 2012, ApJS, 203, 13

Gong, M., Ostriker, E. C., & Wolfire, M. G., A Simple and Accurate Network for Hydrogen and Carbon Chemistry in the Interstellar Medium. 2017, ApJ, 843, 38

Gorski, K. M., Wandelt, B. D., Hansen, F. K., Hivon, E., & Banday, A. J., The HEALPix Primer. 1999, arXiv e-prints, astro

Griffin, M. J., Abergel, A., Abreu, A., et al., The Herschel-SPIRE instrument and its in-flight performance. 2010, A&A, 518, L3

Guevara, C., Stutzki, J., Ossenkopf-Okada, V., et al., [C II] 158 μm self-absorption and optical depth effects. 2020, A&A, 636, A16

Habart, E., Walmsley, M., Verstraete, L., et al., Molecular Hydrogen. 2005, Space Sci. Rev., 119, 71

Habing, H. J., The interstellar radiation density between 912 A and 2400 A. 1968, Bull. Astron. Inst. Netherlands, 19, 421

Haffner, L. M., Dettmar, R. J., Beckman, J. E., et al., The warm ionized medium in spiral galaxies. 2009, Reviews of Modern Physics, 81, 969

Haid, S., Walch, S., Naab, T., et al., Supernova blast waves in wind-blown bubbles, turbulent, and power-law ambient media. 2016, MNRAS, 460, 2962

Haid, S., Walch, S., Seifried, D., et al., The relative impact of photoionizing radiation and stellar winds on different environments. 2018, MNRAS, 478, 4799

Haid, S., Walch, S., Seifried, D., et al., SILCC-Zoom: The early impact of ionizing radiation on forming molecular clouds. 2019, MNRAS, 482, 4062

Harada, T., Koshizuka, S., & Kawaguchi, Y. 2007, in EG Short Papers, ed. P. Cignoni & J. Sochor (The Eurographics Association)

Hartmann, L., Ballesteros-Paredes, J., & Bergin, E. A., Rapid Formation of Molecular Clouds and Stars in the Solar Neighborhood. 2001, ApJ, 562, 852

Hennebelle, P. & Falgarone, E., Turbulent molecular clouds. 2012, A&A Rev., 20, 55

Hennebelle, P. & Inutsuka, S.-i., The role of magnetic field in molecular cloud formation and evolution. 2019, Frontiers in Astronomy and Space Sciences, 6, 5

Henning, T., Linz, H., Krause, O., et al., The seeds of star formation in the filamentary infrared-dark cloud G011.11-0.12. 2010, A&A, 518, L95

Herrera-Camus, R., Sturm, E., Graciá-Carpio, J., et al., SHINING, A Survey of Far-infrared Lines in Nearby Galaxies. II. Line-deficit Models, AGN Impact, [C II]-SFR Scaling Relations, and Mass-Metallicity Relation in (U)LIRGs. 2018, ApJ, 861, 95

Heyminck, S., Graf, U. U., Güsten, R., et al., GREAT: the SOFIA high-frequency heterodyne instrument. 2012, A&A, 542, L1

Hildebrand, R. H., The determination of cloud masses and dust characteristics from submillimetre thermal emission. 1983, QJRAS, 24, 267

Holdship, J., Viti, S., Jiménez-Serra, I., Makrymallis, A., & Priestley, F., UCLCHEM: A Gas-grain Chemical Code for Clouds, Cores, and C-Shocks. 2017, AJ, 154, 38

Hollenbach, D. & McKee, C. F., Molecule Formation and Infrared Emission in Fast Interstellar Shocks. III. Results for J Shocks in Molecular Clouds. 1989, ApJ, 342, 306

Hopkins, P. F., The stellar initial mass function, core mass function and the last-crossing distribution. 2012, MNRAS, 423, 2037

Hopkins, P. F. 2014, GIZMO: Multi-method magneto-hydrodynamics+gravity code, Astrophysics Source Code Library, record ascl:1410.003

Hopkins, P. F., A new class of accurate, mesh-free hydrodynamic simulation methods. 2015, MNRAS, 450, 53

Hoyle, F. & Lyttleton, R. A., On the accretion theory of stellar evolution. 1941, MNRAS, 101, 227

Hu, C.-Y., Schruba, A., Sternberg, A., & van Dishoeck, E. F., Dependence of X_{CO} on Metallicity, Intensity, and Spatial Scale in a Self-regulated Interstellar Medium. 2022, ApJ, 931, 28

Iffrig, O. & Hennebelle, P., Mutual influence of supernovae and molecular clouds. 2015, A&A, 576, A95

Ikeda, M., Oka, T., Tatematsu, K., Sekimoto, Y., & Yamamoto, S., The Distribution of Atomic Carbon in the Orion Giant Molecular Cloud 1. 2002, ApJS, 139, 467

Ingalls, J. G., Chamberlin, R. A., Bania, T. M., et al., Atomic Carbon in Southern Hemisphere High-Latitude Clouds. 1997, ApJ, 479, 296

Inutsuka, S.-i., Inoue, T., Iwasaki, K., & Hosokawa, T., The formation and destruction of molecular clouds and galactic star formation. An origin for the cloud mass function and star formation efficiency. 2015, A&A, 580, A49

Janka, H.-T., Hanke, F., Hüdepohl, L., et al., Core-collapse supernovae: Reflections and directions. 2012, Progress of Theoretical and Experimental Physics, 2012, 01A309

Jeans, J. H., The Stability of a Spherical Nebula. 1902, Philosophical Transactions of the Royal Society of London Series A, 199, 1

Kabanovic, S., Schneider, N., Ossenkopf-Okada, V., et al., Self-absorption in [C II], ^{12}CO, and H I in RCW120. Building up a geometrical and physical model of the region. 2022, A&A, 659, A36

Kainulainen, J., Ragan, S. E., Henning, T., & Stutz, A., High-fidelity view of the structure and fragmentation of the high-mass, filamentary IRDC G11.11-0.12. 2013, A&A, 557, A120

Katz, H., Galligan, T. P., Kimm, T., et al., Probing cosmic dawn with emission lines: predicting infrared and nebular line emission for ALMA and JWST. 2019, MNRAS, 487, 5902

Katz, H., Kimm, T., Sijacki, D., & Haehnelt, M. G., Interpreting ALMA observations of the ISM during the epoch of reionization. 2017, MNRAS, 468, 4831

Kawamura, A., Mizuno, Y., Minamidani, T., et al., The Second Survey of the Molecular Clouds in the Large Magellanic Cloud by NANTEN. II. Star Formation. 2009, ApJS, 184, 1

Kennicutt, Robert C., J., The Global Schmidt Law in Star-forming Galaxies. 1998, ApJ, 498, 541

Klessen, R. S. & Glover, S. C. O., Physical Processes in the Interstellar Medium. 2016, Saas-Fee Advanced Course, 43, 85

Kolmogorov, A., The Local Structure of Turbulence in Incompressible Viscous Fluid for Very Large Reynolds' Numbers. 1941, Akademiia Nauk SSSR Doklady, 30, 301

Kroupa, P., On the variation of the initial mass function. 2001, MNRAS, 322, 231

Lada, E. A. & Blitz, L., Two Populations of Diffuse Molecular Clouds. 1988, ApJ, 326, L69

Lagache, G., Cousin, M., & Chatzikos, M., The [CII] 158 μm line emission in high-redshift galaxies. 2018, A&A, 609, A130

Langer, W. D., Pineda, J. L., Goldsmith, P. F., et al., The dense warm ionized medium in the inner Galaxy. 2021, A&A, 651, A59

Langer, W. D., Pineda, J. L., & Velusamy, T., The scale height of gas traced by [C ii] in the Galactic plane. 2014a, A&A, 564, A101

Langer, W. D., Velusamy, T., Morris, M. R., Goldsmith, P. F., & Pineda, J. L., Kinematics and properties of the central molecular zone as probed with [C II]. 2017, A&A, 599, A136

Langer, W. D., Velusamy, T., Pineda, J. L., et al., C^+ detection of warm dark gas in diffuse clouds. 2010, A&A, 521, L17

Langer, W. D., Velusamy, T., Pineda, J. L., Willacy, K., & Goldsmith, P. F., A Herschel [C ii] Galactic plane survey. II. CO-dark H_2 in clouds. 2014b, A&A, 561, A122

Leroy, A. K., Rosolowsky, E., Usero, A., et al., Low-J CO Line Ratios from Single-dish CO Mapping Surveys and PHANGS-ALMA. 2022, ApJ, 927, 149

Leroy, A. K., Walter, F., Bigiel, F., et al., Heracles: The HERA CO Line Extragalactic Survey. 2009, AJ, 137, 4670

Leroy, A. K., Walter, F., Brinks, E., et al., The Star Formation Efficiency in Nearby Galaxies: Measuring Where Gas Forms Stars Effectively. 2008, AJ, 136, 2782

Leung, C. M., Radiation transport in dense interstellar dust clouds. 1975, ApJ, 199, 340

Leung, T. K. D., Olsen, K. P., Somerville, R. S., et al., Predictions of the $L_{[CII]}$-SFR and [CII] Luminosity Function at the Epoch of Reionization. 2020, ApJ, 905, 102

Li, Z.-Y., Krasnopolsky, R., & Shang, H., Non-ideal MHD Effects and Magnetic Braking Catastrophe in Protostellar Disk Formation. 2011, ApJ, 738, 180

Liang, L., Feldmann, R., Murray, N., et al., [C_{II}] 158 ¯m emission as an indicator of galaxy star formation rate. 2023, arXiv e-prints, arXiv:2301.04149

Lohner, R., An adaptive finite element scheme for transient problems in CFD. 1987, Computer Methods in Applied Mechanics and Engineering, 61, 323

Lucy, L. B., A numerical approach to the testing of the fission hypothesis. 1977, AJ, 82, 1013

Lucy, L. B., Computing radiative equilibria with Monte Carlo techniques. 1999, A&A, 344, 282

Luisi, M., Anderson, L. D., Schneider, N., et al., Stellar feedback and triggered star formation in the prototypical bubble RCW 120. 2021, Science Advances, 7, eabe9511

Lupi, A., Pallottini, A., Ferrara, A., et al., Predicting FIR lines from simulated galaxies. 2020, MNRAS, 496, 5160

Mac Low, M.-M. & Klessen, R. S., Control of star formation by supersonic turbulence. 2004, Reviews of Modern Physics, 76, 125

Mackey, J., Walch, S., Seifried, D., et al., Non-equilibrium chemistry and destruction of CO by X-ray flares. 2019, MNRAS, 486, 1094

MacNeice, P., Olson, K. M., Mobarry, C., de Fainchtein, R., & Packer, C., PARA-MESH: A parallel adaptive mesh refinement community toolkit. 2000, Computer Physics Communications, 126, 330

Madden, S. C., Cormier, D., Hony, S., et al., Tracing the total molecular gas in galaxies: [CII] and the CO-dark gas. 2020, A&A, 643, A141

Martins, F., Schaerer, D., Hillier, D. J., & Heydari-Malayeri, M., Puzzling wind properties of young massive stars in SMC-N81. 2004, A&A, 420, 1087

Mathis, J. S., Rumpl, W., & Nordsieck, K. H., The size distribution of interstellar grains. 1977, ApJ, 217, 425

Matzner, C. D., On the Role of Massive Stars in the Support and Destruction of Giant Molecular Clouds. 2002, ApJ, 566, 302

McKee, C. F. & Ostriker, E. C., Theory of Star Formation. 2007, ARA&A, 45, 565

McKee, C. F. & Ostriker, J. P., A theory of the interstellar medium: three components regulated by supernova explosions in an inhomogeneous substrate. 1977, ApJ, 218, 148

Meijerink, R. & Spaans, M., Diagnostics of irradiated gas in galaxy nuclei. I. A far-ultraviolet and X-ray dominated region code. 2005, A&A, 436, 397

Meisner, J., Lamberts, T., & Kästner, J., Atom Tunneling in the Water Formation Reaction H2 + OH $\rightarrow$ H2O + H on an Ice Surface. 2017, ACS Earth and Space Chemistry, 1, 399

Mendoza, C. 1983, in Planetary Nebulae, ed. L. H. Aller, Vol. 103, 143–172

Mookerjea, B., Israel, F., Kramer, C., et al., Velocity resolved [C II] spectroscopy of the center and the BCLMP 302 region of M 33 (HerM 33es). 2016, A&A, 586, A37

Muraoka, K., Kondo, H., Tokuda, K., et al., ALMA Observations of Giant Molecular Clouds in M33. II. Triggered High-mass Star Formation by Multiple Gas Colliding Events at the NGC 604 Complex. 2020, ApJ, 903, 94

Naab, T. & Ostriker, J. P., Theoretical Challenges in Galaxy Formation. 2017, ARA&A, 55, 59

Nelson, R. P. & Langer, W. D., The Dynamics of Low-Mass Molecular Clouds in External Radiation Fields. 1997, ApJ, 482, 796

Nelson, R. P. & Langer, W. D., On the Stability and Evolution of Isolated BOK Globules. 1999, ApJ, 524, 923

Nishi, R., Nakano, T., & Umebayashi, T., Magnetic Flux Loss from Interstellar Clouds with Various Grain-Size Distributions. 1991, ApJ, 368, 181

Offner, S. S. R., Bisbas, T. G., Bell, T. A., & Viti, S., An alternative accurate tracer of molecular clouds: the 'XCi-factor'. 2014, MNRAS, 440, L81

Oort, J. H., Outline of a theory on the origin and acceleration of interstellar clouds and O associations. 1954, Bull. Astron. Inst. Netherlands, 12, 177

Ossenkopf, V., The Sobolev approximation in molecular clouds. 1997, New A, 2, 365

Ossenkopf, V., Ormel, C. W., Simon, R., Sun, K., & Stutzki, J., Spectroscopic [C I] mapping of the infrared dark cloud G48.65-0.29. 2011, A&A, 525, A9

Pabst, C. H. M., Goicoechea, J. R., Hacar, A., et al., [C II] 158 μm line emission from Orion A. II. Photodissociation region physics. 2022, A&A, 658, A98

Pabst, C. H. M., Goicoechea, J. R., Teyssier, D., et al., Expanding bubbles in Orion A: [C II] observations of M 42, M 43, and NGC 1977. 2020, A&A, 639, A2

Pabst, C. H. M., Goicoechea, J. R., Teyssier, D., et al., [C II] emission from L1630 in the Orion B molecular cloud. 2017, A&A, 606, A29

Padoan, P., Nordlund, A., & Jones, B. J. T., The universality of the stellar initial mass function. 1997, MNRAS, 288, 145

Pallottini, A., Ferrara, A., Decataldo, D., et al., Deep into the structure of the first galaxies: SERRA views. 2019, MNRAS, 487, 1689

Palmeirim, P., André, P., Kirk, J., et al., Herschel view of the Taurus B211/3 filament and striations: evidence of filamentary growth? 2013, A&A, 550, A38

Papadopoulos, P. P. & Greve, T. R., C I Emission in Ultraluminous Infrared Galaxies as a Molecular Gas Mass Tracer. 2004, ApJ, 615, L29

Parker, E. N., The Dynamical State of the Interstellar Gas and Field. 1966, ApJ, 145, 811

Pérez-Beaupuits, J. P., Wiesemeyer, H., Ossenkopf, V., et al., The ionized and hot gas in M17 SW. SOFIA/GREAT THz observations of [C II] and ^{12}CO J = 13-12. 2012, A&A, 542, L13

Peters, T., Naab, T., Walch, S., et al., The SILCC project - IV. Impact of dissociating and ionizing radiation on the interstellar medium and Hα emission as a tracer of the star formation rate. 2017, MNRAS, 466, 3293

Pilbratt, G. L., Riedinger, J. R., Passvogel, T., et al., Herschel Space Observatory. An ESA facility for far-infrared and submillimetre astronomy. 2010, A&A, 518, L1

Pineda, J. L., Fischer, C., Kapala, M., et al., A SOFIA Survey of [C II] in the Galaxy M51. I. [C II] as a Tracer of Star Formation. 2018, ApJ, 869, L30

Pineda, J. L., Langer, W. D., Velusamy, T., & Goldsmith, P. F., A Herschel [C ii] Galactic plane survey. I. The global distribution of ISM gas components. 2013, A&A, 554, A103

Pitann, J., Linz, H., Ragan, S., et al., G048.66-0.29: Physical State of an Isolated Site of Massive Star Formation. 2013, ApJ, 766, 68

Planck Collaboration, Ade, P. A. R., Aghanim, N., et al., Planck intermediate results. XXXV. Probing the role of the magnetic field in the formation of structure in molecular clouds. 2016, A&A, 586, A138

Planck Collaboration, Aghanim, N., Akrami, Y., et al., Planck 2018 results. XII. Galactic astrophysics using polarized dust emission. 2020, A&A, 641, A12

Poglitsch, A., Waelkens, C., Geis, N., et al., The Photodetector Array Camera and Spectrometer (PACS) on the Herschel Space Observatory. 2010, A&A, 518, L2

Pontoppidan, K. M., Meijerink, R., Dullemond, C. P., & Blake, G. A., A New Raytracer for Modeling AU-Scale Imaging of Lines from Protoplanetary Disks. 2009, ApJ, 704, 1482

Press, W. H., Teukolsky, S. A., Vetterling, W. T., & Flannery, B. P. 2007, Numerical Recipes 3rd Edition: The Art of Scientific Computing, 3rd edn. (Cambridge University Press)

Rathjen, T.-E., Naab, T., Walch, S., et al., SILCC VII – Gas kinematics and multiphase outflows of the simulated ISM at high gas surface densities. 2022, arXiv e-prints, arXiv:2211.15419

Redondo, P., Pauzat, F., Markovits, A., & Ellinger, Y., Revisiting the OH + $H_2 \rightarrow$ H_2O + H reaction at the molecular level: the plausible catalytic role of ice in its own reconstruction. 2021, A&A, 646, A163

Risacher, C., Güsten, R., Stutzki, J., et al., The upGREAT Dual Frequency Heterodyne Arrays for SOFIA. 2018, Journal of Astronomical Instrumentation, 7, 1840014

Röllig, M., Abel, N. P., Bell, T., et al., A photon dominated region code comparison study. 2007, A&A, 467, 187

Röllig, M., Ossenkopf, V., Jeyakumar, S., Stutzki, J., & Sternberg, A., [CII] 158 μm emission and metallicity in photon dominated regions. 2006, A&A, 451, 917

Röllig, M., Simon, R., Güsten, R., et al., [C II] 158 μm and [N II] 205 μm emission from IC 342. Disentangling the emission from ionized and photo-dissociated regions. 2016, A&A, 591, A33

Rosen, A. L., Li, P. S., Zhang, Q., & Burkhart, B., Massive-star Formation via the Collapse of Subvirial and Virialized Turbulent Massive Cores. 2019, ApJ, 887, 108

Roueff, E., Abgrall, H., Czachorowski, P., et al., The full infrared spectrum of molecular hydrogen. 2019, A&A, 630, A58

Rybicki, G. B. & Lightman, A. P. 1979, Radiative processes in astrophysics

Saintonge, A., Catinella, B., Tacconi, L. J., et al., xCOLD GASS: The Complete IRAM 30 m Legacy Survey of Molecular Gas for Galaxy Evolution Studies. 2017, ApJS, 233, 22

Saito, T., Michiyama, T., Liu, D., et al., The 300-pc scale ALMA view of [C I] $^3P_1$-$^3P_0$, CO J = 1-0, and 609-μm dust continuum in a luminous infrared galaxy. 2020, MNRAS, 497, 3591

Salpeter, E. E., The Luminosity Function and Stellar Evolution. 1955, ApJ, 121, 161

Schmidt, M., The Rate of Star Formation. 1959, ApJ, 129, 243

Schneider, N., Güsten, R., Tremblin, P., et al., Globules and pillars seen in the [CII] 158 μm line with SOFIA. 2012, A&A, 542, L18

Schneider, N., Simon, R., Guevara, C., et al., FEEDBACK: a SOFIA Legacy Program to Study Stellar Feedback in Regions of Massive Star Formation. 2020, PASP, 132, 104301

Schöier, F. L., van der Tak, F. F. S., van Dishoeck, E. F., & Black, J. H., An atomic and molecular database for analysis of submillimetre line observations. 2005, A&A, 432, 369

Seifried, D., Haid, S., Walch, S., Borchert, E. M. A., & Bisbas, T. G., SILCC-Zoom: H_2 and CO-dark gas in molecular clouds - the impact of feedback and magnetic fields. 2020, MNRAS, 492, 1465

Seifried, D., Sánchez-Monge, Á., Suri, S., & Walch, S., Modelling the chemistry of star-forming filaments - II. Testing filament characteristics with synthetic observations. 2017, MNRAS, 467, 4467

Sembach, K. R., Howk, J. C., Ryans, R. S. I., & Keenan, F. P., Modeling the Warm Ionized Interstellar Medium and Its Impact on Elemental Abundance Studies. 2000, ApJ, 528, 310

Shetty, R., Glover, S. C., Dullemond, C. P., & Klessen, R. S., Modelling CO emission - I. CO as a column density tracer and the X factor in molecular clouds. 2011, MNRAS, 412, 1686

Snow, T. P. & McCall, B. J., Diffuse Atomic and Molecular Clouds. 2006, ARA&A, 44, 367

Sobolev, V. V., The Diffusion of Lα Radiation in Nebulae and Stellar Envelopes. 1957, Soviet Ast., 1, 678

Soler, J. D., Ade, P. A. R., Angilè, F. E., et al., The relation between the column density structures and the magnetic field orientation in the Vela C molecular complex. 2017, A&A, 603, A64

Spitzer, Lyman, J., The Dynamics of the Interstellar Medium. III. Galactic Distribution. 1942, ApJ, 95, 329

Spitzer, L. 1978, Physical processes in the interstellar medium

Stahler, S. W. & Palla, F. 2004, The Formation of Stars

Strömgren, B., The Physical State of Interstellar Hydrogen. 1939, ApJ, 89, 526

Strong, A. W., Moskalenko, I. V., & Reimer, O., Diffuse Continuum Gamma Rays from the Galaxy. 2000, ApJ, 537, 763

Sutherland, R. S. & Dopita, M. A., Cooling Functions for Low-Density Astrophysical Plasmas. 1993, ApJS, 88, 253

Tan, J. C., Krumholz, M. R., & McKee, C. F., Equilibrium Star Cluster Formation. 2006, ApJ, 641, L121

Taylor, C. L., Hüttemeister, S., Klein, U., & Greve, A., Giant molecular clouds in the dwarf galaxy NGC 1569. 1999, A&A, 349, 424

Tielens, A. G. G. M. 2005, The Physics and Chemistry of the Interstellar Medium

Tielens, A. G. G. M. & Hollenbach, D., Photodissociation regions. I. Basic model. 1985, ApJ, 291, 722

Tiwari, M., Karim, R., Pound, M. W., et al., SOFIA FEEDBACK Survey: Exploring the Dynamics of the Stellar Wind-Driven Shell of RCW 49. 2021, ApJ, 914, 117

Truelove, J. K., Klein, R. I., McKee, C. F., et al., The Jeans Condition: A New Constraint on Spatial Resolution in Simulations of Isothermal Self-gravitational Hydrodynamics. 1997, ApJ, 489, L179

Vallini, L., Ferrara, A., Pallottini, A., Carniani, S., & Gallerani, S., High [O III]/[C II] surface brightness ratios trace early starburst galaxies. 2021, MNRAS, 505, 5543

Vallini, L., Gallerani, S., Ferrara, A., Pallottini, A., & Yue, B., On the [CII]-SFR Relation in High Redshift Galaxies. 2015, ApJ, 813, 36

Vallini, L., Pallottini, A., Ferrara, A., et al., CO line emission from galaxies in the Epoch of Reionization. 2018, MNRAS, 473, 271

van der Tak, F. F. S., Black, J. H., Schöier, F. L., Jansen, D. J., & van Dishoeck, E. F., A computer program for fast non-LTE analysis of interstellar line spectra. With diagnostic plots to interpret observed line intensity ratios. 2007, A&A, 468, 627

van Dishoeck, E. F. & Black, J. H., The Photodissociation and Chemistry of Interstellar CO. 1988, ApJ, 334, 771

van Dishoeck, E. F., Glassgold, A. E., Guelin, M., et al. 1992, in Astrochemistry of Cosmic Phenomena, ed. P. D. Singh, Vol. 150, 285

Vázquez-Semadeni, E., Palau, A., Ballesteros-Paredes, J., Gómez, G. C., & Zamora-Avilés, M., Global hierarchical collapse in molecular clouds. Towards a comprehensive scenario. 2019, MNRAS, 490, 3061

Velusamy, T. & Langer, W. D., Origin and z-distribution of Galactic diffuse [C II] emission. 2014, A&A, 572, A45

Visser, R., van Dishoeck, E. F., & Black, J. H., The photodissociation and chemistry of CO isotopologues: applications to interstellar clouds and circumstellar disks. 2009, A&A, 503, 323

Waagan, K., A positive MUSCL-Hancock scheme for ideal magnetohydrodynamics. 2009, Journal of Computational Physics, 228, 8609

Waagan, K., Federrath, C., & Klingenberg, C., A robust numerical scheme for highly compressible magnetohydrodynamics: Nonlinear stability, implementation and tests. 2011, Journal of Computational Physics, 230, 3331

Wakelam, V. & Herbst, E., Polycyclic Aromatic Hydrocarbons in Dense Cloud Chemistry. 2008, ApJ, 680, 371

Walch, S., Girichidis, P., Naab, T., et al., The SILCC (SImulating the LifeCycle of molecular Clouds) project - I. Chemical evolution of the supernova-driven ISM. 2015, MNRAS, 454, 238

Walch, S. & Naab, T., The energy and momentum input of supernova explosions in structured and ionized molecular clouds. 2015, MNRAS, 451, 2757

Walker, K. M., Song, L., Yang, B. H., et al., Quantum Calculation of Inelastic CO Collisions with H. II. Pure Rotational Quenching of High Rotational Levels. 2015, ApJ, 811, 27

Walmsley, C. M., Bertout, C., Combes, F., et al., GREAT special feature. 2012, A&A, 542, E1

Wardle, M., Star Formation and the Hall Effect. 2004, Ap&SS, 292, 317

Wardlow, J. L., Simpson, J. M., Smail, I., et al., An ALMA survey of CO in submillimetre galaxies: companions, triggering, and the environment in blended sources. 2018, MNRAS, 479, 3879

Weingartner, J. C. & Draine, B. T., Dust Grain-Size Distributions and Extinction in the Milky Way, Large Magellanic Cloud, and Small Magellanic Cloud. 2001, ApJ, 548, 296

Wiese, W. L. & Fuhr, J. R., Improved Critical Compilations of Selected Atomic Transition Probabilities for Neutral and Singly Ionized Carbon and Nitrogen. 2007, Journal of Physical and Chemical Reference Data, 36, 1287

Wolfire, M. G., Hollenbach, D., & McKee, C. F., The Dark Molecular Gas. 2010, ApJ, 716, 1191

Wolfire, M. G., Hollenbach, D., McKee, C. F., Tielens, A. G. G. M., & Bakes, E. L. O., The Neutral Atomic Phases of the Interstellar Medium. 1995, ApJ, 443, 152

Wolfire, M. G., McKee, C. F., Hollenbach, D., & Tielens, A. G. G. M., Neutral Atomic Phases of the Interstellar Medium in the Galaxy. 2003, ApJ, 587, 278

Wright, E. L., Eisenhardt, P. R. M., Mainzer, A. K., et al., The Wide-field Infrared Survey Explorer (WISE): Mission Description and Initial On-orbit Performance. 2010, AJ, 140, 1868

Wünsch, R., Walch, S., Dinnbier, F., et al., Tree-based solvers for adaptive mesh refinement code FLASH - II: radiation transport module TreeRay. 2021, MNRAS, 505, 3730

Wünsch, R., Walch, S., Dinnbier, F., & Whitworth, A., Tree-based solvers for adaptive mesh refinement code FLASH - I: gravity and optical depths. 2018, MNRAS, 475, 3393

Yan, M. 1997, PhD thesis, Harvard University, Massachusetts

Young, E. T., Becklin, E. E., Marcum, P. M., et al., Early Science with SOFIA, the Stratospheric Observatory For Infrared Astronomy. 2012, ApJ, 749, L17

Zuckerman, B. & Evans, N. J., I., Models of Massive Molecular Clouds. 1974, ApJ, 192, L149

DATA AVAILABILITY

The data underlying this thesis will be shared on reasonable request to the supervisor.
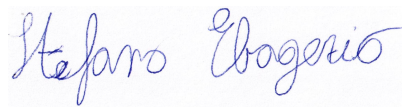
Selbstständigkeitserklärung

Hiermit versichere ich an Eides statt, dass ich die vorliegende Dissertation selbstständig und ohne die Benutzung anderer als der angegebenen Hilfsmittel und Literatur angefertigt habe. Alle Stellen, die wörtlich oder sinngemäß aus veröffentlichten und nicht veröffentlichten Werken dem Wortlaut oder dem Sinn nach entnommen wurden, sind als solche kenntlich gemacht. Ich versichere an Eides statt, dass diese Dissertation noch keiner anderen Fakultät oder Universität zur Prüfung vorgelegen hat; dass sie - abgesehen von unten angegebenen Teilpublikationen und eingebundenen Artikeln und Manuskripten - noch nicht veröffentlicht worden ist sowie, dass ich eine Veröffentlichung der Dissertation vor Abschluss der Promotion nicht ohne Genehmigung des Promotionsausschusses vornehmen werde. Die Bestimmungen dieser Ordnung sind mir bekannt. Darüber hinaus erkläre ich hiermit, dass ich die Ordnung zur Sicherung guter wissenschaftlicher Praxis und zum Umgang mit wissenschaftlichem Fehlverhalten der Universität zu Köln gelesen und sie bei der Durchführung der Dissertation zugrundeliegenden Arbeiten und der schriftlich verfassten Dissertation beachtet habe und verpflichte mich hiermit, die dort genannten Vorgaben bei allen wissenschaftlichen Tätigkeiten zu beachten und umzusetzen. Ich versichere, dass die eingereichte elektronische Fassung der eingereichten Druckfassung vollständig entspricht."

Teilpublikationen:

- *CO and [CII] line emission of molecular clouds - the impact of stellar feedback and non-equilibrium chemistry* (Ebagezio et al., in prep, 2023)

- *The origin of the [CII]-deficit in HII regions and star forming molecular clouds* (Ebagezio et al., in prep, 2023)

Köln, den 09.02.2023

(Stefano Ebagezio)

Personal information

First name /Surname	Stefano Ebagezio
Address	Kornblumenweg, 10 – 50354 Hürth, Germany
Telephone	+393393935417
E-mail	ebagezio@ph1.uni-koeln.de
Nationality	Italian
Date of birth	24/10/1994
Place of birth	Moncalieri (TO), Italy

Education

1st June 2019 -	PhD Candidate in Astronomy at the University of Cologne (Germany)
11th April 2019	Master's Degree in Physics; grade: 110/110 *cum laude*
	The title of the Thesis is "Hypervelocity Stars: a study of ejection mechanisms"; it reports the results of numerical simulations of two possible ejection mechanisms for the Hypervelocity Stars in the Galactic Center. Consistency between the two hypothesized mechanisms and observations is investigated.
3 – 13 August 2017	Participation in the "Petnica Summer Institute", a summer school in Cosmology held in Serbia with professors working in prestigious institutions such as Stanford University (CA, USA), SISSA (Trieste, Italy), INFN and Lapth-CNRS (Annecy-les-Vieux, France)
Autumn 2016	Beginning of Master in Astrophysics at the University of Torino
18th October 2016	Bachelor's Degree in Physics; grade: 110/110
	The title of the Thesis is "Computational Study of the Bell Instability"; it reports the results of a numerical simulation of this interstellar plasma instability, whose presence may have an important role in the acceleration of cosmic rays.
23rd – 29th August 2015	Participation in the "Plas@Par" Summer School, organized by the Sorbonne University in Roscoff (Brittany, France)
September 2014	Participation in the "Alphaclass" project, a summer school in Mathematics organized in Torino by the Departments of Mathematics of both the University and the Polytechnic of Torino, together with the CRT Bank Foundation.
July 2013	Scientific high school degree; grade: 100/100 *cum laude*.

Work Experience

October 2019 -	Tutor on Electromagnetism, Interstellar Medium, and computational Hydrodynamics courses within my PhD Program
October 2018 – May 2019	Collaboration with INFN (Istituto Nazionale di Fisica Nucleare) in a refresher course addressed to Middle School teachers. The course has the purpose of showing them some Physics experiments they can easily repeat in their classes in order to grow up the interest in Physics in 11 – 13 years old students.
September 2017 – May 2018	Guide at *L'infinita Curiosità* exhibition in Torino.
	I provided several dozens guided tours of the exhibition to classes from Elementary to High School and to general public. The exhibition was about different aspects of contemporary Physics, which were introduced following the academic activity of the Italian physicist Tullio Regge. Apart from knowledge of the exhibition contents, ability of adapting complicated concepts to general public (or to Elementary School children) was the most important heritage this experience left to me.
April 2017 – June 2018	Laboratory tutor in the Geometrical Optics and Physics Laboratory I courses at the Department of Physics of the University of Torino
	I helped Optics and Physics students at their first laboratory experience in completing their assignments, such as testing thin lenses, measuring the refractive index of a prism or specific heat of a certain object. I also helped them with data analysis.
November 2016 – January 2018	Tutor in the General Physics I (Mechanics, Fluids and Thermodynamics) course at the Department of Physics of the University of Torino.
	I provided extra exercises for Optics students who had some difficulties in preparing the written part of the exam. I also helped them in solving them in individual or group activities.

Other relevant experiences

October 2021 -	Member of the SB956 Student Council, first speaker from June 2022. I organised seminars for PhD students in Cologne and Bonn, student retreats, and presented the activity of the Student Council in faculty events.
April 2021 - November 2022	Student Representative at the IMPRS Bonn.

June 2017 - March 2018	Member of the committee for quality evaluation of Bachelor's and Master's courses of the Natural Science Faculty at the University of Torino

Foreign languages

English	Certificate of Advanced English (Council of Europe level C1) obtained in October 2015. The entire PhD program (June 2019 -) is held in English.
German	Intermediate level. Knowledge comparable with Council of Europe level B1 - B2
French	Intermediate level reading, beginner level in listening and speaking

Programming skills	Medium level knowledge of C++ language (four courses attended at the University, also object-oriented); good level of Python. Basic knowledge of *ROOT* and *Mathematica* packages for data analysis.
Hobbies	I studied piano and music theory for six years (2006 – 2012). I have been playing organ in some churches of my home town since 2012.